Electrical Stress Induced Structural Dynamics in Silicon Oxide Resistive Memories

Kamal Patel

A dissertation submitted in partial fulfillment

of the requirements for the degree of

Doctor of Philosophy

of

University College London.

Department of Physics and Astronomy

University College London

March 2, 2021

I, Kamal Patel, confirm that the work presented in this thesis is my own. Where information has been derived from other sources, I confirm that this has been indicated in the work.

Abstract

In this thesis, the effects of electrical stress on silicon oxide resistive random-access memory (RRAM) devices are studied with a view of understanding the individual mechanisms involved during RRAM operation. This is achieved through a combination of density functional theory (DFT) modelling and characterisation using transmission electron microscopy (TEM).

In Part I of the thesis, DFT is applied to model the incorporation, diffusion, reduction, and cluster nucleation of Ag in Ag/SiO_2/Pt RRAM devices. It is found that Ag incorporates into SiO_2 as a Ag^{+1} ion, which is mobile through large rings, grain boundaries and column boundaries. An O vacancy (V_O) mediated Ag cluster model is then proposed, where Ag^{+1} reduction is shown to occur at 33% and 11% of V_O sites at the Ag and Pt electrodes, respectively. In this case, Ag^{+1} ions bind to V_O forming the $[Ag_i/V_O]^{+1}$ complex, which is favoured to trap an electron from the respective electrode. The energy gained through the metallic Ag-Ag bonding of additional Ag^{+1} ions to the $[Ag_i/V_O]$ complex compensates strain in the lattice leading to the breaking of Si-O bonds. The broken Si-O bonds open access to new voids into which small Ag clusters may break from the original Ag cluster and form, providing new sites for cluster nucleation.

In Part II of the thesis, Au-Ti-SiO_x-Mo, Au-SiO_x-Mo and Ti-SiO_x-Mo ($x \approx 1.95$) RRAM devices are characterised through TEM. It is shown the roughness of the Mo layer leads to patterning in the device, where voids and column boundaries form in SiO_x at the troughs of the SiO_x/Mo interface. The column boundaries are shown to facilitate the transport of Ti and Mo during positive electroforming leading to conductive metal-oxide filaments in the SiO_x layer. Conversely, oxygen is

dispelled from SiO_x under negative electroforming, allowing electron tunneling *via* trap assisted tunnelling through V_O sites.

In this thesis, the effects of electrical stress on silicon oxide resistive random access memory (RRAM) devices are studied with a view of understanding the individual mechanisms involved in RRAM operation. This is achieved through a combination of density functional theory (DFT) modelling and characterisation using transmission electron microscopy (TEM).

In Part I of the thesis, DFT is used to model the incorporation, diffusion, reduction, and cluster nucleation of Ag in Ag/SiO_2/Pt RRAM devices. It is found that Ag incorporates into SiO_2 as a Ag^{+1} ion, which is mobile through large rings, grain boundaries and column boundaries. An O vacancy (V_O) mediated Ag cluster model is then proposed, where Ag^{+1} reduction is shown to occur at 33% and 11% of V_O sites at the Ag and Pt electrodes, respectively. In this case, Ag^{+1} ions bind to V_O forming the $[Ag_i/V_O]^j$ complex, which is favoured to trap electrons from the electrodes. In this way, as a Ag cluster grows, the metallic Ag-Ag bonding compensates strain in the lattice leading to the breaking of Si-O bonds. The broken Si-O bonds open access to new voids into which small Ag clusters may break from the original Ag cluster and form, providing new sites for cluster nucleation.

In Part II of the thesis, Au-Ti-SiO_x-Mo, Au-SiO_x-Mo and Ti-SiO_x-Mo ($x \approx 1.95$) RRAM devices are characterised through TEM. It is shown the roughness of the Mo layer leads to patterning in the device, where voids and column boundaries form in SiO_x at the troughs of the SiO_x/Mo interface. The column boundaries are shown to facilitate the transport of Ti and Mo during positive electroforming leading to conductive metal-oxide filaments in the SiO_x layer. Conversely, oxygen is
dispelled from SiO_x under negative electroforming, allowing electron tunneling *via* trap assisted tunnelling through V_O sites.

Impact Statement

Resistive random access memories (RRAM) have the potential to provide an energy efficient, low-cost, and highly scalable alternative to current memory technologies. In particular, silicon oxide RRAM devices offer great integration with current technology, whilst already being a well studied and used material. For devices to realise their potential however, it is imperative they operate in a controlled and reliable manner. This project acts to unlock this potential by systematically looking at the fundamental mechanisms involved in silicon oxide RRAM operation at the atomic scale. More specifically, the work in this thesis provides understanding of the structural changes observed in silicon oxide RRAM devices under electrical stress.

Previous research shows that devices typically operate under the electrochemical metallisation mechanism or the valence change mechanism. In this work, a combination of theoretical and experimental techniques have been used to study Ag, Au-Ti, Au and Ti top electrode devices, with the results showing that both mechanisms occur simultaneously in silicon oxide devices. Subsequently, the interplay of these mechanisms can lead to highly performing RRAM devices. Though providing a step in the right direction, it should be noted that a lot of work is still needed to improve devices for industrial use.

Acknowledgements

I would like to this opportunity to thank all of the people who have helped me over the course of this PhD. First and foremost, I am grateful to Prof. Alexander Shluger who has provided me with this amazing opportunity to develop over the course of the project. His excellent guidance, support and rigorous debate have been paramount to the completion of this work. I also thank Assoc. Prof. Michel Bosman whose training and guidance has been equally important. He did an amazing job passing on his expertise in TEM, and helped make my time in Singapore very enjoyable. I would also like to thank Prof. Anthony Kenyon who has contributed his time and expertise for the development of the project, and had an equally important role in providing this opportunity.

I would also like to thank the group of Prof. Alexander Shluger for many useful discussions and support. In particular, I would like to express my appreciation to Jon Cottom for his mentorship throughout the entire PhD. He has gone above and beyond to assist me complete this work and provided many insightful discussions and explanations. Also, I want to thank my fellow colleagues Adnan Mehonic and Wing Ng from UCL and Siew Lang Teo and Hui Kim from the Institute of Materials Research and Engineering for their help and support in different aspects of the project. I would also like to thank Prof. Kin Leong Pey and his group at the Singapore University of Technology and Design (SUTD), for providing additional support during my time in Singapore. The entire group, including Alok Ranjan and Mei Sen made an incredible effort to assist me wherever possible.

Finally, I would like to thank Zhimei Du and the UK Centre for Doctoral Training in Molecular Modelling and Materials Science as well as ES-

PRC (EP/L015862/1) for funding during my time at UCL. Additionally, I thank A*STAR for funding my time in Singapore through the A*STAR Research Attachment Programme (ARAP). I also thank the UK Materials Chemistry Consortium (EP/L000202) for computer time with ARCHER, the UK National Supercomputing Service. The Leverhulme Trust is also acknowledged for funding part of this work (RPG-2016-135).

Special mentions go to my family and friends for their support throughout the process.

Contents

1 Introduction **37**

1.1 Background . . . 37

1.2 Motivation . . . 38

1.3 Resistive Random Access Memory (RRAM) Devices . . . 38

1.4 Thesis Outline . . . 41

2 Theoretical Background and Methods **44**

2.1 Introduction . . . 44

2.2 Implementation of DFT in CP2K . . . 45

2.2.1 Gaussian plane wave (GPW) method . . . 45

2.2.2 Exchange Correlation Functionals . . . 47

2.2.3 Auxiliary Density Matrix Method (ADMM) . . . 50

2.3 Defect Calculations with DFT . . . 51

2.3.1 Defect Formation Energy . . . 51

2.3.2 Nudged Elastic Band (NEB) method . . . 53

2.4 Molecular Dynamics . . . 55

2.4.1 Classical Potential Energy Functions . . . 57

2.4.2 Integration of Newton's Law . . . 58

2.4.3 NVT Ensemble . . . 58

2.4.4 Nose-Hoover thermostat . . . 59

3 Experimental Background and Methods **60**

3.1 Introduction . . . 60

3.2 Device Fabrication 62
3.2.1 Reactive Sputtering 62
3.2.2 Thermal Evaporation 64
3.2.3 Fabrication Summary 65
3.3 Transmission Electron Microscopy 66
3.3.1 Transmission Electron Microscopes 67
3.3.2 Imaging and Spectroscopy 76
3.3.3 Lamella preparation - FIB 82
3.4 Summary 83

I Electrical Stress Induced Structural Dynamics in Ag-SiO_2-Pt RRAM Devices: A DFT Case Study 85

4.1 Research Question 86
4.2 Outline 86
4.3 Background & Literature 87
4.3.1 Ag Incorporation 93
4.3.2 Ag Diffusion 94
4.3.3 Ag Reduction 95
4.3.4 Ag Clustering and Filament Formation 96

5 Ag interactions in α-quartz 97

5.1 Introduction 97
5.2 Previous Studies of Ag in α-quartz 98
5.2.1 Electron Paramagnetic Resonance of Ag^0 Centre 98
5.2.2 Ag^{+1} Photoluminescence 99
5.3 Theoretical Methodology 100
5.3.1 Convergence Testing 100
5.3.2 Functional Testing 102
5.3.3 DFT Parameters 104
5.3.4 Vibrational Analysis 105
5.3.5 Ag Defect in α-quartz 105

5.3.6 Electron Paramagnetic Resonance (EPR) calculations 105
5.4 Results 107
5.4.1 α-quartz 107
5.4.2 Ag in α-quartz 109
5.5 Summary of Main Results 125
5.5.1 Experimental Verification 125
5.5.2 Ag-SiO_2-Pt RRAM 126
5.6 Conclusion 128

6 Ag Redox Reactions and Migration in a-SiO_2 130
6.1 Introduction 130
6.2 Theoretical Methodology 131
6.2.1 Ag/a-SiO_2 interface 131
6.2.2 Grain and Column Boundaries 133
6.2.3 Ag in a-SiO_2 133
6.3 Results 135
6.3.1 Ag incorporation 135
6.3.2 a-SiO_2 models 138
6.3.3 Ag^0 in a-SiO_2 140
6.3.4 Ag^{+1} in a-SiO_2 142
6.3.5 Ag in a-SiO_2 143
6.3.6 Ag diffusion in a-SiO_2 bulk 144
6.3.7 Ag in Grain and Column Boundaries 146
6.3.8 V_O mediated Ag^{+1} reduction in a-SiO_2 148
6.4 Summary of Main Results 153
6.4.1 Ag Incorporation and Migration in a-SiO_2 153
6.4.2 O vacancy mediated Ag^{+1} reduction 154
6.5 Conclusion 156

7 Ag Clustering in a-SiO_2 157
7.1 Introduction 157

7.2 Theoretical Methodology 157
7.3 Results 158
7.3.1 V_O mediated Ag cluster nucleation mechanism 158
7.3.2 Ag Cluster Induced Strain in a-SiO_2 165
7.3.3 Vacancy generation by electron injection 169
7.3.4 Molecular dynamics simulations 170
7.4 Summary of Main Results 174
7.4.1 Ag cluster nucleation 174
7.5 Conclusion 177

8 Part I: Summary and Future Work 179
8.1 Summary 179
8.2 Future Work 181

II Electrical Stress Induced Structural Dynamics in SiO_x RRAM Devices: An Electron Microscopy Study 182
9.1 Research Question 183
9.2 Outline 183
9.3 Part II: Background & Literature 185
9.3.1 VCM mechanism in SiO_x RRAM devices 185
9.3.2 O Vacancy Generation and Electron Transport in SiO_x RRAM devices 187
9.4 Methods 189
9.4.1 EELS Fine Structure 190
9.4.2 Average Scan 194

10 Ti-SiO_x-Mo (Ti) RRAM device 195
10.1 Introduction 195
10.2 Pristine Ti-SiO_x-Mo (Ti) RRAM device 196
10.2.1 HAADF Analysis 196
10.2.2 EELS Analysis 201

10.3 Electroformed Ti-SiO_x-Mo (Ti) RRAM device . . . 206
10.3.1 IV curve . . . 206
10.3.2 Positive electroformed Ti Device . . . 207
10.3.3 Negative Electroformed Ti Device . . . 214
10.3.4 Ti Device comparison . . . 219
10.4 Summary of Main Results . . . 222
10.4.1 Device Microstructure (Pristine) . . . 222
10.4.2 Structural Dynamics Due to Electrical Stress . . . 223
10.5 Conclusion . . . 224

11 Au-SiO_x-Mo (Au) RRAM device 225

11.1 Introduction . . . 225
11.2 Pristine Au-SiO_x-Mo (Au) RRAM device . . . 226
11.2.1 HAADF Analysis . . . 226
11.2.2 EDX Analysis . . . 229
11.2.3 EELS Analysis . . . 231
11.3 Electroformed Au-SiO_x-Mo (Au) RRAM device . . . 237
11.3.1 IV curve . . . 237
11.3.2 Positive electroformed Au Device . . . 238
11.3.3 Negative Electroformed Au Device . . . 244
11.3.4 Au Device Comparison . . . 249
11.4 Summary of Main Results . . . 252
11.4.1 Device Microstructure (Pristine) . . . 252
11.4.2 Structural Dynamics Due to Electrical Stress . . . 252
11.5 Conclusion . . . 254

12 Au-Ti-SiO_x-Mo (Au-Ti) RRAM device 255

12.1 Introduction . . . 255
12.2 Pristine Au-Ti-SiO_x-Mo (Au-Ti) Device . . . 257
12.2.1 HAADF Analysis . . . 257
12.2.2 EDX Analysis . . . 263

12.2.3 EELS Analysis 264
12.3 Columnar Boundaries 267
12.4 Electroformed Au-Ti-SiO_x-Mo (Au-Ti) RRAM device 270
12.4.1 IV curve 270
12.4.2 Positive electroformed Au-Ti Device 272
12.4.3 Negative electroformed Au-Ti Device 276
12.5 Summary of Main Results 280
12.5.1 Device Microstructure (Pristine) 280
12.5.2 Structural Dynamics Due to Electrical Stress 280
12.6 Conclusion 283

13 Part II: Summary and Future Work 284
13.1 Summary 284
13.2 Future Work 286

14 Final Conclusions 287

Bibliography 289

List Of Publications

1) K. Patel, J. Cottom, M. Bosman, A. J. Kenyon and A. L. Shluger, "Theoretical Study of Ag Interactions in Amorphous Silica RRAM Devices." 2018 IEEE International Symposium on the Physical and Failure Analysis of Integrated Circuits (IPFA), Singapore, 2018, pp. 1-5, doi: 10.1109/IPFA.2018.8452536.
2) K. Patel, J. Cottom, M. Bosman, A. J. Kenyon, A. L. Shluger, (2019). "An Oxygen Vacancy Mediated Ag Reduction and Nucleation Mechanism in SiO_2 RRAM Devices." Microelectronics Reliability. 98. 144-152. 10.1016/j.microrel.2019.05.005.
3) M. Mistry, J. Cottom, K. Patel, A. M. El-Sayed, G. Pobegen, T. Aichinger, A. L. Shluger (2019). "First Principles Study of the Influence of the Local Steric Environment on the Incorporation and Migration of NO in a-SiO_2." Materials Science Forum. 963. 10.4028/www.scientific.net/MSF.963.194.
4) J. Cottom, A. Bochakrev, E. Olsson, K. Patel, M. Munde, J. Spitaler, M. Popov, M. Bosman, A. L. Shluger, (2019). "Modeling of Diffusion and Incorporation of Interstitial Oxygen Ions at the TiN/SiO_2 Interface." ACS Applied Materials & Interfaces. 11. 10.1021/acsami.9b10705.

List Of Abbreviations

A*STAR = Agency of Science, Technology and Research

AES = Auger Electron Microscopy

AFM = Atomic Force Microscopy

CBM = Conduction Band Minimum

CMOS = Complementary Metal-Oxide-Semiconductor

CRN = Continuous Random Network

DFE = Defect Formation Energy

DFT = Density Functional Theory

DOS = Density of States

ECM = Electrochemical Metalisation Memory

EELS = Electron Energy-Loss Spectroscopy

EDX = Energy-dispersive X-ray

EPR = Electron Paramagnetic Resonance

FFT = Fast Fourier Transform

FIB = Focused Ion Beam

GGA = Generalised Gradient Approximation

GTO = Gaussian Type Orbital

HAADF = High-Angle Annular Dark Field

HF = Hartree-Fock

HOMO = Highest Occupied Molecular Orbital

HRTEM = High-Resolution Transmission Electron Microscopy

IMRE = Institute of Materials Research and Engineering (in Singapore)

LDA = Local Density Approximation

LUMO = Lowest Unoccupied Molecular Orbital

MD = Molecular Dynamics

MIM = Metal-Insulator-Metal

NEB = Nudged Elastic Band

PBE = Generalised gradient approximation density functional developed by Perdew, Burke, and Ernzerhof

PL = Photoluminescence

PLE = Photoluminescence Excitation

RRAM = Resistive Random Access Memory

SEM = Scanning Electron Microscopy

STEM = Scanning Transmission Electron Microscopy

STM = Scanning Tunnelling Microscopy

SUTD = Singapore University of Technology and Design

TAT = Trap-Assisted Tunnelling

TCM = Thermochemical Memory

TEM = Transmission Electron Microscopy

UCL = University College London

VBM = Valence Band Maximum

VCM = Valence Change Memory

XPS = X-ray Photoelectron Spectroscopy

List of Figures

1.1 Example of typical metal-insulator-metal RRAM device 39

3.1 Schematic of the reactive sputtering process. 62

3.2 Diagram showing the Thornton Model. 64

3.3 Schematic of thermal evaporation process 65

3.4 Schematic of the FEI TITAN used in this study. 68

3.5 Schematic of the electron source used in the FEI TITAN. 69

3.6 Schematic of an electromagnetic lens. 71

3.7 Schematic of the different electron scattering processes. 73

3.8 Schematic of a typical STEM detector. 78

3.9 Schematic of the EELS detector used in this work. 79

3.10 Schematic of the EDX detector used in this work. 82

3.11 SEM images showing the FIB process. 83

4.1 Schematic of the ECM filament formation process. a) high ion mobility - high reduction rate regime, b) low ion mobility - low reduction rate regime, c) high ion mobility - low reduction rate regime, d) low ion mobility - high reduction rate regime. The blue and green dots represent active electrode ions and electrons respectively. The Blue arrows represent the filament growth direction. 88

4.2 (a) a pristine Ag-SiO_2-Pt device imaged after fabrication. (b) the device post forming at 8 V. A metallic filament spans the dielectric connecting the electrodes. Incomplete dendrite type filaments grow from the Pt electrode. (d) The I-V curve measured during forming shows the conductive filament results in a large decrease in resistance (ON-state). (c) shows the same device after erasing, where a reverse bias of -10 V is applied. Here we see the dissolution of the filament beginning at the Pt electrode, demonstrating the importance of the insulator-inert electrode interface interactions. (h) and (i) show the set (10 V) and reset (-10 V) processes respectively, where again there is dissolution of the filament at the Pt electrode (OFF-state). The dissolution is thought to occur at the Pt electrode due to Joule heating, where the filament is at its thinnest. 90

4.3 SEM images capturing the dynamic conductive filament growth processes in the Ag/SiO_2/Pt planar device. a) Fresh device. b–d) After 10 s, 150 s and 210 s under a 30 V constant voltage stress with I CC = 10 μA, respectively 91

4.4 Morphology and component of conductive filament observed in Ag/SiO_2/Pt planar structure after electroforming with various I CC . As-prepared fresh device without any electrical treatment. b–d) Morphologies of the conductive filament with I CC = 5 nA, I CC = 100 nA and I CC = 100 μ A, respectively. e) Cross-sectional TEM image along the nanocrystal chain. f) HRTEM images of a single nanoparticle. g) The diffraction pattern extracted by Fourier transform of (f) showing Ag (111) crystal plane. h) Enlarged TEM images taken from the red rectangular region in (e). i–k) EELS mapping images of Si, O and Ag elements, respectively, corresponding to the region in (h). 92

4.5 Schematic showing the activation barriers for the thermal diffusion of Ag from the Ag electrode into the dielectric layer. 93

5.1 EPR spectrum of the A_{Ag-Si} centre in X-ray irradiated α-quartz doped with Ag. a) ^{29}Si hyperfine lines are formed on either side of each peak of the primary ^{107}Ag doublet. b) Primary doublet arising from the residual ^{107}Ag. The remaining lines are due to c) Al/Ag centres, d) Al/Li centres and e) Ge(I) centres. 99
5.2 Absorption and Photoluminescence spectra of the Ag^{+1} interstitial in α-quartz. 100
5.3 Graph showing the planewave cut-off convergence test. 101
5.4 Graph showing the relative cut-off convergence test. 102
5.5 Graph showing the total density of states for 72-atom and 243-atom α-quartz cells. The 0 on the x-axis indicates the position of the highest energy electron, those states above the 0 position are unoccupied while those below are occupied. From this, it can be seen that the α-quartz valence and conduction bands in each case form at almost the same energies showing convergence. 103
5.6 Graph showing DOS of a pristine α-quartz cell. The blue, red and yellow lines mark the total, Si and O contributions. The 0 on the x-axis indicates the position of the highest energy electron, those states above the 0 position are unoccupied while those below are occupied. 104
5.7 Hexagonal crystal structure of α-quartz with indexes of lattice directions 106
5.8 Graph showing the DFT derived vibrational spectrum of a pristine α-quartz cell. The black and red vertical bars represent the positions of experimentally measured Raman and IR modes, respectively. . . 108

5.9 Schematic of the Ag^0 interstitial in α-quartz. a) Shows the interaction between the Ag^0 interstitial and two SiO_4 tetrahedra. b) Shows the Ag^0 interstitial position in the c-axis channel. c) Shows the Ag^0 interstitial in the 2-fold symmetry axis, in the plane of the Si atoms in the SiO_4 tetrahedra. The grey, blue and red atoms represent Ag, Si and O, respectively. 109

5.10 Graph showing the DFT derived EPR spectrum of the Ag^0 interstitial in α-quartz. 111

5.11 Schematic of the a) Ag^{+1}, b) Ag^{+2}, c) Ag^{-1}, d) Ag^{-2} interstitials in α-quartz. The grey, blue and red atoms represent Ag, Si and O, respectively. 112

5.12 The defect formation energy diagram of the Ag interstitial in the -2 $\leq q \leq$ +2 charge states in α-quartz as a function of Fermi energy, where the Fermi energy is 0 at the α-quartz VBM. 112

5.13 Graph showing the filled (black) and empty states (red) of the Ag interstitial in the -2 $\leq q \leq$ +2 charge states α-quartz. In this case, the states are projected over the α-quartz band gap where 0 represents the α-quartz VBM. 113

5.14 Schematic of the absorption and luminescence of the Ag^{+1} centre for the singlet to triplet and the triplet to singlet transitions respectively 115

5.15 Graph showing the adiabatic diffusion barriers for Ag^0 and Ag^{+1} along the [001] and [110] directions calculated from CI-NEB calculations. 117

5.16 Schematic of the Ag_2 dimer in α-quartz. b) showing the dimer location is symmetric about the 2-fold symmetry axis. 118

5.17 The defect formation energy diagram of Ag_2 and 2 Ag systems in α-quartz as a function of Fermi energy, where the Fermi energy is 0 at the α-quartz VBM. 119

5.18 Schematic of the a) Ag_3^0, b) Ag_3^{+1} and c) 3 non-interacting Ag^{+1} systems in α-quartz. 120

5.19 The defect formation energy diagram of Ag_3 and 3 non-interacting Ag^{+1} systems in α-quartz as a function of Fermi energy, where the Fermi energy is 0 at the α-quartz VBM. 121
5.20 The defect formation energy diagram of O vacancy in α-quartz as a function of Fermi energy, where the Fermi energy is 0 at the α-quartz VBM. 121
5.21 The defect formation energy diagram of [AgV_O] complex in α-quartz as a function of Fermi energy, where the Fermi energy is 0 at the α-quartz VBM. 123
5.22 The defect formation energy diagram of [Ag_2V_O] complex in α-quartz as a function of Fermi energy, where the Fermi energy is 0 at the α-quartz VBM. 123
5.23 Graph showing the filled (black) and empty states (red) of the [Ag_2V_O] complex in the q = 0, +1 and +2 charge states α-quartz. In this case, the states are projected over the α-quartz band gap where 0 represents the α-quartz VBM. 124

6.1 Element projected density of states for the Ag/α-cristobalite interface. 132
6.2 a) shows the α-cristobalite (202) grain boundary. b) shows the α-cristobalite (202) column boundary generated with a 20 Å vacuum between each α-cristobalite (202) surface. 133
6.3 Graph showing the total energy difference of an α-cristobalite (202) surface slab as the vacuum between the surfaces is increased. 0 nm marks the GB separation of 3 Å 134
6.4 Structure of the Ag/SiO_2 interface formed between a Ag cluster and the hydroxylated (202) α-cristobalite surface. a)-c) show the view from the x, y and z axis, respectively From c), it can be seen that the cluster is periodic in y direction. 136
6.5 Image of the Ag/SiO_2 showing the incorporation of a Ag species into α-cristobalite, following the path of the black arrow. 137

6.6 Graph showing the results of a CI-NEB simulation for the incorporation of the first Ag (red) and second (blue) Ag into α-cristobalite. 138

6.7 Bar graph showing the ring statistics of the 30 a-SiO_2 cells produced. 139

6.8 a) The formation energy diagram of one O vacancy as a function of Fermi energy, (ΔE_F), where $\Delta E_F = 0$ at the a-SiO_2 VBM. The cross over points between the lines at 1.4 and 7.7 eV correspond to the Fermi energy at which the lowest energy charge state transitions from (+1/0) and (0/-1), respectively; b) the distribution of (+1/0) charge transition level positions for all 144 O vacancies; c) the distribution of (0/-1) charge transition level positions for all 144 O vacancies. The transitions seen in a) are shown as darkened bars in b) and c). 140

6.9 Schematic of the two configurations of the Ag^0 defect. The silver, blue and red spheres correspond to Ag, Si and O atoms respectively. The positive and negative charge density are shown as blue and yellow iso-surfaces respectively at a value of ± 0.07. a) shows the void type configuration whilst b) shows the wide angle O-Si-O configuration where as Ag^0 comes into proximity of the O-Si-O angle bond, the O-Si-O angle increases, with charge donation from Ag to Si. 141

6.10 Graphs showing the relationship of the incorporation energy (a), and the Mulliken charge (b) to the number of atoms within 3 Å of Ag^0 142

6.11 Histogram comparing the nearest neighbour distances of Ag^0 and Ag^{+1}. 143

6.12 Formation energy diagram of the Ag interstitial with respect to the a-SiO_2 VBM. The lines represent the mean incorporation energy of the unique Ag sites in a-SiO_2 for each charge state. 144

6.13 a) shows the α-cristobalite (202) grain boundary. b) shows the α-cristobalite (202) column boundary generated with a 20 Å vacuum between each α-cristobalite (202) surface. 146

6.14 Plot showing the incorporation energy of Ag^0 and Ag^{+1} in the α-cristobalite grain and column boundaries. Z = 0 represents the surface of the boundaries and negative Z values represent Ag incorporation towards the α-cristobalite bulk. 147

6.15 Schematic showing the HOMO state of the V_O and $[Ag/V_O]^{+1}$ defect. The silver, blue and red spheres correspond to Ag, Si and O atoms, respectively. The positive and negative charge density are shown as blue and yellow iso-surfaces, respectively, at a value of ± 0.07. a) Neutral V_O, with the HOMO state residing on the two Si atoms involved in the vacancy. b) and c) show the $[Ag/V_O]^{+1}$ defect with b) additionally showing the interaction between $[Ag/V_O]^{+1}$ defect and proximate O atoms. In both configurations of $[Ag/V_O]^{+1}$ charge density is donated from Si to Ag. 149

6.16 The distribution of Ag^{+1} to V_O binding energies using the lowest energy interstitial method and the interstitial 5 Å away method. . . . 151

6.17 Histogram showing the distribution of the q = (+1/0) charge transition Fermi energy positions of the 144 $[Ag/V_O]$ complexes sampled. 152

7.1 Schematic showing the mechanism of initial stages of Ag clustering in O vacancies. V_O acts as a Ag^{+1} reduction site and subsequent cluster nucleation site. The silver, blue and red spheres correspond to Ag, Si and O atoms, respectively. The positive and negative charge density are shown as blue and yellow iso-surfaces respectively at a value of ± 0.07. 159

7.2 Graph showing the incorporation energy per atom of Ag clusters up to 9 atoms at 3 vacancy sites. 161

7.3 Graph showing the CP2K cell optimised relaxed lattice vector as a function of Ag cluster size. 162

7.4 Graphs showing the energetics at each picosecond of 9 atom cluster during a MD simulated anneal at 500 K and 1000 K. a) The DFT re-optimised and cooled total energy of the system at each picosecond of the MD simulation including the lattice and the [Ag_9/V_O] complex. b) The isolated energy of the 216 atom a-SiO_2 lattice at each picosecond of the MD simulation compared to the lattice at t = 0. c) The isolated energy of the 9 atom Ag cluster at each picosecond of the MD simulation compared to the cluster at t = 0. d) The binding energy of the 9 atom Ag cluster to the lattice at each picosecond of the MD simulation compared to t = 0. 164

7.5 Shows the Ag cluster embedded into a pristine (a) 216-atom cell and a (b) 1,728-atom supercell. The silver, blue and red spheres correspond to Ag, Si and O atoms respectively. 165

7.6 Graph showing the filled (black) and empty (red) state positions along the a-SiO_2 band gap for [Ag_i/V_O]^0 for i = 0, 3, 6, 9, 12 and 15 166

7.7 Graph showing the density of states for the [Ag_{15}/V_O]^0 complex. . . 167

7.8 Table showing the number of broken Si-O bonds as a function of charge state and Ag cluster size 168

7.9 Graph comparing the ratio of Ag-Si bonds to Ag-O bonds to the charge state of the system. 169

7.10 Graph showing the vacancy formation energy for 17 V_O sites around the [Ag_{15}/V_O]^q complex in the -4 $\leq q \leq$ 4 charge states. . . 171

7.11 Formation energy diagram of the [Ag_{15}/V_O] in a-SiO_2 relative to the VBM using the chemical potential calculated from Ag_2O 172

7.12 Graph showing the filled (black) and empty (red) state positions along the a-SiO_2 band gap for [Ag_{15}/V_O]^q for the -4 $\leq q \leq$ 4 charge states 173

7.13 Schematic of the $[Ag_{15}/V_O]^{+3}$ complex after a MD simulation at 1000 K. After the widening of a Si-O bond to open access to a secondary void, a Ag_3^{+1} cluster breaks from $[Ag_{15}/V_O]^{+3}$ to form in the new void. 174

9.1 Schematic showing the O vacancy generation process. A) two electrons trap at an intrinsic wide angle (> 132° O-Si-O bond. B) The trapped electrons lead to the lengthening and weakening of an Si-O bond. C) The Si-O bond breaks leaving two electrons trapped in a three coordinated Si atom. D) An O vacancy is formed after the O^{-2} interstitial diffuses away 187

9.2 EELS spectra of the Ti $L_{2,3}$ and O K edges taken on a TiO_2/SiO_2 stack. The top curve corresponds to the total EELS spectrum summed across the TiO_2/SiO_2 stack, the middle curve is the sum of EELS spectra taken at the centre of the TiO_2 layer and the bottom curve is the sum of spectra taken at the centre of the SiO_2 layer. 191

9.3 EELS spectra of the Si $L_{2,3}$ edge taken across a SiO_2/Si interface. The bottom curve (1) corresponds to the EELS spectrum measured in SiO_2, whilst the top curve (5) is measured in a Si region. The intermediate spectra (2-4) represent SiO_x regions of decreasing O content, respectively. 192

9.4 EEL spectra of the a) Ti $L_{2,3}$ edge and b) O K edge measured for TiO_x where x = $1 \leq x \leq 2$. 193

9.5 HAADF image of a Ti-SiO_x-Mo RRAM device. The horizontal white line marks the region at the Ti/SiO_x from which an EELS average scan is taken 194

10.1 HAADF image of the pristine Ti device 197

10.2 HAADF image of the Mo layer in the Ti device. The horizontal red lines mark the minimum and maximum heights of the interface, from which the min/max roughness is measured to be 11 nm 198

10.3 HAADF image of the Ti device showing the effect of the SiO_x/Mo interface roughness on SiO_x microstructure. a) HAADF image of the Ti device, b) HAADF image of the Ti device with the intensity limits adjusted to elucidate the SiO_x layer. The vertical red lines mark the region the normalised HAADF intensity profile c) is taken. The blue arrows show the position of peaks in the normalised HAADF intensity occur at trough positions in the SiO_x/Mo interface 199
10.4 HAADF analysis of the Ti device showing the presence of a void region located at a large trough at the SiO_x/Mo interface. a) HAADF image of the Ti device, b) HAADF image of the Ti device with the intensity limits adjusted to elucidate the SiO_x layer. The vertical red lines mark the region the normalised HAADF intensity profile c) is taken. The blue arrows show the normalised HAADF is significantly reduced at the trough position in the SiO_x/Mo interface . . . 200
10.5 HAADF image of the Ti layer, showing the layer is polycrystalline . 200
10.6 EELS data for the pristine Ti device. a) shows a HAADF image of the device where an EELS measurement is taken within the orange box. The extracted Ti $L_{2,3}$, O K and Si $L_{2,3}$ edge maps are shown in b) - d) respectively 201
10.7 Line profile of the Ti $L_{2,3}$, O K and Si $L_{2,3}$ edges for Ti device taken within the blue vertical lines marked in Fig. 10.6 202
10.8 EELS data for the pristine Ti device. a) shows a HAADF image of the device where an EELS measurement is taken within the orange box. The extracted Ti $L_{2,3}$, O K (total), O K prepeak (O_{Pre}) and O K SiO_x (O_{Si}) edge maps are shown in b) - e) respectively 203
10.9 Line profile of the Ti $L_{2,3}$, O K (total), O K prepeak (O_{Pre}) and O K SiO_x (O_{Si}) edges for Ti device taken within the blue vertical lines marked in Fig. 10.8 203

10.10 EELS spectra taken across the Ti/SiO_x interface and up to 10 nm into the SiO_x layer. Measurements in the SiO_x layer were taken in increments of 2 nm away from the Ti/SiO_x interface measurement. For each spectra, the average scan method as described in section 9.4.2 was used to collect the data. 205

10.11 IV curves of the Ti device after positive (blue) and negative (orange) electroforming. 206

10.12 HAADF image of the positive electroformed Ti device. Dark regions in the SiO_x layer are marked at the troughs of the SiO_x/Mo interface whilst bright regions in the SiO_x can be seen at the Ti/SiO_x interface. 208

10.13 EELS data for the positive electroformed Ti device. a) shows a HAADF image of the device where an EELS measurement is taken within the orange box. The extracted Ti $L_{2,3}$, Si $L_{2,3}$ and O K edge maps are shown on b) - d) respectively. The blue lines mark two regions (R1 and R2) from which the lineprofiles shown on Fig. 10.14 are taken. 209

10.14 Line profiles of the Ti $L_{2,3}$, Si $L_{2,3}$ and O K edges for positive electroformed Ti device taken within two regions (R1 and R2) marked by the blue vertical lines on Fig. 10.13 210

10.15 EELS data for the positive electroformed Ti device. a) shows a HAADF image of the device where an EELS measurement is taken within the orange box. The extracted Ti $L_{2,3}$, O K (total), O K prepeak (O_{Pre}) and O K SiO_x (O_{Si}) edge maps are shown on b) - e) respectively. The blue lines mark the region from which the lineprofiles shown on Fig. 10.16 are taken. 210

10.16 Line profiles of the Ti $L_{2,3}$, O K (total), O K prepeak (O_{Pre}) and O K SiO_x (O_{Si}) edges for the positive electroformed Ti device taken within the blue vertical lines marked on Fig. 10.15 211

10.17 EELS spectra taken across the Ti/SiO_x interface and up to 12 nm into the SiO_x layer for the positive electroformed Ti device. Measurements in the SiO_x layer were taken in increments of 2 nm below the Ti/SiO_x interface measurement. For each spectra, the average scan method as described in section 9.4.2 was used to collect the data. 213

10.18 EELS data for the negative electroformed Ti device. a) shows a HAADF image of the device where an EELS measurement is taken within the orange box. The extracted Ti $L_{2,3}$, Si $L_{2,3}$ and O K edge maps are shown on b) - d) respectively. The blue lines mark the from which the lineprofiles shown on Fig. 10.19 are taken. 214

10.19 Line profiles of the Ti $L_{2,3}$, Si $L_{2,3}$ and O K edges for negative electroformed Ti device taken within the region marked by the blue vertical lines on Fig. 10.18 215

10.20 EELS data for the negative electroformed Ti device. a) shows a HAADF image of the device where an EELS measurement is taken within the orange box. The extracted Ti $L_{2,3}$, O K (total), O K prepeak (O_{Pre}) and O K SiO_x (O_{Si}) edge maps are shown on b) - e) respectively. The blue lines mark the region from which the lineprofiles shown on Fig. 10.21 are taken. 216

10.21 Line profiles of the Ti $L_{2,3}$, O K (total), O K prepeak (O_{Pre}) and O K SiO_x (O_{Si}) edges for negative electroformed Ti device taken within the blue vertical lines marked on Fig. 10.20 217

10.22 EELS spectra taken across the Ti/SiO_x interface and up to 12 nm into the SiO_x layer for the negative electroformed Ti device. Measurements in the SiO_x layer were taken in increments of 2 nm below the Ti/SiO_x interface measurement. For each spectra, the average scan method as described in section 9.4.2 was used to collect the data. 218

10.23 Graph showing the normalised Ti $L_{2,3}$ counts as a function of distance from the Ti/SiO_x interface. For all data points, the counts were determined through analysis of the 'averaged scan' results on Figs. 10.10, 10.17 and 10.22 respectively. 219
10.24 Graph showing the normalised O K edge (total) counts as a function of distance from the Ti/SiO_x interface. For all data points, the counts were determined through analysis of the complete EELS O K edge maps shown on Figs. 10.8, 10.15 and 10.20 respectively. . . 220
10.25 Graph showing the normalised Ti $L_{2,3}$ to O K edge prepeak counts as a function of distance from the Ti/SiO_x interface. For all data points, the counts were determined through analysis of the 'averaged scan' results on Figs. 10.10, 10.17 and 10.22 respectively. . . . 221

11.1 HAADF image of the pristine Au device 227
11.2 HAADF image of the pristine Au device with the contrast adjusted to highlight the SiO_x layer 228
11.3 Graph showing the normalised HAADF intensity taken for the Au (blue line) and Ti (orange line) devices respectively. 228
11.4 HAADF image of the Au electrode of the Au device 229
11.5 EDX results taken across the pristine Au device. a) shows an HAADF image of the pristine Au device, where the EDX spectra for the Au, SiO_x, MoO_x and Mo regions (marked by red boxes) are given on b) respectively. 230
11.6 EELS data for the pristine Au device. a) shows a HAADF image of the device where the EELS measurement is taken within the orange box. b) shows the same HAADF image with the contrast limits set to show the SiO_x layer. The extracted Mo M_3, Si $L_{2,3}$ and O K edge maps are shown on c) - e) respectively 231
11.7 Line profile of the Si $L_{2,3}$, O K and Mo M_3 edges for Au device taken within the blue vertical lines marked on Fig. 11.6 232

11.8 EELS data for the pristine Au device. a) shows a HAADF image of the device where the EELS measurement is taken within the orange box. b) shows the same HAADF image with the contrast limits set to show the SiO_x layer. The extracted O K edge and O K edge prepeak maps are shown on c) and d) respectively 233
11.9 Line profile of the O K edge and O K edge prepeak for Au device taken within the blue vertical lines marked on Fig. 11.8 234
11.10 Plots of the extracted O K edge taken across the pristine Au device . 235
11.11 Graphs of the extracted O K edge taken in the Mo layer of the pristine Au device 236
11.12 Raw EELS signal in the 370 - 520 eV range taken for the Au device, showing the Mo M_3 edge 236
11.13 IV curves of the Au device after positive (orange) and negative (blue) electroforming. 237
11.14 HAADF image of the positive electroformed Au device. A layer can be seen to form between the SiO_x and Mo layers from the left to the right of the image. 239
11.15 EDX results taken across the positive electroformed Au device. a) HAADF image of the positive electroformed Au device, where the EDX spectra for the Au, SiO_x (R1 and R2), MoO_x and Mo regions (marked by red boxes) are given in b) respectively. 240
11.16 EELS data for the positive electroformed Au device. a) HAADF image of the device where an EELS measurement is taken within the orange box. The extracted Si $L_{2,3}$ and O K edge maps are shown on b) and C) respectively. 241

11.17 EELS data for the positive electroformed Au device. a) HAADF image of the device where an EELS measurement is taken within the orange box. The extracted O K (total), O K prepeak (O_{Pre}) and O K SiO_x (O_{Si}) edge maps are shown on b) - d) respectively. The blue lines mark the region from which the lineprofiles shown in Fig. 11.18 are taken. 242
11.18 Line profiles of the O K (total), O K prepeak (O_{Pre}) and O K SiO_x (O_{Si}) edges for positive electroformed Au device taken within the blue vertical lines marked in Fig. 11.17 243
11.19 HAADF image of the negative electroformed Au device. 244
11.20 EDX results taken across the negative electroformed Au device. a) HAADF image of the positive electroformed Au device, where the EDX spectra for the Au, SiO_x, MoO_x and Mo regions (marked by red boxes) are given in b) respectively. 245
11.21 EELS data for the negative electroformed Au device. a) HAADF image of the device where an EELS measurement is taken within the orange box. The extracted Si $L_{2,3}$ and O K edge maps are shown in b) and c), respectively. 246
11.22 EELS data for the positive electroformed Au device. a) HAADF image of the device where an EELS measurement is taken within the orange box. The extracted O K (total), O K SiO_x (O_{Si}) and O K prepeak (O_{Pre}) edge maps are shown in b) - d) respectively. 248
11.23 Graph showing the normalised O K edge counts as a function of distance from the Au/SiO_x interface. For all data points, the counts were determined through analysis of 'averaged scans' taken at the Au/SiO_x interface and in the SiO_x and Mo layers. In this case, average scans were taken as described in section 9.4.2, in increments of 5 nm from the Au/SiO_x interface. 250

11.24 Graph showing the normalised O K edge prepeak counts as a function of distance from the Au/SiO_x interface. For all data points, the counts were determined through analysis of 'averaged scans' taken at the Au/SiO_x interface and in the SiO_x and Mo layers. In this case, average scans were taken as described in section 9.4.2, in increments of 5 nm from the Au/SiO_x interface. 251

12.1 a) STEM BF and b) STEM HAADF image of a pristine Au-Ti-SiO_x-Mo device. 257

12.2 STEM HAADF image of a pristine Au-Ti-SiO_x-Mo device. The two horizontal red lines are separated by 18nm to mark the min/max of the Mo electrode roughness. 258

12.3 STEM HAADF of a pristine Au-Ti-SiO_x-Mo device showing bright clusters in the Ti layer 259

12.4 STEM HAADF image of a pristine Au-Ti-SiO_x-Mo device showing the patterning of the top (Au-Ti) electrode to the Mo electrode roughness. The peaks marked for the Mo electrode match the peak locations of the Au-Ti electrode. The red lines show the more smooth regions in the Mo electrode also pattern to the Au-Ti electrode. 260

12.5 HAADF STEM image of a pristine Au-Ti-SiO_x-Mo device highlighting bright vertical column boundaries protruding from troughs at the SiO_x/Mo interface 260

12.6 a) TEM image, b) HAADF STEM image and c) BF STEM image of a pristine Au-Ti-SiO_x-Mo device with metallic clusters formed in the SiO_x layer. 261

12.7 TEM image of metal cluster in SiO_x showing metallic nature. The blue line represents the region from which a line profile is taken. . . 262

12.8 Profile taken from blue line on Fig. 12.7 showing the periodic and metallic nature of a cluster found in SiO_x. The vertical black lines represent the peak positions from which the lattice spacing for the metallic cluster is calculated. 262

12.9 EDX measurements taken in the pristine Au-Ti device. The red box in a) and c) mark the regions the EDX spectra shown in b) and d) are collected respectively 263

12.10 EELS data for the pristine Au-Ti device. a) HAADF image of the device where the EELS measurement is taken within the orange box. The extracted O K, Ti $L_{2,3}$ and Si $L_{2,3}$ edge maps are shown on b) - d) respectively 264

12.11 Shows the O:Si ratio taken of the pristine Au-Ti device. a) HAADF image of the region within which the O K and Si $L_{2,3}$ edges are measured. b) shows the ratio of the O K edge to Si $L_{2,3}$ edge, calculated by dividing the extracted image maps of each EELS signal 265

12.12 EELS data for the pristine Au-Ti device. a) HAADF image of the device where the EELS measurement is taken. The extracted Ti $L_{2,3}$, O K edge (total), O K edge (prepeak) and O K edge (SiO_x) maps are shown on b) - e) respectively 266

12.13 Line profile of the Ti $L_{2,3}$, O K edge (total), O K edge (prepeak) and O K edge (SiO_x) taken within the blue lines marked on Fig. 12.12 266

12.14 EELS measurement of columnar boundaries in the pristine Au-Ti device. a) HAADF image where the EELS measurement of the Si $L_{2,3}$ edge shown on b) is taken. The orange and blue boxes on b) mark column boundary and column bulk regions from which the Si $L_{2,3}$ spectra shown on c) are taken 268

12.15 a) An Si $L_{2,3}$ edge image map of columnar boundaries in the pristine Au-Ti device. b) Line profile taken across the image map a) showing the reduction in Si $L_{2,3}$ in the columnar boundary regions. . 269

12.16 IV curves of the Au-Ti device after positive (blue) and negative (orange) electroforming. 271

12.17 EELS data for the positive electroformed Au-Ti device. a) HAADF image of the device where an EELS measurement is taken within the orange box. The extracted Si $L_{2,3}$, Ti $L_{2,3}$, O K (total), O K SiO_x (O_{Si}) and O K prepeak (O_{Pre}) edge maps are shown on b) - f) respectively. The blue lines mark the region from which the lineprofiles shown in Fig. 12.18 are taken. 272

12.18 Line profiles of the Ti $L_{2,3}$, Si $L_{2,3}$, O K (total) and O K prepeak (O_{Pre}) edges for positive electroformed Au-Ti device taken within regions marked by the blue vertical lines in Fig. 12.17 273

12.19 EELS data for the positive electroformed Au-Ti device. a) HAADF image of the device where an EELS measurement is taken within the orange box. The extracted Si $L_{2,3}$, Ti $L_{2,3}$, O K (total) and O K prepeak (O_{Pre}) edge maps are shown on b) - e) respectively. f) shows the O K edge spectra for the column boundary (blue and orange boxes) and column bulk (yellow box) regions. 274

12.20 SEM images of the negative electroformed Au-Ti device. a) An example bubble that appears during electroforming, whilst b) shows the a trench formed by ion beam milling during lamella preparation. c) and d) show SEM images of the Mo layer delaminated from the substrate 276

12.21 EELS data for the negative electroformed Au-Ti device. a) HAADF image of the device where an EELS measurement is taken within the orange box. The extracted Ti $L_{2,3}$, O K (total), O K prepeak (O_{Pre}) and O K SiO_x (O_{Si}) edge maps are shown on b) - e) respectively. The blue lines mark the region from which the lineprofiles shown on Fig. 12.22 are taken. 277

12.22 Line profiles of the Ti $L_{2,3}$, O K (total), O K prepeak (O_{Pre}) and O K SiO_x (O_{Si}) edges for negative electroformed Au-Ti device taken within the blue vertical lines marked in Fig. 12.21 278

12.23 HAADF image of the negative electroformed Au-Ti device 279

List of Tables

5.1 Table showing basis set convergence test. 101
5.2 Table comparing the PBE, PBE0_TC_LRC, BLYP and B3LYP exchange correlation functionals to experimentally observed parameters. 104
5.3 Table showing the excitation energies for the Ag^{+1} center in α-quartz. 115
5.4 Table showing the excitation energies for the [AlO_4-Ag^{+1}] center in α-quartz. 116

6.1 Table showing the forward and reverse barriers for Ag^0 and Ag^{+1} in a-SiO_2 calculated by DFT CI-NEB simulations through n = 5 - 8 atom rings. 145
6.2 Table showing the diffusion barriers of Ag^0 and Ag^{+1} in the α-cristobalite grain and column boundaries 148
6.3 Table showing the number of vacancy sites that will act as Ag reduction sites. 152

7.1 The results of CI-NEB calculations for a Ag^{+1} ion to bind to five different [Ag/V_O]^0 complexes. Negative values correspond to images lower in energy (more energetically favoured). In each case, image 1 represents the Ag^{+1} ion 5 Å from the vacancy complex. The values in image 5 represent the binding energy of the Ag^{+1} ion to the vacancy complex. 160

7.2 The results of CI-NEB calculations for Ag^{+1} ions to cluster at one $Ag_2/V_O]^0$ complex. Negative values correspond to images lower in energy (more energetically favoured). In each case, image 1 represents the Ag^{+1} ion 5 Å from the vacancy complex. The values in image 5 represent the binding energy of the Ag^{+1} ion to the vacancy complex 160

7.3 Table comparing the Ag atom embedded in a pristine 216-atom cell to a pristine 2x2x2 supercell. 166

Chapter 1

Introduction

1.1 Background

The work in this thesis contains a systematic study of silicon oxide resistive random-access memory (RRAM) devices. The project includes many years of collaboration with my group under Alexander Shluger at the Department of Physics and Astronomy at University of College London (UCL), Anthony Kenyon's group at the Electronic and Electrical Engineering department also from UCL, and Michel Bosman at the Institute of Materials Research and Engineering (IMRE) from the Agency of Science, Technology and Research (A*STAR) in Singapore. As a result of the collaboration, this PhD was created to study the structural dynamics associated with silicon oxide RRAM devices under electrical stress. In particular, the focus is toward developing an understanding of the mechanisms involved in the devices at the atom scale. Funded by both UCL and A*STAR, the first year of the project was spent under the tutelage of Alexander Shluger at UCL. During this time, the objective was to develop atom scale simulations of silicon oxide RRAM devices using density functional theory (DFT) and molecular dynamics (MD). From this, Part I of this thesis was born, which uses DFT and MD to study Ag-SiO_2-Pt RRAM devices. As discussed in the thesis, the Ag-SiO_2-Pt devices were selected due to their optimal RRAM properties and the wealth of experimental data available to model towards. The second and third years of the PhD were spent under the guidance of Michel Bosman at IMRE in Singapore. During this time, theoretical work on Ag-SiO_2-Pt RRAM devices continued, whilst time was also spent analysing silicon oxide RRAM devices using transmission electron microscopy (TEM). The results of the TEM work is given in Part II of the thesis, which contains studies on Au-

Ti-SiO_x-Mo (Au-Ti), Ti-SiO_x-Mo (Ti) and Au-SiO_x-Mo (Au) RRAM devices (x $\approx$ 1.95). These devices were grown by Wing Ng at UCL and have been studied extensively by Adnan Mehonic and others in Anthony Kenyon's group. It should be noted that the original intention was to also study Ag-SiO_2-Pt RRAM devices through TEM in Singapore, but this was not possible due to external factors.

1.2 Motivation

The arrival of modern computing has brought with it countless innovations in memory technology, many of which have been pivotal in meeting the demands of the 'information age'. A report from the World Economic Forum (WEF) found that 90 percent of all stored information in 2014 was created in the previous two years [1]. With such high requirements placed on data storage, and the current forms of memory such as flash, static random access-memory (SRAM) and dynamic random access-memory (DRAM) each reaching their limit of optimisation, a new technology is needed that can not only capture the benefits of each type of memory, but outperform them. This thesis is focused on one such alternative, resistive random-access memory (RRAM), which combines the non-volatility, high scalability, high data retention, high endurance and low energy consumption of flash memory with the low operation times of SRAM and DRAM. RRAM devices using amorphous silicon dioxide (a-SiO_2) and amorphous silicon sub-oxide (SiO_x, where $x < 2$) are of particular interest due to their many favourable qualities. To begin with, silicon oxide is an incredibly abundant material and is therefore unlikely to face issues with scarcity. Furthermore, silicon oxide is a well understood material due to its already ubiquitous use in microelectronic technology, such as a gate dielectric in field effect transistors. Additionally, silicon oxide RRAM devices have been shown to be very versatile, with applications ranging from computer memory to memristor [2] technology and neuromorphic applications [3].

1.3 Resistive Random Access Memory (RRAM) Devices

A typical RRAM device consists of a metal-insulator-metal stack as shown on Fig. 1.1. Their application as computer memory relies on the resistive switching phe-

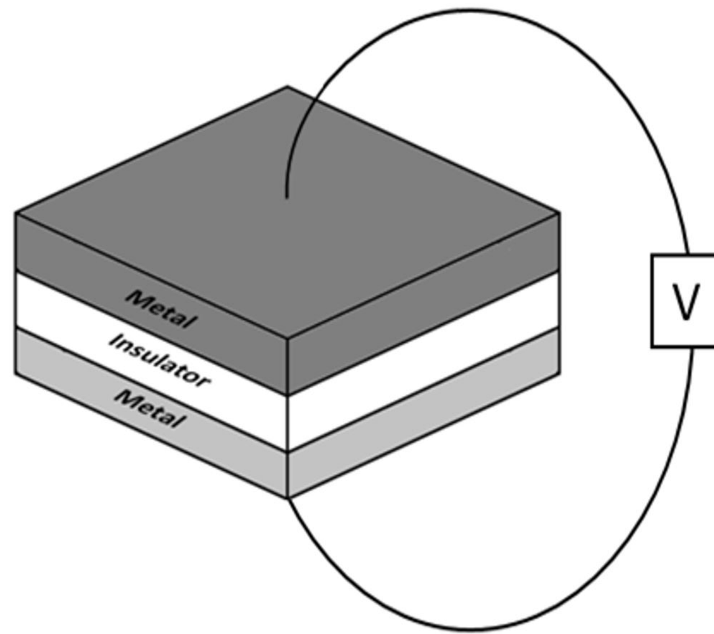

Figure 1.1: Example of typical metal-insulator-metal RRAM device

nomenon, where the resistance across the device is switched between high and low states. This is achieved through the generation and control of electron transport modes across the insulating layer. As a result, probing the resistance for high (0) or low (1) states provides storage of, and accessibility to, a two valued logic system. The resistance switching phenomenon was first discovered in 1962, where a negative resistance effect was observed in metal-oxide-metal sandwiches [4]. In this case, the application of a voltage sweep across an Al-Al_2O_3-Au stack measured a sharp increase in current at 4.1 V. On lowering the voltage, a negative resistance effect occurred where the current through the stack continued to increase. Bi-stable resistance RRAM technology was proposed a year layer, leading to an extensive amount of research carried out in the field throughout the 1960's and 70's [5, 6, 7]. Due to the prevalence of FLASH memory however, a dip in interest in RRAM occurred thereafter before becoming relevant again in the 2000's [8, 9].

Before RRAM devices exhibit repeatable resistive switching, an electroforming process is typically required. In this process, a forming voltage is applied across the device to generate a soft dielectric breakdown in the insulating layer. This results in the formation of a conductive filament (or path) in the insulating layer, signifi-

cantly decreasing the resistance across the device. The nature of this breakdown is the primary concern of this work, in which the electrochemical metallisation mechanism (ECM) and the valence change mechanisms (VCM) are explored [8, 9]. The resistive switching processes in the devices involve the breaking (reset / off state) and reforming (set / on state) of the conductive filament through the application of electrical bias. The resistance state can then be probed with low voltage electrical pulses, which themselves do not cause a resistance change. It should be noted that many other electroforming mechanisms can also occur, and detailed studies of them can be found in the literature [8, 9].

The nature of the conductive filaments and the mechanisms involved in silicon oxide RRAM devices varies greatly with device structure and microstructure. Even identical RRAM devices can display very different properties depending on their use and application. In this study, silicon oxide devices with a top electrode of Ag and Au are examined in Parts I and II of the thesis, respectively. In the Ag-SiO_2-Pt (Ag) devices, the Ag top electrode is selected to facilitate the ECM mechanism where the diffusion of metal cations into the dielectric layer occurs. More specifically, under a positive bias at the Ag electrode, Ag cations diffuse into SiO_2 and subsequently nucleate to form a conductive filament of metal clusters bridging the Ag and Pt electrodes. Electron transport then occurs through these metal clusters *via* trap assisted tunnelling. *In situ* TEM measurements of Ag devices show that the nature of the filament varies depending on the microstructure of the device, where Ag clustering in thermal SiO_2 begins at the Ag electrode and clustering in sputtered SiO_2 begins at the Pt electrode (see section 4.3 for more details) [10, 11, 12]. The Ag devices also show great versatility, where Ag devices can exhibit resistive switching at 0.2 V and -0.2 V during the first voltage sweep without an electroforming step [13]. Furthermore, by varying the current compliance limit from 1 mA to 1 μA, it is possible to transform the devices from non-volatile to volatile operation. In this case, the current compliance is the upper limit of the current allowed to flow through the device under bias. This is an important feature as the current compliance determines the resistance of the on state, subsequently allowing

multiple switching levels [14]. This is because increasing the current compliance across the Ag device results in a higher conductance under the same voltage. This shows electron transport through the devices plays a significant role in controlling the conductive filament geometry during forming and set processes.

Conversely, Au-SiO_x-Mo (Au) devices have been shown to operate through the VCM mechanism. In this case, the Au top electrode is selected for the low Au ion mobility in SiO_x, as well as the very low O affinity and workfunction of Au. Under a negative bias to the Au electrode, electrons are injected into the dielectric layer resulting in the generation of defects, such as O vacancies. Electron transport then occurs through the dielectric layer *via* trap assisted tunnelling though these defect states or intrinsic charge traps. The conductive defects in VCM devices can either form a filament similar to the ECM mechanism, or span the whole dielectric layer. Again, the microstructure of the device plays a significant role. It has been shown that an increased electrode-dielectric interface roughness in Au devices leads to favourable switching properties [15]. This was attributed in part to an increase in columnar structure, where the column boundaries in the SiO_x layer are suggested to facilitate defect formation and defect transport. Additionally, it is suggested that the roughness leads to increased electron injection due to local electric field effects [15].

Silicon oxide RRAM devices therefore pose an interesting topic of research, where a number of competing mechanisms are known to occur. However, it is only when these mechanisms are properly understood that they can be developed and optimised efficiently. After this, the feasibility of RRAM devices for industrial production can be assessed. As such, the work in this thesis is focused on understanding these mechanisms to better understand silicon oxide RRAM devices.

1.4 Thesis Outline

Following this introduction, chapters 2 and 3 contain the theoretical and experimental methods used throughout this work. Chapter 2 provides a background of both DFT and MD, as well as a discussion on how each method is employed. Similarly, chapter 3 provides a background on TEM operation and TEM characterisation. This

includes a discussion on TEM and STEM imaging as well as chemical analysis measurements using electron microscopy. Also included in chapter 3 is a description of the RRAM devices studied in Part II of the thesis and their fabrication methods.

The results of this work are then given in two parts, with each part containing three results chapters. Part I contains the results of the theoretical study on Ag-SiO_2-Pt (Ag) RRAM devices. Chapter 4 introduces Part I of the thesis, and includes a literature review of Ag RRAM devices, and the relevant operational mechanisms that are explored throughout the work. In chapter 5, Ag RRAM devices are studied through DFT calculations of Ag in α-quartz. This begins with a study of the Ag-α-quartz interaction, where experimental measurements including infrared (IR), Raman, electron paramagnetic resonance (EPR), absorption and photoluminescence spectra are each modelled. This is followed by a study of Ag incorporation, migration, reduction and clustering in α-quartz, including a model of the Ag-O vacancy interaction with regard to its potential as a Ag reduction and cluster nucleation site. Chapter 6 contains an expansion of the study into amorphous silicon dioxide (a-SiO_2). In this case, the incorporation, diffusion and reduction of Ag is studied in a 216-atom a-SiO_2 cell. Attention is paid to the Ag-O vacancy interaction and its role in Ag reduction. Subsequently, chapter 7 studies the Ag clustering process at O vacancy sites, where Ag clusters up to 15 atoms are developed. Particular interest is given to the breakdown of the a-SiO_2 lattice in proximity to the Ag cluster as well as the effects of electron injection. Chapter 8 provides a summary of Part I of the thesis along with suggestions for future work.

Part II contains the results obtained when studying Au-Ti-SiO_x-Mo (Au-Ti), Ti-SiO_x-Mo (Ti) and Au-SiO_x-Mo (Au) RRAM devices($x \approx 1.95$). Chapter 9 introduces the SiO_x devices, providing a brief literature review of the VCM mechanism. This is followed by chapters 10, 11 and 12 which cover the results obtained when characterising the Ti, Au and Au-Ti devices respectively. For each of these chapters, the devices are first characterised in their pristine states, followed by a characterisation of the same devices in their electroformed states. The effects of electroforming are then discussed by comparing the structure and chemistry of each device in their

electroformed states to their pristine states. Chapter 13 provides a summary of Part II of the thesis along with suggestions for future work.

Finally, in chapter 14, the thesis is concluded.

Chapter 2

Theoretical Background and Methods

2.1 Introduction

The physical properties of a RRAM device can greatly affect the way in which the device operates. Examples include the choice of electrode material, which can alter the switching mechanism between ECM, VCM and TCM [8]; or the deposition technique used to grow the oxide layer, which determines whether clustering begins at the active or inert electrode in ECM devices. Whilst characterisation of RRAM devices using experimental techniques provides this type of information, investigation at the atomic scale is necessary for individual devices to be completely understood and optimised. From this, a mechanistic picture can be developed of the various processes involved during operation. Subsequently, the role that the physical properties of the devices play in these processes and their impact on device operation can be assessed. Theoretical modelling techniques, such as density functional theory (DFT) and molecular dynamics (MD), work at the atomic scale, giving insight beyond the observation limit of experimental techniques. Using these powerful techniques, theoretical models guided by experimental measurements can be developed, allowing the individual properties of devices which give rise to the experimental observations to be evaluated, and critically, guides improvements for the next generation of devices.

In this chapter, the theoretical methods used throughout the project are presented. This begins with a discussion of the implementation of density functional theory in the CP2K code. For a complete derivation and explanation of DFT, the reader is directed to the literature [16]. The use of density functional theory to model defects, defect interactions and defect dynamics is then discussed. Finally, an explanation of both classical and *ab initio* molecular dynamics is given.

2.2 Implementation of DFT in CP2K

In this section, methods specific to the code CP2K are discussed [17, 18]. CP2K is primarily a Γ-point code which means that the systems used are expanded in real space as opposed to in reciprocal space (with the use of k-points) as is with codes such as VASP [19, 20] or CASTEP [21]. The Γ-point method is used in this work to allow the calculation of larger systems, which is important when studying amorphous structures because they by definition do not have the long range order required for methods that use symmetrisation.

2.2.1 Gaussian plane wave (GPW) method

Typically, local basis functions such as Gaussian basis sets [22] or non-local basis functions such as plane wave basis sets [23] are used to describe the Kohn-Sham orbitals, with each having advantages and disadvantages. Local basis sets are atomically centred functions representing the functional form of one electron hydrogenic orbitals. In this regard, Gaussian functions have been employed in many DFT codes due to their efficient implementation as the multiplication of two Gaussian's is a Gaussian. The drawback of Gaussian basis sets is that they are incomplete as they do not describe orbitals well near the nucleus of an atom. Plane wave basis sets derive from Bloch waves, where the wavefunction of particles in a periodic system can be represented as plane waves. These in principle form complete basis sets. The major benefit of representing orbitals in this way is that the fast Fourier transform (FFT) can be implemented to enable faster calculation of the Hartree energy. However, an additional computational expense arises from the fact that plane waves are indifferent to atomic positions such that areas of empty space are equally well rep-

resented by plane waves as regions near atoms. Furthermore, the electron density in the plane wave method usually requires a higher number of functions to be used than in the Gaussian method [16].

The Gaussian and plane waves (GPW) method, implemented in CP2K, uses both Gaussian and plane wave basis sets to enable faster overall calculation whilst retaining accuracy [17]. Gaussian basis sets are used to calculate the kinetic energy and potential energy analytically. The density from the Gaussian basis sets is mapped to the plane wave basis where the fast Fourier transform is utilised to solve for the Hartree energy, considerably reducing computational time. The density represented using Gaussian basis sets is given by [24];

$$\rho\left(r\right)=\sum_{i=1}^{N}\left|\psi_i\left(\mathbf{r}\right)\right|^2 \tag{2.1}$$

where $\rho\left(r\right)$ the density, N is the number of electrons and $\psi_i\left(\mathbf{r}\right)$ is the i'th molecular orbital. Molecular spin orbitals can then be expressed as a linear combination of atomic orbitals [16]:

$$\psi_i=\sum_{\mu=1}^{K}c_{i\mu}\phi_\mu \tag{2.2}$$

where $c_{i\mu}$ is the mixing coefficient and ϕ_μ is one of K atomic orbitals. Each atomic orbital is in turn a contracted sum of Gaussian functions [16]:

$$\phi_\mu=\sum_{k=1}^{L}d_{\mu k}\phi_k\left(\alpha_{\mu k}\right) \tag{2.3}$$

where $d_{\mu k}$ is the coefficient of the primitive Gaussian function ϕ_i which has the exponent $\alpha_{\mu k}$, and L is the number of functions in the expansion. During the calculation, the coefficients for the atomic orbitals $d_{\mu k}$ are usually kept constant, and the coefficients for the molecular orbitals $c_{i\mu}$ are varied to obtain the ground state density. The density obtained using the Gaussian basis sets is then mapped to the plane wave basis, described as:

$$\widetilde{\rho}\left(\mathbf{r}\right)=\frac{1}{\Omega}\sum_{\mathbf{G}}\widetilde{\rho}\left(\mathbf{G}\right)e^{i\mathbf{G}\cdot\mathbf{r}} \tag{2.4}$$

where $\widetilde{\rho}(\mathbf{r})$ is the density, Ω is the volume of the cell, $\widetilde{\rho}(\mathbf{G})$ are the expansion coefficients and $\mathbf{G}$ are the reciprocal lattice vectors. The Hartree energy is then computed using the FFT in the plane wave basis.

2.2.1.1 Pseudopotentials

Typically, DFT calculations using an all-electron basis set can be computationally expensive. This is because the core electron wavefunctions oscillate rapidly near the center of the atom, requiring very high quality basis sets. However, because the core electrons are minimally involved in bonding, detailed descriptions of them are not required to model a wide range of interesting phenomena. Instead, it is usually the valence electrons which play an important role in bond breaking and making. As a result, it can be computationally efficient to use a 'pseudopotential' to represent the core electrons and nucleus, removing the need to describe the core electrons with full quantum mechanical molecular orbitals. This leaves the valence electrons to be solved completely during calculation, where they experience the effect of the pseudopotentials. In this thesis the Goedecker-Teter-Hutter (GTH) pseudopotentials have been used, which are fitted to provide optimal accuracy and efficiency when using a plane waves basis set [25]. The GTH pseudopotentials have been used extensively by CP2K users [26, 27], with versions available for a number of exchange correlation functionals [28]. A detailed description of the GTH pseudopotentials can be found in [25, 29]

2.2.2 Exchange Correlation Functionals

2.2.2.1 LDA and GGA

The exchange correlation functional (V_{XC}) can be described as a function of the exchange correlation energy E_{XC} [16]:

$$V_{XC}[\mathbf{r}] = \left(\frac{\delta E_{XC}[\rho(\mathbf{r})]}{\delta \rho(\mathbf{r})} \right). \tag{2.5}$$

The two classes of commonly used approximations for the exchange correlation functional are the local density approximation (LDA) [30] and the generalised gradient approximation (GGA) [31]. The local density approximation determines the

exchange correlation energy by considering the electron density at each point in space of a system. It assumes that each point in an inhomogeneous electron distribution will have the same exchange correlation energy as a point in a homogeneous electron gas (HEG) with the same electron density [32]. In this approach, the exchange correlation energy is typically approximated using the homogeneous electron gas model, where positive charges (protons) are distributed equally in a volume such that the electron density is also a uniform quantity in space. The number of protons and electrons (N) as well as the volume (V) are then taken to infinity such that the density ($\rho = N/V$) is finite and constant. The exchange energy of a HEG has been solved analytically [33]:

$$E_X^{LDA}[\rho] = -\frac{3}{4}\left(\frac{3}{\pi}\right)^{1/3}\int \rho(\mathbf{r})^{4/3}\,d\mathbf{r} \tag{2.6}$$

and the correlation energy can be calculated using quantum Monte Carlo simulation or many-body perturbation theory. In practice, the exchange and correlation energies are calculated for a small volume around each spacial point in the system and integrated over the whole electron density:

$$E_{XC}^{LDA} = \int \rho(\mathbf{r})\,\varepsilon_{XC}(\rho(\mathbf{r}))\,d\mathbf{r}. \tag{2.7}$$

The LDA was found to perform well for densities with limited variation in electron density such as metals, but poorly for inhomogeneous systems [30]. Generalised gradient approximation functionals were introduced to overcome this problem by adding functions that include the gradient of the electron density at each point [31].

$$E_{XC}^{GGA} = E_{XC}[\rho(\mathbf{r}), \nabla\rho(\mathbf{r})]. \tag{2.8}$$

There are many functionals that incorporate gradient dependent terms, such as PBE [31], BLYP [34] and PW91 [35]. Each of which give vastly improved representations of structure and energetics over the LDA for a wide range of materials. However, it should be noted that both approximations still have some significant

drawbacks. The local or semi-local character of the approximations do not correctly consider long range correlation interactions. These non-local interactions, known as dispersion interactions, are required to properly describe non-covalent interactions such as van der Waals forces.

2.2.2.2 Dispersion Corrections

Dispersion corrections are used to incorporate an energetic term for the otherwise neglected dispersion interactions. This is vital for systems such as those with intermolecular interactions or surfaces as well as those exploring potential energy surfaces. The total energy computed from a density functional approximated method can be augmented with a dispersion term giving an approximate solution to the non-local correlation problem as:

$$E_{DFT-D} = E_{DFT} + E_{Disp}. \tag{2.9}$$

In this work, Grimme's D3 dispersion has been used to study systems where non-local interactions may be prevalent (*e.g.* surfaces) [36]. The dispersion energy $E_{Disp}^{D3(zero)}$ is given as:

$$E_{Disp}^{D3(zero)} = -\sum_{n=6,8} s_n \sum_{i,j>i}^{N_{at}} \frac{C_n^{ij}}{\left(R_{ij}\right)^n} f_{damp}\left(R_{ij}\right), \tag{2.10}$$

where s_n are scaling terms dependent on the exchange correlation functional, N_{at} is the total number of atoms, C_n^{ij} are the n-order dispersion coefficients for atom pairs ij, R_{ij} is the inter-atomic distance between atoms i and j and f_{damp} is the damping factor. The damping factor used in this study is the 'zero' damping factor:

$$f_{damp}^{D3(zero)}\left(R_{ij}\right) = \frac{1}{1+6\left(R_{ij}/\left(s_{r,n}R_0^{ij}\right)\right)^{-\alpha_n}}, \tag{2.11}$$

where $R_0^{ij} = \sqrt{\frac{C_{8ij}}{C_{6ij}}}$ and α_n controls the damping rate. The parameters α_6, α_8 and $s_{r,8}$ are typically fixed to 14, 16 and 1 respectively and the remaining parameters s_6, s_8 and $s_r, 6$ are dependent on the exchange-correlation functional.

2.2.2.3 Self-interaction error and hybrid Functionals

An important consideration during DFT calculations is the self-interaction error found in the Hartree energy, defined as [37, 38, 39]:

$$E_H\left[\rho\left(\mathbf{r}\right)\right] = \frac{1}{2}\iint \frac{\rho\left(\mathbf{r_1}\right)\rho\left(\mathbf{r_2}\right)}{\left|\mathbf{r_1}-\mathbf{r_2}\right|}d\mathbf{r_1}d\mathbf{r_2}. \tag{2.12}$$

In this formalism, each electron in the system will feel average repulsion from all electrons in the system, including itself. Due to this increased repulsion the electron densities become more delocalised. This results in both LDA and GGA approximations underestimating the band gap and failing to properly describe localised defect states. To reduce the self interaction error, hybrid functionals can be used where a fraction, α, of Hartree-Fock exchange is added to LDA and GGA functionals. In Hartree-Fock theory, the self-interaction does not occur as the self interacting terms reduce to zero upon expansion of the Slater determinant. The exchange correlation energy E_{XC}^{Hyb} can then be calculated as:

$$E_{XC}^{Hyb} = \alpha_{Hyb}E_X^{HF} + \left(1-\alpha\right)E_X^{DFT} + E_C^{DFT}. \tag{2.13}$$

Because calculating the HF exchange integrals is computationally very expensive, hybrid calculations in this work are carried out with the PBE0-TC-LRC functional with the auxiliary density matrix method (see section 2.5.2), where the HF exchange is truncated to zero above a cut-off value [40]. This reduces the computational cost due to the HF exchange only being evaluated for a short range:

$$E_{XC}^{PBE0-TC-LRC} = \alpha E_X^{HF,TC} + \alpha E_X^{PBE,LRC} + \left(1-\alpha\right)E_X^{PBE} + E_C^{PBE}, \tag{2.14}$$

where α is the fraction of HF exchange. An α of 0.25 and a cut-off of 2 Å was used for all calculations unless otherwise stated.

2.2.3 Auxiliary Density Matrix Method (ADMM)

The auxiliary density matrix method (ADMM) is implemented in CP2K to reduce the computational expense of calculating the HF exchange [41]. The ADMM

method constructs a reduced density matrix using a smaller set of auxiliary basis functions. The HF exchange calculated from the reduced density matrix requires far fewer calculations as a result, significantly reducing the computational time. The auxiliary basis set is given as:

$$\psi' = \sum_{\mu} C_{\mu i} \psi_i' (r) \tag{2.15}$$

where ψ' is the wave function in the smaller auxiliary basis set, $C_{\mu i}$ is the orbital coefficient and $\psi_i' (r)$ is the orbital. The density matrix can then be constructed from the orbital coefficients as:

$$P^{\mu\nu} = \sum_{i} C_{\mu i} C_{\nu i}. \tag{2.16}$$

The orbital coefficients for the auxiliary basis set and auxiliary density matrix can be obtained by minimising the square difference between the wave functions in the original basis set and the auxiliary basis set. The HF exchange energy can then be calculated as:

$$E_x^{HF}[\rho] = E_x^{HF}[\rho'] + (E_x^{HF}[\rho] - E_x^{HF}[\rho']), \tag{2.17}$$

$$E_x^{HF}[\rho] \approx E_x^{HF}[\rho'] + (E_x^{DFT}[\rho] - E_x^{DFT}[\rho']), \tag{2.18}$$

where $E_x^{HF}[\rho']$ is the HF exchange energy and $E_x^{DFT}[\rho]$ is the exchange energy calculated using the GGA functional. The difference in the exchange energy calculated using the auxiliary and full basis sets using GGA and HF is assumed to be the same. Using the auxiliary density matrix therefore, can greatly reduce the cost of a DFT calculation when using a hybrid functional.

2.3 Defect Calculations with DFT

2.3.1 Defect Formation Energy

Through DFT calculations, thermodynamic, electronic, and optical parameters of artificially designed systems can be obtained, making them indispensable in the study of complex systems. Perturbations in these systems such as the addition of defects or electrons can then be studied giving the defect formation energy. This

is an important parameter, defined as the energy difference between an investigated system and the components of the system in their reference states. In this project, the formalism of Northrup and Zhang is employed [42]:

$$E_{form} = E_{Defect} - E_{Bulk} - \sum_{i} \mu_i n_i + q\left(\mu_e + E_V\right) + E_{corr}, \tag{2.19}$$

where E_{form} is the defect formation energy, E_{Defect} is the energy of the system with the defect, E_{Bulk} is the energy of the defect free system, μ_i is the chemical potential of the defect species i, n_i is the number species of type i added ($n_i > 0$) or removed ($n_i < 0$) from the system, q is the charge of the system, μ_e is a free parameter representing the electron chemical potential, E_V is the potential alignment and E_{corr} is the charge correction.

The chemical potential of a species is defined as the energy that is absorbed or released due to a change in the particle number of that species and can be calculated by dividing total energy of the defect species bulk by the number of species used. For example, the chemical potential of Ag from metallic Ag is calculated by dividing the total energy of the Ag bulk system by the number of Ag atoms it contains. However, the calculation of the chemical potential is also dependant on the ability of the exchange correlation functional to describe the bulk material. In this project, a significant number of calculations were carried out for Ag defects using the PBE and the PBE0_TC_LRC functionals. Whilst PBE functional gives an accurate representation of bulk metal, hybrid functionals poorly describe metals because they over bind electron density to nuclei. As such, the method used to calculate the chemical potential of Ag, μ_{Ag}, is different for PBE and the hybrid functional with a different bulk material selected for each functional:

$$\mu_{Ag}^{PBE} = \frac{1}{n} E_{Ag}, \tag{2.20}$$

where n is the number of Ag atom units in the Ag bulk system and E_{Ag} is the DFT calculated total energy of the bulk system. In the case of the hybrid functional calculations, μ_{Ag} is calculated from Ag_2O as hybrid functionals poorly describe

metallic Ag:

$$\mu_{Ag}^{PBE_TC_LRC} = \frac{1}{2n}\left(E_{Ag_2O} - \frac{1}{2}n\mu_{O_2}\right), \tag{2.21}$$

where n is the number of Ag_2O units in the system, E_{Ag_2O} is the total energy of the Ag_2O system and μ_{O_2} is the chemical potential of an oxygen molecule in the triplet state. For this investigation, all defect formation energies include the Lany-Zunger charge correction [43]:

$$E_{LZ} = \left[1 - c_{sh}\left(1 - \frac{1}{\varepsilon}\right)\right]\frac{q^2\alpha}{2\varepsilon L}, \tag{2.22}$$

where E_{LZ} is the Lany-Zunger correction energy, c_{sh} is the shape factor, ε is the dielectric constant, q is the charge state, α is the Madelung constant and L is the separation between defects [44, 45].

Defect calculations using DFT in periodic systems can be problematic due to the interaction of defects with themselves. This is further complicated by charged defects, where the long-ranged Coulomb potential can lead to unwanted interactions. As such, it is important to ensure the 'supercell' used is large enough to prevent interactions of defects with its periodic images. This can be achieved by converging the defect formation energy to the cell size.

2.3.2 Nudged Elastic Band (NEB) method

DFT can only be used to determine the electronic structure and total energy of a static system. Therefore, a method is required to model dynamics in the system and determine the lowest energy path for a reaction, where a reaction is defined as a rearrangement of atoms from one stable configuration to another. From this path, known as the minimum energy path (MEP), activation energies for reactions and subsequently the rates of reaction can be determined [46]. In this regard, the nudged elastic band (NEB) method can be used to calculate saddle points and minimum energy paths along a reaction [47, 48]. The method uses linear interpolation to create a series of intermediate images (bands) along the reaction path between the initial and final configurations of the reaction. These images are subsequently optimised such that each image finds the minimum energy possible whilst maintaining

equal spacing to neighboring images. The overall system is constrained by adding spring forces between the images which project out the component of the force due to the potential perpendicular to the band. The NEB method originates from the plain elastic band (PEB) method where the force **F** acting on an image i is given by [49]:

$$\mathbf{F}_i = -\vec{\nabla} V(\mathbf{r}_i) + \mathbf{F}_i^{spring}. \tag{2.23}$$

Here $V(\mathbf{r}_i)$ is the total potential energy of the image i and $\mathbf{F}_i^{spring}$ is the force on i image due to the springs attached:

$$\mathbf{F}_i^{spring} = k_{i+1}(\mathbf{r}_{i+1} - \mathbf{r}_i) - k_i(\mathbf{r}_i - \mathbf{r}_{i-1}), \tag{2.24}$$

where k is the spring constant. The PEB method is an example of a chain of state method, where several images (or 'states') of a system are connected together to trace out a path. The object function is defined as [48]:

$$S^{PEB}(\mathbf{r}_1, \ldots, \mathbf{r}_{P-1}) = \sum_{i=0}^{P} V(\mathbf{r}_i) + \sum_{i=1}^{P} \frac{Pk}{2}(\mathbf{r}_i - \mathbf{r}_{i-1})^2, \tag{2.25}$$

where the first term sums the potential energies of each of the images and the second term sums the potential energies arising due to the springs connecting the images. If the images are connected with springs of zero natural length, the chain is mathematically analogous to a Feynman path integral for an off-diagonal element of a density matrix describing a quantum particle. To find the MEP in PEB method, the object function is minimised with respect to the intermediate images while keeping the start and end point images $\mathbf{r}_0$ and $\mathbf{r}_P$ fixed.

The PEB inherently fails to provide the MEP in most situations. When the spring constant is high, the elastic band becomes too stiff such that the path cuts corners in the energy landscape missing the saddle point region. This is a consequence of the component of the spring force which is perpendicular to the path which tends to pull images away from the MEP. When a smaller spring constant is used, the elastic band becomes closer to the saddle point but the images slide down

avoiding the barrier region. This reduces the resolution of the band at the transition point region. This is due to the component of the true force $\vec{\nabla}V(\mathbf{r}_i)$ in the direction of the path. The distance between images becomes uneven such that the net spring force balances out the parallel component of the true potential force.

In the NEB method, the elastic band is minimised such that the perpendicular component of the spring force and the parallel component of the true force are projected out. The force on image i becomes:

$$\mathbf{F}_i^0 = -\vec{\nabla}V(\mathbf{r}_i)|_\perp + \mathbf{F}_i^{spring} \cdot \hat{\tau}_\parallel \hat{\tau}_\parallel, \tag{2.26}$$

where $\hat{\tau}_\parallel$ is the unit tangent to the path. The perpendicular component of the true force $-\vec{\nabla}V(\mathbf{r}_i)$ is given by:

$$-\vec{\nabla}V(\mathbf{r}_i)|_\perp = \vec{\nabla}V(\mathbf{r}_i) - \vec{\nabla}V(\mathbf{r}_i) \cdot \hat{\tau}_\parallel \hat{\tau}_\parallel. \tag{2.27}$$

Projecting the force in this way decouples the dynamics of the path itself from the distribution of images chosen in the representation of the path. Therefore, the spring force then does not interfere with the relaxation of the images perpendicular to the path. As a result, the relaxed configuration of the images satisfies $-\vec{\nabla}V(\mathbf{r}_i)|_\perp = 0$ such that the images lie on the MEP. Because the spring force only affects the distribution of the images within the path, the choice of the spring constant becomes less restrained. This decoupling of the relaxation of the path and the discrete representation of the path is essential to ensure convergence to the MEP. A further improvement is the climbing image nudged elastic band (CI-NEB) [47]. In this case the springs connected to the highest energy image are allowed to relax giving a better approximation of the saddle point.

2.4 Molecular Dynamics

Molecular dynamics is a computational method that determines the time evolution of a system of interacting particles by integrating Newton's laws of motion [50]. This results in a trajectory that describes how the positions and velocities of the

particles in the system progress with time. Newton's second law dictates that the force imposed on a particle is equal to the rate of change of the momentum of that particle:

$$\mathbf{F}_i = m_i \ddot{\mathbf{r}}_i(t) \quad for \quad i = 1 \ldots N, \tag{2.28}$$

where $\mathbf{F}_i$ is the force acting on particle i, m_i is the mass of particle i, $\mathbf{r}_i(t)$ is the position of the particle i at time t, and N is the number of particles in the system. In a system of interacting particles, the forces exerted on each particle can be expressed the gradient of the potential V_{pot};

$$\mathbf{F}_i(\mathbf{r}_1 \ldots \mathbf{r}_n) = -\nabla_i V_{pot}(\mathbf{r}_1 \ldots \mathbf{r}_n), \tag{2.29}$$

where $\nabla_i = \partial / \partial \mathbf{r}_i$. The origin of the potential energy surface $V_{pot}(\mathbf{r}_1 \ldots \mathbf{r}_n)$ is from quantum mechanics and can be defined as a function of the positions (3N) of all the particles in the system. Due to the many body nature of this function, analytical solutions cannot be made and instead numerical solutions must be found. This can be done using either *ab initio* methods such as DFT or classical methods, each of which have their benefits.

In *ab initio* methods, electronic structure calculations allow for an accurate representation of the potential energy surface [51]. This in turn provides accurate models of particle dynamics at the cost of high computational expense. Classical methods, however, use a comparatively simplified potential energy function to predict the potential energy surface. In this case an accurate representation can be made though this relies on the choice of potential energy function and how well it represents the system. In theory, a well selected potential energy function will give equally accurate predictions of particle dynamics as *ab initio* methods using a fraction of the computation expense. This is particularly useful when considering large systems to be studied where *ab initio* methods cannot be used. In this project, both *ab initio* and classical MD have been used.

2.4.1 Classical Potential Energy Functions

A large number of classical potential energy functions have been developed to give simplified descriptions of the potential energy surface [52]. The form of these functions, or potentials, can range in levels of complexity and vary with the type of bonding. A logical method to describe the potential energy surface is to expand it in terms of one-body, two-body and higher order terms:

$$\begin{aligned} V_{pot}(\mathbf{r}_1 \ldots \mathbf{r}_n) = & \sum_i v_1(\mathbf{r}_i) + \sum_i \sum_{j>i} v_2(\mathbf{r}_i, \mathbf{r}_j) \\ & + \sum_i \sum_{j>i} \sum_{k>j>i} v_3(\mathbf{r}_i, \mathbf{r}_j, \mathbf{r}_k) + \ldots, \end{aligned} \tag{2.30}$$

where v_1 represents the effect of an externally applied field and the remaining terms represent inter-atomic interactions. v_1 is usually set to zero in periodic calculations and the potential is evaluated starting from the two-body term. In general, evaluating the two-body term alone can give a good representation of the PES, especially for describing systems with ionic or van der Waals bonding. The most commonly used two-body potential is the Lennard-Jones potential [53], which can be fitted to experimental or theoretical data for a given system;

$$v^{LJ}(r) = 4\varepsilon \left[\left(\frac{\sigma}{r} \right)^{12} - \left(\frac{\sigma}{r} \right)^{6} \right], \tag{2.31}$$

where ε is the potential well depth, σ is the finite distance at which the inter-particle potential is zero and r is the distance between the particles. If electrostatic charges are present, the Coulomb potentials are added;

$$v^{Coulomb}(r) = \frac{Q_1 Q_2}{4\pi\varepsilon_0 r}, \tag{2.32}$$

where Q_1 and Q_2 are the charges of each particle and ε_0 is the permittivity of free space.

2.4.2 Integration of Newton's Law

Once a potential energy surface has been defined, one must still integrate Newton's equation of motion. The Verlet algorithm, is commonly used and can be derived by making the Taylor expansion of the position coordinate both forward and backward in time [54]:

$$\mathbf{r}(t+\Delta t) = \mathbf{r}(t) + \mathbf{v}(t)\Delta t + \frac{1}{2}\mathbf{a}(t)\Delta t^2 + \ldots, \tag{2.33}$$

$$\mathbf{r}(t-\Delta t) = \mathbf{r}(t) - \mathbf{v}(t)\Delta t + \frac{1}{2}\mathbf{a}(t)\Delta t^2 + \ldots \tag{2.34}$$

These two equations can be added together to create the Verlet algorithm, which is a symmetric function with time conservation in both directions:

$$\mathbf{r}(t+\Delta t) = 2\mathbf{r}(t) - \mathbf{r}(t-\Delta t) + \mathbf{a}(t)\Delta t^2 + O\left(\Delta t^4\right). \tag{2.35}$$

The algorithm is properly centered such that $\mathbf{r}(t+\Delta t)$ and $\mathbf{r}(t-\Delta t)$ play symmetrical roles, making it time-reversible and it shows excellent energy-conserving properties over long times. It is assumed that the forces only depend on the position coordinates. The velocities do not enter explicitly in the algorithm, however, they are needed for estimating the kinetic energy and hence the temperature. They can be obtained by subtracting Eq. 2.33 with Eq. 2.35.

$$\mathbf{v}(t) = \frac{\mathbf{r}(t+\Delta t) - \mathbf{r}(t-\Delta t)}{2\Delta t} + O\left(\Delta t^2\right). \tag{2.36}$$

2.4.3 NVT Ensemble

Molecular dynamics simulations rely on thermodynamic ensembles, which are used to allow the properties of real thermodynamic systems to be extracted from the calculations [55]. One example of this is the canonical ensemble (NVT) [56], which is used for all molecular dynamics simulations carried out in this thesis. In the NVT ensemble, the number of atoms (N), volume (V) and temperature (T) are conserved quantities. Subsequently, the energy of the endothermic and exothermic processes in the simulation are exchanged with a thermostat. In this way, control of the thermostat provides a way to add and remove energy from the boundaries of the system

in a realistic way, approximating the canonical ensemble. An in depth discussion of the practical applications of the NVT ensemble in molecular dynamics simulations can be found in the literature [56].

2.4.4 Nose-Hoover thermostat

The Nose-Hoover thermostat is an algorithm that is used in molecular dynamics simulations to re-scale the velocities of the particles in the system to control the simulation temperature [57]. This is achieved by modifying the equations of motion for each atom in the system to include a non-Newtonian term in order to maintain the total kinetic energy to a set constant. A detailed explanation of the Nose-Hoover thermostat and its use in the NVT ensemble can be found in the literature [58].

Chapter 3

Experimental Background and Methods

3.1 Introduction

During the course of this project, three silicon oxide based RRAM devices were characterised using experimental methods. This was done in collaboration with Anthony Kenyon, Adnan Mehonic and Wing Ng from the Electronic and Electrical Engineering Department at UCL who have been investigating silica RRAM devices for a significant period of time [59, 60]. Their work shows that Au-Ti-SiO_x-Mo (Au-Ti) RRAM devices give favourable operational properties including low switching voltages, high switching speeds, high data retention times and high endurance [15]. To determine how and why these devices performed well, a significant portion of this project was spent characterising them in their pristine and electroformed states using a transmission electron microscope (TEM). This allowed characterisation of the devices at the atomic scale, providing a complimentary technique to the DFT calculations also carried out in the project. Measurements were focused on the changes induced in the Au-Ti device during electroforming, where a number of processes are thought to occur. This includes the generation and formation of oxygen ions, molecules and vacancies as well as the diffusion of Ti into the silica layer. It is assumed that each of these processes contribute conductive pathways in the silica layer, therefore playing a role in the switching process.

Au-SiO_x-Mo (Au) and Ti-SiO_x-Mo (Ti) devices were also fabricated and characterised in this work. Devices with a Au top electrode are expected to operate primarily via the generation of oxygen and oxygen vacancies. In addition to O vacancy generation, devices with a Ti electrode exhibit migration of Ti into the silica layer thus forming an alternative conductive pathway. As such, the role of these mechanisms and which dominates in a Ti-Au device is unclear. In this way, studying the Au and Ti devices is hoped to give further insights regarding the Au-Ti device. Previous work has also shown that the silica microstructure plays a significant role during device operation. The Au-Ti device was grown with rough electrode-silica interfaces and a high concentration of columnar grains. The column boundaries are assumed to aid RRAM operation by facilitating O and Ti ion mobility. In this regard, the Au and Ti devices were grown with smoother interfaces to better study interface-electrode interactions whilst also reducing columnar structure. This in turn was hoped to aid in the investigation on the role silica microstructure plays during device operation. Throughout the investigation, specific interest was given to the nature of the metal-silica interfaces and the diffusion of the electrode material into the oxide.

The three devices were fabricated by Wing Ng using a combination of reactive sputtering and thermal evaporation at UCL. In the Au-Ti device, magnetron sputtering was used to deposit the bottom Mo layer, reactive sputtering for the silica layer and thermal evaporation for the top layer (Au-Ti). In the Au and Ti devices, the top and bottom electrode layers were grown by thermal evaporation and the silica layer was grown with reactive sputtering. The Au and Ti devices were electroformed by Adnan Mehonic at UCL and the Au-Ti devices were electroformed at the Singapore University of Technology and Design with assistance and equipment provided by Kin Leong Pey and Alok Ranjan. The TEM lamellas for all measurements were prepared using a focused ion beam (FIB) by Siew Lang Teo from IMRE at A*STAR.

This chapter begins with a brief overview of the device fabrication methods starting with an introduction to the reactive sputtering and thermal evaporation tech-

niques, followed by a fabrication summary of each device. The methods used to prepare and characterise the devices using transmission electron microscopy are then discussed including the layout of a TEM and its individual components. The interactions of the electron beam with the sample and image collection modes are then described followed by an outline of the focused ion beam sample preparation method.

3.2 Device Fabrication

3.2.1 Reactive Sputtering

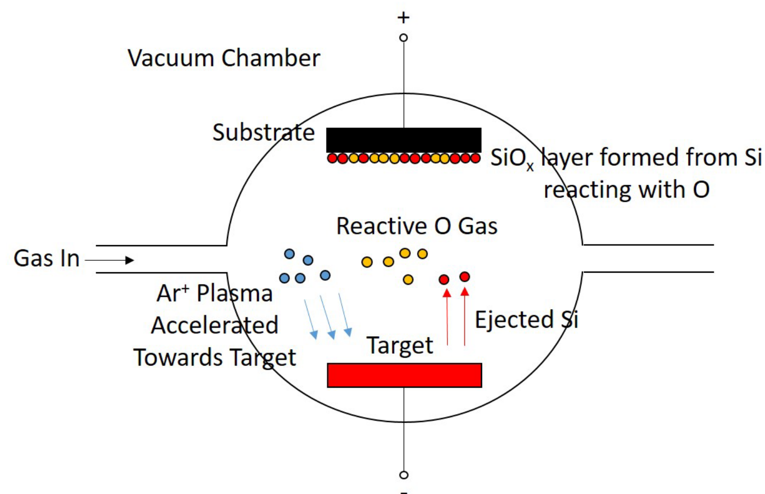

Figure 3.1: Schematic of the reactive sputtering process.

Magnetron sputter deposition was used to grow the Mo layer in the Au-Ti device and reactive sputter deposition used to grow the SiO_x layer in the Au-Ti, Au and Ti devices. The sputtering process occurs when particles of a solid material are ejected from its surface after the material is bombarded by energetic particles in a plasma or gas (as shown in Fig. 3.1). The sputtered particles ejected from the material then traverse a vacuum to form onto a substrate. The vacuum is kept to maximise the mean free path of the sputtered particles allowing them to travel to the substrate unhindered. The vacuum chamber is also partially filled with Ar gas which is ionised to form a plasma. The Ar^+ ions in the plasma are subsequently accelerated with high energy towards a high purity target which is kept at a nega-

tive potential. Upon collision with the target, target material particles are ejected into the vacuum chamber with enough kinetic energy to traverse the chamber to the sample. In reactive sputtering, a reactive gas is introduced into the plasma along with Ar. The reactive gas becomes activated in the chamber and chemically combines with the atoms that are sputtered forming a new compound consisting of the target material and the reactive gas. In this regard, reactive sputtering is a combination of physical, electrical, and chemical processes. It should be noted that sputter deposition has long been used as a technique to deposit SiO_2 films for use in microelectronics, such as the gate dielectric in transistor devices [61].

During sputter deposition, conditions such as the target voltage, the vacuum level, the relative pressure of the reactive gas, and the temperature determine the microstructure and topology of the films. Adjustment of these parameters allows control over film thickness, stoichiometry, porosity and uniformity. An important property observed in sputtered films is the emergence of columnar growth, which is thought to play a crucial role in RRAM devices [62, 63, 64]. Fig. 3.2 shows how the structure of sputtered films changes with substrate temperature and vacuum chamber pressure. As the substrate temperature is increased, a transition from a porous phase (zone 1) to densely packed fibrous grains (zone T) is observed. As the substrate temperature is increased further, columnar grains (zone 2) begin to form and at high substrate temperature recrystallised grain structure (zone 3) or zones of single crystals are observed. The vacuum pressure plays a similar but inverse role to temperature, where increased pressure yields more porous (zone 1) films.

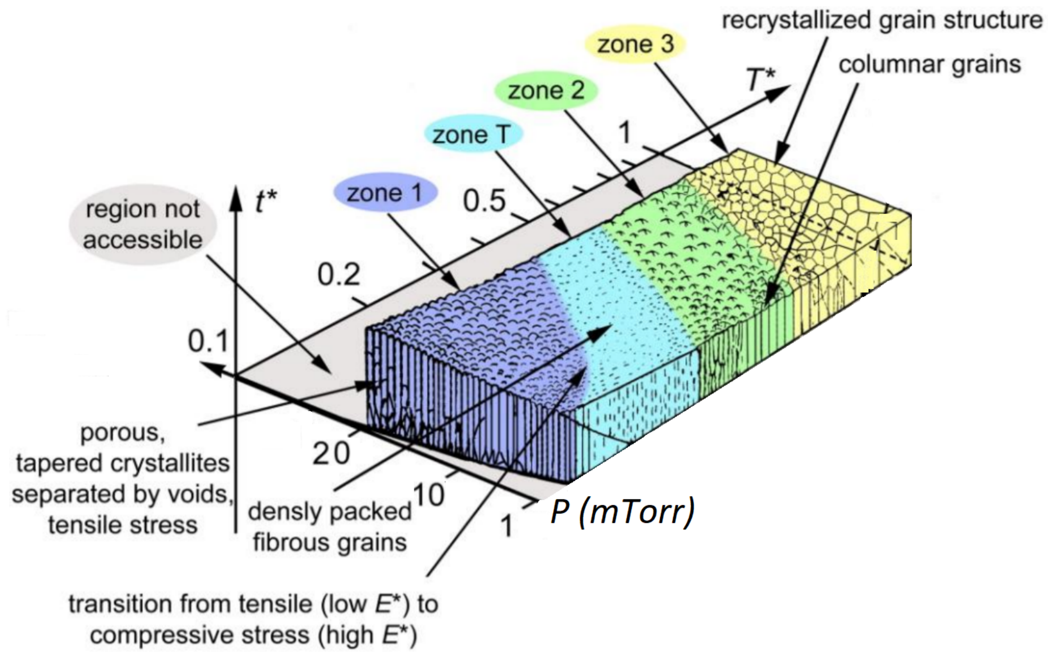

Figure 3.2: Diagram showing the Thornton Model [64].

The substrate was kept at room temperature during the growth of the devices in this project to promote the formation of columnar grains and rough interfaces (Zone 2 in Fig. 3.2). However, the exact nature of these columns at the microscopic scale and their role in RRAM operation is unclear. Previous work suggests that columns facilitate migration of atomic and ionic species resulting in better performing memories. Investigation into columnar structure forms a significant topic of interest for the research carried out in this project.

3.2.2 Thermal Evaporation

Thermal evaporation was used to grow the top electrode layers for all three devices and the Mo bottom electrode layer in the Au and Ti devices [65]. The use of thermal evaporation to grow the Mo layer in the Au and Ti devices was to produce a smoother electrode-silica interface compared with the sputter deposition technique. The smoother interface in turn allows the chemistry of the electrode-silica interface to be better studied *via* TEM.

The thermal evaporation technique is a thin film deposition method in which a target material is heated to evaporation temperatures in a vacuum chamber. This results in a vapour from which particles traverse the vacuum and condense onto a

substrate (Fig. 3.3). The vacuum is kept at low pressures, typically 10^{-5} to 10^{-6} Torr to minimise reaction between the vapour and atmosphere. At these low pressures, the mean free path of the vapour atoms are of the order of the vacuum chamber dimensions, such that the particles travel in straight lines from the evaporation source towards the substrate. The source material is usually held in a crucible which is heated by a heating element, usually *via* joule heating.

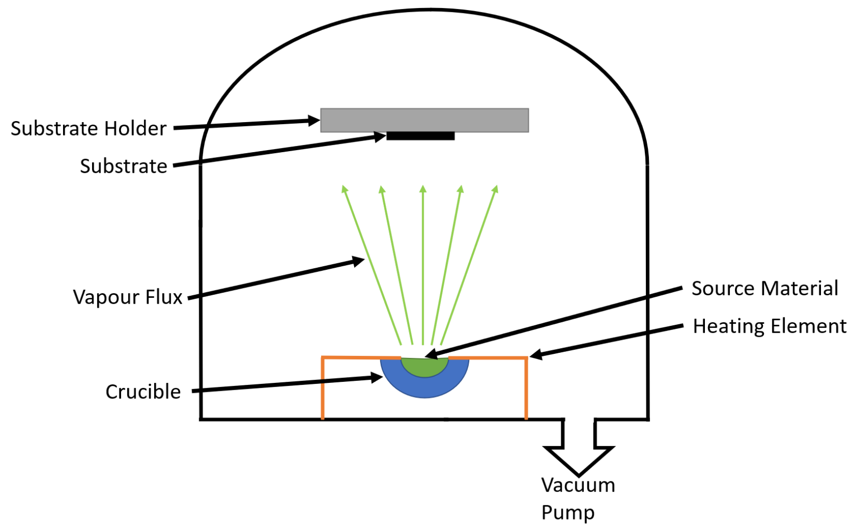

Figure 3.3: Schematic of thermal evaporation process

3.2.3 Fabrication Summary

3.2.3.1 Au-Ti-SiO$_x$-Mo (Au-Ti) device

The base wafer for the Au-Ti device is a Si wafer with 4 μm of thermally oxidised SiO_2 on top. In this case, the SiO_2 layer serves to electrically isolate the RRAM stack from the Si base wafer. A 210 nm layer of Mo was deposited directly onto the base wafer by magnetron sputtering to form the bottom electrode. A 35 nm layer of SiO_x was then deposited on top of the Mo layer using reactive sputtering. For this, an undoped Si target was sputtered in an O/Ar environment where the stoichiometry of the SiO_x film could be controlled by the ratio of O/Ar gas flow. After the SiO_x layer was deposited, a combination Ti and Au was was deposited by thermal evaporation to give the top electrode. First a 5 nm Ti layer was deposited followed by a 100 nm layer of Au. A shadow mask was used during the top electrode deposition to define individual device sizes. The device sizes were selected to be 200 x 200

μm, 400 x 400 μm, 600 x 600 μm and 800 x 800 μm. There was no annealing of the devices as this would promote inter-diffusion and no other treatments were applied.

3.2.3.2 Au-SiO_x-Mo (Au) and Ti-SiO_x-Mo (Ti)

The fabrication method and stack composition for Au and Ti was similar to that of Au-Ti. A Si base wafer was used with a 1 μm thermally oxidised SiO_2 layer on top. A 65 nm layer of Mo was then deposited by thermal evaporation giving the bottom electrode. The SiO_x layer was then deposited using the same reactive sputtering method as used in the Au-Ti device, at a thickness of 25 nm. After the SiO_x layer was deposited, the wafer was cleaved into two separate pieces. For the Ti device, a top electrode of Ti (85 nm) deposited by thermal evaporation. For the Au device, a top electrode of Au (85 nm) was deposited by thermal evaporation. The same shadow mask was used during the top electrode deposition as the Au-Ti device to define the device sizes again ranging from 200 x 200 μm to 800 x 800 μm. Similarly no annealing or other treatments were applied.

3.3 Transmission Electron Microscopy

Transmission electron microscopes (TEMs) were first developed in the early 1930's with the intent of directly imaging and characterising materials at the atomic resolution [66]. With RRAM devices designed to be as small as possible to enable efficient scaling, TEMs have become a powerful tool for their characterisation. In particular, measurements can be extremely insightful as they allow the observation of the chemical and structural changes induced in the devices as a result of electroforming. Furthermore, collecting data at such small scales allows the results to be combined with DFT calculations to develop models and mechanisms for the changes observed.

In principle, the operation of a TEM is similar to that of an optical microscope with electrons substituted for photons. The limit of resolution for optical microscopes depends on the numerical aperture and the wavelength of the photons. Similarly, this relationship holds true for electron microscopes where the energy or

speed of electrons determines their wavelength. The higher the speed of an electron, the smaller it's wavelength resulting in an increased resolution of the microscope. The electrons in TEM are produced by applying an acceleration voltage to an electron source (such as a tungsten tip) causing it to emit high energy electrons towards the sample. An acceleration voltage of 200 kV gives a wavelength of approximately 2.5 pm which is well beyond the limits of optical microscopes and other imaging techniques. Once produced, the electrons are focused into a beam onto the sample by a series of electromagnetic lenses and apertures. Subsequently, the electrons are collected by various detectors to give an image, a diffraction pattern, or a spectrum. TEMs have been developed extensively to provide a range of different imaging modes making them an incredibly unique and versatile tool to characterise materials. In addition to allowing high resolution images to be taken, accurate and precise analysis of the elemental composition and electronic structure of materials is possible. The modes used extensively throughout this project include scanning transmission electron microscopy (STEM) [67], electron energy loss spectroscopy (EELS) [68] and energy dispersive X-ray spectroscopy (EDX) [69]. The TEM used for this project is the FEI Titan S/TEM which operates with acceleration voltages of 80, 200 and 300 keV though it should be noted that an acceleration voltage of 200 keV has been used to collect the data presented in this work.

In this section, a brief but technical understanding of a TEM will be given. This includes an overview of electron sources, electromagnetic lenses, sample holders and stages followed by a description of the various electron-sample interactions. In the final part of the section, the various electron detection modes used in this work are described, including TEM imaging, STEM imaging, EELS spectroscopy and EDX spectroscopy.

3.3.1 Transmission Electron Microscopes

The make up and operation of a TEM can be separated into a series of processes as shown on 3.4. This begins with the generation of an electron beam *via* a field emission gun. This beam is then conditioned by a series of electromagnetic lenses and apertures onto the sample such that accurate high magnification electron images

can be formed. The electron images are then transformed into images perceptible to the human eye using either a fluorescent screen for viewing and focusing or by a camera to take permanent images [70].

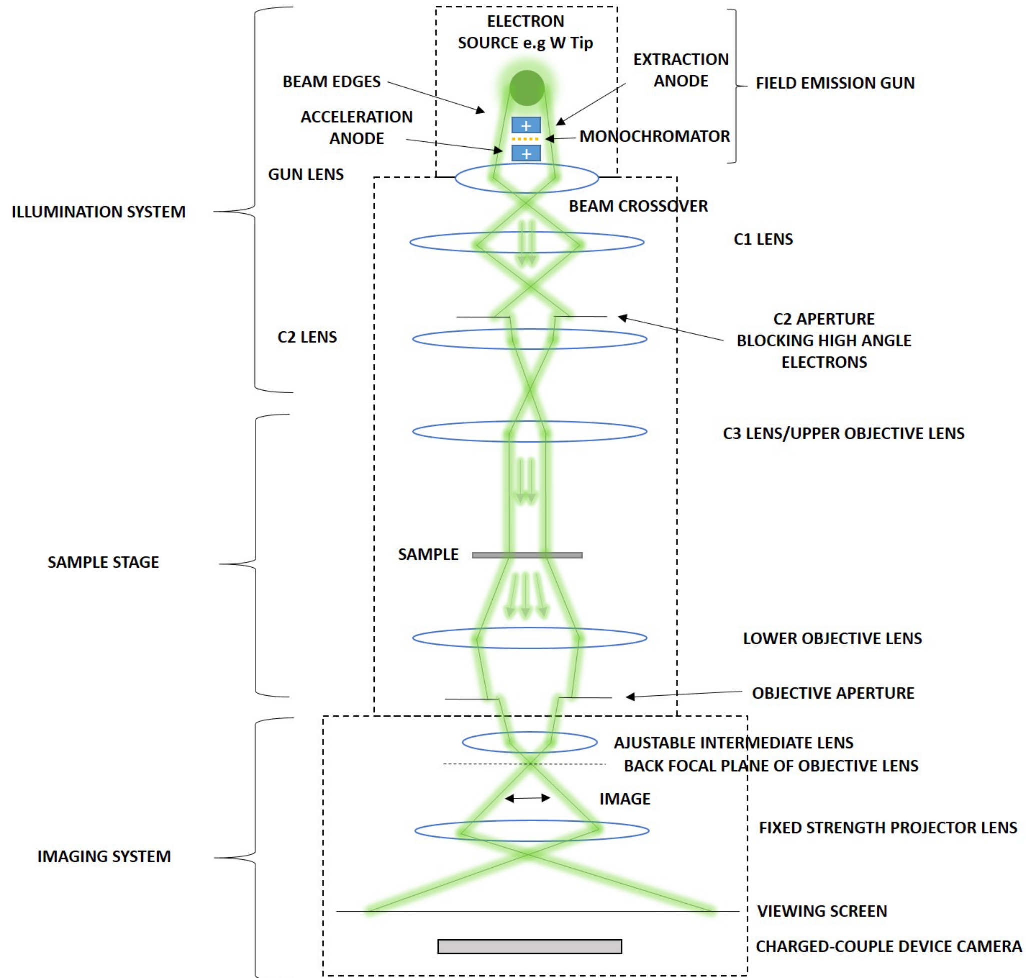

Figure 3.4: Schematic of the FEI TITAN used in this study.

3.3.1.1 Electron Sources

Electrons are produced by one of two processes, namely thermionic emission or 'cold' field emission [70]. During thermionic emission, an electrical current is applied across an electron source (usually a very fine W filament), such that the filament is heated by the current flowing through it. This causes electrons within the filament to escape with low energy, requiring acceleration before entering the electron column. Acceleration can be achieved by applying a high voltage difference between the electron source (cathode) and an anode plate. This results in a strong

electrostatic field which accelerates the electrons to the desired speed. During cold field emission an extremely fine single crystal W filament is used such that electrons can escape the filament without heating. In this case, only an anode plate is required to extract the electrons from the electron source. The advantage of cold field emission sources is that they produce a high yield of more monochromatic electrons compared to thermionic emission sources. The electrons in cold field emission are emitted from a smaller area of the source giving a source size of a few nanometers, compared to up to 50 μm for the W filament in a thermionic emission source. [70]

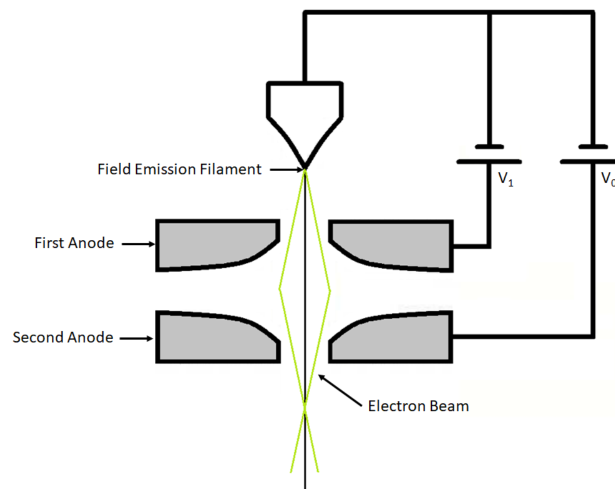

Figure 3.5: Schematic of the electron source used in the FEI TITAN.

The FEI Titan used for measurements in this project employs a Schottky field emission gun which combines the thermionic and field emission methods (Fig. 3.5). In this case, both heating and an electric field are employed to extract electrons from a W filament. As such, two anodes are positioned are positioned below the filament one after the other. The first anode acts to extract the electrons from the filament, whilst the second accelerates the electrons up to the required voltage. In this case, the emitted electrons are accelerated to $\approx$ 0.7 times the speed of light by a series of electrostatic plates. This high kinetic energy gives the electrons the short wavelength required for high-resolution imaging. It should also be noted that the electron source is kept under high vacuum conditions and can be separated from the rest of the system by a valve.

3.3.1.2 Electromagnetic lenses

Once electrons have been emitted from the electron source, the microscope is required to gather and focus them onto the sample to illuminate only the area being examined. This is achieved using electromagnetic lenses, which function to focus or deflect electrons passing through the TEM column via the Lorentz force [70]. Lenses consist of a series of windings of wire (usually copper) about a ferromagnetic cast and pole pieces usually made from soft iron (Fig. 3.6). The pole piece is usually located centrally in the cast, close to the path through the lens the electron beam takes. The magnetic field is induced in the cast by a current applied in the windings such that the field generated is maximum at the pole pieces. The electrons that enter the magnetic field produced by electromagnetic lenses are deviated such that the resultant force on the electrons is always perpendicular to the plane defined by the direction of the magnetic field and the direction of the electrons.

The focal depth of a lens is directly dependent on the strength of the magnetic field and therefore, the current applied in the windings. Electromagnetic lenses are subject to aberrations similar to those observed in glass lenses such as spherical aberration, chromatic aberration, distortion and astigmatism. The most common aberration in electron microscopy is spherical aberration, which is caused when the outer parts of a lens do not bring the electrons into the same focus as the central part of the lens, leading to a blurring of the image. Astigmatism is caused by inhomogeneities and contamination of the lenses as well as from apertures and inadvertent charging of the sample. Aberration corrected TEMs exist to correct these issues, though have not been employed in this work [71].

The FEI Titan microscope uses six lenses in the 'illuminating system', which serves to collect the electrons from the electron source and focus them through the sample. These include the 'gun' lens, the first condenser lens (C1), the second condenser lens (C2), the third condenser lens (C3), the minicondenser lens (MC) and objective lens (Obj). Each of these lenses serve an important function in generating high quality and useful data and will be briefly discussed.

The 'gun' lens is used to condition the electron beam produced by the electron

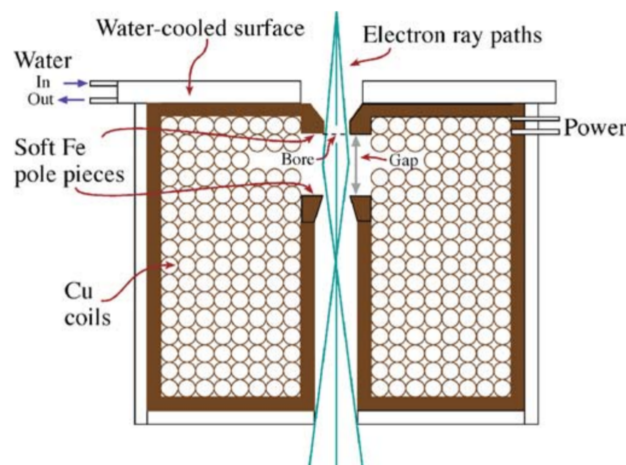

Figure 3.6: Schematic of an electromagnetic lens [70]

source and direct it into the TEM column. The condenser lenses are used in the TEM column to gather the electrons from the first crossover image outputted by the gun lens and focus them onto the sample. The C1 and C2 lenses are used in conjunction with the C2 aperture to determine the beam current or probe size. The C1 lens focuses the electron beam onto the specific focal plane of the C2 lens. The C2 lens subsequently focuses the beam through the C2 aperture to the C3 lens where the C2 aperture blocks high angle electrons. By blocking these electrons, changing the size of the C2 aperture alters the beam intensity and subsequently the spectral resolution of the beam. Apertures usually consist of a metal strip with holes in it, typically made of platinum or molybdenum. The C1 - C2 system is controlled by the ’spot number’ setting which, together with the gun lens, controls the beam current. For TEM and STEM images a small beam current is typically used to obtain maximum resolution. Conversely, for chemical analysis higher beam current is used to obtain a larger signal to noise ratio.

The C2 and C3 lenses are used in conjunction to control the beam width in TEM or the beam convergence in STEM. This is achieved by changing the position of the intermediate image between the C2 and C3 lenses. This in turn changes the diameter of the beam at the C3 lens controlling the size of the illuminated area. The C2 and C3 lenses are therefore used to determine the ’area zoom’, where the TEM software changes both values to keep the electron beam parallel in TEM.

The gun lens and the C1, C2 and C3 lenses to this point are primarily used to condition the beam for imaging and data collection. From here, the lenses focus the beam onto the specific sample area. The sample is located in the middle of the magnetic field of the objective lens acting both above and below the sample, known as the upper objective lens and the lower objective lens. The C3 lens images the beam onto the focal plane of the upper objective lens to control how parallel or focused the beam is leading up to the sample. A minicondensor lens is added after the C3 lens and before the upper objective lens to improve illumination of very large areas and very small areas of the sample. The upper objective lens is essential for STEM imaging, but makes it difficult to get good TEM illumination, especially for very large areas and for very small areas (see section 3.3.2.1).

As such, each of the lenses operate in unison to condition the electrons emitted from the electron source to and through the sample. The gun lens, C1 lens, C2 lens and C2 aperture primarily focus on the beam intensity and beam current. The C2 lens, C3 lens, objective lens and mini-condenser lens then work to focus the beam through the specific region of interest in the sample. As such, during measurements it is imperative that the correct settings are used.

3.3.1.3 Sample holders and stages

The TEM stage serves two main functions, namely to firmly hold the sample in the microscope and to bring the region of interest in the sample into the path of the electron beam. This is because the sample must be located in the focal plane of the electron beam to achieve maximum resolution. Also, the stage requires the ability to move the sample in the XY plane, the Z height direction as well as to tilt the sample. Furthermore, the stage must be highly resistant to mechanical drift and instability which leads to blurring or loss of sharpness in images, especially at high magnifications. Therefore, the stage must minimise drift to the nm/minute range whilst being able to move the sample at a rate of several µm/minute. The stage should also have a re-positioning accuracy on the order of nanometers, though this is not necessary.

The TEM samples used in this project were prepared into lamellas and attached

to onto 3 mm Cu grids (see section 3.3.3). The copper grids were then placed into a sample holder, which is paired with the sample stage. A wide variety of stages and holders designs exist depending upon the type of experiment being performed. The stage includes an airlock to allow the insertion of the sample holder into the TEM with minimal loss of vacuum in the other areas of the microscope. Once the sample holder has been inserted into the airlock and the pressure has pumped down, the holder is further inserted into the goniometer. The goniometer is a mechanical apparatus that enables highly precise and stable control of the sample holder during imaging including the tilting of the holder. As such, the goniometer is manipulated during measurements to bring the sample into the focal plane of the objective lens.

3.3.1.4 Electron Sample Interactions

When a high-energy electron encounters an atom, it first penetrates the outer electron cloud or valence electrons (Fig. 3.7). It may then propagate to the more tightly bound inner-shell electrons, and finally approach the nucleus. In each of these phases, a number of different interactions between the electron and the atom can occur, with almost all types being used to generate information about the sample. In this section, the ways in which electrons interact with the sample are discussed with a view to explain the information that can be obtained from the outgoing electrons. We begin with an explanation of the terms that will be used throughout the section followed by a breakdown of the most common electron-sample interactions.

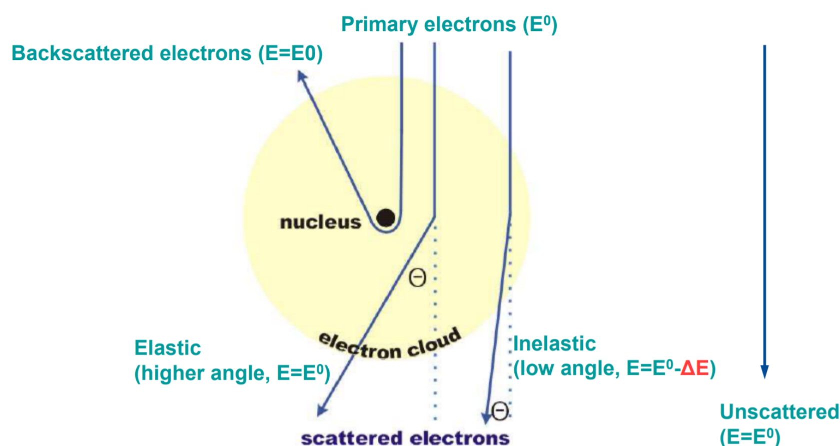

Figure 3.7: Schematic of the different electron scattering processes.

There are principally two types of interactions electrons can have with an atom,

namely elastic scattering interactions (elastic electrons) and inelastic scattering interactions (inelastic electrons). Elastic electrons are defined as those that have the same energy as the electrons in the primary beam. They are fundamental in TEM imaging giving the primary source of contrast. Inelastic electrons have lost energy and are used to provide information about the chemistry of the sample. Elastic scattering usually occurs at relatively low angles between 1 and 10°. Comparatively, inelastic scattering occurs at small angles within a few degrees of the primary beam. It should also be noted that electrons can be scattered more than once. Furthermore, less electrons are forward scattered and more are backscattered as the sample gets thicker giving an upper limit of the thickness of the sample.

Forward scattering forms a significant proportion of the TEM signal that is detected. When a sample is sufficiently thin, the electrons in the primary beam undergo fewer interactions with the sample reducing multiple scattering. In this case, contrast in the forward scattered image is directly dependent on the atomic number of the atoms passing though. This is because heavier atoms scatter electrons more strongly due to increased electrostatic interaction. It should be noted that this is true primarily for elastic scattering compared to inelastic scattering.

Inelastic electrons provide more information about the chemistry of the sample than elastic electrons. The signals associated with all losses in electron energy are encompassed in electron energy-loss spectroscopy (EELS). As a result of inelastic scattering, X-rays may also be emitted. Many TEMs detect both EELS electrons (EELS spectroscopy) and the emitted X-rays (EDX spectroscopy) to analyse sample chemistry. The detection methods for EELS and EDX can be seen in sections 3.3.2.2 and 3.3.2.3 respectively. The inelastic processes can be split into three components, namely, those that generate X-rays, those that produce secondary electrons and those that are caused by collective interactions such as plasmons or phonons (described below).

There are two types of X-ray emission that occurs in TEM, characteristic X-ray emission and Bremsstrahlung X-rays emission. When an electron inelastically interacts with inner-shell electrons, energy is transferred from the primary electron

to the inner-shell electron. If more than a critical amount of energy is transferred, that electron is excited above the Fermi level into the unfilled states such that the atom is considered to be in an ionised state. This process is known as inner-shell ionisation. Ionised atoms can return almost to the ground state by filling the hole with an electron from the outer-shell in a transition that is accompanied by the emission of either a characteristic X-ray or an Auger electron. In both cases, the energy of the emission is characteristic to the difference in energy between the inner and outer shells involved in the transition. These energies are unique to individual atoms and as such, the characteristic X-rays can detected in energy-dispersive X-ray (EDX) spectroscopy to provides useful chemical analysis of samples. In principle, EDX provides information on the chemical composition of a sample containing elements with atomic number (Z) > 3, though in practice, greater signal intensity is often only found for heavier elements. EDX has been used in this study to detect the electrodes materials during measurements. Bremsstrahlung X-ray emission occurs when electrons in the primary beam penetrate through the electron cloud and interact inelastically with the nucleus causing a substantial change in momentum. During this process the electron emits an X-ray where the amount of energy loss can range up to the energy of the primary beam depending on the strength of its interaction with the nucleus.

Secondary electrons are electrons that are ejected from the sample as a result of the interaction with the primary electron beam. Relatively small electron energies, typically below 50 eV, are required to eject electrons from the valence or conduction band. Electrons can also be ejected from an inner-shell by the energy released when an ionised atom returns to the ground state in a non-radiative transition known as Auger electrons. Though not used in this work, Auger electron spectroscopy can be employed to detect the Auger electrons providing chemical information about the sample.

Inelastic scattering due to collective interactions is primarily due to plasmon and phonon interactions. A plasmon is a longitudinal oscillation of the free electron gas that is stimulated when electrons from the primary beam interact with the

free electron gas. The oscillations are strongly localised (< 10 nm) and have an extremely fast relaxation time ($< 10^{15}$s). The plasmon process is the most common inelastic interaction occurring in materials and forms strong features in EEL spectra. Plasmons occur in any material with weakly bound or free electrons, predominantly in metals with a high free-electron density. The plasmon oscillations themselves are quantised, with the plasmon energy being a function of the free-electron density, which is a value that changes with material composition. This results in a chemical dependence of the plasmon peaks to the sample chemistry. The plasmon peaks occur at low energy loss and can provide useful information about the electronic structure of the sample. Furthermore, careful analysis of the plasmon peaks can be used to estimate the thickness of the sample [70].

Phonons are collective oscillations of the individual atoms in a solid. Phonons can be stimulated when electrons from the primary beam strike the sample. In this case, the high-energy electron strikes an atom in the sample inducing a vibration in the lattice. It should be noted that this is permitted due to the elastic nature of the bonding between the atoms. Phonons can also be generated by other inelastic processes where energy can be converted from Auger or X-ray emission internally to lattice vibrations. As atomic vibrations, phonons generate heat in the sample which can be damaging to the sample. As such, inducing phonons is detrimental to the work carried out in this project and can be mitigated by reducing the primary beam current.

3.3.2 Imaging and Spectroscopy

3.3.2.1 TEM and STEM Imaging

The electrons in the primary beam can change in both amplitude and phase as they interact with the sample [72]. Both amplitude change and phase change are fundamental to image formation and provide image contrast. In TEM and STEM, amplitude contrast is the primary contributor for bright-field and dark-field imaging involving, the detection of direct or scattered electrons respectively. There are primarily two types of amplitude contrast, namely mass-thickness contrast [73] and diffraction contrast [74]. Mass-thickness contrast arises from the incoherent elastic

scattering (Rutherford scattering) of electrons. Mass-thickness variation produces contrast because electrons interact with different amounts of material. Diffraction contrast is a result of the diffraction of the primary beam by the sample. A TEM is typically able to separate the diffracted and direct beams by switching to diffraction mode, which displays the diffraction pattern. The intensity of a diffracted beam depends strongly on the local structure of the region being studied. In this case, the diffraction pattern of in defective crystal regions compared to pristine crystal regions lead to diffraction contrast depending on the properties of the defect itself.

TEM and STEM imaging differ in that the primary beam is parallel during TEM and focused to a small probe in STEM [75]. The focused probe in STEM is scanned across the region of interest to collect an image. Due to this difference, a series of lenses are used for magnification during TEM imaging, whereas the magnification in STEM is defined by a set scanning area. In TEM imaging, a camera placed on the optical axis of the primary beam is used to collect images. STEM imaging, however, is typically done with two detectors, one on the optical axis of the primary beam to collect the bright-field image and a second high angle annular dark-field (HAADF) detector to collect the scattered electrons (Fig. 3.8). In TEM imaging, the objective aperture allows selection of the direct or the scattered electron beams. An image taken without the aperture results in lower contrast because many beams then contribute to the image thereby reducing diffraction contrast. The aperture size controls which electrons contribute to the image and therefore the contrast. In a STEM, greater flexibility can be introduced by changing the camera length, which alters the collection angle of the STEM detectors. This has the effect of introducing a variable objective aperture where the camera length can be adjusted to maximise the number of scattered electrons hitting the HAADF detector. This serves as the fundamental difference between the TEM and STEM dark-field modes, where dark-field TEM images are usually formed by allowing only a fraction of the scattered electrons to enter the objective aperture. STEM dark-field images are taken using an annular dark-field detector which collects high angle scattered electrons.

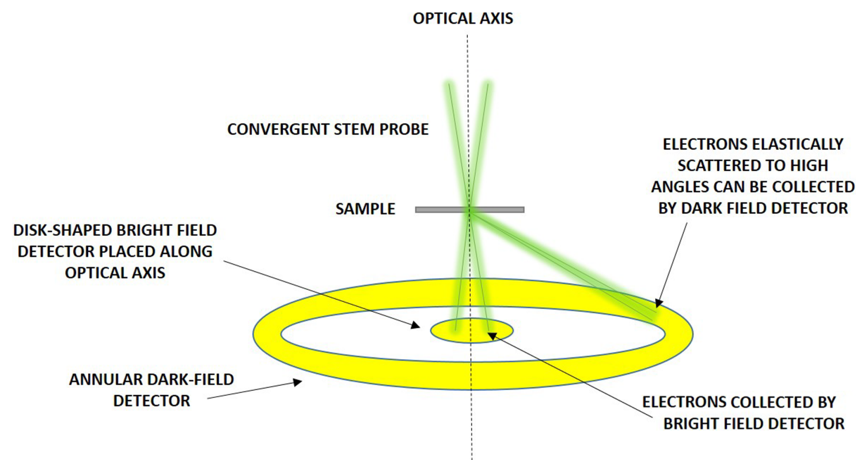

Figure 3.8: Schematic of a typical STEM detector.

3.3.2.2 Electron Energy Loss Spectroscopy

Electron energy-loss spectroscopy (EELS) is the analysis of the energy distribution of electrons that have traversed through the sample [76, 77]. This is possible because of the characteristic nature of the interaction between electrons and the sample. In principle EELS is able detect and quantify all the elements in the periodic table, though the limited detector dispersion and low signal to noise ratio results in EELS being primarily used to detect light elements. This is because EELS signals at higher energies give a weaker signal intensity as higher energy loss interactions are less likely to occur. Analysis of EELS data provides significant insight to the chemistry of the sample including its electronic structure, bonding and valence state, the nearest-neighbor atomic structure, dielectric response, free electron density, band gap and thickness.

An EELS detector separates the inelastic electrons from the zero-loss electrons into a spectrum which can be measured using a charge coupled device (CCD) (see in Fig. 3.9). The data can then be interpreted and quantified to form contrast images for electrons of specific energies or in an energy range. As the electron beam enters the EELS detector through an aperture, the path of the beam is deviated by a magnetic prism such that electrons with a lower energy are deviated more than the zero-loss electrons. This splits the beam into an energy separated spectrum which is then focused through a series of lenses and detected using a CCD. A slit is in-

serted after the magnetic prism to filter the electrons passing through to the CCD. The energy dispersion is controlled by setting the eV per channel in the CCD. This allows setting a narrow energy range to measure specific edges.

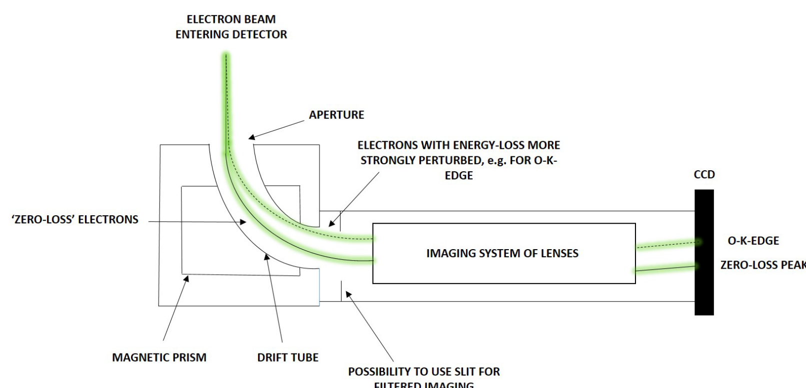

Figure 3.9: Schematic of the EELS detector used in this work.

The EELS measurements in this project were taken with the microscope in STEM mode, where the beam is focused to a point and scanned across the region of interest in the sample. In the measurement, the beam will move to and stop at the relevant point or pixel in the image and the EELS detector will collect electrons for a set acquisition time. This means that the EELS signal can be increased by two methods: i) by increasing the beam current thereby increasing the number of electrons collected per second; ii) by increasing the acquisition time, therefore increasing the total number of electrons collected over a period of time. During measurements, a trade is made between the signal to noise ratio, damage to the sample and time. Measuring the O K edge at 532 eV for example requires a larger beam current to obtain a reasonable signal to noise ratio but this can lead to sample damage. Instead, it is possible to reduce the beam current and increase the acquisition time, though this becomes problematic as drift becomes more of an issue. It should be noted that drift corrected EELS measurements were taken in this work. In this case, an initial 'drift image' image is taken in a separate region to the measurement and its position is used as a reference. After scanning a set number of pixels, the drift area will be re-scanned and image produced is compared to the initial reference image. The position of the electron beam for the next pixel is then adjusted to account for any

drift. As such the priority for measurements in this work was to minimise damage to the sample by using the lowest beam current whilst obtaining a good signal to noise ratio. The beam damage was checked by taking STEM images before and after EELS scans to observe any damage caused.

The electron energy loss spectrum is generally studied in two regions, namely the low-loss region and the high-loss region. The low-loss spectrum is usually below 50 eV and contains the zero-loss peak as well as the plasmon peaks. The low-loss spectrum provides information about the band structure and dielectric properties of the sample. The high-loss spectrum contains information about the ionisation edges of inner-shell electrons in the sample. These are characteristic to the chemistry of the sample, and are seen in the spectrum by an increase in signal intensity at an energy corresponding to the excitation of a core electron to the conduction band. Core-loss edges are representative of the local unoccupied electron density of states of the sample. The nature of the onset of an edge varies with different inner-shell ionisations, where major edges have a sharp rise in a small energy interval and minor edges have a more flattened peak. As such, minor edges can be more difficult to detect and observe in spectra. Edges are classed as K, L, M, or N edges referring to excitations from atomic shells with principal quantum numbers 1, 2 ,3, and 4, respectively. The L, M, and N edges can then be separated by the the total angular momentum quantum number of the electrons involved in the transitions. The fine structure of an edge, known as the Energy-Loss Near Edge Spectrum (ELNES) is unique for different compounds thus allowing the determination of local bonding structure by comparison.

EELS edges in this project were extracted from the EEL spectra using the Digital Micrograph software. Typically, an EEL spectrum contains signals from many types of interactions as well as a background signal across the energy spectrum. As such, the background signal must be removed to give the desired edge. The background signal represented as an exponential of the form:

$$f(E) = \alpha E^{-k} \tag{3.1}$$

where f is the background signal, and α and k are fitting constants. A window preceding edge onset is selected from which the constants α and k are determined. The background signal calculated from this window is assumed to accurately represent the complete background signal across the full spectrum and is subtracted from the EEL spectrum. The extracted EELS edge can be used to determine the elements present in the sample and their abundance.

EELS is a well-established technique for RRAM devices that use SiO_2[12]. It has also been used to image dielectric/semiconducting body interfaces and to look at the chemical nature of microelectronic devices similar to those discussed in this thesis [78, 79, 80]. This technique has also been used in-conjunction with DFT calculations to see the interplay between electronic structure and chemical composition.

3.3.2.3 Energy dispersive X-ray spectroscopy

Energy dispersive X-ray (EDX) spectroscopy is a powerful technique that enables the analysis of the elemental composition of a sample [81]. In general, EDX gives more intense signals for heavier elements making it a very complimentary technique to EELS which gives higher signals for lighter elements. This is achieved by employing an EDX detector to collect the X-rays that are emitted as the electron beam interacts with the sample. The detector generates a current pulse proportional to the energy of a collected X-ray, which is subsequently translated into a count in an energy channel. The counts in each of the energy channels are then displayed as a spectrum.

The EDX detector used in this investigation is made by EDAX and is located above the TEM stage. The detector is isolated from the stage section by a window composed of a thin beryllium (Be) sheet. X-rays that pass through the window fall on to a p- and n-doped Si semiconductor that generates electron-hole pairs. These pairs can be separated by applying a reverse bias across the p-n junction, where the electrons are subsequently detected. X-rays that are emitted for elements below Na ($Z = 11$) are usually absorbed by the window, reducing the signal strength. In some systems, an ultra-thin window or a windowless detector can be employed to avoid

this problem. The detector is cooled using liquid nitrogen to minimise noise in the Si semiconductor.

In the same way as EELS, the focus when taking EDX measurements is to obtain a high signal to noise ratio whilst minimising sample damage. Measurements were again taken in STEM mode, where the beam current was set to increase the count rate in the detector whilst ensuring the detector did not reach saturation. Once the beam current has been set in this way, the EDX scan can start, though in it should be noted that scans use a much shorter acquisition time per pixel compared to EELS. In this case, drift corrected scans can be repeated where the signal to noise ratio increases as the square root of the number of scans taken.

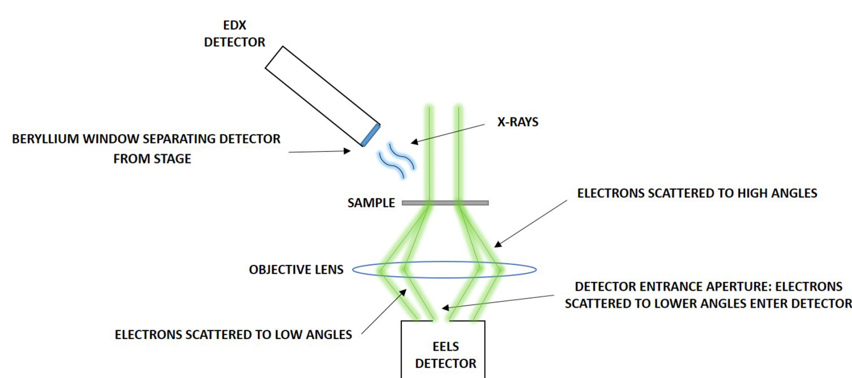

Figure 3.10: Schematic of the EDX detector used in this work.

3.3.3 Lamella preparation - FIB

Sample preparation is a very important step to ensure the TEM characterisation of samples can occur. This is because the sample must be electron transparent such that the electrons can penetrate the specimen and form an image, whilst also being representative of the material or device under study. The average thickness of a sample should be 50 to 100 nm for a TEM with an electron acceleration voltage of 200 kV. The sample should also be uniformly thin, stable under the electron beam and in laboratory conditions and conducting. It should be noted that this this is not always possible and as such, some compromises must be made. Many techniques are available for sample preparation including electropolishing, grinding and crushing, cleaving, and lithography. All samples studied in this project were

prepared using a focused-ion beam (FIB) as discussed below [82].

A FIB is a combination of a scanning electron microscope and a built-in ion gun which produces a beam of Ga ions to mill the sample. The SEM uses an electron beam to visualize the region of interest on the sample whilst the ion gun mills the sample at the region of interest to produce a lamella, which can be attached to a TEM grid. Each stage in the preparation process is shown in Fig. 3.11. First, a Pt coating is deposited onto the sample at the region of interest (Fig. 3.11a). Then, two staircases are cut out on either side of the Pt coating to leave the thin wall shown (Fig. 3.11b). The wall is then trimmed away at the sides so that it is only supported at the top (Fig. 3.11c). The wall is then ion-polished and attached to a probe for lift out (Fig. 3.11d). The lamella is then welded to the TEM grid (Fig. 3.11e) and is thinned further until it is smooth and electron transparent (Fig. 3.11f).

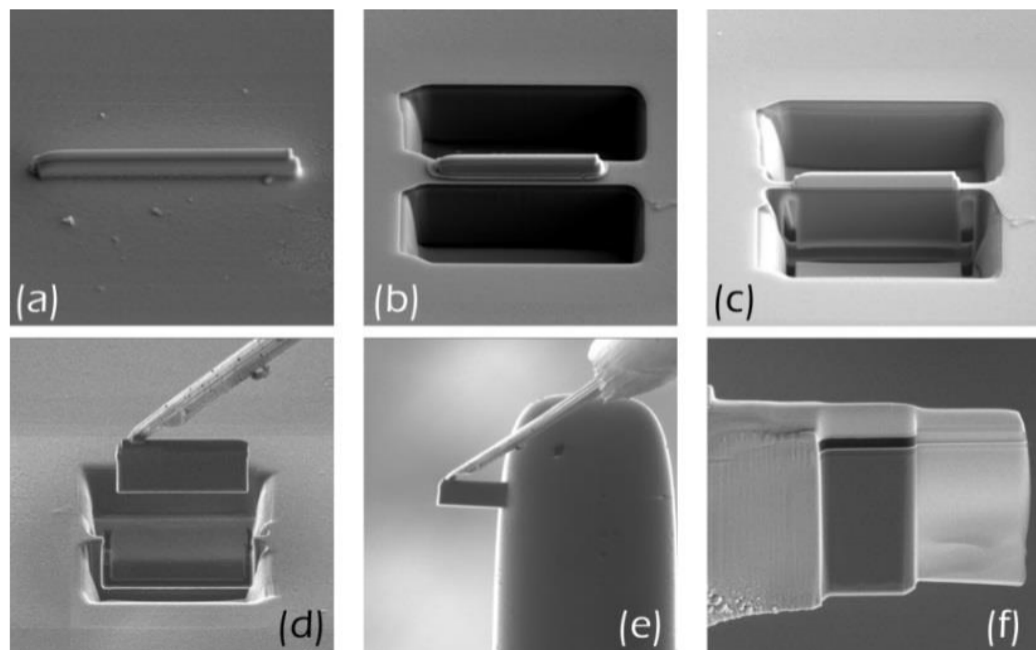

Figure 3.11: SEM images showing the FIB process [70].

3.4 Summary

In this chapter the experimental techniques used to fabricate and probe the Au-Ti, Au and Ti devices have been discussed. The devices are fabricated using sputter deposition for the a-SiO_x layers and a combination of sputter deposition or thermal

deposition for the electrodes. Each device is then characterised *via* TEM, EELS, STEM and EDX to determine their chemistry and microstructure in the pristine and electroformed states. Subsequently, the mechanisms of operation for each device is explored.

Part I

Electrical Stress Induced Structural Dynamics in Ag-SiO_2-Pt RRAM Devices: A DFT Case Study

4.1 Research Question

What are the fundamental mechanisms involved in the operation of Ag-SiO_2-Pt RRAM devices?

4.2 Outline

The electrochemical metallisation (ECM) of insulating layers, described in detail in the next section, is well studied experimentally in RRAM technologies. For ECM devices to fulfil their potential, however, it is important to understand their mode of operation from a mechanistic perspective. However, detailed experimental studies of the ECM mechanism at the atomic scale have not been carried out due to the limitations of experimental techniques, such as TEM. In this part of the thesis, I attempt to elucidate some of the mechanisms of conductive filament formation using DFT calculations and MD simulations of Ag-SiO_2-Pt (Ag) RRAM devices.

To date, *in situ* TEM imaging of Ag devices have provided some of the best data available for the ECM mechanism, where the individual processes involved in ECM memories have been shown. This begins with the electroforming process, where a positive bias is applied at the Ag electrode. Subsequently, Ag incorporates into the a-SiO_2 layer, where clusters are seen to nucleate to form a conductive filament of Ag clusters spanning the Ag and Pt electrodes. However, *in situ* TEM imaging also shows that this process is very variable, where the growth methods of the a-SiO_2 layer determines whether cluster nucleation begins at the Ag or the Pt electrode. Furthermore, the morphology of the filament is also very variable, with dendrite like filaments forming in some devices, whilst large wide conical filaments form in others.

As such, it is expected that theoretical calculations on the atomistic scale can be extremely important to determine the nature of the mechanisms involved in Ag filament formation and the cause of the differences discussed above. This is because *ab initio* methods, such as DFT and MD, allow individual defects and mechanisms to be modelled, from which their impact during device operation can be determined.

With regard to Ag devices, this can be separated into four processes: i) the generation and incorporation of Ag^{+1} cations into the a-SiO_2 layer; ii) the diffusion of Ag^{+1} ions through the a-SiO_2 layer; iii) the reduction of Ag^{+1} ions in proximity to either the Ag or Pt electrode, and finally iv) the nucleation of Ag clusters. Each of these processes are studied in this part of the thesis.

The remainder of this chapter provides a literature review of the ECM mechanism in Ag devices, followed by a study of Ag RRAM devices using a Ag in α-quartz model in chapter 5. This begins with a verification of the feasibility of the Ag-SiO_2 DFT system through the modelling of the α-quartz infrared (IR) and Raman spectra, the Ag^0 interstitial electron paramagnetic resonance (EPR) spectrum and the Ag^{+1} interstitial absorption and photoluminescence spectra. This is followed by a study of Ag incorporation, migration, reduction and clustering in α-quartz, including a model of the Ag-O vacancy interaction with regard to its potential to act as a Ag reduction and cluster nucleation site. The study is then expanded to an amorphous (a-) SiO_2 system in chapter 6. In this case, the incorporation of Ag is first studied through the development of the Ag-α-cristobalite interface. This is continued with models of the Ag interstitial in the $-2 \leq q \leq 2$ charge states in a 216-atom a-SiO_2 cell. The diffusion of Ag^0 and Ag^{+1} is then studied through the a-SiO_2 bulk, grain boundary and column boundary. In this case, the migration through boundaries is modelled through the development of hydroxylated α-cristobalite (202) surface slab grain boundary and column boundary models. The reduction of Ag^{+1} is then studied *via* its interaction with O vacancies. Finally, in chapter 7, the Ag clustering process at O vacancy sites is studied. In this case, clusters up to 15 Ag atoms are developed and the breakdown of the a-SiO_2 network in proximity to the Ag cluster is modelled.

4.3 Background & Literature

The ECM mechanism relies on the mobility of metal ions in the insulating layer, where devices include stacks of an active electrode (Ag) - ion conductor (a-SiO_2) - inert electrode (Pt) layers. This is based on the fact that Ag and Cu, unlike other metals, can easily diffuse inside SiO_2 films. In the case of the Ag-based device,

upon applying a positive positive bias at the active electrode, Ag^{+1} ions are formed at the Ag/a-SiO_2 interface. The Ag^{+1} ions then diffuse through the a-SiO_2 layer *via* field assisted diffusion, where they can be reduced in the a-SiO_2 layer at the Ag or Pt electrode. A conductive filament subsequently forms via the nucleation of a chain of Ag clusters. The geometry of the conductive filament is determined by two factors, the ion mobility (μ) and the ion reduction rate (Γ), as shown in Fig. 4.1 [10]. In the high μ-high Γ (Fig. 4.1a) and high μ-low Γ regimes (Fig. 4.1c), the high ion mobility allows the metal cations to diffuse to the inert electrode where they are reduced to form large conical or dendrite filaments, respectively. In this case, the metal filament grows from the inert electrode back towards the active electrode. In the low μ-high Γ (Fig. 4.1d) and low μ-low Γ (Fig. 4.1b) regimes, the low ion mobility results in metal clusters nucleating in the proximity to the active electrode, where the filament grows towards the inert electrode. In this case, the low reduction rate regime results in the formation of multiple spread out clusters, whilst a high reduction rate regime results in the formation of a closely packed cluster filament.

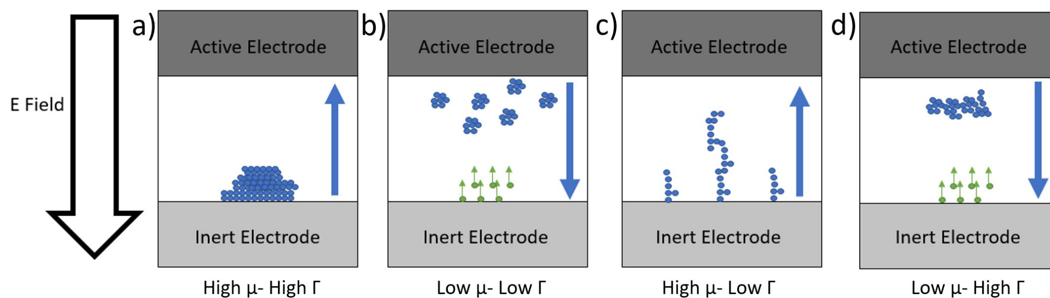

Figure 4.1: Schematic of the ECM filament formation process. a) high ion mobility - high reduction rate regime, b) low ion mobility - low reduction rate regime, c) high ion mobility - low reduction rate regime, d) low ion mobility - high reduction rate regime. The blue and green dots represent active electrode ions and electrons respectively. The Blue arrows represent the filament growth direction.

Figs. 4.2 and 4.3 show different stages of the Ag filament formation in planar Ag devices [11, 12]. Planar devices are employed to allow the location of the filament to be determined and observed during the TEM measurement. Fig. 4.2 gives *in situ* TEM of a high μ-low Γ regime Ag device (Device A), whilst Fig. 4.3 shows *in situ* SEM images of a low μ-low Γ regime Ag device (Device B). The difference between the two devices is a result of the respective fabrication methods

of the a-SiO_2 layer. In Device A, the a-SiO_2 layer was grown using radio frequency sputter deposition at room temperature, whilst thermal oxidation of a Si layer was used in Device B. A high density of defects and grain boundaries are known to form in sputtered a-SiO_2 layers, and is suggested to facilitate very high Ag^{+1} mobility in Device A. This, coupled with a low Ag^{+1} reduction rate, results in the nucleation of dendrite like filaments at the Pt electrode. In thermal oxidation a-SiO_2 layers, however, there is a relatively low concentration of defects and boundaries compared to the sputter deposited oxide. This lowers ion mobility resulting in a filament formation at the Ag electrode. Furthermore, the reduction rate of Ag is still low, leading to the nucleation of clusters spread apart in the a-SiO_2 layer (Fig. 4.3c). The newly formed clusters are subsequently suggested to act as bipolar electrodes under an electric field. This facilitates the oxidation of Ag in these clusters to form ions which may then migrate deeper into the oxide layer [10]. As these ions drift toward the Pt electrode *via* field assisted diffusion, they are then suggested to undergo a second cluster nucleation process deeper into the dielectric [83]. The process continues until a filament consisting of clusters has formed across the device. Once a filament forms, current through that filament dominates over incomplete filaments leading to its further increase in size and thickness.

Due to the devices shown in Figs. 4.2 and 4.3 being planar, a major consideration is whether the Ag filament forms on the surface or inside the a-SiO_2 layer. Fig. 4.4 shows additional measurements on Device B, where a cross section of the device was cut and characterised through TEM and EELS. From this, it can be seen that Ag clusters form on both the surface and inside the a-SiO_2 layer. In RRAM devices, the surfaces are not exposed so it is expected that the Ag filament will only form inside the a-SiO_2 layer.

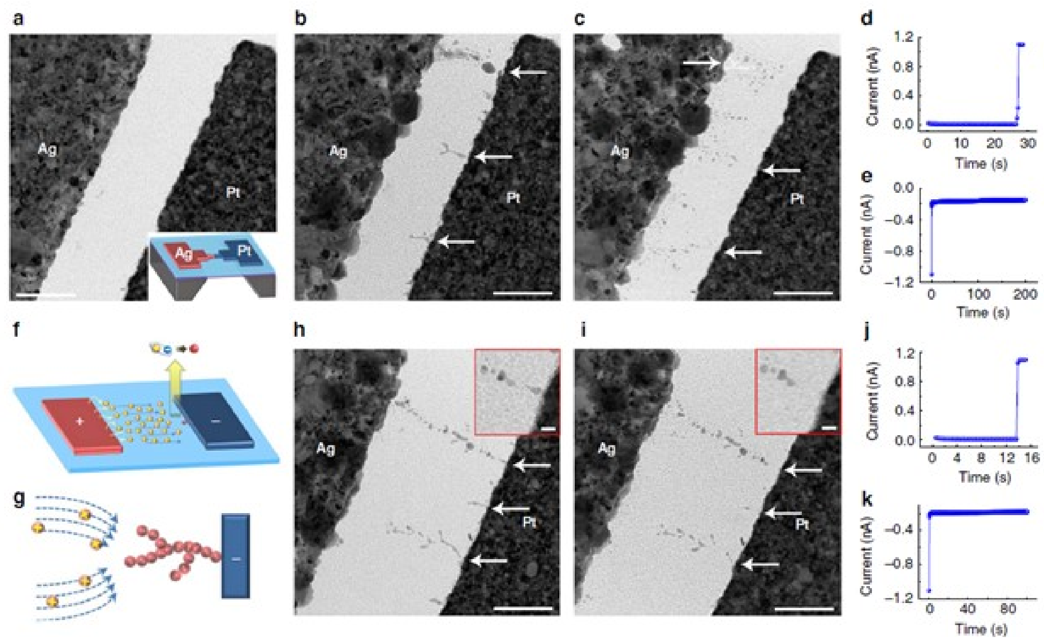

Figure 4.2: (a) a pristine Ag-SiO_2-Pt device imaged after fabrication. (b) the device post forming at 8 V. A metallic filament spans the dielectric connecting the electrodes. Incomplete dendrite type filaments grow from the Pt electrode. (d) The I-V curve measured during forming shows the conductive filament results in a large decrease in resistance (ON-state). (c) shows the same device after erasing, where a reverse bias of -10 V is applied. Here we see the dissolution of the filament beginning at the Pt electrode, demonstrating the importance of the insulator-inert electrode interface interactions. (h) and (i) show the set (10 V) and reset (-10 V) processes respectively, where again there is dissolution of the filament at the Pt electrode (OFF-state). The dissolution is thought to occur at the Pt electrode due to Joule heating, where the filament is at its thinnest. [11]

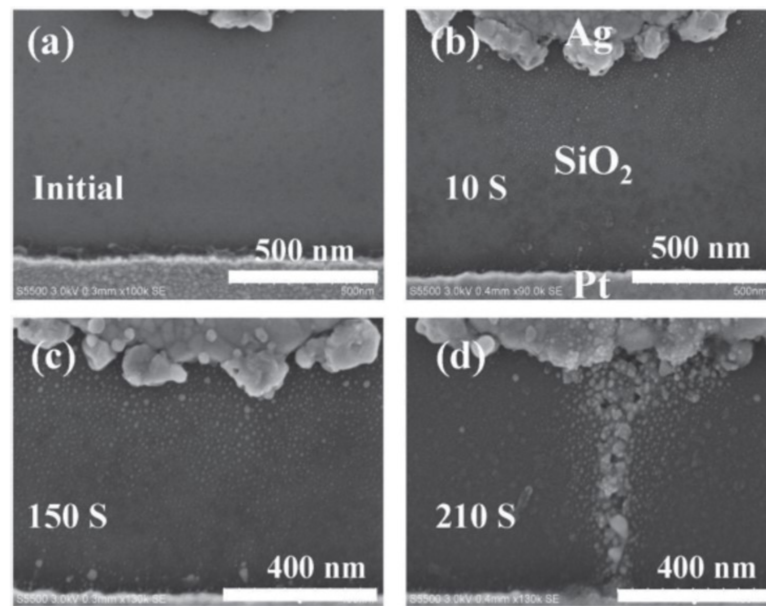

Figure 3. SEM images capturing the dynamic CF growth processes in the Ag/SiO_2/Pt planar device. a) Fresh device. b–d) After 10 s, 150 s and 210 s under a 30 V constant voltage stress with I_{CC} = 10 μA, respectively.

Figure 4.3: SEM images capturing the dynamic conductive filament growth processes in the Ag/SiO_2/Pt planar device. a) Fresh device. b–d) After 10 s, 150 s and 210 s under a 30 V constant voltage stress with I CC = 10 μA, respectively [12]

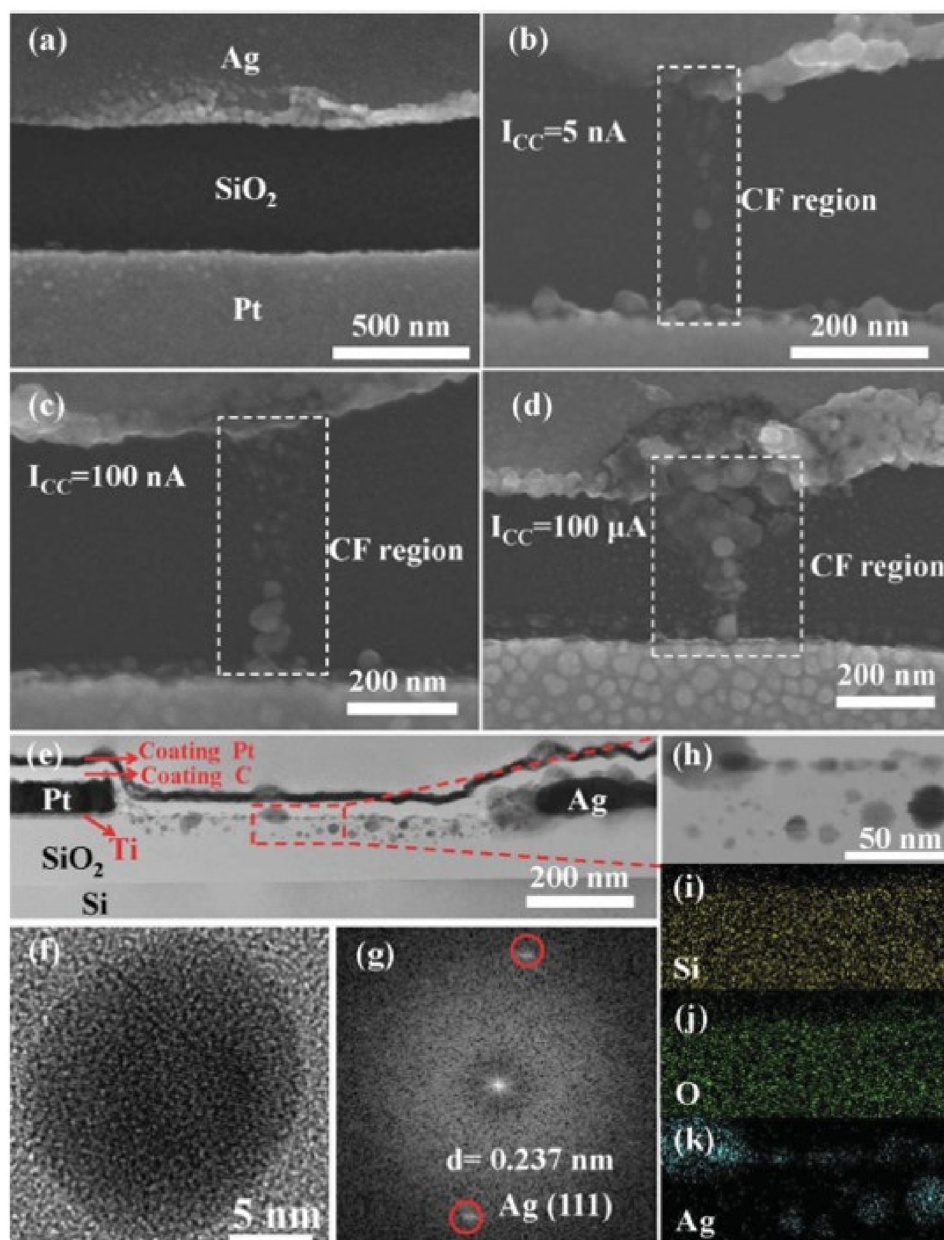

Figure 4.4: Morphology and component of conductive filament observed in Ag/SiO_2/Pt planar structure after electroforming with various I CC . As-prepared fresh device without any electrical treatment. b–d) Morphologies of the conductive filament with I CC = 5 nA, I CC = 100 nA and I CC = 100 μA, respectively. e) Cross-sectional TEM image along the nanocrystal chain. f) HRTEM images of a single nanoparticle. g) The diffraction pattern extracted by Fourier transform of (f) showing Ag (111) crystal plane. h) Enlarged TEM images taken from the red rectangular region in (e). i–k) EELS mapping images of Si, O and Ag elements, respectively, corresponding to the region in (h). [12]

4.3.1 Ag Incorporation

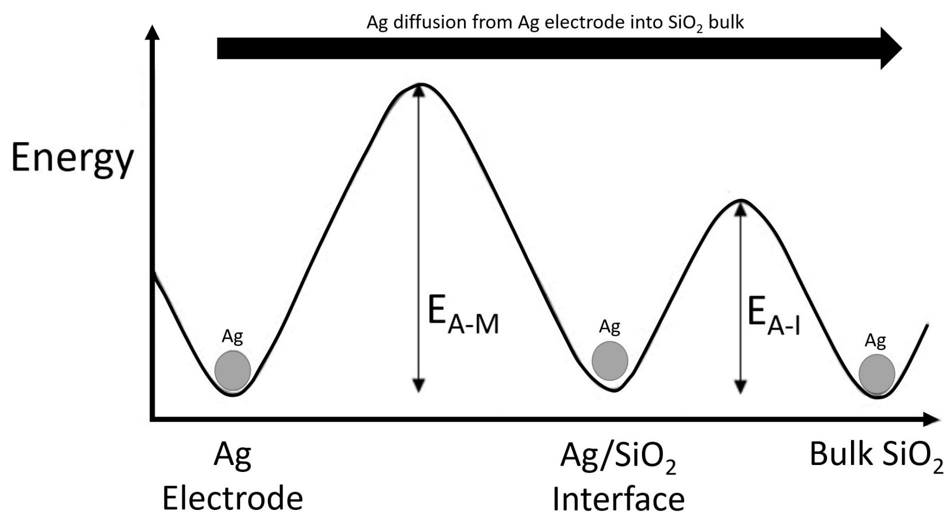

Figure 4.5: Schematic showing the activation barriers for the thermal diffusion of Ag from the Ag electrode into the dielectric layer.

A Ag interstitial entering the a-SiO_2 layer must overcome two barriers (Fig. 4.5). The first barrier is a result of the interstitial breaking its bond with the metal matrix ($E_{A\text{-}M}$ in Fig. 4.5), and the second is caused by the diffusion of the interstitial through the a-SiO_2 surface into the dielectric layer ($E_{A\text{-}I}$ in Fig. 4.5). At an ideal interface where there is a sharp transition from metal to dielectric, the activation energy to overcome metallic bonding is strongly related to the melting point of the metal. In this case, the binding energy of Ag atoms to bulk Ag is high (Ag = 2.95 eV), grossly decreasing the probability of Ag incorporation into a pristine SiO_2 surface. However, the interaction of Ag with defects, such as the non-bridging O at the interface, may play some role in reducing the binding energy and subsequent incorporation barrier [84].

Furthermore, it is unclear whether Ag diffuses into a-SiO_2 in the 0 or +1 charge state. In the case that a Ag^0 atom enters a-SiO_2, it is possible Ag^0 is oxidised *via* electron tunneling to either the metal electrode or an intrinsic defect site. Conversely, depending on the chemical interaction at the interface, ions may be generated which drift into the a-SiO_2 under the electric field by field assisted diffusion. During field assisted diffusion, the barrier for Ag^{+1} diffusion is reduced in the direction of the electric field inside the a-SiO_2 layer [85]. DFT calculations for Ag^0

and Ag^{+1} interstitials penetrating an α-quartz surface find the barriers of 2.12 and 0.98 eV, respectively [86]. In this case, the barrier for Ag^{+1} incorporation would be further reduced under bias. It is expected that the metallic bonding of Ag will provide the largest barrier for Ag incorporation into amorphous a-SiO_2, especially in the case of Ag^{+1}. It should be noted that the barriers for Ag to incorporate into SiO_2 grain and column boundaries at the Ag/SiO_2 interface my be drastically different.

4.3.2 Ag Diffusion

The diffusion of metal ions, such as Ag, has long been known to occur in a-SiO_2. Experimentally, the activation barrier for Ag diffusion through a-SiO_2 has been measured to be 1.24 eV, where measurements were carried out in an N_2 atmosphere at 300°C [87]. In this case, Ag-SiO_2-Si stacks were annealed at various temperatures before bias application. Rutherford backscattering spectroscopy was then used to measure metal contamination at the Si electrode to track the rate of diffusion. From this, it was determined that Ag diffuses as cations as diffusion did not occur under a reverse potential. Interestingly, in the same study the diffusion of Ag was not detected in vacuum conditions. However, by adding N_2 into the vacuum chamber, they again measured Ag to diffuse. Residual gas analysis of the N_2 found traces of H_2O and O_2, which were suggested to form deep level traps in the a-SiO_2. These traps were thought to assist Ag ionisation by providing acceptor levels for electrons resulting in a higher concentration of Ag^{+1} ions. Without these defects, Ag^{+1} ions were understood to recombine with electrons. The measurements therefore show that the fabrication methods of the a-SiO_2 layer and the presence of defects, such as water, affect the Ag^{+1} mobility. This includes factors such as vacuum level during sputter deposition or whether devices are annealed, each of which may determine water or defect concentrations. Furthermore, this explains why devices can range from low to high ion mobility in bulk a-SiO_2. This is more complicated when diffusion through structural features, such as grain and column boundaries, is considered, which are expected to increase Ag^{+1} mobility [88].

4.3.3 Ag Reduction

Due to the electrostatic repulsion of like charges, Ag^{+1} ions must be reduced for clustering to begin. As such, a mechanism for Ag^{+1} reduction at the Ag and Pt electrodes must be determined. The accepted mechanism at the Pt electrode involves the tunnelling of electrons from Pt to the Ag^{+1} ions. In this case, DFT provides a valuable method to study the feasibility of this mechanism as it allows the position of the Ag defect states in the a-SiO_2 band gap to be determined. This is valuable because electron tunnelling is a quantum mechanical effect, where the probability (P) for an electron to tunnel through a barrier is determined by the barrier height (E_0) and width (x);

$$P \propto e^{-x\sqrt{E_0-E}}, \tag{4.2}$$

Where E is the energy of the electron. This means is that electrons may tunnel from the Ag or Pt electrode to the Ag^{+1} ion when two conditions are met. Firstly, the Ag^{+1} ion must be in proximity to the electrode as the probability of reduction exponentially decreases with distance (x) from the electrode. Secondly, the Fermi level of the electrode must be close in energy to the energy the Ag^{+1} unoccupied defect states. In this case, the position of the Ag defect states are dependent on its charge and local environment. As such, the interaction of Ag ions with the full range of intrinsic defects in a-SiO_2 is important to understand mechanisms of ion reduction.

It should be noted that the reduction of Ag^{+1} ions by intrinsic defects in a-SiO_2 has also been observed. In this case, Ag^{+1} ions were implanted into a SiO_2 glass matrix using ion exchange [89]. Upon annealing above 410 °C, large Ag clusters were seen to form without any additional reducing agent or electrical bias. The reduction mechanisms therefore rely entirely on defects intrinsic to a-SiO_2. In this case, Ag^{+1} ions are suggested to interact with non-bridging O resulting in the formation of an O^{-1} ion and Ag_2^{+1} as follows [90];

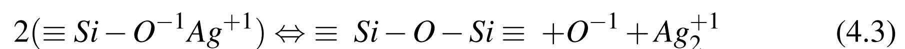

$$2(\equiv Si - O^{-1}Ag^{+1}) \Leftrightarrow \equiv Si - O - Si \equiv + O^{-1} + Ag_2^{+1} \tag{4.3}$$

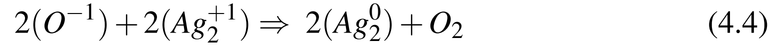

$$2(O^{-1}) + 2(Ag_2^{+1}) \Rightarrow 2(Ag_2^0) + O_2 \quad (4.4)$$

Subsequently, electron exchange between the Ag_2^{+1} and O^{-1} ions is can to occur giving Ag_2 dimers. The results show there are multiple mechanisms available for Ag^{+1} reduction and provide a strong justification to study the system with DFT.

4.3.4 Ag Clustering and Filament Formation

Once Ag^0 atoms have formed in the a-SiO_2 layer, it is suggested that the strength of metallic bonding provides a thermodynamic driver for Ag clustering. This is supported by experimental measurements of the gaseous phase Ag_2 and Ag_2^{+1} bond dissociation energies, which were found to be 1.6 eV and 1.7 eV, respectively [91]. However, it it should be noted that the exact mechanisms of cluster nucleation are unknown. It is expected that factors including the Ag^0/Ag^{+1} concentration, Ag^{+1} reduction rate, cluster nucleation site density, temperature and the total Ag electrode material available determine the rate. It is most likely that the clusters grow at voids in the a-SiO_2 network to minimise the strain and distortion. However, it is also possible that the clusters are intercalated into the matrix, similar to that observed in crystalline MoS_2 [92]. In this case large clusters can form with less distortion in the lattice.

As the initial clusters grow in proximity to the electrodes, additional unoccupied states form to allow additional electrons to tunnel into the clusters. Electrons can then tunnel from these clusters further into the dielectric to reduce new Ag^{+1} ions, forming precursors for new clusters. In this way, the cluster filament growth process continues until clusters sufficiently bridge the dielectric. At this point a conductive filament is formed, and electrons can cross between the Ag and Pt electrodes. In this study, DFT calculations are used to not only model initial stages of the clustering process, but also to provide information on the charge states of these clusters. This is important as the relative ionisation potentials and electron affinities play a role in the electron tunnelling process.

Chapter 5

Ag interactions in α-quartz

5.1 Introduction

Silicon oxide RRAM devices require an electroforming process before they exhibit resistive switching. In this process, defects that facilitate electron transport are generated across the oxide layer resulting in a low resistance state across the electrodes. Modelling the electroforming process is therefore vital towards understanding and optimising device operation. However, this is difficult to achieve in practice with the continuous random network (CRN) models typically used to model amorphous structures. This is because there are a broad range of defect configurations, and possible interactions in a representative CRN. To account for these variations, a large number of calculations are required to obtain a statistically accurate representation of the role that defects and defect interactions play. In this regard, it can be insightful to develop models first using a crystalline form of SiO_2. These models inherently provide a strong basis for the types of defects and defect interactions that will be observed in amorphous systems, and the results can be used to guide future calculations in the amorphous case. Crystalline systems are better defined and characterised experimentally, providing data for the DFT models to be compared and verified against. These results then provide useful insights when developing an understanding of the effect of amorphisation on a given defect.

The work carried out in this chapter focuses on modelling the interactions of Ag in α-quartz in the context of Ag-SiO_2-Pt RRAM devices. Ag-SiO_2-Pt devices

have been the subject of intense study, with a vast array of experimental data characterising the device operation, thus providing a strong base to model to (see section 4.3). Furthermore, α-quartz and its interactions with Ag are well studied, with α-quartz also being the most stable form of SiO_2 under standard conditions.

In the first part of the chapter, the optimal DFT parameters for modelling the Ag in α-quartz are determined and verified against experimental measurements beginning with a model of pure α-quartz. From this, the α-quartz vibrational modes are calculated and the results compared to experimentally measured infrared (IR) and Raman spectra. This is followed by calculations of the Ag interstitial in α-quartz for the $-2 \leq q \leq +2$ charge states. Results are again experimentally verified through calculations of the Ag^0 electron paramagnetic resonance (EPR) signal, the Ag^{+1} photoluminescence excitation (PLE) spectrum and Ag^{+1} photoluminescence (PL) energies.

In the second part of the chapter, the focus shifts to modelling Ag-SiO_2-Pt RRAM operation directly using the Ag in α-quartz system. This involves systematically studying the various processes involved in ECM filament formation, namely, the incorporation of Ag in α-quartz, the diffusion of Ag through α-quartz, the reduction of Ag^{+1} ions in proximity to the electrodes, and finally the clustering of Ag in α-quartz. The reduction of Ag^{+1} ions is considered at the electrodes as a result of *in situ* TEM data which shows that Ag cluster nucleation propagates from the electrodes [10, 12]. The interaction of Ag with oxygen vacancies (V_O) is also studied as a potential Ag^{+1} reduction and cluster nucleation site supporting Ag filament growth in the bulk regime.

5.2 Previous Studies of Ag in α-quartz

5.2.1 Electron Paramagnetic Resonance of Ag^0 Centre

The Ag^0 interstitial in α-quartz has been extensively characterised through EPR [93]. Interestingly, it was found that Ag^0 is unstable at room temperature with no EPR signal detected. Subsequently, a paramagnetic Ag-Si centre was created by X-ray irradiation, which is understood to excite electrons into the Ag $5s^1$ state. This

results in the detection of electrons with a hyperfine splitting on Ag and Si (^{107}Ag = 39.8 mT, ^{109}Ag = 45.9 mT and Si = 12.7 mT). The higher splitting on the Ag atoms shows the unpaired electron remains mostly localised on Ag whilst partially bonding to a cationic Si. Through analysis of the g-tensor, Ag^0 was determined to lie very nearly along the two-fold symmetry axis. The deviation from the perfect 2-fold axis was confirmed to be real and beyond the limits of experimental uncertainty. The orientation of the Ag hyperfine interaction tensor strongly showed that Ag^0 lies on the a-axis and in the c-axis channel. It has been proposed that the Ag interstitial sits in the c-axis channel at the intersection of a 3-fold screw and 2-fold symmetry axis, surrounded by 4 oxygen anions forming a distorted tetrahedral cage.

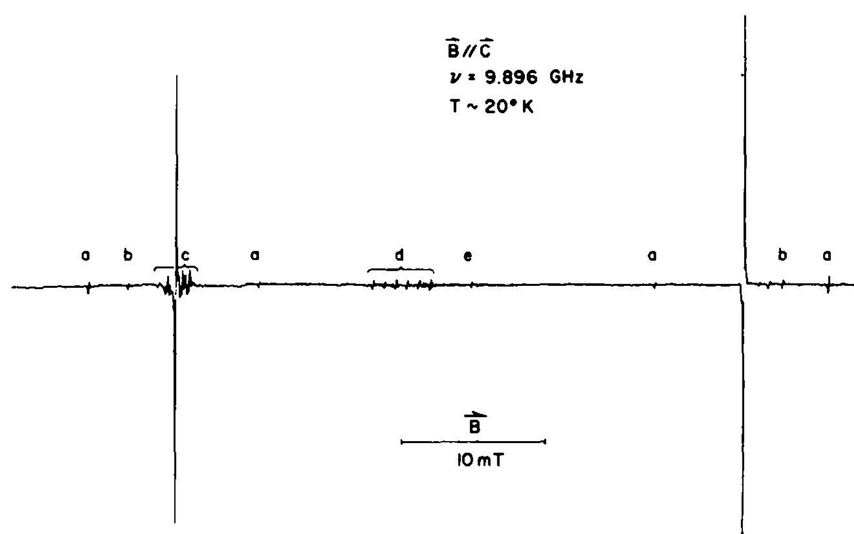

Figure 5.1: EPR spectrum of the A_{Ag-Si} centre in X-ray irradiated α-quartz doped with Ag [93]. a) ^{29}Si hyperfine lines are formed on either side of each peak of the primary ^{107}Ag doublet. b) Primary doublet arising from the residual ^{107}Ag. The remaining lines are due to c) Al/Ag centres [94], d) Al/Li centres [95] and e) Ge(I) centres [95].

5.2.2 Ag^{+1} Photoluminescence

The measured PLE and PL of the Ag^{+1} center (Fig. 5.2) exhibits several excitation bands beginning at 5.3 eV giving two photoluminescence (PL) peaks at 3.4 eV and 4.75 eV [96]. The PL intensity was found to be independent of temperature up to 300 K and quenched at 500 K. Additionally, the relaxation time was found to increase from τ = 32 μs in the temperature range of 20 - 300 K and to τ = 80 μs

at 5 K, suggesting a triplet nature of the luminescence states. The first PL peak at 4.75 eV is suggested to be caused by the Ag^{+1} center and the second PL peak at 3.4 eV is suggested to be caused by the interaction of Ag^{+1} ions with Al centres in α-quartz.

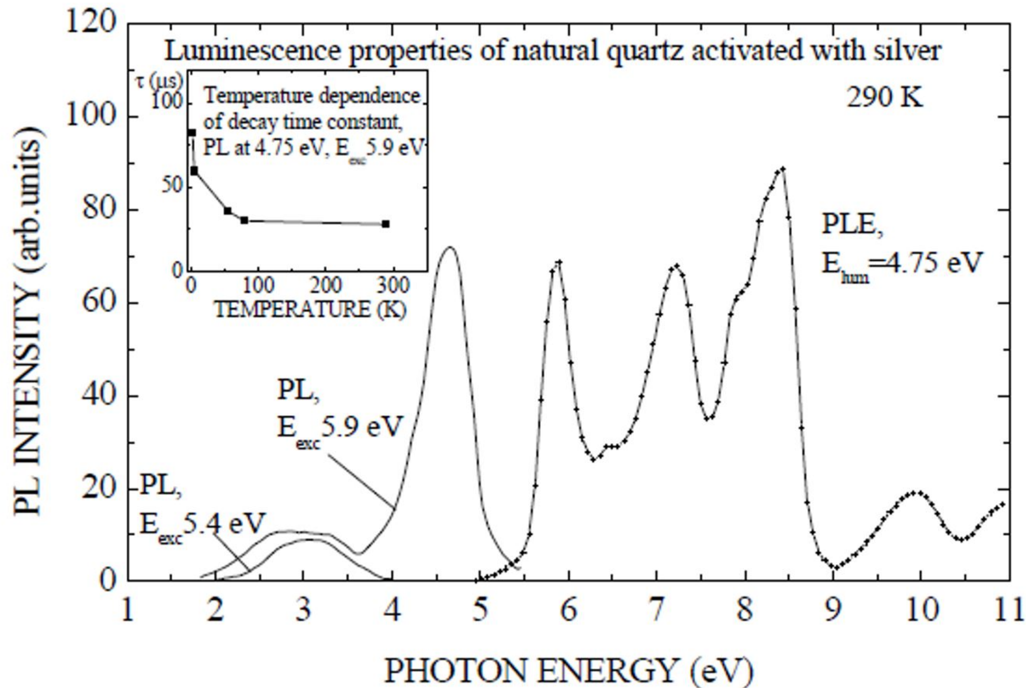

Figure 5.2: Absorption and Photoluminescence spectra of the Ag^{+1} interstitial in α-quartz [96].

5.3 Theoretical Methodology

5.3.1 Convergence Testing

To develop the α-quartz model, the DFT input parameters were first determined through convergence testing. In the order of the planewave cut-off (Fig. 5.3), relative cut-off (Fig. 5.4), basis sets (Table 5.1) and pseudopotentials, each input parameter was increased in complexity until the DFT total energy was converged. This ensures reliable and consistent results whilst minimising the computational cost of calculations.

Figs. 5.3 show the results for the planewave cut-off test. In this case, testing was carried for planewave cut-off values between 100 and 1000 Ry (50 Ry incre-

ments) showing convergence to within 0.001 eV at 600 Ry. Subsequently, keeping the planewave cut-off constant at 600 Ry, the relative cut-off was tested for values between 10 and 100 Ry in 10 Ry increments. From this, convergence to within 0.001 eV was found at 40 Ry. As such, planewave cut-off and relative cut-off values of 600 Ry and 40 Ry are used for all calculations in this work.

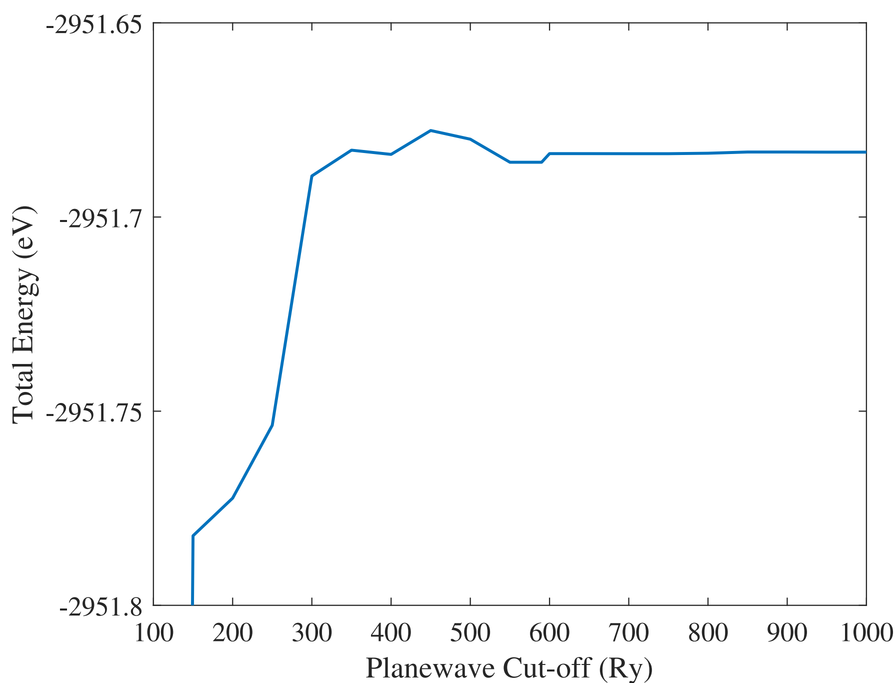

Figure 5.3: Graph showing the planewave cut-off convergence test.

Table 5.1 shows the results of increasing the basis set and pseudopotential complexity. In this case, the CP2K GTH basis sets and pseudopotentials from a single-zeta-valence-polarised (SVP) basis to a triple-zeta-valence-double-polarised (TZ2V2P) basis set was tested [25, 97]. From this, convergence within 0.01 eV per SiO_2 unit is reached for the double-zeta-valence-polarised DZVP basis set and is used for all calculations.

Table 5.1: Table showing basis set convergence test.

Basis Set	SVP	DZVP	TZVP	TZV2P
Band Gap	6.15	6.01	5.90	5.83
Total Energy (eV)	-2927.85	-2929.37	-2929.67	-2929.99
Energy/SiO_2 Unit (eV)	-36.15	-36.17	-36.17	-36.17

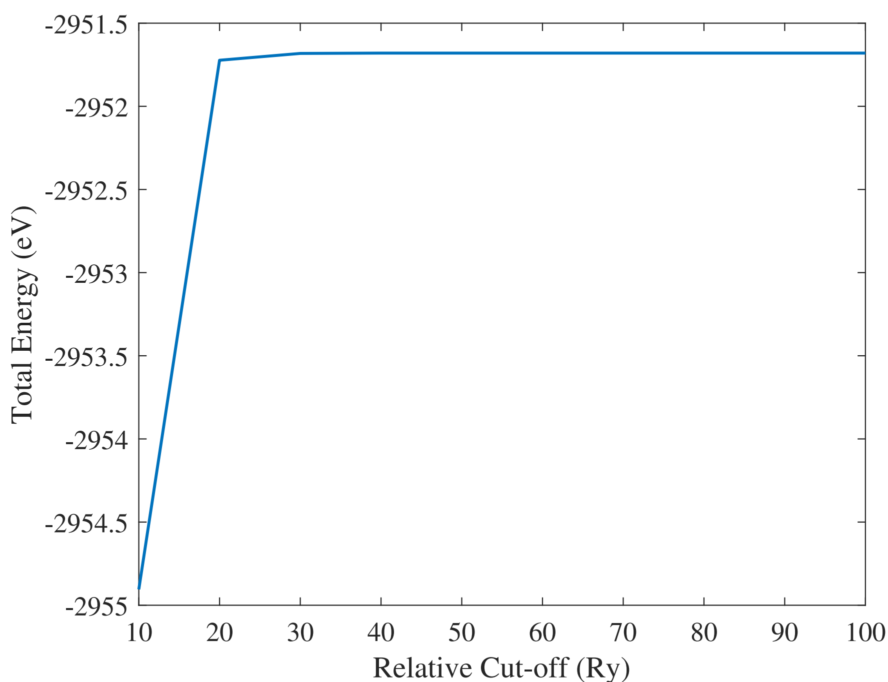

Figure 5.4: Graph showing the relative cut-off convergence test.

The minimum cell size for calculations was then determined, which is required in CP2K as the code only samples the Brillouin zone at the Gamma-point. Cell convergence can be achieved by increasing the cell size until the energy per atom and the density of states (DOS) have converged. In this case, total energy convergence within 0.01 eV per per SiO_2 unit and DOS convergence was found for a 3x3x3 cell with 243 atoms as seen on Fig. 5.5. As such, a minimum size for 243-atom cells are used for calculations in this chapter.

5.3.2 Functional Testing

The PBE [98], PBE0_TC_LRC [40], BLYP [99, 100] and B3LYP [101] exchange correlation functionals were tested to find which best reproduced the experimentally measured lattice parameters, bond lengths, tetrahedral volume and the band gap of α-quartz. The DFT derived lattice parameters were calculated *via* a cell optimisation with each functional, followed by a geometry optimisation giving the lowest energy structures. All hybrid functional calculations were made using the ADMM (as discussed in section 2.2.3) to reduce the computational cost of calculating the non-local exchange integrals [41].

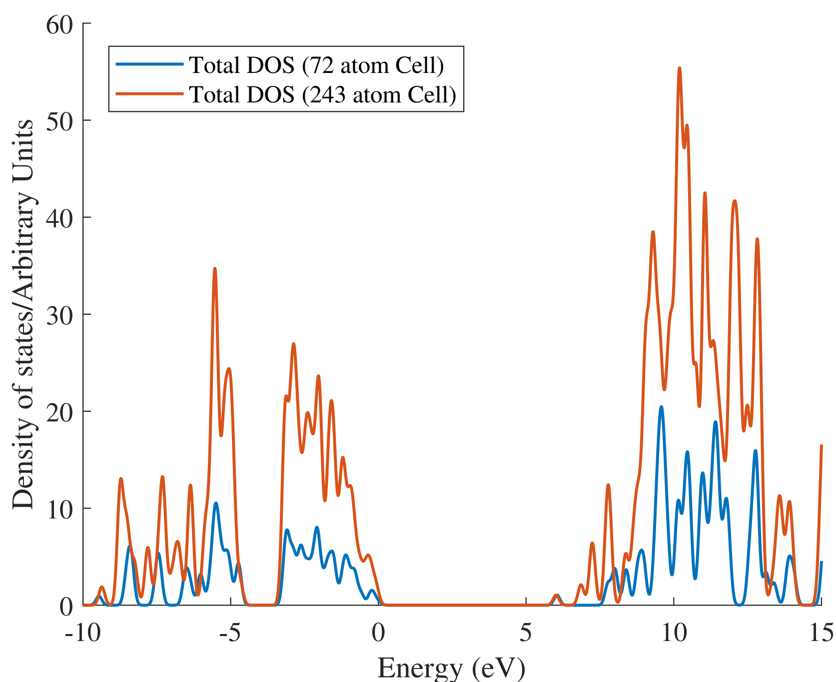

Figure 5.5: Graph showing the total density of states for 72-atom and 243-atom α-quartz cells. The 0 on the x-axis indicates the position of the highest energy electron, those states above the 0 position are unoccupied while those below are occupied. From this, it can be seen that the α-quartz valence and conduction bands in each case form at almost the same energies showing convergence.

The results (Table 5.2) show that all functionals give an accurate representation of geometry compared to experiment. However, the Kohn-Sham highest occupied molecular orbital (HOMO) – lowest unoccupied molecular orbital (LUMO) gap is significantly underestimated with the GGA functionals. This can be problematic when modelling RRAM devices as an accurate representation of the band gap is required. This is because the position of defect levels within the band gap provides vital information on favourable charge states of defects and the probability of electrons tunneling into and out of them at different Fermi level positions. The PBE0_TC_LRC functional gives the closest agreement to the experimental data, and is therefore used for all calculations carried out in this chapter and most of this work. In some cases where stated, the PBE functional is used to minimise computational cost or when studying metallic systems.

Table 5.2: Table comparing the PBE, PBE0_TC_LRC, BLYP and B3LYP exchange correlation functionals to experimentally observed parameters.

	Experiment	PBE	PBE0_TC_LRC	BLYP	B3LYP
a (Å)	4.92	4.98	4.92	4.97	4.91
c (Å)	5.41	5.49	5.41	5.48	5.40
V/SiO_2 ($Å^3$)	37.37	39.39	37.42	39.07	37.58
Si-O (Å)	1.61	1.63	1.61	1.62	1.62
Si-O (Å)	1.60	1.62	1.61	1.62	1.61
Band Gap (eV)	8.8	6.01	8.55	6.19	8.44

5.3.3 DFT Parameters

Convergence was found for all parameters tested in this section. As a result, planewave cut-off and relative cut-off values of 600 Ry and 40 Ry, respectively, are used with the DZVP basis sets and pseudopotentials for all theoretical calculations in this work. This is in combination with the PBE0_TC_LRC functional unless otherwise stated. The α-quartz DOS using these parameters is shown on Fig. 5.6, giving a band gap of 8.55 eV.

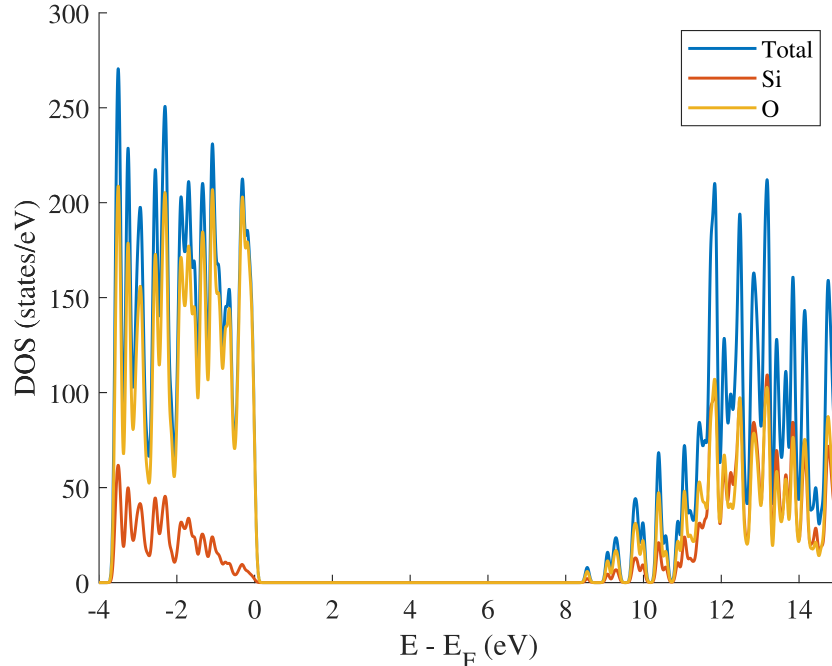

Figure 5.6: Graph showing DOS of a pristine α-quartz cell. The blue, red and yellow lines mark the total, Si and O contributions. The 0 on the x-axis indicates the position of the highest energy electron, those states above the 0 position are unoccupied while those below are occupied.

5.3.4 Vibrational Analysis

The CP2K vibrational analysis method was then used to calculate the α-quartz vibrational modes. This was done numerically by calculating small displacements in the x, y and z directions of each atom. From this, the force required to displace each atom in each direction is calculated and used to generate a Hessian matrix. The eigenvalues of the Hessian give the vibrational frequencies and the eigenvectors are the vibrational normal modes of the system.

5.3.5 Ag Defect in α-quartz

After developing the α-quartz model, calculations for the Ag interstitial in α-quartz were carried out in the $-2 \leq q \leq +2$ charge states. To find the Ag interstitial sites, Ag was added to 10 symmetry inequivalent sites in a 432-atom orthorhombic α-quartz cell and the geometry was optimised for each charge state. An orthorhombic cell was used to maximise the distance between Ag and its periodic images. The hyperfine coupling tensor and EPR spectrum were then calculated for the Ag^0 interstitial (see section 5.3.6). This was followed by time-dependent DFT (TDDFT) calculations for the Ag^+ photoluminescence excitation spectrum and photoluminescence energy. These calculations were carried out as discussed in the recent paper [102] detailing the implementation of TDDFT in CP2K.

Finally, the climbing image – nudged elastic band (CI-NEB) method was used to model the adiabatic diffusion barriers for Ag^0 and Ag^+ in α-quartz in the [001] and [110] directions as seen in Fig. 5.7. For all calculations a band of 5 replica images was used with a spring constant of 4.86 eVÅ^2 between images.

5.3.6 Electron Paramagnetic Resonance (EPR) calculations

Electron paramagnetic resonance is an experimental technique used to study systems with unpaired electrons [103]. The process is similar to nuclear magnetic resonance, where instead of nuclear spins, the magnetic moments of unpaired electrons align parallel ($m_s = +1/2$) or antiparralel ($m_s = -1/2$) to an externally applied magnetic field, B_0. The energy of the two spin states differs proportionally to

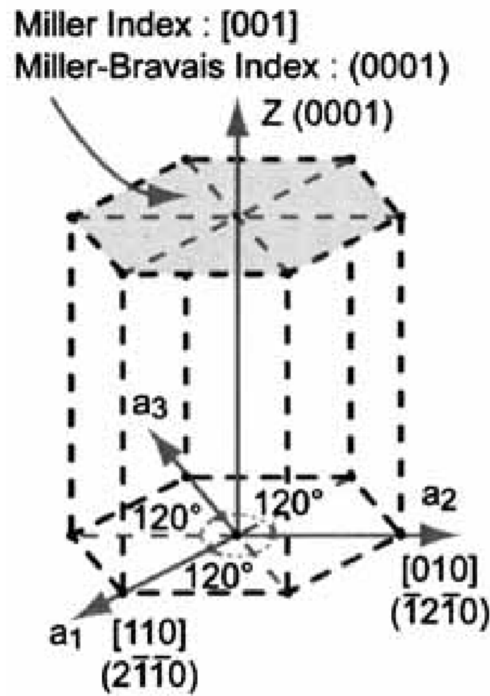

Figure 5.7: Hexagonal crystal structure of α-quartz with indexes of lattice directions

the amplitude of B_0, described by the Zeeman effect:

$$E = m_s g_e \mu_B B_0 \quad (5.1)$$

where g_e is the electron g-factor and μ_B is the Bohr magneton. The unpaired electron can subsequently transition between the two states by absorbing or emitting a photon of energy hv such that the resonance condition is met.

$$hv = g\mu_B B_0 \quad (5.2)$$

where g is the g-factor, reflects the alignment of the electron spin with the applied field, the max/min conditions are defined by the spin (m_s) aligned and opposed to the applied magnetic field. As the source of an EPR spectrum is the manipulation of an electron's spin state, the EPR spectrum for a radical (S = 1/2) system consists of one line [103]. However the hyperfine (HF) coupling, which can be defined as the interaction of the electron's magnetic moment with neighbouring nuclear spins, gives rise to a multi-line spectrum with characteristic splitting patterns. The

magnitude of the coupling is proportional to the magnetic moment of the coupled nuclei and depends on the mechanism of the coupling. Typically two mechanisms for coupling occur, namely, dipolar coupling (through space) and isotropic coupling (through bond). The unpaired electron in this study is in the s-shell (Ag (s)) such that the interaction between the electron and the atomic nuclei will be primarily due to the Fermi contact interaction, which gives an isotropic hyperfine coupling [103].

The HF parameters in this work were calculated using the Gaussian Augmented Plane Wave (GAPW) approximation in the CP2K code [17]. In the GAPW method, the auxiliary plane wave basis set is similarly described as in the GPW method, but is augmented with primitive periodic Gaussians. As a result, the basis sets must contain an explicit description of the core electrons, therefore requiring an all electron basis. To this end, the polarised consistent basis set pcj-2 is used, where the pcj-2 basis is fitted to give a function with an angular momentum two higher than is required for an isolated atom [104]. This family of basis sets are chosen as they have been shown to work well when modelling EPR systems [105]. It should be noted that calculations were made for the Ag^0 interstitial EPR signal using geometries optimised by both the pseudopotential basis as well as the all-electron basis. In each case, the optimised geometries and EPR signals of both methods gave very similar results.

5.4 Results

5.4.1 α-quartz

5.4.1.1 Vibrational modes of α-quartz

The normal modes of vibration for α-quartz were calculated to test whether the PBE0_TC_LRC functional could reproduce bonding characteristics observed experimentally. For this calculation, a 324 atom α-quartz cell was used giving a total of 966 normal modes of vibration. From the DFT calculation, the resonant frequency of each mode is determined along with an associated intensity, therefore allowing a direct comparison to the corresponding Raman and IR spectra. In Fig. 5.8, the calculated vibrational spectrum can be seen with the black and red vertical bars rep-

resenting the measured Raman and IR modes, respectively [106, 107]. To generate the spectrum, a normal probability density function was added about each calculated vibrational mode. The amplitude of each function was scaled to the intensity determined from the calculation. The vibrational mode frequency was used as the mean for each function with a standard deviation of 2 cm^{-1}. The standard deviation broadens or narrows the peaks adding variation in the observed spectrum. A value of 2 cm^{-1} was selected to highlight the individual peaks whilst allowing some coalescence.

Fig. 5.8 shows a reasonable agreement between the frequencies of calculated and experimentally measured vibrational modes, Raman active modes and IR active modes. This shows that DFT and the parameters chosen can model the bonding and vibrational characteristics of α-quartz well, and in turn indicates that the system is suited to studying SiO_2 systems. An in depth analysis of the nature of the Raman and IR modes can be found in the relevant studies, but further discussion is beyond the scope of this investigation [106, 107].

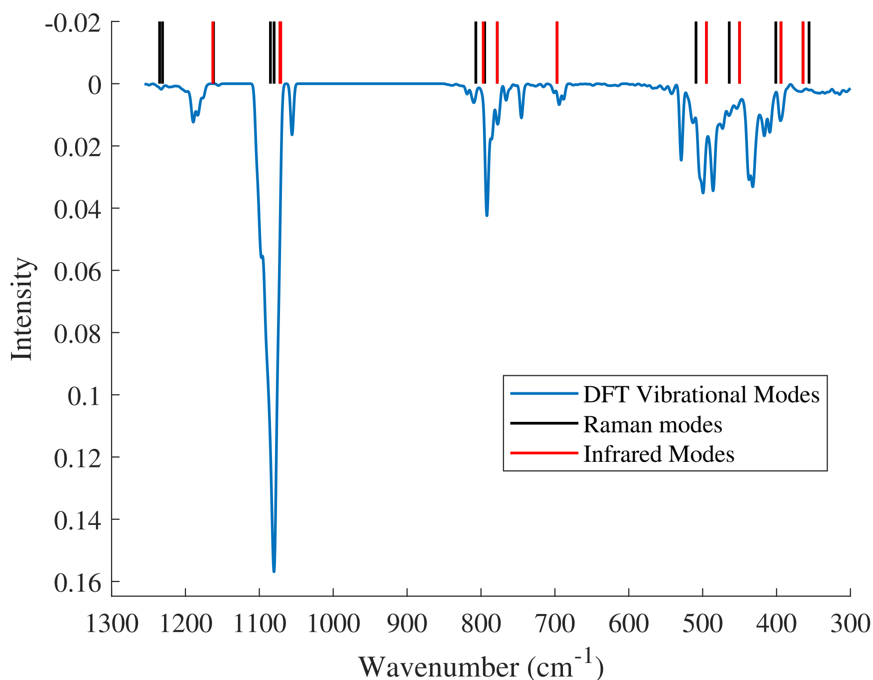

Figure 5.8: Graph showing the DFT derived vibrational spectrum of a pristine α-quartz cell. The black and red vertical bars represent the positions of experimentally measured Raman and IR modes, respectively.

5.4.2 Ag in α-quartz

5.4.2.1 Ag^0 interstitial

Calculations for the neutral Ag^0 interstitial in α-quartz show that two interstitial configurations exist, with defect formation energies (DFE) of 5.2 eV and 5.5 eV, respectively. In this case, the DFE is derived using the Ag chemical potential calculated from Ag_2O as discussed in section 2.3.1. The lowest energy configuration involves the spontaneous relaxation of an O-Si-O bond angle from 109.5° to 149.3°, with Ag^0 relaxing to the 3-fold screw and 2-fold symmetry axis intersection, as depicted in Fig. 5.9. Mulliken charge analysis of the defect shows that Ag is partially oxidised (0.22 $|e|$) with much of that charge donated to a neighbouring Si atom (-0.13 $|e|$ compared to the pristine cell). The charge donation can be observed in Fig. 5.9, where the isosurface shows the electron localisation of the HOMO state. The geometry of this defect and charge analysis are in strong agreement with the EPR measurements discussed earlier in this chapter. The higher energy Ag^0 interstitial site involves a similar charge transfer from Ag (0.17 $|e|$) to Si (-0.17 $|e|$) and the widening of a O-Si-O bond angle from 109.5° to 131.4°. In this case Ag^0 resides in the lowest density region possible in the α-quartz structure.

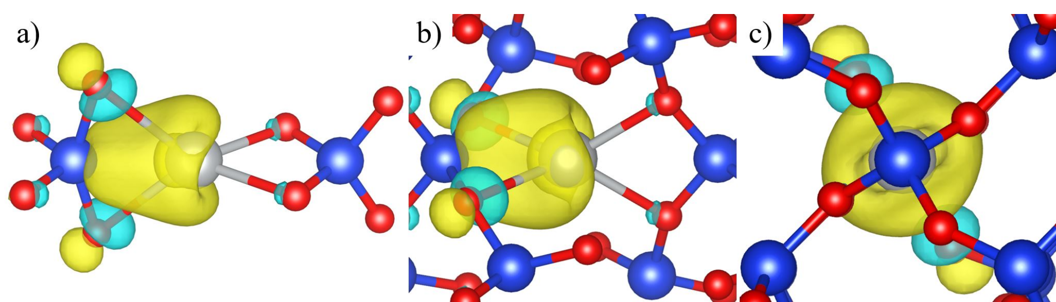

Figure 5.9: Schematic of the Ag^0 interstitial in α-quartz. a) Shows the interaction between the Ag^0 interstitial and two SiO_4 tetrahedra. b) Shows the Ag^0 interstitial position in the c-axis channel. c) Shows the Ag^0 interstitial in the 2-fold symmetry axis, in the plane of the Si atoms in the SiO_4 tetrahedra. The grey, blue and red atoms represent Ag, Si and O, respectively.

A DFE of 5.2 eV suggests that Ag^0 is highly unfavourable in α-quartz. This can in part be attributed to the higher density of α-quartz (2.65 g/cm^3) compared to a-SiO_2 (2.2 g/cm^3). To test the effect of confinement, calculations were performed to determine the energetic cost of the lattice distortion induced by Ag^0 in α-quartz.

This allows the total energy of the pristine and distorted cells to be compared, showing the lattice distortion energy is 2 eV, whilst the energy gained from Ag binding to the Si cation is 0.18 eV. The remaining energy in the DFE is associated with the chemical potential, which shows Ag has a lower energy state in the Ag_2O form compared to a Ag^0 interstitial. To confirm this, parallel calculations were carried out using the PBE functional with the Ag chemical potential calculated from bulk Ag metal. In this case, the DFE was found to be 4.8 eV with a distortion energy of 2.0 eV and the energy gained from Ag binding to the Si cation is 0.14 eV. This shows the DFE calculated using the Ag chemical potential from Ag_2O are accurate.

5.4.2.2 EPR Calculation of Ag^0

The geometry of the low energy Ag^0 interstitial site from the previous section is in strong correlation to the Ag-Si center observed experimentally. In both cases, Ag^0 sits off-centre in the two-fold symmetry axis, along the 3-fold symmetry axis and involves charge donation from the Ag s-orbital to a Si cation. The EPR spectrum for this defect was calculated to more conclusively test the validity of studying Ag-SiO_2 interactions using our DFT setup.

The calculated EPR signal can be seen on Fig. 5.10, where a Ag doublet with a 34.6 mT splitting (experimentally measured = 39.8 mT) is observed giving an approximate 10 % error between the pcj-2 results and the experimental observation. This is in accordance with previous studies using this basis set [105]. About each peak in the primary Ag doublet, there is a secondary doublet with a 9.9 mT splitting (experimentally measured = 12.7 mT) due to the hyperfine interaction induced by the Ag s-electron partially localising on the Si in the wide O-Si-O bond. As such, the calculated Ag^0 defect and its corresponding EPR signal are in a very good agreement to the Ag^0 defect observed in the literature [93]. This not only confirms and elaborates on the geometry of the Ag^0 site proposed experimentally, but validates the computational parameters used.

5.4.2.3 Charged Ag Interstitial

The geometries of the Ag interstitial in the q = -2, -1, +1 and +2 charge states in α-quartz can be seen on Fig. 5.11. By removing an electron and setting the system into

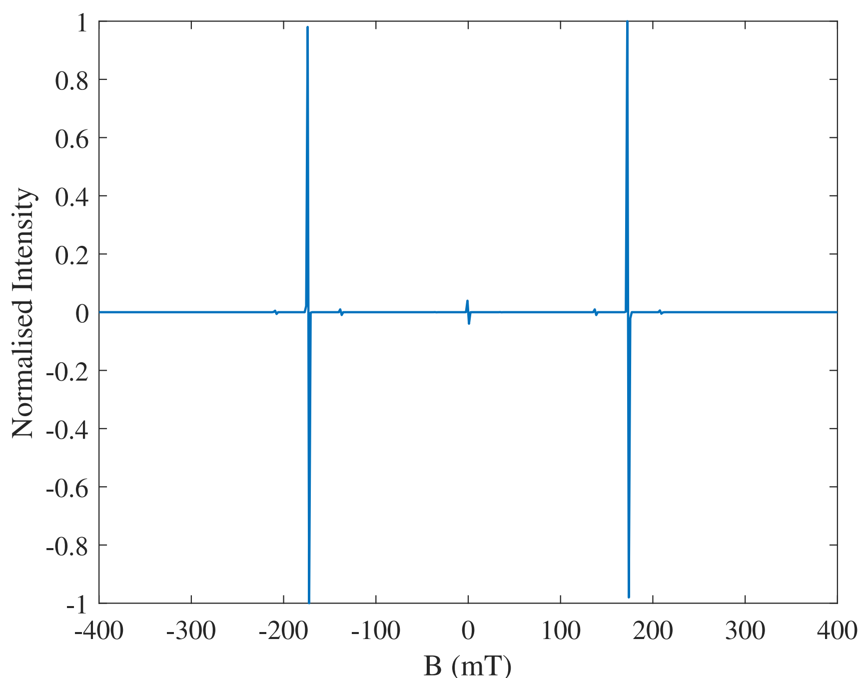

Figure 5.10: Graph showing the DFT derived EPR spectrum of the Ag^0 interstitial in α-quartz.

the +1-charge state, an electron is lost from the Ag-Si centre, with Mulliken charge analysis showing Ag (Mulliken charge = 0.65 $|e|$) has become ionised. The Ag^{+1} ion shifts along the c-axis to the 3-fold screw symmetry axis where it minimises the distance with neighbouring O atoms in the lattice. The HOMO of this defect shows that the Ag d-state forms a weak interaction with neighbouring O atoms, where charge is donated from these O atoms to Ag.

In the +2-charge state, the geometry of Ag is similar to the one in the +1-charge state. The Ag ion (Mulliken charge = 1.03 $|e|$) subsequently draws in the neighbouring O atom, reducing the average Ag-O bond length by 0.1 Å. The HOMO in this case is delocalised on the α-quartz away from the defect.

In the -1-charge state, the added electron localises on the Ag-Si centre filling the Ag (s) shell. The O-Si-O bond angle involved in the Ag-Si interaction subsequently increases from 149.28° (0-charge) state to 171.82°. In the -2-charge state, the second electron fills an α-quartz conduction band state such that the HOMO is delocalised over the α-quartz lattice. In this case, the Ag-Si defect is minimally

perturbed compared to the -1-charge state.

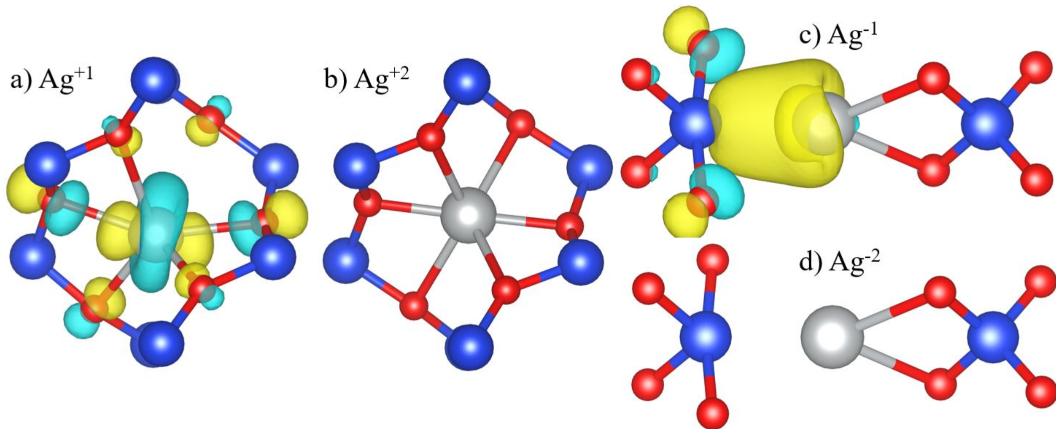

Figure 5.11: Schematic of the a) Ag^{+1}, b) Ag^{+2}, c) Ag^{-1}, d) Ag^{-2} interstitials in α-quartz. The grey, blue and red atoms represent Ag, Si and O, respectively.

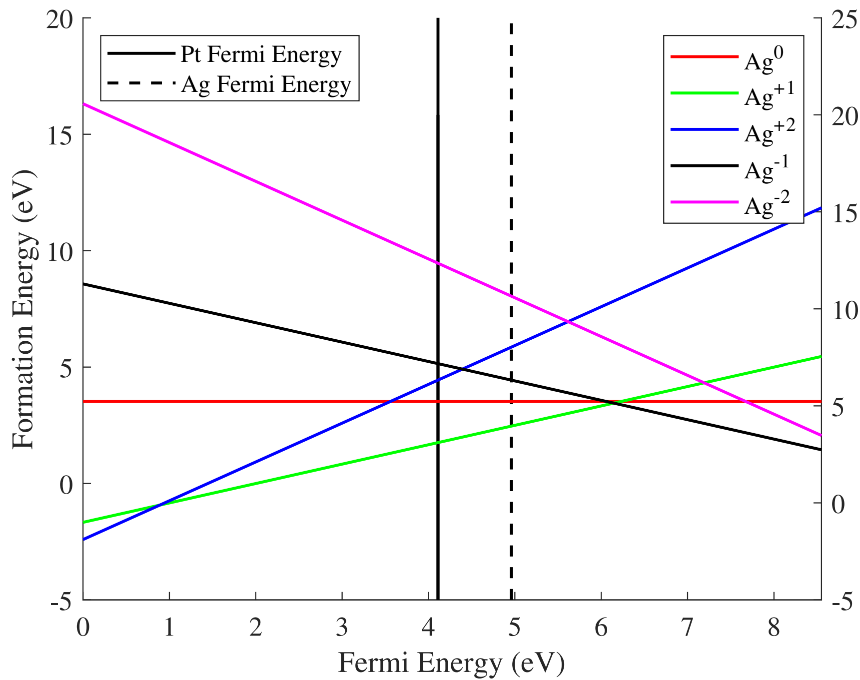

Figure 5.12: The defect formation energy diagram of the Ag interstitial in the -2 $\leq q \leq$ +2 charge states in α-quartz as a function of Fermi energy, where the Fermi energy is 0 at the α-quartz VBM.

The generally accepted mechanism of operation for ECM RRAM in the literature suggests that Ag^{+1} ions are incorporated at the Ag-SiO_2 interface [10]. Ag^{+1} ions then migrate into a-SiO_2 where they are reduced to allow the formation of Ag

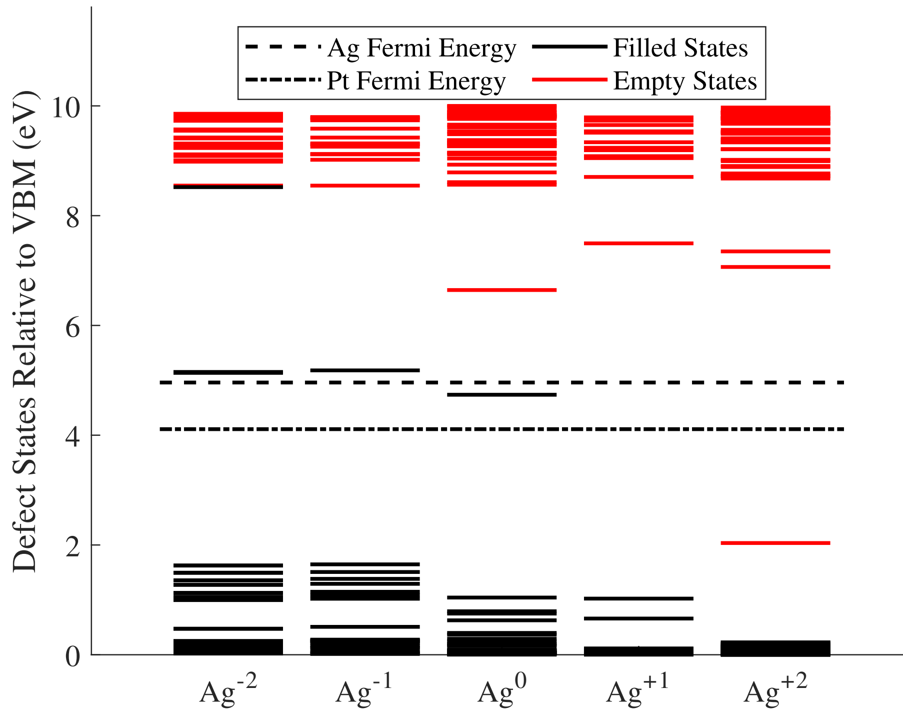

Figure 5.13: Graph showing the filled (black) and empty states (red) of the Ag interstitial in the -2 $\leq q \leq$ +2 charge states α-quartz. In this case, the states are projected over the α-quartz band gap where 0 represents the α-quartz VBM.

clusters at either electrode. The reduction process is assumed to occur *via* electron tunneling from the electrodes to Ag^{+1} under bias. The formation energy diagram of Ag in α-quartz (Fig. 6.12) shows that the Ag^{+1} ion is favoured at the Fermi energies of bulk Ag and Pt. This suggests that Ag is either incorporated as a positive ion, or that once an atom is incorporated the Ag s-electron will tunnel to the Ag electrode. This is in good agreement with the ECM mechanism, however, and most importantly, the Ag^{0} interstitial is not favoured at any Fermi energy. This result, although consistent with the observations during the EPR experiment, is problematic for RRAM operation as alternative mechanism is now required for the reduction of Ag^{+1} ions.

Fig. 5.13 shows the filled (black) and empty (red) defect state levels of the Ag in the -2 $\leq q \leq$ +2 charge states relative to the α-quartz valence band maximum (VBM). For the Ag^{+1} ion, which is favored at the Ag and Pt Fermi energies,

the HOMO d-state described in the previous section is located just above the α-quartz valence band maximum and the LUMO state is 1 eV below the conduction band minimum (CBM). In this case there are no states in proximity to the electrode Fermi energy positions. Furthermore, the charge transition levels seen on Fig. 6.12 show electron trapping/detrapping occurs at Fermi energies $>$ 1 eV above or below the electrode Fermi energy positions, suggesting there are no probable modes for electron transport. Though unstable in α-quartz, it may be possible that Ag^0 can form in the amorphous phase (a-SiO_2). Ag^0 has filled and empty states found at 4.7 and 6.6 eV, respectively, above the α-quartz VBM. During the electroforming step in ECM RRAM operation, a positive bias is applied at the Ag electrode. In this case, electrons are drawn from the electrode causing the position of the Ag Fermi energy to shift down towards the α-quartz VBM. From this, it is highly unlikely that Ag^0 states will provide a conductive pathway.

5.4.2.4 Ag^{+1} Photoluminescence

The PLE spectrum was modeled for the Ag^{+1} ion in α-quartz using TDDFT. The results, shown on Table 5.3, provide the energy of each excitation state and the corresponding oscillator strength. Oscillator strengths provide information on the transition probability to each excited state, where states with high oscillator strengths are more accessible and are assumed to contribute to the PLE spectrum. PLE peaks were found at 5.4, 6.0, 6.2, 6.4, 6.5 and 7.3 eV in very good agreement to the spectrum observed experimentally [96].

The PL of the Ag^{+1} center was then tested by taking the Ag^{+1} center geometry and optimising it in the triplet state, as shown on Fig. 5.14. The excitation energy from the singlet to the triplet state was found to be 4.87 eV suggesting that this state is not the one excited into to give the PL peak. By using the ΔSCF method [108] and relaxing the geometry of the triplet state, a relaxation energy of 0.14 eV was found. Taking the relaxed geometry of the triplet state and calculating the singlet state (vertical triplet-singlet transition), a transition energy of 4.59 eV was found. This correlates well to the PL peak at 4.75 eV observed in experiment, providing further validation of the DFT system and parameter choice. Furthermore, the nature

of the luminescence is confirmed to be an inner ion electronic transition from the triplet to singlet state for the Ag^{+1} center.

Table 5.3: Table showing the excitation energies for the Ag^{+1} center in α-quartz.

State Number	Excitation energy (eV)	Oscillator strength (a.u)
1	4.48	0.00000
2	5.39	0.00371
3	5.55	0.00001
4	5.60	0.00001
5	5.83	0.00001
6	5.85	0.00001
7	5.92	0.00198
8	6.15	0.00425
9	6.37	0.00194
10	6.42	0.01062
11	6.90	0.00004
12	7.21	0.04111
13	7.32	0.00004
14	7.38	0.00007
15	7.46	0.00035

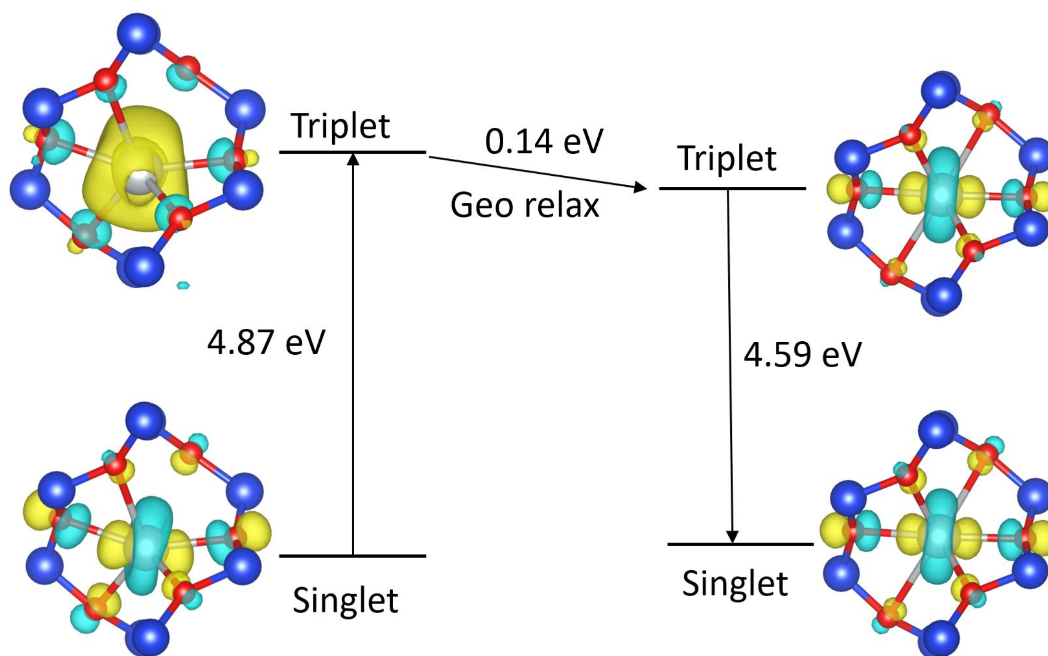

Figure 5.14: Schematic of the absorption and luminescence of the Ag^{+1} centre for the singlet to triplet and the triplet to singlet transitions respectively

To determine the origin of the second PL peak at 3.4 eV, the [AlO_4-Ag^{+1}]

center was modelled. From this, it was found that Ag^{+1} sits in the 2-fold symmetry axis in a site similar to the normal Ag^{+1} ion site. The Mulliken charge on Ag is 0.87 $|e|$ showing that Ag is ionic and the Ag to Al bond length is 2.8 Å. TD-DFPT calculations were made for the defect, with the excitation states can be seen on Table 5.4. The excitation state at 5.3 eV has by far the largest oscillator strength and is in good agreement with the 5.4 eV excitation peak observed in experiment. When the [AlO_4-Ag^{+1}] center is modelled in the triplet state, an excitation energy of 4.9 eV was found for the transition from the singlet to triplet state. A geometry relaxation of 0.46 eV was then found in the triplet state before a 3.8 eV transition from the triplet to singlet state. The experimentally measured PL peak was found to be 3.4 eV suggesting the [AlO_4-Ag^{+1}] center is a strong candidate for the second PL peak.

Table 5.4: Table showing the excitation energies for the [AlO_4-Ag^{+1}] center in α-quartz.

State Number	Excitation energy (eV)	Oscillator strength (a.u)
1	4.51	0.00001
2	4.94	0.00000
3	5.30	0.02194
4	5.45	0.00001
5	5.52	0.00001
6	5.54	0.00899
7	5.65	0.00000
8	5.89	0.00911
9	6.02	0.00237
10	6.29	0.00054
11	6.90	0.00003
12	6.91	0.00002
13	7.03	0.01328
14	7.16	0.00001
15	7.25	0.00656

5.4.2.5 Ag diffusion α-quartz

Through the DFT calculations carried out in this section, it is expected that Ag^{+1} ions will be produced at the Ag-SiO_2 interface. During RRAM operation, these ions diffuse into the SiO_2 layer where they are then reduced. To model this diffusion, CI-NEB calculations were made to determine the adiabatic diffusion barriers of Ag^0

and Ag^{+1} in the [001] and [110] directions. The [001] direction, through the *c*-axis channel, is expected to give the most correlation to diffusion in a-SiO_2 as this is the lowest density diffusion path, resembling voids in the amorphous network. The adiabatic diffusion barriers for Ag^0 and Ag^{+1} in the [001] direction were 0.27 eV and 0.06 eV, respectively (Fig. 5.15). This shows Ag^{+1} to be the more mobile species in SiO_2, and is in excellent agreement with Ag diffusion characteristics discussed in section 4.3.2 [87, 109]. Furthermore, the almost barrier-less diffusion supports the notion that Ag^{+1} can diffuse through the SiO_2 layer to the Pt electrode in the nanosecond time scales observed during the electroforming step [10]. Diffusion barriers of 0.96 and 0.92 were found for Ag^0 and Ag^{+1}, respectively, in the [110] direction. This suggests Ag will not be mobile in or through more dense areas in a-SiO_2.

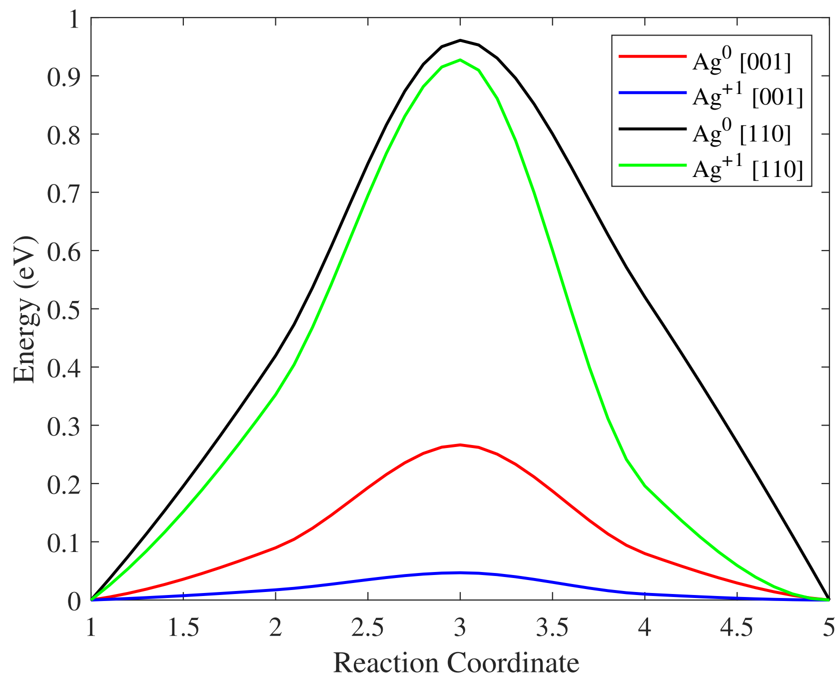

Figure 5.15: Graph showing the adiabatic diffusion barriers for Ag^0 and Ag^{+1} along the [001] and [110] directions calculated from CI-NEB calculations.

5.4.2.6 Ag_2 Formation

The *in situ* TEM images of Ag-SiO_2-Pt RRAM devices during operation show that Ag clusters nucleate to form a filament spanning the oxide, with clustering begin-

ning at the Ag or Pt electrodes depending on a-SiO_2 microstructure [11, 10]. In this regard, the Ag_2 dimer and Ag_3 trimer were modelled to study the very initial phase of Ag clustering.

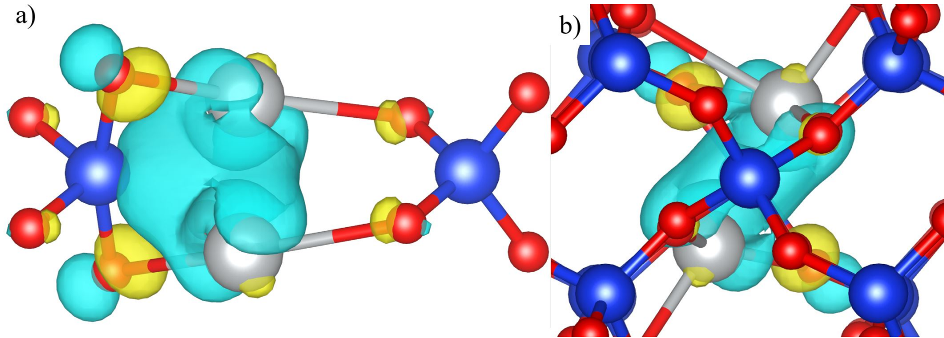

Figure 5.16: Schematic of the Ag_2 dimer in α-quartz. b) showing the dimer location is symmetric about the 2-fold symmetry axis.

DFT Calculations for Ag_2 predict a 2.2 eV binding energy between two Ag^0 atoms. This was calculated by comparing systems with the Ag atoms starting 2.5 Å and 5 Å apart. When the Ag atoms begin 5 Å apart, they spontaneously form a dimer configuration with a 2.5 Å Ag-Ag bond length (Fig. 5.16). Mulliken charge analysis shows a slight charge transfer between the Ag atoms spaced 5 Å apart (Ag_1 = -0.12 $|e|$ and Ag_1 = 0.26 $|e|$). As the atoms form the dimer, a O-Si-O bond angle increases to 165.5 °. In the dimer configuration, both Ag atoms donate charge to the Si in the wide angle O-Si-O to form a symmetric defect about the 2-fold symmetry axis. Mulliken analysis shows both Ag atoms are equivalent (0.17 $|e|$) with Si reduced by 0.22 $|e|$.

The formation energy diagram for Ag_2 shows two non-interacting Ag^{+1} ions are 0.48 eV lower in energy than a Ag_2^{+2} dimer (Fig. 5.17). As a result, two Ag^{+1} ions are favoured below a Fermi energy 4.85 eV relative to the α-quartz VBM. Above this, the Ag_2^0 dimer is favoured. This is an important result as it shows that the clustering methods will be different at the Ag and Pt electrodes. At the Ag electrode, Ag_2^0 is favoured, suggesting that clustering at the Ag-SiO_2 interface will occur providing an Ag^{+1} ion is reduced. Calculations show that having two Ag species 5 Å apart in the cell gives a Ag^0 and a Ag^{+1} ion. Furthermore, there is a 0.67 eV binding energy to form a Ag_2^{+1} dimer. Ag_2^{+1} is then favoured to trap an electron

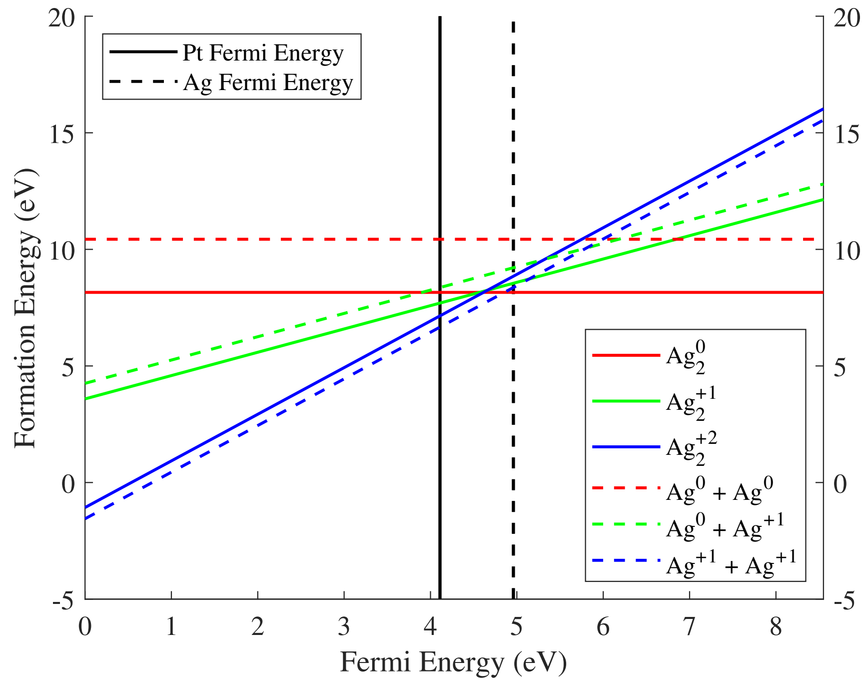

Figure 5.17: The defect formation energy diagram of Ag_2 and 2 Ag systems in α-quartz as a function of Fermi energy, where the Fermi energy is 0 at the α-quartz VBM.

from the Ag electrode to give Ag_2^0. This could occur if a Ag atom incorporates into SiO_2 in close proximity Ag^{+1}. A further possibility is that Ag_2^0 dimers break from the Ag electrode into SiO_2, remaining stable. Conversely, at the SiO_2-Pt interface (4.11 eV above the valence band) the lowest energy configuration is of two Ag^{+1} ions 4.5 Å apart.

5.4.2.7 Ag_3 Formation

The lowest energy configuration for Ag_3^0 (Fig. 5.19a) is with the three Ag atoms forming an isosceles triangle, where the binding energy of Ag^0 to Ag_2^0 is 1.2 eV. In this case, two 158° wide angle O-Si-O bonds form with charge transfer from two of the Ag atoms to two Si atoms. Mulliken charge analysis shows the charge to be 0.16 $|e|$ for the Ag atoms in the Ag-Si centres, with the remaining Ag atom having a charge of 0.09 $|e|$. Calculations show that the triangular geometry is 0.8 eV lower in energy than a linear configuration. The formation energy diagram for Ag_3 shows that three unbound Ag^{+1} ions far apart (Fig. 5.19c) are favoured below a Fermi energy of 4.30 eV. Ag_3^{+1} (Fig. 5.19b) is favoured at a Fermi energy between 4.30

eV and 5.66 eV and Ag_3^0 above 5.66 eV.

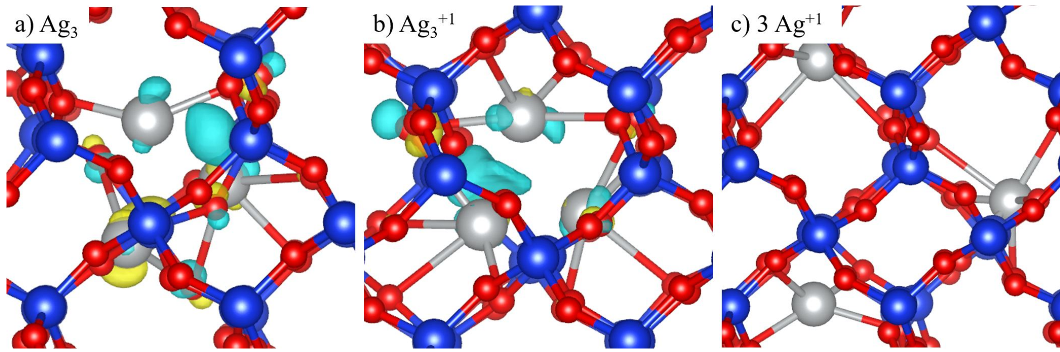

Figure 5.18: Schematic of the a) Ag_3^0, b) Ag_3^{+1} and c) 3 non-interacting Ag^{+1} systems in α-quartz.

This suggests that Ag_3^{+1} will be favoured at the Ag electrode, where there is a binding energy of 0.53 eV between Ag^{+1} and Ag_2^0 to give Ag_3^{+1}. Therefore, a clustering mechanism where an Ag^{+1} ion binds to Ag_2^0 is feasible near the Ag-SiO_2 interface and is consistent with the mechanism described in low Ag mobility, low reduction rate regime RRAM devices [110]. However, it should be noted that this mechanism does not explain how clustering will occur at the Pt electrode, hence a Ag interaction with an as yet unknown entity is required.

5.4.2.8 Oxygen Vacancy

A strong candidate to mediate the reduction of Ag^{+1} ions is the oxygen vacancy, V_O, which is known to occur with high concentrations in SiO_2. Before Ag-V_O defects were studied, however, the V_O in the $-2 \leq q \leq +2$ charge states were calculated to determine which charge state is favourable at the Ag and Pt Fermi energies.

The DFE of the neutral V_O was found to be 5.4 eV, with the HOMO state localised on two Si atoms. Two geometries were found for the +1-charge state, in the first the HOMO electron is localised between two Si atoms as with the neutral vacancy. In this case, the Si-Si bond length increases from 2.43 Å for the neutral V_O to 3.07 Å. In the second geometry, a Si atom is back projected through the plane of its bonded oxygens where it interacts with a neighbouring oxygen (the so-called puckered configuration). Mulliken charge analysis shows that the charge in the back projected case is localised on the back projected Si. The DFE for the back projected state is 0.22 eV higher in energy than the normal ${V_O}^{+1}$.

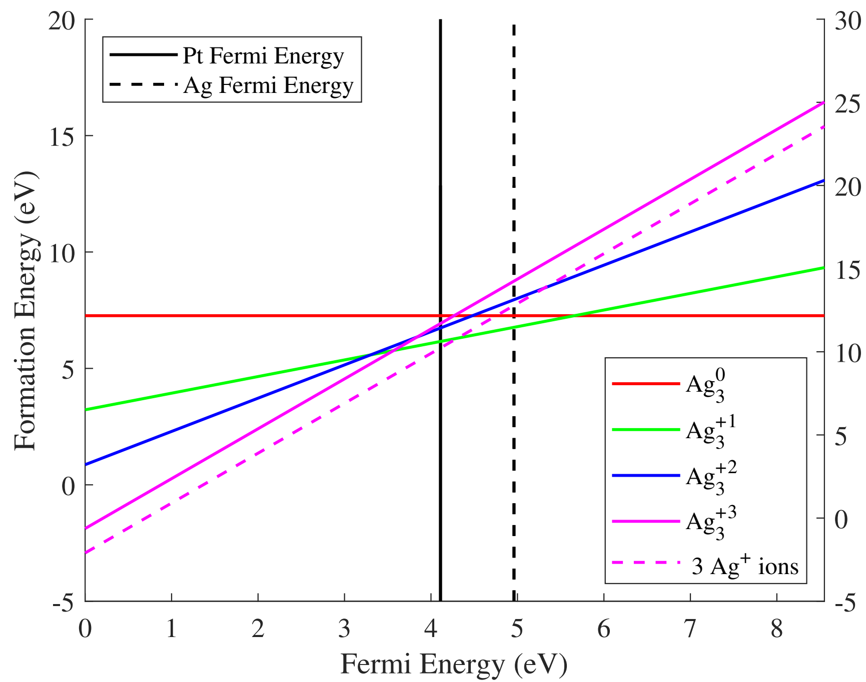

Figure 5.19: The defect formation energy diagram of Ag_3 and 3 non-interacting Ag^{+1} systems in α-quartz as a function of Fermi energy, where the Fermi energy is 0 at the α-quartz VBM.

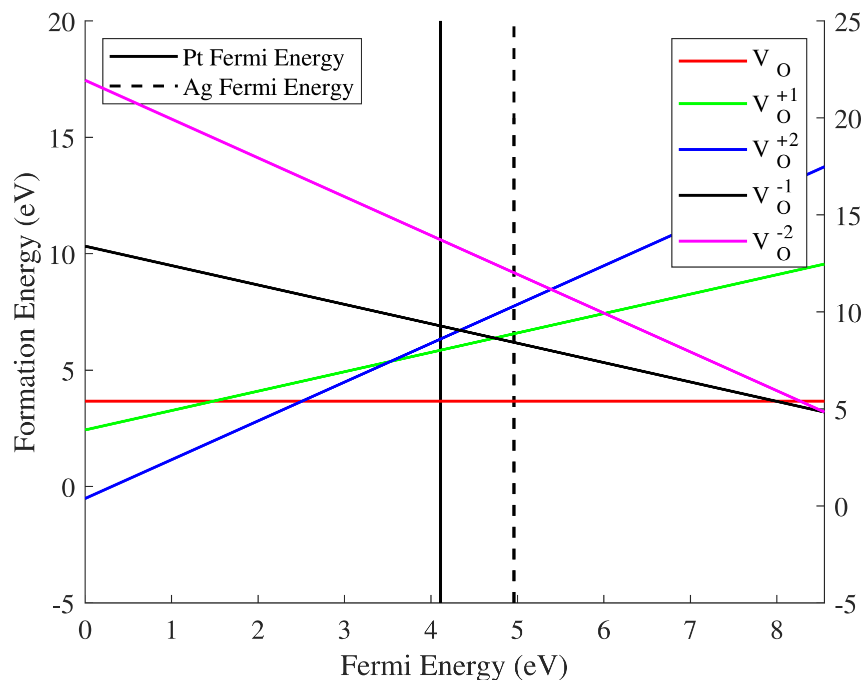

Figure 5.20: The defect formation energy diagram of O vacancy in α-quartz as a function of Fermi energy, where the Fermi energy is 0 at the α-quartz VBM.

The V_O^{-1} adds an electron in the Si-Si anti-bonding orbital. These results are consistent with previous studies, within which more detailed analysis of the defects can be found [111]. For the purpose of this project, the primary observation is that the neutral vacancy is favoured at both the Ag and Pt Fermi energies; representative of regions in proximity with the Ag-SiO_2 and Pt-SiO_2 interfaces (Fig. 5.20). Therefore the interaction of Ag with V_O^0 is studied further.

5.4.2.9 Ag - Oxygen Vacancy interaction

The interaction of Ag with the neutral oxygen vacancy was studied in the -1 $\leq q \leq$ +2 charge states by adding a Ag atom centrally between the two Si atoms involved in the V_O and the optimising the geometry. Results show that a [AgV_O] complex is formed in each charge state. Mulliken charge analysis on the Ag atoms show 0.25 $|e|$, 0.42 $|e|$ and 0.52 $|e|$ charge is donated from the two Si atoms in the vacancy to Ag in the 0, +1, and +2-charge states, respectively. In the -1-charge state, the additional electron localises on Ag. The formation energy diagram (Fig. 5.21) for the [Ag-V_O] defect shows that the +1 charge state is favoured at Fermi energies below 5.07 eV, and the neutral charge state at Fermi energies between 5.07 and 5.88 eV. Above 5.88 eV the -1-charge state is favoured. Although the complex is not favoured to trap an electron at the Fermi energy of the electrodes, this is an interesting result as for the first time, the neutral charge state is possible in a system with a Ag^{+1} ion.

Calculations with Ag placed 6 Å away from V_O were then carried in the 0, +1, and +2-charge states to determine the binding energies of Ag to the vacancy. In each case, it was found that Ag behaved as an interstitial when 6 Å from the vacancy with no interaction observed. As seen on Fig. 5.21), the [AgV_O] complex was found to be lowest energy configuration giving binding energies of 2.14, 1.00, and 1.44 eV for Ag^0, Ag^{+1} and Ag^{+2} to bind to V_O^0, respectively. From this, it can be seen that Ag^{+1} ions diffusing into α-quartz, and perhaps a-SiO_2, can be trapped by oxygen vacancies.

To model the clustering process at the vacancy, a second Ag atom was added to the system, with the results showing that the [Ag_2V_O] complex is favoured to form.

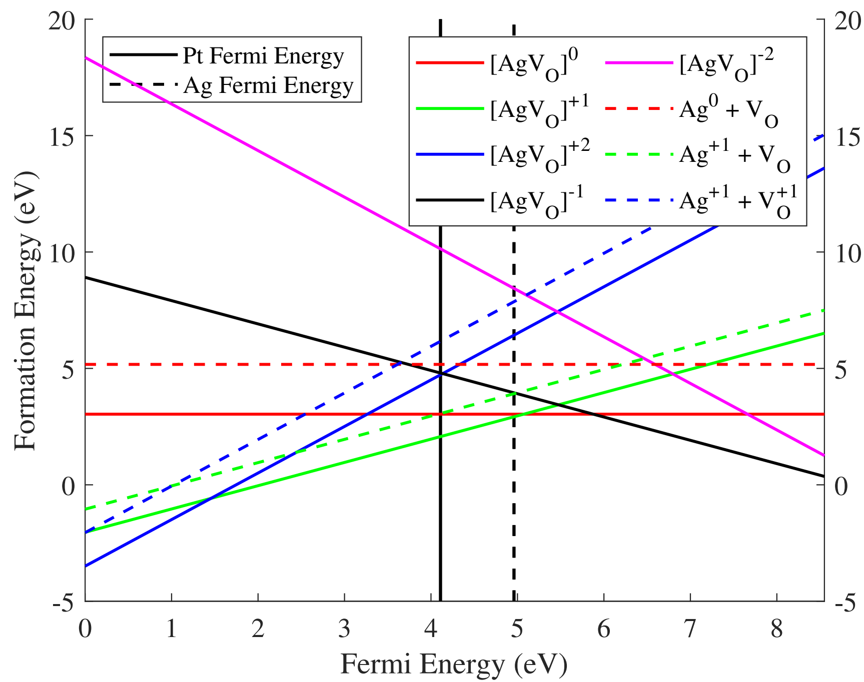

Figure 5.21: The defect formation energy diagram of [AgV_O] complex in α-quartz as a function of Fermi energy, where the Fermi energy is 0 at the α-quartz VBM.

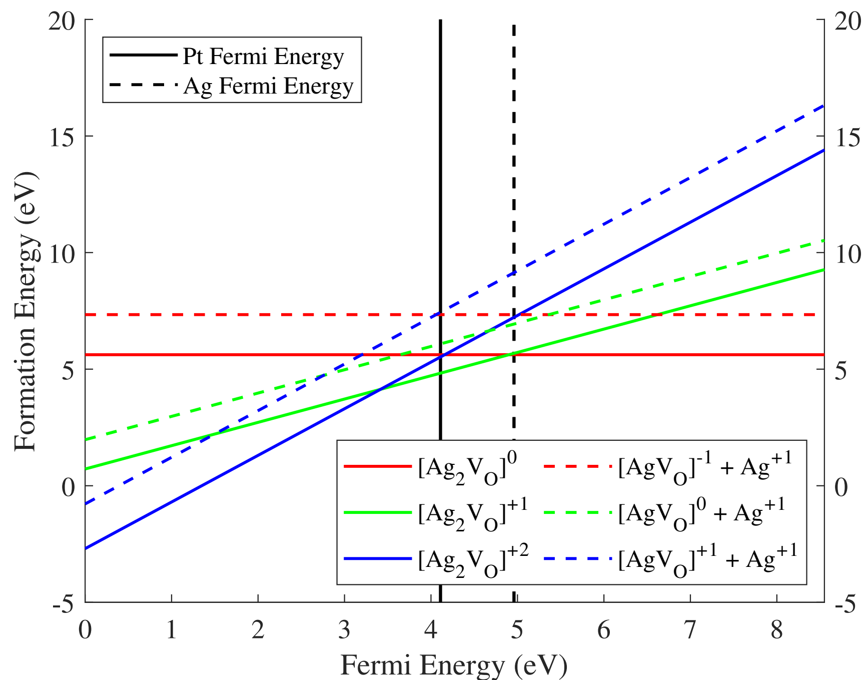

Figure 5.22: The defect formation energy diagram of [Ag_2V_O] complex in α-quartz as a function of Fermi energy, where the Fermi energy is 0 at the α-quartz VBM.

In the 0, +1, and +2-charge states, when Ag is is 6 Å from [AgV_O], Ag remains as a positive Ag^{+1} ion, where the electrons are lost from the [AgV_O] complex. From Fig. 5.22, it can be seen that the $[Ag_2V_O]^{+2}$ is favoured at Fermi energies below 3.42 eV, $[Ag_2V_O]^{+1}$ at Fermi energies between 3.42 and 4.90 eV and $[Ag_2V_O]^0$ above 4.90 eV. A binding energy of 1.44 eV for Ag^{+1} to bind to $[AgV_O]^{+1}$ to form $[Ag_2V_O]^{+2}$ was found, suggesting the V_O will act as a cluster nucleation site in α-quartz. However, it is observed once more that the clustering process at the Ag and Pt electrodes will occur differently, with the $[Ag_2V_O]^{+2}$ complex favouring to trap an electron to become $[Ag_2V_O]^{+1}$ at the Ag Fermi energy but will remain $[Ag_2V_O]^{+2}$ at the Pt Fermi energy.

Fig. 5.23 shows the defect states within the band gap for the [Ag_2V_O] in the 0, +1 and +2-charge states. The +1 and +2-charge states are favoured at the Ag and Pt electrodes respectively, empty states are found in proximity to the Fermi energy of the electrodes.

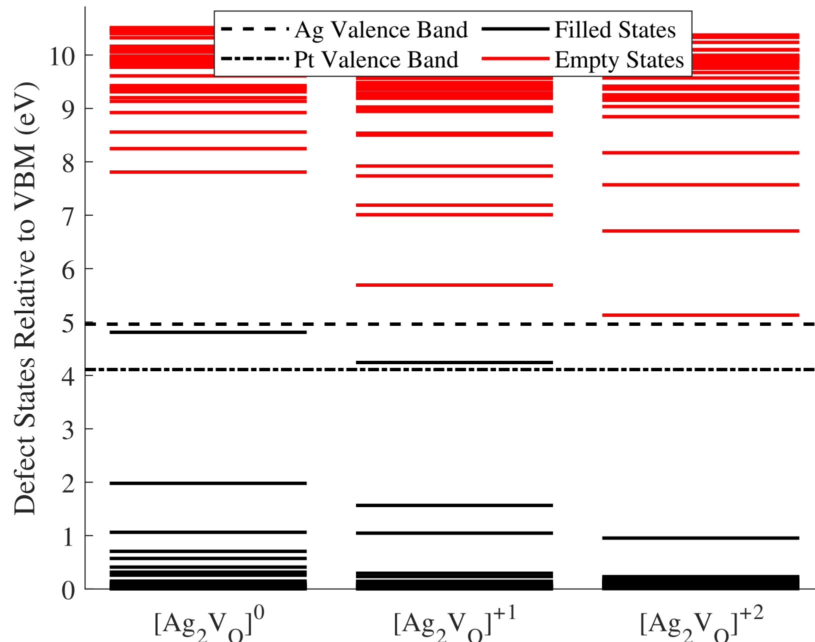

Figure 5.23: Graph showing the filled (black) and empty states (red) of the [Ag_2V_O] complex in the q = 0, +1 and +2 charge states α-quartz. In this case, the states are projected over the α-quartz band gap where 0 represents the α-quartz VBM.

5.5 Summary of Main Results

5.5.1 Experimental Verification

The models for α-quartz and its interaction with Ag developed in this chapter have been shown to accurately reproduce experimental measurements. Each functional tested (PBE, PBE0_TC_LRC, BLYP and B3LYP) gave accurate structure parameters for α-quartz, though only hybrid functionals accurately reproduced the band gap. The hybrid PBE0_TC_LRC functional was found to give the closest representation of α-quartz, and was chosen for calculations. Using the PBE0_TC_LRC functional, the α-quartz vibrational modes were calculated giving bands well matched to measured IR and Raman modes. This shows the bonding characteristics of α-quartz are well reproduced, and in turn, suggests the model will be suited to studying amorphous systems.

The interaction of Ag in SiO_2 was studied with models of the Ag interstitial in α-quartz. The models were verified experimentally through calculations of the Ag^0 hyperfine tensor and EPR signal as well as the Ag^{+1} PLE and PL spectra. Once again a good agreement to experiment was found, both in terms of the individual spectra, and in terms of the observations made about the nature of the defects. Results show that the Ag^0 interstitial is unstable at any Fermi energy along the α-quartz band gap, with a +1 to -1 transition occurring at 6.15 eV above the VBM. When formed, Ag^0 sits off-centre at the intersection of the 2-fold symmetry and 3-fold screw axis, as suggested in the literature. The unpaired electron fills the Ag s-orbital whilst donating charge to an adjacent Si atom in a wide angle O-Si-O bond. It is this interaction that causes Ag^0 to sit off-centre in the 2-fold symmetry axis, closer to the bonded Si. The calculated Ag^0 EPR signal was found to have a primary Ag doublet at 34.6 mT with a 9.9 mT about each Ag peak due to Si and is consistent to the measured spectrum. Calculations for Ag^{+1} shows the ion sits in the 3-fold screw axis, maximising interaction with lattice O. Modelling of the PLE showed a strong correlation to the measured spectrum with excitation peaks beginning at 5.39 eV (5.3 eV experimentally). Calculations of the Ag^{+1} PL shows a triplet to singlet transition at 4.59 eV (4.75 eV experimentally) confirming that

the PL is due to an inner-ion electronic transition from the triplet state to the singlet state. A secondary PL peak was found at 3.8 eV (3.4 eV experimentally) caused by the interaction of Ag^{+1} with an Al center in α-quartz, as suggested in the literature.

5.5.2 Ag-SiO_2-Pt RRAM

The results in this chapter allow several observations to be made about how Ag will behave in α-quartz. Most interestingly, the Ag^{+1} ion is favoured at the Ag and Pt Fermi energies whilst Ag^0 is not favoured anywhere along the band gap. This has significant implications for RRAM operation as Ag must therefore incorporate into the SiO_2 layer as a positive ion, or as an atom which quickly loses an s-electron by way of electron tunnelling back to the Ag electrode. Whilst this may differ in a-SiO_2, this suggests that Ag will remain as a positive ion in proximity to either electrode. As a result, the mechanism for reduction, and the subsequent formation of Ag clusters requires Ag to interact with intrinsic defects in α-quartz.

Calculations for the Ag interstitial in the +1-charge states show that the process of removing an electron from the system empties the Ag s-shell. Ag^{+1} ions maximise interaction with neighbouring O atoms where electron charge is donated from O to Ag. From this, it can be expected that Ag^{+1} ions will reside in proximity to O in large voids in a-SiO_2. Furthermore, Ag^{+1} was found to be very mobile in α-quartz with a 0.06 eV adiabatic diffusion barrier along the c-axis channel compared to a 0.27 eV barrier for Ag^0. Moreover, diffusion barriers of 0.92 and 0.96 eV were observed for diffusion Ag^{+1} and Ag^0 along the ab-axis channel respectively. The higher barrier of Ag^0 is attributed to the larger steric size of the atom compared to the ion, requiring more distortion in the lattice to accommodate transport.

These results have large implications during the electroforming phase, where a positive bias is applied at the Ag electrode. The bias induces an electric field across the SiO_2 layer, serving to reduce the barrier for Ag^{+1} to diffuse deeper into the SiO_2 layer toward the Pt electrode. As such, it is clear that Ag^{+1} will be very mobile, with an almost barrier-less transport, provided a suitable diffusion path. It is therefore consistent with experimental observations showing Ag^{+1} migrate across the SiO_2 layer in nanosecond timescales. However, it should be noted that high

density regions remain inaccessible, instead requiring large regions of low density, grain boundaries or column boundaries for diffusion.

Once Ag^{+1} is sufficiently incorporated into the SiO_2 layer, results suggest the Ag clustering mechanism is very different at the Ag and Pt electrodes. Calculations for Ag_2^{+2} show the double positive dimer is 0.48 eV higher in energy that two non-interacting Ag^{+1} ions, confirming Ag^{+1} ions must be reduced or interact with intrinsic defects in α-quartz before clustering can occur. The stability of the subsequent clusters is then dependant on the Fermi energy position of the electrodes, as highlighted by the defect formation energies of Ag_2 and Ag_3. At the Pt Fermi energy, two non-interacting Ag^{+1} ions are favoured over Ag_2^{+2}, showing clustering will not occur without the presence of an intrinsic defect. Conversely, the Ag_2^0 dimer is favoured at the Ag Fermi energy, suggesting that clustering will occur in the presence of Ag^0.

A binding energy of 0.67 eV was found for Ag^{+1} to bind to Ag^0 to form Ag_2^{+1} showing this process is thermodynamically favourable. Ag_2^{+1} is in turn favoured to trap an electron from the Ag electrode to become Ag_2^0. The stability of Ag_2^0 also allows the possibility that a neutral dimer can incorporate into a-SiO_2 at the Ag electrode, though this is unlikely in α-quartz due to a 8.15 eV incorporation energy. Calculations for Ag_3 show that another Ag^{+1} ion can bind to Ag_2^0 to form Ag_3^{+1} with a binding energy of 0.53 eV, with the Ag_3^{+1} cluster the lowest energy configuration at the Ag Fermi energy. From this, a strong thermodynamic driver for Ag clustering at the Ag electrode is observed provided a neutral Ag^0 or Ag_2^0 is present for the initial cluster nucleation. At the Pt Fermi energy, however, three Ag^{+1} ions are favoured showing clustering will not occur under any circumstances without interaction with other defects.

To determine how Ag clusters at the Pt electrode, the O vacancy was studied with results showing it is a strong candidate to mediate cluster nucleation. In this process the neutral V_O, which was found to be favoured at the Fermi energies of Ag and Pt, traps a Ag^{+1} ion to form $[AgV_O]^{+1}$ with a binding energy of 1.00 eV. The resulting $[AgV_O]^{+1}$ complex will remain positive at either electrode, and trap an-

other Ag^{+1} ion with a binding energy of 1.44 eV. The resulting $[Ag_2V_O]^{+2}$ complex is favoured to remain double positive at the Pt electrode, but to trap one electron at Ag to become $[Ag_2V_O]^{+1}$.

As discussed in section 4.3, the electroforming phase in Ag-SiO_2-Pt RRAM devices can be considered to be controlled by two parameters, namely the Ag^{+1} ion mobility (μ), and the Ag^{+1} ion reduction rate (Γ). In the low μ regime, Ag clustering is observed at the Ag electrode and in the high μ regime clustering occurs at the Pt electrode. The nature of the filament is controlled by Γ, where a low Γ results in a narrow dendrite type filament or through a small number of clusters compared to the high Γ regime where a large conical filament or a filament consisting of a high concentration of Ag clusters grows. In the initial phase, Ag^{+1} ions incorporate into a-SiO_2 under bias. The ions diffuse toward the Pt electrode where μ is the controlling factor.

The results show that this is controlled by the SiO_2 microstructure, where high mobility is only possible through regions of low density. This is suggested to include not only regions of low density in the bulk lattice, but also grain and column boundaries. The nature of the filament is then controlled by Γ, which has been shown to rely on the Fermi energy position of the electrodes and the concentration of oxygen vacancies. A higher concentration of oxygen vacancies is proposed to increase Γ, with the probability of the vacancy to reduce Ag controlled by the Fermi energy position. This is seen in experiments of sputtered oxide layers, which are known to contain column boundaries and show clustering at the Pt electrode. In these devices, the filament is wider at the Ag electrode, suggesting the Fermi energy position of Ag increases Γ at the Ag electrode. Conversely, thermal oxides are known to be less defective, with measurements showing Ag begins clustering at the Ag electrode.

5.6 Conclusion

The electroforming process in Ag-SiO_2-Pt RRAM devices has been studied using α-quartz as a control. The DFT models of α-quartz and Ag in α-quartz were shown to be in good agreement with experimental data. This includes accurate reproduc-

tions of the α-quartz IR and Raman modes, the Ag^0 hyperfine tensor and EPR signal and the Ag^{+1} PLE spectrum and PL energies. Subsequently it was shown that the Ag^{+1} ion is favoured at the Ag and Pt Fermi energies and is very mobile in α-quartz, giving a 0.06 eV adiabatic diffusion barrier along the c-axis channel. It was then shown that the O vacancy mediates Ag^{+1} reduction allowing Ag clustering to occur. In this case the neutral V_O, which is favoured at the Fermi energies of Ag and Pt, was found to trap a Ag^{+1} ion to form a $[AgV_O]^{+1}$ complex with a binding energy of 1.00 eV. The resulting $[AgV_O]^{+1}$ complex will remain positive at either electrode, and trap another Ag^{+1} ion with a binding energy of 1.44 eV. The resulting $[Ag_2V_O]^{+2}$ complex is favoured to remain double positive at the Pt electrode, but to trap one electron at the Ag electrode to become $[Ag_2V_O]^{+1}$. In this way it is suggested that additional Ag^{+1} ions and electrons can trap to the vacancy cluster complex. The charge state of the complex is then determined by the Fermi energy position of the electrode the complex is in proximity to.

Chapter 6

Ag Redox Reactions and Migration in a-SiO_2

6.1 Introduction

In the previous chapter, a methodology for studying Ag-SiO_2-Pt RRAM devices using α-quartz models was developed to provide insight into the individual processes involved in ECM filament formation. The models for the Ag/α-quartz system were shown to reproduce the Ag/SiO_2 interaction accurately, justifying the use of the same DFT system to model the interactions in an amorphous context. Expanding the study in this way to a-SiO_2 systems is vital to allow a complete and statistical understanding of the mechanisms that occur in Ag-SiO_2-Pt devices. From this, the variations of defects and defect interactions allowed by the CRN can be considered and their effects understood. Additionally, the impact of local structure can be modelled directly, where up until this stage only large voids are assumed to play a significant role in Ag incorporation, transport and clustering. Furthermore, with previous research showing the V_O can adopt a number of geometric configurations, their potential to mediate Ag^{+1} reduction is unclear [111].

In this chapter, the individual processes involved in ECM filament formation are systematically studied beginning with the incorporation of Ag in a-SiO_2. This is achieved through the development of a Ag/SiO_2 interface between a metallic

bulk Ag cluster and an α-cristobalite (202) surface, as well as studying the various interstitial positions of Ag in the a-SiO_2 bulk. Additionally, the incorporation of Ag is studied in crystalline α-cristobalite grain boundary (GB) and column boundary (CB) models with a view of determining the effect of microstructure on device performance. This is followed by CI-NEB calculations of Ag^0 and Ag^{+1} diffusion in bulk a-SiO_2 and the α-cristobalite GB and CB to model the migration of Ag observed *in-situ* TEM images [11, 10, 12]. Guided by the results in chapter 4, the reduction of Ag^{+1} ions in proximity to the electrodes is then studied through the interaction of Ag with V_O.

6.2 Theoretical Methodology

The optimal DFT parameters determined in section 5.4.1 are used for all calculations in this chapter, unless otherwise stated. This includes the use of the Gaussian Plane Wave method (GPW) in the CP2K code[17], with the plane wave cut-off and relative cut-off set to 600 Ry and 40 Ry, respectively, and a convergence criterion of 1x10^{-6} eV per formula unit. The double zeta valence polarised (DZVP) molecularly optimised (MOLOPT) basis sets and Goedecker-Teter-Hutter (GTH) pseudopotentials [25] are also used with the PBE0_TC_LRC functional with exchange term truncated at 2 Å. The auxiliary density matrix method (ADMM) is used to reduce computational cost of calculating the non-local exchange integrals. [41]

6.2.1 Ag/a-SiO_2 interface

The Ag/SiO_2 interface was created using a crystalline α-cristobalite (202) surface model with the PBE functional and the addition of the D3-dispersion correction. The D3-dispersion was added to account for the interactions at the surface of the GB and CB as described in section 2.2.2.2. To develop the interface, a hydroxylated α-cristobalite (202) surface was constructed for use in this work by Cottom *et al.* [26, 112]. The surface was selected to match the Si-OH concentration of a-SiO_2 systems at standard conditions [113], as determined in the literature [114]. The models have also been verified through bulk a-SiO_2 surface calculations and IR experiments [115, 116].

The interface was built using a cluster-based approach with the intention of minimising the number of atoms in the cell whilst retaining the metallic bulk nature of Ag in the DOS at the Fermi level. To achieve this, a connection scheme approach was used to introduce 6-atom Ag clusters onto the α-cristobalite surface one at a time [26]. This began by introducing an initial 6-atom Ag cluster onto the α-cristobalite surface translating its position to minimise the Ag-O bond lengths. The cluster was then rotated to minimise the Ag-Si distances as this interaction has previously been shown to be favoured at Ag-SiO_2 interfaces [117]. The system was then geometry optimised using DFT to reach a local minimum, before a second 6 Ag atom cluster was added, translated, rotated and optimised. This process was repeated to imitate the sputtering process that is typically used to deposit the Ag layer in devices. The process was continued until a 108 atom Ag cluster was grown, which gives a good approximation of the bulk Ag DOS at the Fermi level as shown on Fig.6.1. In this case, the system shows metallic nature at the Fermi level due to the Ag states. It should be noted that to achieve metallic Ag DOS, the Ag cluster is periodic in one direction. It was possible to increase this to periodic in 2 directions (slab model) but this was not done to reduce the computational expense.

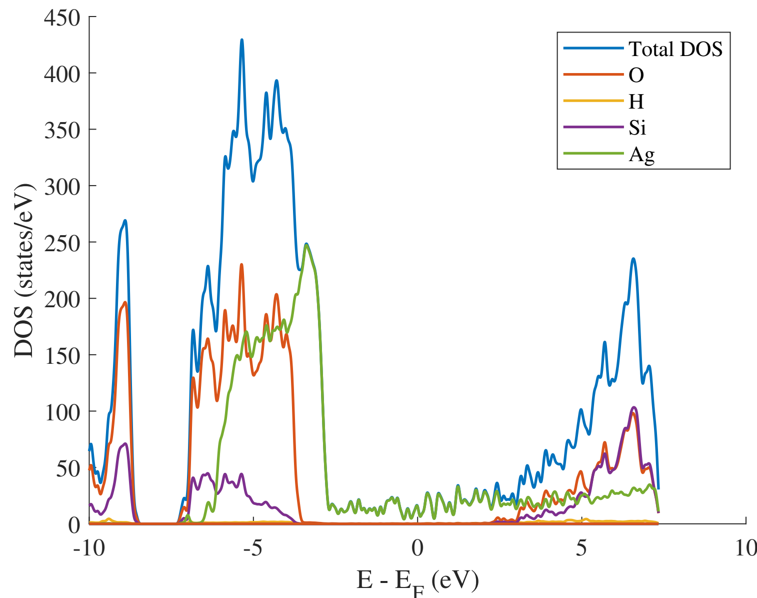

Figure 6.1: Element projected density of states for the Ag/α-cristobalite interface.

6.2.2 Grain and Column Boundaries

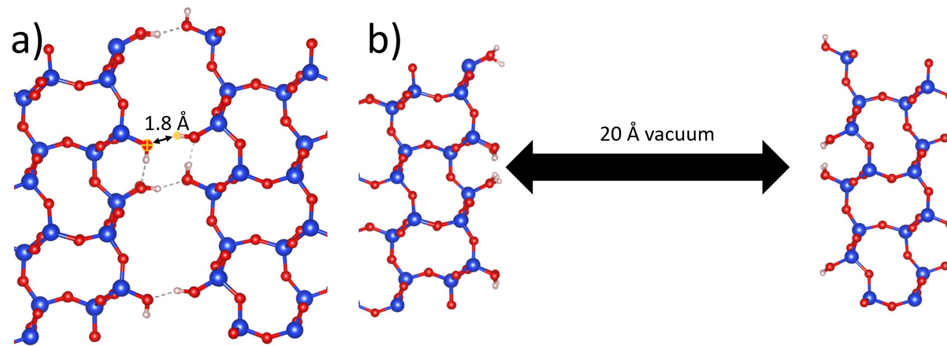

Figure 6.2: a) shows the α-cristobalite (202) grain boundary. b) shows the α-cristobalite (202) column boundary generated with a 20 Å vacuum between each α-cristobalite (202) surface.

The SiO_2 GB and CB models (Fig. 6.2) were constructed using a crystalline α-cristobalite (202) surface model with the PBE functional and the addition of the D3-dispersion correction. The D3-dispersion was added to account for the interactions at the surface of the GB and CB as described in section 2.2.2.2. To produce the boundary, a hydroxylated α-cristobalite (202) slab was constructed to match the surface SiOH concentration of a-SiO_2 systems at standard conditions [113]. In this case, the boundary is formed between the two surfaces of the α-cristobalite (202) surface slab. Subsequently, a CP2K cell optimisation was used to find the optimal separation between each surface of the α-cristobalite slab. From this, it was found that a 1.8 Å separation gives the lowest energy distance between the hydroxylated surfaces and is therefore used for the GB model. The vacuum gap between the two surfaces was then increased in increments of 5 Å to model the CB (Fig. 6.3). From this, it can be seen that the surfaces do not interact past a 10 Å separation. As such, a 20 Å separation is used for the CB models.

6.2.3 Ag in a-SiO_2

The a-SiO_2 models used in this work were created by El Sayed *et al.* using the molecular dynamics melt and quench method implemented in LAMMPS [118]. From this, 30 216-atom a-SiO_2 structures were re-optimised using the DFT parameters discussed in section 5.4.1, beginning with a cell-optimisation followed by a geometry optimisation with the PBE0_TC_LRC functional truncated at 2 Å. The

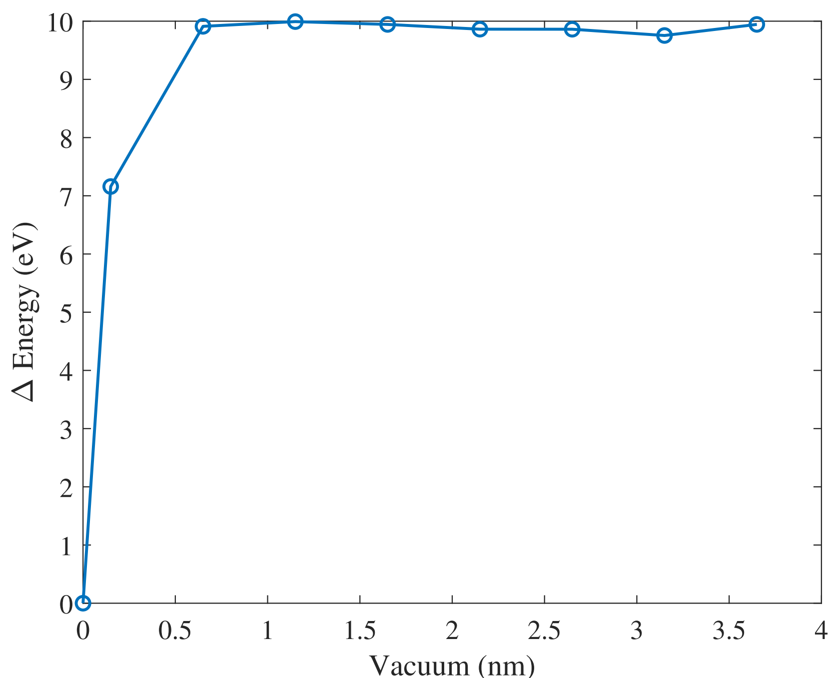

Figure 6.3: Graph showing the total energy difference of an α-cristobalite (202) surface slab as the vacuum between the surfaces is increased. 0 nm marks the GB separation of 3 Å

Ag interstitial was then sampled using the a-SiO_2 cell with the density closest to the mean density of the 30 cells re-optimised. To do this, a grid based sampling method was developed, further discussed below in section 6.2.3.1.

The diffusion characteristics of Ag in a-SiO_2 were modelled using CI-NEB calculations described in section 2.3.2, each with spring constant of 4.86 eVÅ^2 and 5 replica images, unless otherwise stated.

The *ab initio* MD simulations were carried out with the PBE functional to reduce computation expense. Calculations using the PBE functional were found to give similar defect formation energies as the hybrid calculations, whilst the band-gap is large enough to prevent the delocalisation of the defect states. A fixed volume NVT ensemble [56] is used along with a Nose-Hoover thermostat (see section 2.4.3) [58]. The volume was kept constant to best model experimental conditions, where the expansion of the a-SiO_2 layer in the devices of interest is constrained by the metal electrodes. Simulations are also run with a 1 fs time step. This is to ensure that the time step is large enough to reduce computational expense whilst small enough

to keep the energy, pressure and temperature values stable. In a similar fashion, the Nose-Hoover thermostat was selected to update every 10 time steps to ensure stable temperature, with higher values causing large fluctuations in temperature.

6.2.3.1 Grid based interstitial sampling

To achieve complete spacial sampling, a 3-dimensional grid with 2 Å spacing was mapped across the a-SiO_2 super-cell giving 512 grid points as initial interstitial sites. Subsequently, grid points were excluded if there was Si or O atom within 1.34 Å corresponding to the atomic radius of Ag [119]. The remaining 259 points were used as initial Ag interstitial site locations. Ag was then added at each of the 259 points individually, and the geometry was optimised using the PBE functional for each charge state. Following the geometry optimisations, many of the Ag starting locations relaxed to the same final interstitial sites. The geometries of all different Ag interstitial sites were further optimised using the PBE0_TC_LRC functional to allow a better approximation of the a-SiO_2 band gap. A particular site is considered to be different with respect to other Ag positions if any atom in the cell is displaced by more than 0.2 Å as a result of lattice relaxation, the system total energy differs by more than 0.1 eV, or the Mulliken charge on Ag differs by greater than 0.05 $|e|$.

6.3 Results

6.3.1 Ag incorporation

Ag has been shown to incorporate into a-SiO_2 in each of the studies concerning Ag-SiO_2 RRAM devices. To model this process, and to determine the respective incorporation energies and migration barriers, the Ag/SiO_2 interface was developed using a crystalline α-cristobalite (202) surface model as described in section 6.2.1.

Fig. 6.4 shows the final structure of the Ag/SiO_2 interface formed between the Ag cluster and the α-cristobalite surface. To minimise the computational cost of having more Ag atoms, the Ag cluster is periodic along one axis to allow a metallic DOS at the Fermi level (Fig. 6.4c). A vacuum of 20 Å was used, determined by increasing the vacuum in 5 Å increments until convergence of the total energy of the system was achieved. Using this model, the diffusion barrier for Ag into

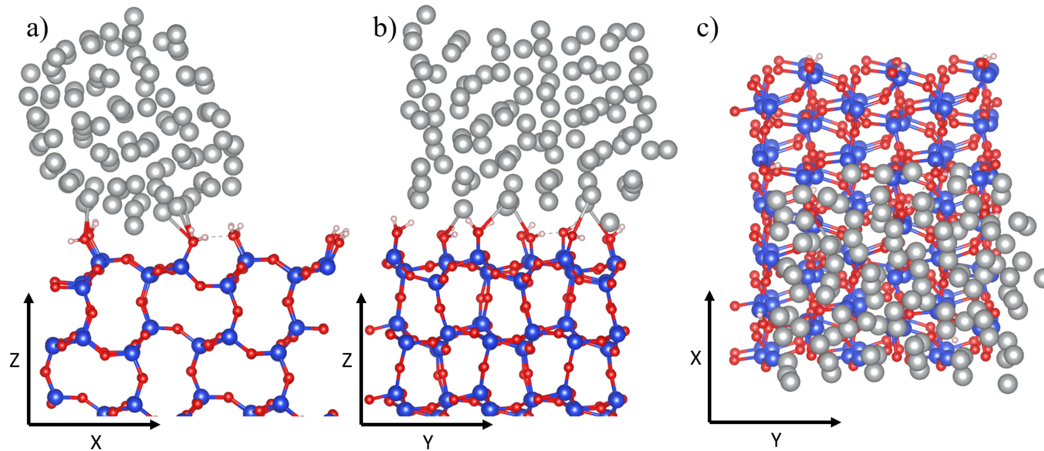

Figure 6.4: Structure of the Ag/SiO_2 interface formed between a Ag cluster and the hydroxylated (202) α-cristobalite surface. a)-c) show the view from the x, y and z axis, respectively From c), it can be seen that the cluster is periodic in y direction.

SiO_2 was calculated using a CI-NEB calculation with 7 bands (Fig. 6.5). From this, an incorporation barrier of 3.41 eV and a Ag incorporation energy of 2.87 eV were found (Fig. 6.6). Mulliken charge analysis shows that Ag, when part of the Ag cluster, is in a neutral charge state (Mull = 0.09 $|e|$). As the Ag interstitial breaks from the Ag cluster, charge is donated from the Ag interstitial back to the Ag cluster (Mull = 0.33 $|e|$). Subsequently, as Ag passes through the α-cristobalite surface it acquires Ag^{+1} character (Mulliken charge = 0.54 $|e|$). Once through the interface, Ag behaves as a Ag^{+1} ion in bulk α-cristobalite, relaxing to the Ag^{+1} bulk interstitial site with the bulk Mulliken charge (Mull = 0.60 $|e|$). From this we see a forward barrier of 3.41 eV for Ag to incorporate in α-cristobalite and a 0.55 eV reverse barrier. This suggests it is more likely for Ag^{+1} to leave SiO_2 than stay incorporated.

Then, another CI-NEB calculation was carried out to model a second Ag incorporating into α-cristobalite to form a Ag_2 dimer (Fig. 6.6). In this case, the second Ag is incorporated through the same surface region and into the same cavity of the α-cristobalite surface as the first Ag. From this a forward barrier of 2.70 eV was found with a reverse barrier of 0.72 eV. The incorporation energy of the second Ag is 1.98 eV, where the reduced incorporation energy is due to the metallic Ag-Ag

bond formed for the Ag_2 dimer.

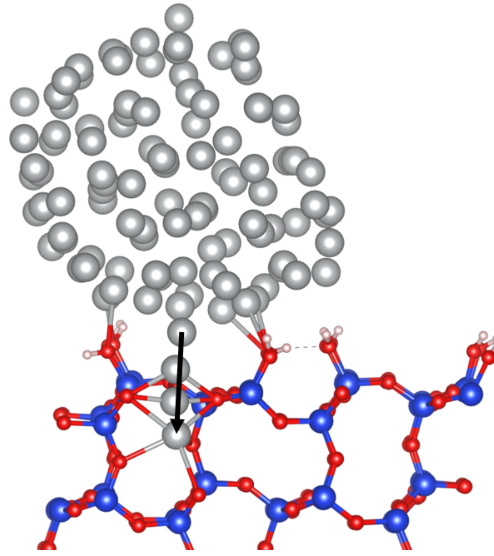

Figure 6.5: Image of the Ag/SiO_2 showing the incorporation of a Ag species into α-cristobalite, following the path of the black arrow.

These results suggest that the large barrier found for Ag to incorporate into α-cristobalite is dominated by the strong metallic bonding of Ag to the larger cluster and the steric crowding of Ag in α-cristobalite. This is shown through the low reverse barriers of 0.55 eV and 0.72 eV for the first and second Ag incorporation. Calculations for incorporation of second Ag show that the barrier is reduced when Ag is able to form an Ag_2 dimer, hence some energy can be gained through the clustering of Ag in the SiO_2 bulk (Fig. 6.6). Therefore, it can be inferred that Ag may only incorporate into voids in a-SiO_2 though large rings or in GB or CB systems where less strain is induced into the lattice.

By considering this model in reverse, it is analogous to the clustering of Ag on an α-cristobalite surface or within a column boundary. In this way, a barrier of 0.55 eV is seen for Ag^{+1} ion to pass from the α-cristobalite bulk through the surface. Subsequently, there is a binding energy of the Ag^{+1} ion to the Ag cluster of 2.87 eV. This clearly suggests that the clustering of Ag is favoured on SiO_2 surfaces and large column boundaries. It should be noted that Ag^{+1} may also be able to pass through regions of low density in a-SiO_2 to reach the surface or CB reducing the 0.55 eV barrier further.

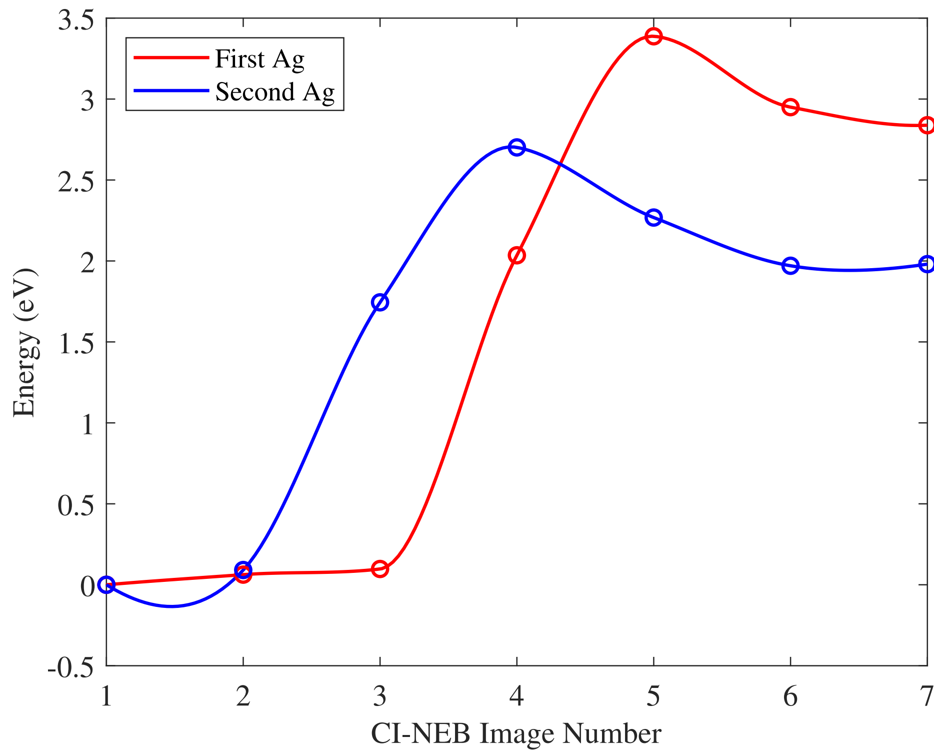

Figure 6.6: Graph showing the results of a CI-NEB simulation for the incorporation of the first Ag (red) and second (blue) Ag into α-cristobalite.

6.3.2 a-SiO_2 models

The methods to produce the a-SiO_2 models used in this chapter are described in section 6.2.3 and their structural characteristics can be found in the literature [118]. The resulting 30 structures show an improved mean density to those produced by El Sayed, increasing from 2.15 to 2.19 g/cm^3. Furthermore, the bond lengths, angles and structure factor of each cell are in good agreement to previous studies [118]. The ring statistics (Fig. 6.7) are also in agreement to previous literature [120, 121]. For the remainder of this chapter, unless otherwise stated, the cell with the density closest to the mean density of the 30 a-SiO_2 structures produced was used to model the Ag/a-SiO_2 interaction and subsequently Ag-SiO_2-Pt RRAM devices.

6.3.2.1 Oxygen Vacancy

As was shown previously, the O vacancy may play a significant role in the reduction of Ag^{+1} ions. Therefore studying the interaction of Ag with V_O forms a significant area for study in this chapter. An in depth study of V_O defects in SiO_2 can be

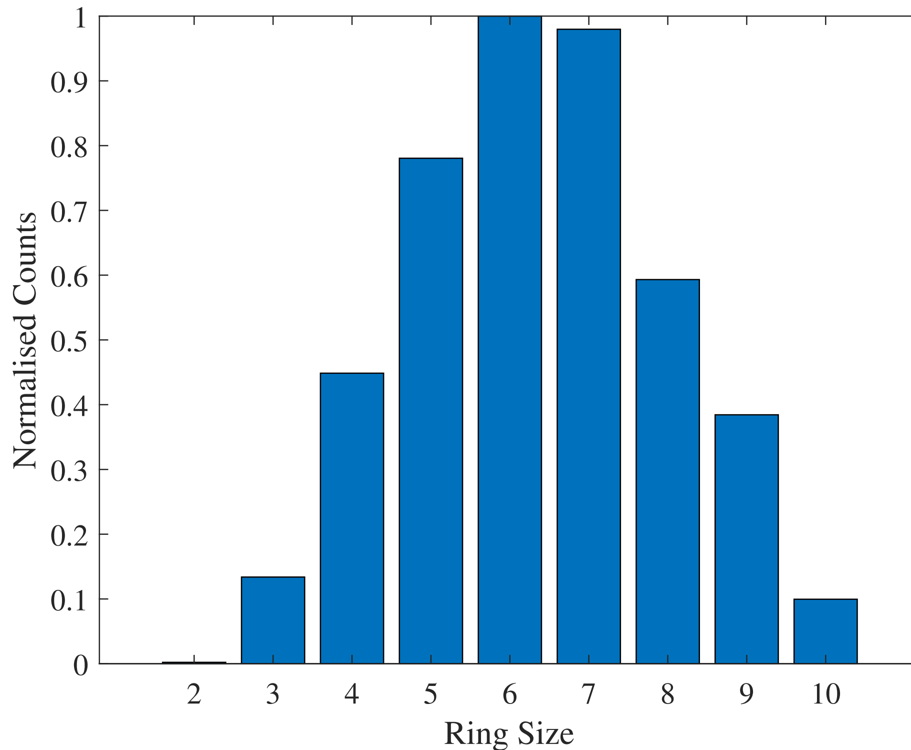

Figure 6.7: Bar graph showing the ring statistics of the 30 a-SiO_2 cells produced.

found in the literature, but is beyond the scope of this investigation [111]. For this work, V_O was sampled using a complete sampling method where a vacancy was generated for every O in the 216-atom cell. Calculations for the 144 O vacancy sites give the mean, minimum and maximum V_O formation energies of 5.3, 4.2 and 6.3 eV, respectively. This is consistent with the literature where the average formation energy for the neutral oxygen vacancies is given as 5.0 eV with a std of 0.7 eV [122]. From Fig. 6.8, the neutral vacancy is seen to be favoured at the Fermi energies of Ag and Pt, and as such, the interaction of Ag with the neutral ${V_O}^0$ is studied further. It was also found that single electron trapping becomes favourable at $E_F > 6$ eV. In this case, the Si-Si bond length of the neutral vacancy was determined to be negatively correlated to the (0/-1) transition, suggesting that vacancies with long Si-Si bond lengths energetically favour the trapping of electrons.

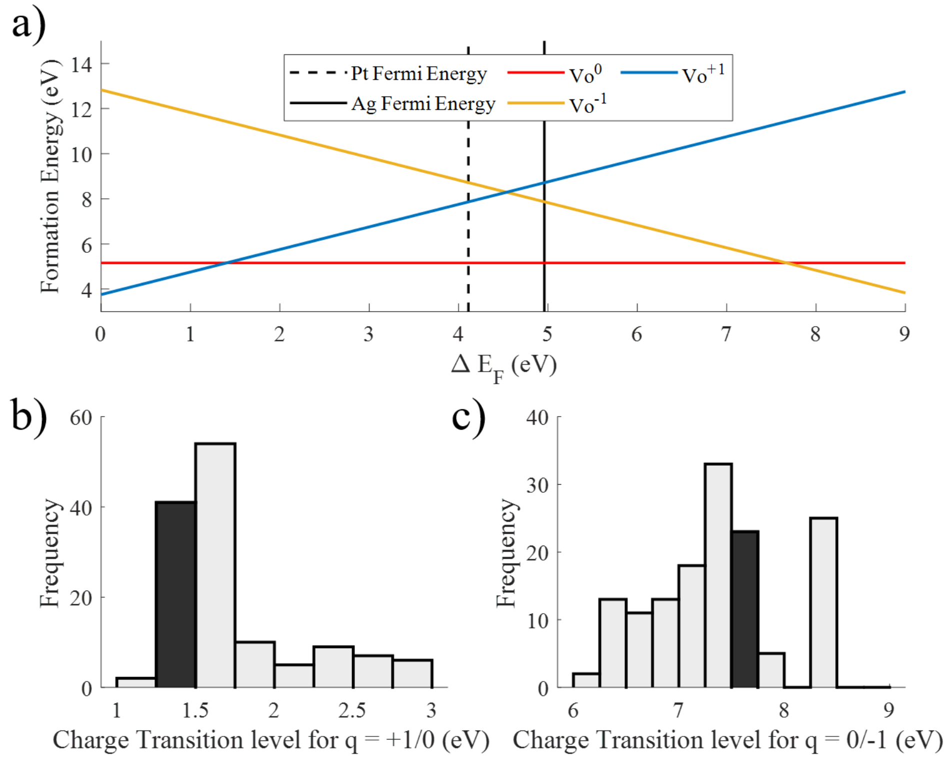

Figure 6.8: a) The formation energy diagram of one O vacancy as a function of Fermi energy, (ΔE_F), where $\Delta E_F = 0$ at the a-SiO_2 VBM. The cross over points between the lines at 1.4 and 7.7 eV correspond to the Fermi energy at which the lowest energy charge state transitions from (+1/0) and (0/-1), respectively; b) the distribution of (+1/0) charge transition level positions for all 144 O vacancies; c) the distribution of (0/-1) charge transition level positions for all 144 O vacancies. The transitions seen in a) are shown as darkened bars in b) and c).

6.3.3 Ag^0 in a-SiO_2

To better understand the Ag interstitial in a-SiO_2, a sampling method that considers Ag in a range of positions is required. To achieve this, a grid based method (described in section 6.2.3.1) was used to allow the complete spatial sampling of the a-SiO_2 cell. From the 259 initial interstitial geometries, 34 unique sites were found for Ag^0 with two types of interstitial defects formed (Fig. 6.9). The first of these (18 of 34 unique sites) involves Ag^0 located in a large void where it has minimal interaction with the lattice. The nearest neighbour distance between Ag^0 and the nearest atom in the lattice ranges between 2.9 - 3.3 Å. Furthermore, the mean Mulliken charge (0.02 $|e|$) of this void defect confirms a negligible interaction between Ag^0 and the lattice. From Fig. 6.9a, the highest occupied molecular orbital (HOMO) is

shown to be Ag with s-character.

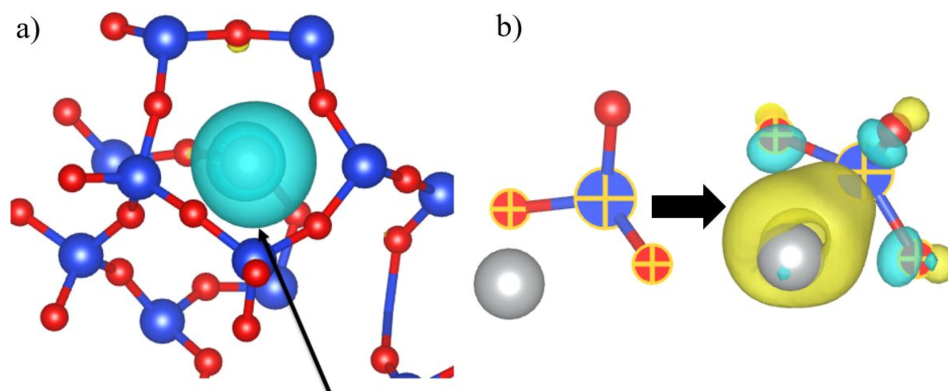

Figure 6.9: Schematic of the two configurations of the Ag^0 defect. The silver, blue and red spheres correspond to Ag, Si and O atoms respectively. The positive and negative charge density are shown as blue and yellow iso-surfaces respectively at a value of ± 0.07. a) shows the void type configuration whilst b) shows the wide angle O-Si-O configuration where as Ag^0 comes into proximity of the O-Si-O angle bond, the O-Si-O angle increases, with charge donation from Ag to Si.

In the second Ag^0 configuration (16 of 34 unique sites), the geometry of Ag^0 is similar to the Ag^0 interstitial in α-quartz. Ag^0 interacts with a wide O-Si-O bond angle, maintaining a nearest neighbour distance of 2.1 - 2.7 Å. The interaction with Ag^0 causes the O-Si-O bond angle to increase by 15 - 43° to 124 - 166 ° as seen in Fig. 6.9b. In a similar fashion to α-quartz, charge is donated from Ag^0 to the Si in the wide O-Si-O angle, with Mulliken charge analysis giving a mean Ag^0 charge of 0.25 $|e|$ and a mean charge of 0.19 $|e|$ donated to Si.

The minimum, and maximum incorporation energies of Ag^0 are 2.8 eV, and 6.1 eV respectively. In this case, the incorporation energies were calculated with a Ag chemical potential taken from Ag_2O (see section 2.3.1). Analysis of the unique sites shows a strong correlation between the incorporation energy and the local steric environment for both types of defect, though this effect is more dominant for the void type configuration (Fig. 6.10). In this case, the incorporation energy for both types of defect increases with the coordination number defined as the number of atoms within 3 Å of Ag^0. From this, Ag^0 is expected to preferentially reside in the less dense areas and voids of a-SiO_2. Furthermore, Ag^0 atoms interacting with a widened O-Si-O bond angles have lower incorporation energies than void type

defects with the same coordination number. From this, it can be inferred that the energetic cost of creating the wide angle O-Si-O is compensated by its interaction with Ag^0.

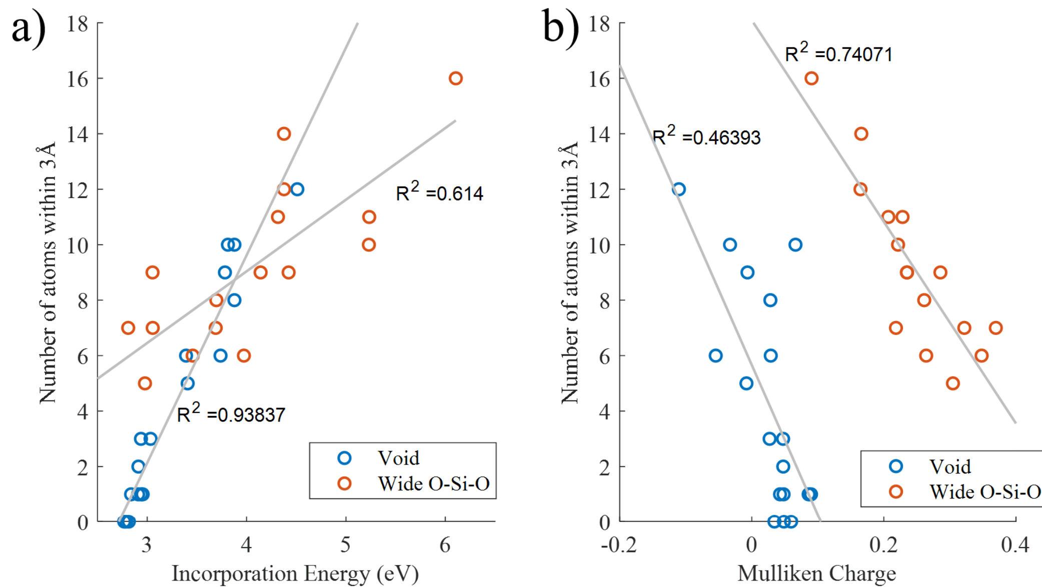

Figure 6.10: Graphs showing the relationship of the incorporation energy (a), and the Mulliken charge (b) to the number of atoms within 3 Å of Ag^0

6.3.4 Ag^{+1} in a-SiO_2

The calculations made for Ag^{+1} reveal 50 unique interstitial sites are possible in the same a-SiO_2 structure. Analysis of each site shows a preference for Ag^{+1} to be in voids, where every ion relaxes to minimise the distance to nearby O atoms in the void upon optimisation. In each case, Ag^{+1} forms a weak interaction with at least one proximate lattice O, maintaining a nearest neighbour distance of 2.2 - 2.6 Å (Fig. 6.11). The mean Mulliken charge of Ag^{+1} is 0.78 $|e|$, where a strong negative correlation is found between the Mulliken charge and the coordination number. This is caused by additional charge donated from neighbouring lattice O to Ag^{+1} in the more dense regions. Similar to Ag^0, a strong correlation is found between the local steric crowding and the incorporation energy, suggesting that both Ag species will propagate though large voids in a-SiO_2, with higher barriers required to migrate into and through dense areas.

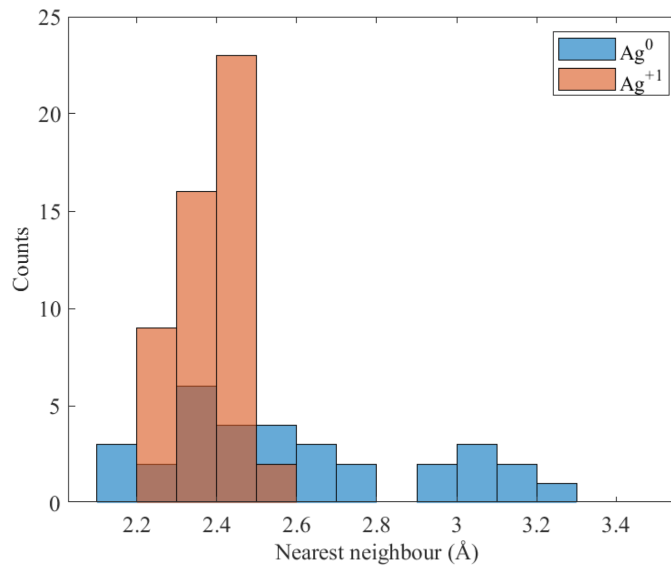

Figure 6.11: Histogram comparing the nearest neighbour distances of Ag^0 and Ag^{+1}.

6.3.5 Ag in a-SiO_2

The incorporation energy of Ag in a-SiO_2 as a function of Fermi level position is shown in Fig. 6.12. Again, the incorporation energies were calculated with respect to a Ag chemical potential taken from Ag_2O. The Ag^{+1} ion is found to be the most stable charge state with an incorporation energy of -2.1 eV for an electron chemical potential at the a-SiO_2 valence band maximum. Furthermore, Ag^{+1} is the lowest energy charge state at the Fermi energy of Ag and Pt with the mean (+1/0) transition at 5.25 eV. The Ag^{+1} ion is 0.3 eV lower in energy than Ag^0 at the Ag electrode in good agreement with the Ag/α-cristobalite interface model showing Ag is incorporated as Ag^{+1}.

During the electroforming phase, mass inter-diffusion of Ag is observed upon application of a positive voltage at the Ag electrode. Under a positive bias, electrons are removed from the Ag Fermi level causing the Fermi energy position of the Ag electrode to shift down in energy and towards the a-SiO_2 valence band. From Fig. 6.12, the shift to lower Fermi energies results in Ag^{+1} becoming more energetically favoured [123]. The incorporation energy of Ag^{+1} is 1.1 eV lower in energy than Ag^0 at the Pt Fermi energy. During operation the Pt electrode is grounded suggesting that a Ag interstitial in proximity to the Pt electrode will remain in the positive

charge state. As such, the system behaves in a similar fashion to Ag in α-quartz where a defect associated mechanism is required for the reduction of Ag^{+1} before Ag clusters can form. This hypothesis was tested by placing two Ag^{+1} ions 2 Å apart from each other in a a-SiO_2 cell. Upon relaxation, the ions separated to a 4.7 Å distance, showing that Ag_2^{+2} does not form. As the results for Ag in a-SiO_2 are in close agreement to those observed in α-quartz, it can be expected that the V_O will be a strong candidate to mediate Ag^{+1} reduction and Ag cluster nucleation.

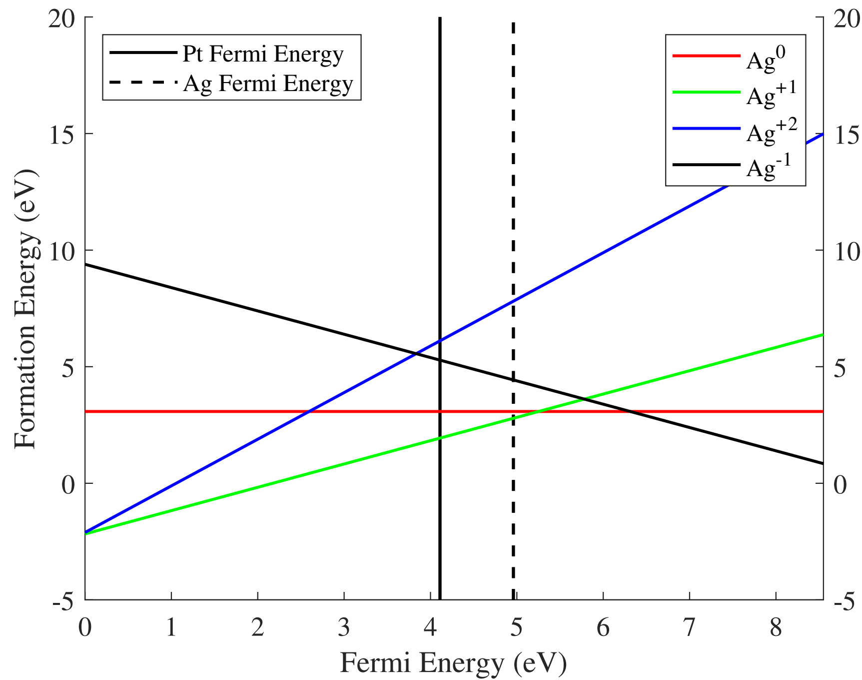

Figure 6.12: Formation energy diagram of the Ag interstitial with respect to the a-SiO_2 VBM. The lines represent the mean incorporation energy of the unique Ag sites in a-SiO_2 for each charge state.

6.3.6 Ag diffusion in a-SiO_2 bulk

The adiabatic diffusion barriers of Ag^0 and Ag^{+1} were calculated for Ag diffusion through 4-member to 8-member rings in a-SiO_2, with the results presented in Table 6.1. In this case, the lowest energy interstitial sites within 3 Å either side of each ring was used as start and end points for the calculations. Similar to α-quartz, Ag^{+1} is found to be the more mobile species in a-SiO_2, with the diffusion barriers of Ag^{+1} being lower than Ag^0 for a given ring size. In both charge states, the diffusion

barrier decreases with increasing ring size. The primary factor to determine the barrier height was found to be the radius of each ring. This is observed in the CI-NEB calculations, where the transition state (or saddle point) in the migration path occurred for each calculation as the Ag species passed directly though the ring. The increase in energy at this point is a result of the energetic cost incurred for the ring to expand to allow the Ag species to pass though. This effect is amplified when Ag^0 and Ag^{+1} passed through the 4-member ring where a Si-O bond is broken. These results are consistent with the same calculations made for Ag in α-quartz, showing Ag favours voids and less dense areas.

The lower barriers for Ag^{+1} compared to Ag^0 can be explained by the small affinity of Ag^{+1} to interact with the partially anionic lattice O atoms. The results in the previous section show that Ag^{+1} maintains nearest neighbour distances of 2.2 - 2.6 Å compared to Ag^0 void defect which maintain distances between 2.9 - 3.3 Å. As such, Ag^{+1} has a lower effective radius than Ag^0 and therefore induces less distortion in the lattice. During the electroforming phase and under a positive bias, the barriers for Ag^{+1} diffusion are reduced in the direction of the electric field. This shows that the results provide strong evidence that Ag^{+1} is incorporated into a-SiO_2 and is the most mobile species. However, it is important to note that low barriers were only found for diffusion though large rings. As a result, and similar to the observations made for Ag in α-quartz, diffusion is limited by the availability of a low density diffusion path.

Table 6.1: Table showing the forward and reverse barriers for Ag^0 and Ag^{+1} in a-SiO_2 calculated by DFT CI-NEB simulations through n = 5 - 8 atom rings.

Ring Size	Ag^0 Forward Barrier (eV)	Ag^0 Reverse Barrier (eV)	Ag^{+1} Forward Barrier (eV)	Ag^{+1} Reverse Barrier (eV)
5	2.36	3.11	2.08	2.54
6	1.25	1.67	1.45	1.56
7	1.20	2.13	0.03	0.99
8	0.87	1.39	0.10	0.26

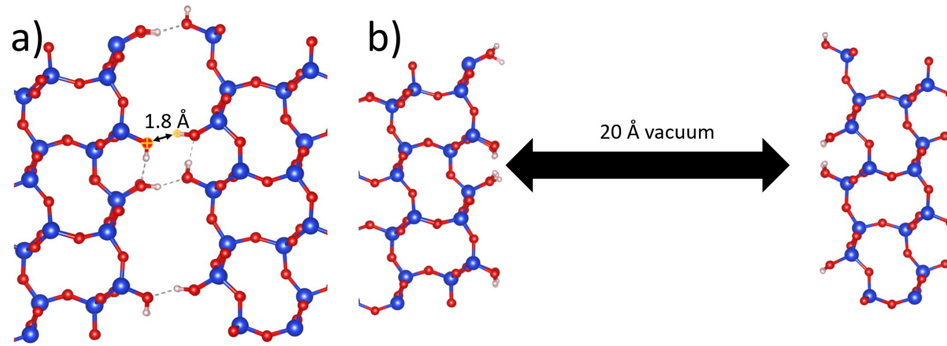

Figure 6.13: a) shows the α-cristobalite (202) grain boundary. b) shows the α-cristobalite (202) column boundary generated with a 20 Å vacuum between each α-cristobalite (202) surface.

6.3.7 Ag in Grain and Column Boundaries

In the previous section and across literature, it is suggested that metal diffusion is facilitated by GB and CB. In this regard, the incorporation and diffusion of Ag^0 and Ag^{+1} in CB and GB were modelled using a hydroxylated α-cristobalite (202) surface slab. The methods used to generate the CB and GB models are discussed in section 6.2.2 and can be seen on Fig. 6.13. To sample Ag incorporation in GB and CB, a grid based method was employed as described in section 6.2.3.1). A 2 Å grid was created across each boundary from the surface through to the α-cristobalite bulk. Subsequently, each grid point was removed if there was an α-cristobalite atom within 1.33 Å. The remaining grid points were used as starting positions for Ag interstitials and the geometries were optimised in the $q = 0$, +1-charge states.

Fig. 6.14 shows the incorporation energy of Ag^0 and Ag^{+1} as a function of distance from the GB and CB surfaces into the bulk (Ag chemical potential taken from Ag_2O). In the bulk, Ag^0 and Ag^{+1} each fill one type of interstitial site, with the 0.1 eV variations in energy at each distance being an artefact of the geometry optimisation and local variations in geometry. As the Ag species reach the surface of the boundaries the incorporation energy reduces. In the case of Ag^0, the bulk incorporation energy of 3.1 eV reduces to 1.8 eV and 2.0 eV for the GB and CB respectively. The lower incorporation energy of Ag in the GB is associated with an increased interaction between Ag^0 and both α-cristobalite surfaces. In the case of Ag^0, Ag interstitials maintain the same z heights in the GB and CB respectively.

Conversely, Ag^{+1} in the CB is a mean of 1 Å closer to the α-cristobalite surface than in the GB. The incorporation energies for Ag^{+1} on Fig. 6.14 are zeroed, where the difference between each interstitial site found and the lowest energy site is given. This allows the Ag sites to be directly compared to the low energy sites found at the GB and CB respectively. From Fig. 6.14 it can be seen that the incorporation energy of Ag^{+1} is 0.7 eV and 0.5 eV lower in GB and CB, respectively.

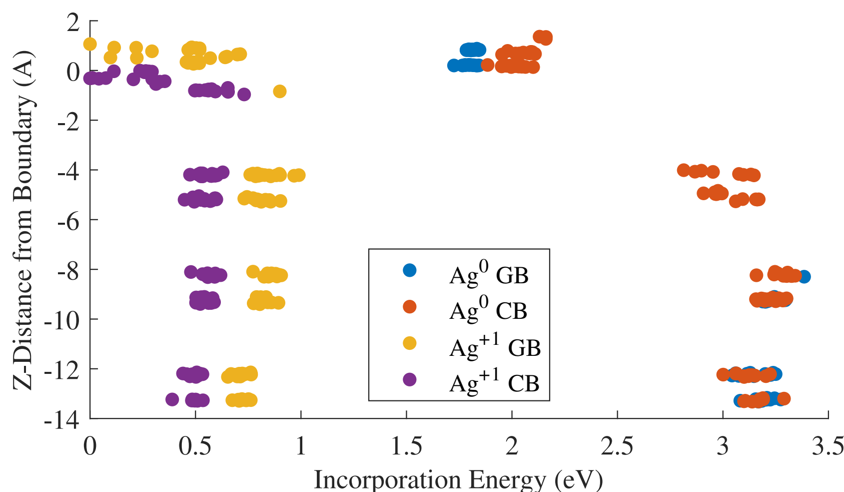

Figure 6.14: Plot showing the incorporation energy of Ag^0 and Ag^{+1} in the α-cristobalite grain and column boundaries. Z = 0 represents the surface of the boundaries and negative Z values represent Ag incorporation towards the α-cristobalite bulk.

The calculated incorporation energies suggest that there is a strong thermodynamic driver for Ag to reside the GB and CB over the bulk. From this it can be inferred that Ag may incorporate more easily into the GB and CB respectively. However, developing a direct DFT model for Ag to incorporate into GB and GB is beyond the scope of this investigation. Instead, the diffusion characteristics for Ag^0 and Ag^{+1} were modelled in GB and CB using CI-NEB calculations. In each case, three CI-NEB calculations were made to model Ag diffusion along the boundaries. The results in Table 6.2 show that the diffusion barriers for both Ag^0 and Ag^{+1} are very low along GB and CB. Barriers of 0.1 eV for Ag^0 in the GB and CB suggest that Ag^0 will be extremely mobile. The barriers for Ag^{+1} diffusion are 0.2 eV suggest Ag^{+1} is also very mobile, though surprising less so than Ag^0. This is a result of Ag^{+1} forming interactions with surface O which need to be overcome.

Table 6.2: Table showing the diffusion barriers of Ag^0 and Ag^{+1} in the α-cristobalite grain and column boundaries

Charge state	Grain Boundary (eV)	Column Boundary (eV)
Ag^0	-0.10	-0.15
	-0.07	-0.05
	-0.10	-0.09
Ag^{+1}	-0.22	-0.20
	-0.62	-0.20
	-0.21	-0.37

6.3.8 V_O mediated Ag^{+1} reduction in a-SiO_2

The O vacancy was shown to facilitate the reduction of Ag^{+1} ions in α-quartz in chapter 5. To this end, the interaction of Ag^{+1} with the neutral O vacancy ($V_O{}^0$), which is favoured at the Ag and Pt Fermi energies, was studied. The Ag/V_O interaction was initially tested using two methods for 10 vacancy sites. In the first instance, Ag was placed centrally between the two Si atoms involved in the vacancy and the geometry was relaxed in the q = 0, +1-charge states. In the second method, Ag was added in various void positions within 3 Å from the vacancy and the geometry was relaxed in the q = 0, +1-charge states. For each of the 10 vacancy sites, the lowest energy configurations were found using the first method. For 8 out of 10 sites in each charge state, the same local minima were found by placing Ag in a void area. As a result, and to save sampling multiple sites in voids near the vacancy, Ag/V_O was calculated for all 144 vacancy sites in the 216-atom cell by inserting Ag between the two Si atoms in the vacancy and relaxing the geometry in the q = 0, +1-charge states.

The results show that Ag^{+1} relaxes into a void near the vacancy for all sites upon geometry optimisation. Of the 144 sites sampled, a $[Ag/V_O]^{+1}$ complex was formed in 117 cases (Fig. 6.15), where charge is donated from the two Si atoms in the vacancy to Ag^{+1}. Mulliken charge analysis of the $[Ag/V_O]^{+1}$ defects show near total neutralisation of Ag^{+1}, with a mean Ag charge of 0.15 $|e|$ compared to 0.77 $|e|$ for the 27 sites where a Ag^{+1} interstitial was formed. Additional charge donation from neighbouring O in the lattice was observed (Fig. 6.15b), further reducing the Ag^{+1} charge in $[Ag/V_O]^{+1}$ complexes to as low as -0.09 $|e|$. Interestingly, a strong

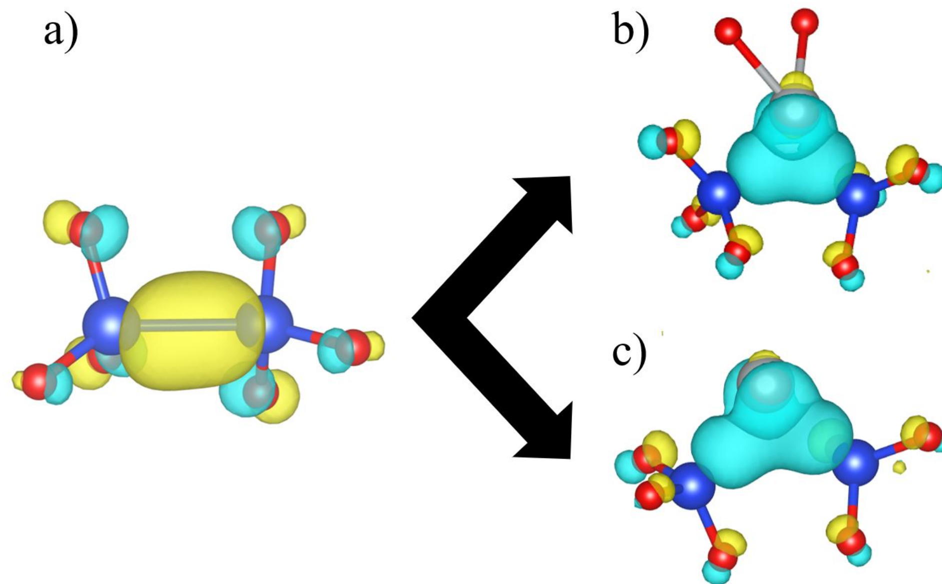

Figure 6.15: Schematic showing the HOMO state of the V_O and $[Ag/V_O]^{+1}$ defect. The silver, blue and red spheres correspond to Ag, Si and O atoms, respectively. The positive and negative charge density are shown as blue and yellow iso-surfaces, respectively, at a value of ± 0.07. a) Neutral V_O, with the HOMO state residing on the two Si atoms involved in the vacancy. b) and c) show the $[Ag/V_O]^{+1}$ defect with b) additionally showing the interaction between $[Ag/V_O]^{+1}$ defect and proximate O atoms. In both configurations of $[Ag/V_O]^{+1}$ charge density is donated from Si to Ag.

correlation was observed between the Si-Si bond length and the propensity for the vacancy to trap Ag^{+1}. Of the 74 vacancies with a Si-Si bond length below 2.46 Å, 64% formed a $[Ag/V_O]^{+1}$ complex compared to 100% of the 70 sites with a Si-Si bond length $>$ 2.46 Å. This can be understood by the charge donation from the Si double bond to Ag^{+1}, which results in the Si-Si bond length to increase from a mean of 2.41 Å to 2.83 Å.

For the 117 $[Ag/V_O]^{+1}$ complexes calculated, a binding energy was determined between Ag^{+1} and V_O using two methods. The first method (M1) involves placing Ag^{+1} in the lowest energy interstitial site of the cell where it is not interacting with the vacancy and relaxing the geometry of the whole system. Using this method, the binding energy is defined as the energy difference between Ag^{+1} in the lowest energy interstitial site and that of the $[Ag/V_O]^{+1}$ complex. A positive binding energy in this case suggests that $[Ag/V_O]^{+1}$ is the lowest energy configuration available in the cell. As such, the results give the lowest bound of the binding en-

ergy. From this, 23% of vacancy sites were found to give a positive binding energy with the distribution of binding energies shown on Fig. 6.16. The second method (M2) involves placing Ag^{+1} in a void 5 Å from the vacancy and relaxing the geometry. To do this, the lowest coordinated position 5 Å away from each vacancy was selected to allow a thermodynamic approach to determine the binding energy. This is because a strong correlation is found between the incorporation energy and the coordination number of Ag^{+1}. Therefore, the site with the lowest coordination is assumed to give the most thermodynamically accessible site for Ag^{+1} near the vacancy. To determine this site, a 0.25 Å mesh was created across the 216-atom cell and the coordination number of each point in the mesh was calculated. Ag was then inserted to the mesh point with the lowest coordination number 4.8 - 5.2 Å from the centre of the two Si atoms in the vacancy and the geometry was relaxed in the $q = +1$-charge state. The binding energy was calculated as the energy difference between the Ag^{+1} in the relaxed interstitial site 5 Å from the vacancy and that of the $[Ag/V_O]^{+1}$ complex. Using this method, a positive binding energy suggests that a Ag^{+1} ion in proximity to a vacancy will have a direct thermodynamic drive to bind to the vacancy. A positive binding energy was found for 38% of vacancies using this method with the distribution of binding energies shown in Fig. 6.16.

Fig. 6.17 shows the (+1/0) charge transition level positions for the 117 $[Ag/V_O]$ complexes. Due to the higher Fermi energy position of Ag, a larger number $[Ag/V_O]^{+1}$ complexes are favoured to trap electrons at the Ag (69%) electrode compared to Pt (17%). However, for a vacancy to act as a Ag^{+1} reduction site, it must meet two criteria. Firstly, Ag must first have a positive binding energy to the vacancy, and secondly, the $[Ag/V_O]^{+1}$ site must be favoured to trap an electron relative to the Fermi energy of the proximate electrode. From Table 6.3, it can been seen that 33% and 11% of vacancy sites meet these criteria at the Ag and Pt electrodes, respectively. It can be seen that the limiting factor for whether a V_O will act as a reduction site is the binding energy of Ag^{+1} to V_O.

These results are consistent with the observations made during *in situ* measurements of the $Ag/SiO_2/Pt$ devices [11, 10, 12]. A feature observed in the devices

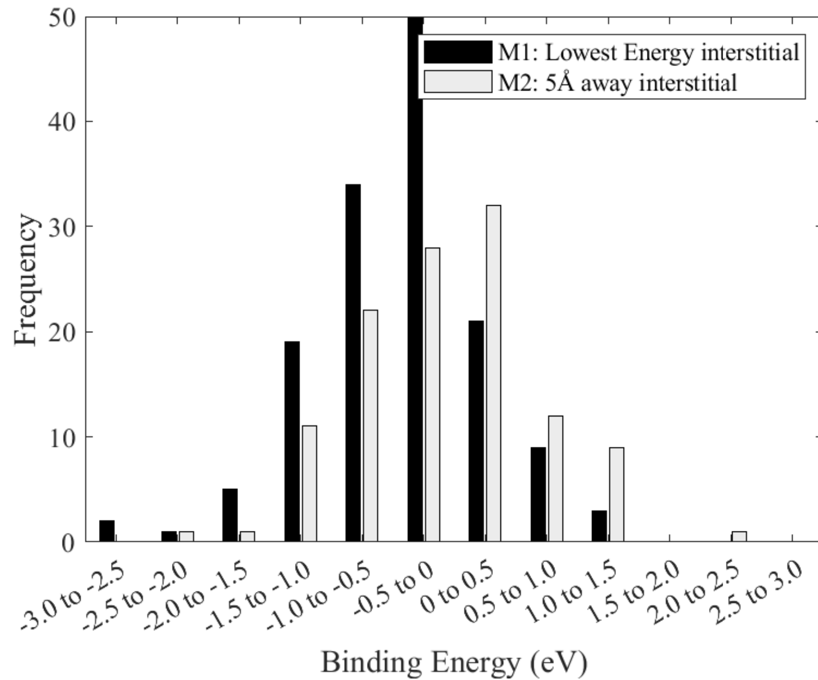

Figure 6.16: The distribution of Ag^{+1} to V_O binding energies using the lowest energy interstitial method and the interstitial 5 Å away method.

during electroforming is that the thinnest part of the filament was located at the Pt electrode. The filament then widens with the thickest part located at the Ag electrode. This can be used as an indication of the Ag^{+1} reduction rates at either electrode, where a low reduction rate regime occurs at the Pt electrode, and a higher reduction rate regime occurs at the Ag electrode. Though suggested in the literature to be due to thermal heating, this is also explained by the Fermi energy positions of the electrodes where there is an increase in the percentage of O vacancies able to act as Ag reduction sites [124]. It should be noted, however, that the direct probing of the vacancy mediated reduction mechanism is difficult due to the atomic scale of the interaction. Indirect testing may be possible in devices by controlling the O vacancy concentration in the oxide. This could be by either applying a negative bias to generate vacancies, as seen in the VCM mechanism, or by growing a-SiO_x layers with different concentrations of O vacancies. By doing this, it would then be expected that *in situ* stressing of the devices would display a shift from a low reduction rate regime to a high reduction rate regime as the concentration of O vacancies

increases, in turn changing the characteristic of the conductive filament.

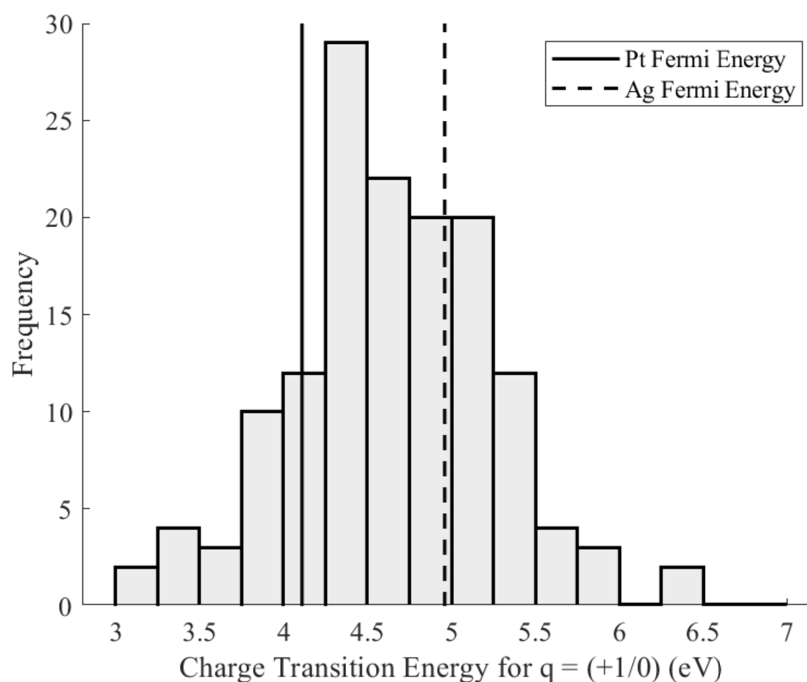

Figure 6.17: Histogram showing the distribution of the q = (+1/0) charge transition Fermi energy positions of the 144 [Ag/V_O] complexes sampled.

Table 6.3: Table showing the number of vacancy sites that will act as Ag reduction sites.

	Interstitial site (M1)	5 Å away (M2)
Non-interacting Ag^{+1} ions	19%	19%
Positive Ag^{+1} to V_O binding energy	22%	38%
V_O reduction sites at Ag	20%	33%
V_O reduction sites at Pt	10%	11%

6.3.8.1 Thermodynamics of $[Ag/Vo]^{+1}$ formation

To determine whether oxygen vacancies will act as a Ag^{+1} reduction site, Ag^{+1} must stay bound to the V_O once a $[Ag/V_O]^{+1}$ complex is formed. For this to occur, the barrier for Ag^{+1} to bind to V_O must be thermodynamically accessible, while the barrier for Ag^{+1} to leave the $[Ag/V_O]^{+1}$ complex must be high. In this way, Ag is prevented from moving on to the another site. Therefore, CI-NEB calculations were carried out to determine the barrier for Ag^{+1} to bind to V_O (forward barrier) and the barrier for Ag^{+1} to leave the $[Ag/V_O]^{+1}$ complex (reverse barrier) for five V_O sites.

Each of the five sites met the reduction site criteria at the Pt Fermi energy, namely sites giving a positive Ag^{+1} to V_O binding energy with the resulting $[Ag/V_O]^{+1}$ complex favoured to trap an electron at the Pt Fermi energy. From this, forward barriers of 0.16, 0.60, 0.39, 0.42 and 0.25 eV, and reverse barriers of 1.22, 1.53, 1.15, 1.76 and 1.40 eV, respectively, were found. The relatively low barriers for Ag^{+1} to bind to the vacancy and barriers over 1 eV to overcome for Ag^{+1} to escape from the vacancy suggest the V_O sites will act as Ag^{+1} traps.

To further assess the stability of $[Ag/V_O]$ complexes, DFT molecular dynamics simulations were run in CP2K with the PBE functional for a $[Ag/V_O]^0$ and $[Ag/V_O]^{+1}$ complex for 20 ps at 1000 K. In both charge states, Ag remained bound to the vacancy maintaining a bond length of 2.2 - 2.8 Å to the Si atoms involved in the vacancy thus highlighting the stability of the complex at high temperatures. During the switching process, self-heating of the device is thought to cause the dissolution of Ag clusters in the reset process. Though it is unclear what impact this self-heating will have on larger clusters, $[Ag/V_O]$ will remain intact, potentially serving as a nucleation site for the formation of a Ag cluster in the set process.

6.4 Summary of Main Results

6.4.1 Ag Incorporation and Migration in a-SiO_2

A model of the Ag/SiO_2 interface was developed through building a metallic Ag cluster on an α-cristobalite (202) surface. From this, the incorporation of Ag into SiO_2 was modelled directly giving an incorporation barrier of 3.41 eV and an incorporation energy of 2.87 eV. Mulliken charge analysis shows that as Ag passes through the SiO_2 surface it is in the +1-charge state, relaxing to the equivalent bulk Ag^{+1} interstitial site. Interestingly, the high forward barrier (3.41 eV) and low reverse barrier (0.55 eV) suggests it is more likely for Ag^{+1} to leave SiO_2 to bind to a Ag cluster or potentially the Ag electrode than be incorporated. Calculations for the second Ag incorporation show a forward barrier of 2.70 eV, with a reverse barrier of 0.72 eV with an incorporation energy of 1.98 eV. The low reverse barriers and high incorporation energies show that steric crowding in SiO_2 is the bottleneck

for Ag incorporation in devices. It can be inferred that Ag may only incorporate into regions of low density in a-SiO_2. This is supported by calculations for Ag^0 and Ag^{+1} in the α-cristobalite GB and CB, where in each case the incorporation energy was lower. For Ag^0, the bulk incorporation energy of 3.1 eV reduces to 1.8 eV and 2.0 eV for the GB and CB, respectively. Similarly, the incorporation energy of Ag^{+1} is 0.7 eV and 0.5 eV lower in GB and CB, respectively.

Once incorporated, the Ag^{+1} ion is the most stable charge state at the Fermi energy of Ag and Pt with the mean (+1/0) transition at 5.25 eV. Analysis of the Ag^{+1} interstitial sites calculated shows a preference for Ag^{+1} to be in voids, where every ion relaxes to minimise the distance to nearby O atoms in the void upon optimisation. CI-NEB calculations show Ag^{+1} can be mobile in a-SiO_2, with barriers of 0.1 - 0.2 eV through large rings. Results show the diffusion barriers of Ag^{+1} are lower than Ag^0 for a given ring size, with each barrier decreasing with increasing ring size showing that transport is determined by the steric environment. The diffusion characteristics for Ag^0 and Ag^{+1} were also modelled in GB and CB. From this, barriers of 0.1 eV for Ag^0 in the GB and CB were found suggesting that Ag^0 will be extremely mobile. The barriers for Ag^{+1} diffusion are 0.2 eV suggesting Ag^{+1} is also very mobile, though surprising less so than Ag^0 due to the interaction between Ag^{+1} and surface O. These observations are in good agreement with *in situ* TEM measurements of Ag-SiO_2-Pt devices, where sputtered a-SiO_2 layers, which are known to contain high concentrations of GBs and CBs, show clustering at the Pt electrodes as a result of high Ag mobility. Conversely, thermal a-SiO_2 layers show clustering at the Ag electrode due low Ag mobility, where the transport is comparable to the diffusion calculations made in the a-SiO_2 bulk.

6.4.2 O vacancy mediated Ag^{+1} reduction

The results in this chapter show that the Ag_2^{+2} dimer will not form due to the electrostatic repulsion of Ag^{+1} ions. Therefore, the interaction between Ag and V_O was studied for its potential to mediate Ag^{+1} reduction, as seen in α-quartz. For V_O to mediate Ag^{+1} reduction, Ag^{+1} ions must bind to V_O with a positive binding energy, and the resulting $[Ag/V_O]^{+1}$ must be favoured to trap an electron relative to

the Fermi energy of the proximate electrode.

Of the 144 sites V_O sites available in the cell, a $[Ag/V_O]^{+1}$ complex was formed in 117 cases, where near total neutralisation of Ag^{+1} occurred through charge transfer from the Si atoms in the vacancy to Ag. The a-SiO_2 cell used was selected as it has the mean density of the 30 cells produced and as such, is expected the number of $[Ag/V_O]^{+1}$ complexes formed well represents the parent population. From these, a binding energy was determined between Ag^{+1} and V_O using two methods. With this in consideration, in the first method, the binding energy is defined as the energy difference between Ag^{+1} in the lowest energy interstitial site in the cell and that of the $[Ag/V_O]^{+1}$ complex. From this, 23% of V_O sites gave a positive binding energy, where a positive binding energy shows that the $[Ag/V_O]^{+1}$ complex is the lowest energy configuration possible. In the second method, the binding energy is calculated as the energy difference between the Ag^{+1} in an interstitial site 5 Å from the vacancy and that of the $[Ag/V_O]^{+1}$ complex giving a positive binding energy 38% of vacancy sites. From this, it is expected that Ag^{+1} will approach and bind to 38 % of vacancy sites in a-SiO_2.

To determine whether V_O will act as a Ag^{+1} reduction site, Ag^{+1} must also stay bound to the V_O once a $[Ag/V_O]^{+1}$ complex is formed. CI-NEB calculations for five V_O sites show the barrier for Ag^{+1} to bind to V_O (0.16, 0.60, 0.39, 0.42 and 0.25 eV) is thermodynamically accessible whilst and the barrier for Ag^{+1} to leave the $[Ag/V_O]^{+1}$ complex (1.22, 1.53, 1.15, 1.76 and 1.40 eV) are comparatively very high. This suggests that V_O sites will act as Ag^{+1} traps. To further assess the stability of $[Ag/V_O]$ in Ag/a-SiO_2/Pt devices, *ab initio* molecular dynamics simulations were run for $[Ag/V_O]^0$ and $[Ag/V_O]^{+1}$ at 1000 K. In both charge states, Ag remained bound to V_O further demonstrating the trapping ability of V_O.

Due to the higher Fermi energy position of Ag, a larger number $[Ag/V_O]^{+1}$ complexes were found to trap electrons at the Ag (69%) electrode compared to Pt (17%). From this, was found that 33% and 11% of V_O sites meet the criteria for Ag^{+1} reduction at the Ag and Pt electrodes respectively.The limiting factor for whether a V_O will act as a reduction site is determined to be the binding energy of

Ag^{+1} to V_O.

6.5 Conclusion

The mechanisms involved in the electroforming process in Ag-SiO_2-Pt RRAM devices have been studied using DFT. Models of the Ag/SiO_2 interface developed with a metallic Ag cluster on an α-cristobalite (202) surface indicate that Ag incorporates into SiO_2 as a positive ion. However, the high forward barrier (3.41 eV) and low reverse barrier (0.55 eV) suggests the steric crowding in SiO_2 limits Ag+ incorporation. Instead, Ag may only incorporate into regions of low density in a-SiO_2. This is supported by calculations for Ag^0 and Ag^{+1} in the α-cristobalite GB and CB, where the incorporation energies are 0.5 to 1.2 eV lower. Once incorporated into a-SiO_2, the Ag^{+1} ion is the most stable charge state at the Fermi energy of Ag and Pt. Results show Ag^{+1} is the more mobile species in a-SiO_2, with the diffusion barriers of Ag^{+1} lower than Ag^0 for a given ring size, giving adiabatic diffusion barriers between 0.1 - 0.2 eV through large rings. Furthermore, both Ag^0 and Ag^{+1} were were found to be very mobile in α-cristobalite GB and CB with barriers of between 0.1 - 0.2 eV. This is in strong correlation with experiment, with sputtered a-SiO_2 layers known to have high concentrations of GB and CB having high Ag mobility.

With Ag^{+1} favoured at each electrode and calculations showing ions repel, the interaction between Ag and V_O was studied. In this process, Ag^{+1} traps at some V_O with small forward (binding) and large reverse (unbinding) barriers. From this, 33% and 11% of V_O were found act as Ag^{+1} reduction sites at the Ag and Pt electrodes, respectively. To meet the reduction site criteria, Ag^{+1} must bind to V_O with a positive binding energy, then be favoured to trap an electron at the respective Fermi energy.

Chapter 7

Ag Clustering in $a\text{-}SiO_2$

7.1 Introduction

In the previous chapter, the incorporation, diffusion and reduction of Ag in $a\text{-}SiO_2$ was modelled. From this, an O vacancy (V_O) mediated Ag^{+1} reduction mechanism was presented showing 33% and 11% of V_O sites act to reduce Ag^{+1} at the Ag and Pt Fermi energies, respectively. In this chapter, the work is continued through the modelling of Ag cluster nucleation at the V_O sites. This begins with a study on Ag^{+1} ions binding to the $[Ag/V_O]$ complex, and whether the subsequent $[Ag_i/V_O]^j$ complexes are favoured to trap electrons. In this way, 10 atom Ag clusters are developed at three V_O sites and discussed. Subsequently, the Ag clustering mechanism is studied in more depth at one V_O, where up to a 15 atom cluster is developed. In this case, CI-NEB calculations and molecular dynamics simulations are employed to model how the $a\text{-}SiO_2$ lattice compensates for the strain induced by the clusters. Additionally, the breakdown of the lattice around the cluster is studied, as well as the effect of electron injection.

7.2 Theoretical Methodology

The optimal DFT parameters determined in section 5.4.1 are used for all calculations in this chapter, unless otherwise stated. This includes the use of the Gaussian Plane Wave method (GPW) in the CP2K code, with the plane wave cut-off and relative cut-off set to 600 Ry and 40 Ry, respectively, and a convergence criterion of

$1x10^{-6}$ eV per formula unit. The double zeta valence polarised (DZVP) molecularly optimised (MOLOPT) basis sets and Goedecker-Teter-Hutter (GTH) pseudopotentials are also used with the PBE0_TC_LRC functional with an exchange term truncated at 2 Å. The auxiliary density matrix method (ADMM) is used to reduce computational cost of calculating the non-local exchange integrals.

The Ag clustering mechanisms were studied using the same a-SiO_2 cell that was used in the previous chapter. This cell was selected as it had the density closest to the mean density of the 30 cells developed in this study. The diffusion characteristics of Ag in SiO_2 were modelled using CI-NEB calculations described in section 2.3.2, each with spring constant of 4.86 eVÅ^2 and 5 replica images unless otherwise stated.

The *ab initio* MD simulations were carried out with the PBE functional to reduce computation expense. Calculations using the PBE functional were found to give similar defect formation energies as the hybrid calculations, whilst the bandgap is large enough to prevent the delocalisation of the defect states. A fixed volume NVT ensemble [56] is used along with a Nose-Hoover thermostat (see section 2.4.3) [57]. The volume was kept constant to best model experimental conditions, where the expansion of the a-SiO_2 layer in the devices of interest is constrained by the metal electrodes. Simulations are also run with a 1 fs time step, which was tested to ensure that the time step was large enough to reduce computational expense whilst small enough to keep the energy, pressure and temperature values stable. In a similar fashion, the Nose-Hoover thermostat was selected to update every 10 time steps to ensure stable temperature, with higher values causing large fluctuations in temperature.

7.3 Results

7.3.1 V_O mediated Ag cluster nucleation mechanism

The mechanism by which Ag clusters can grow at vacancy sites is presented in Fig. 7.1. Once a Ag^{+1} binds to a vacancy to form a $[Ag/V_O]^{+1}$ complex (Fig. 7.1b), the complex traps an electron to form a neutral $[Ag/V_O]^0$ complex (Fig. 7.1c). A

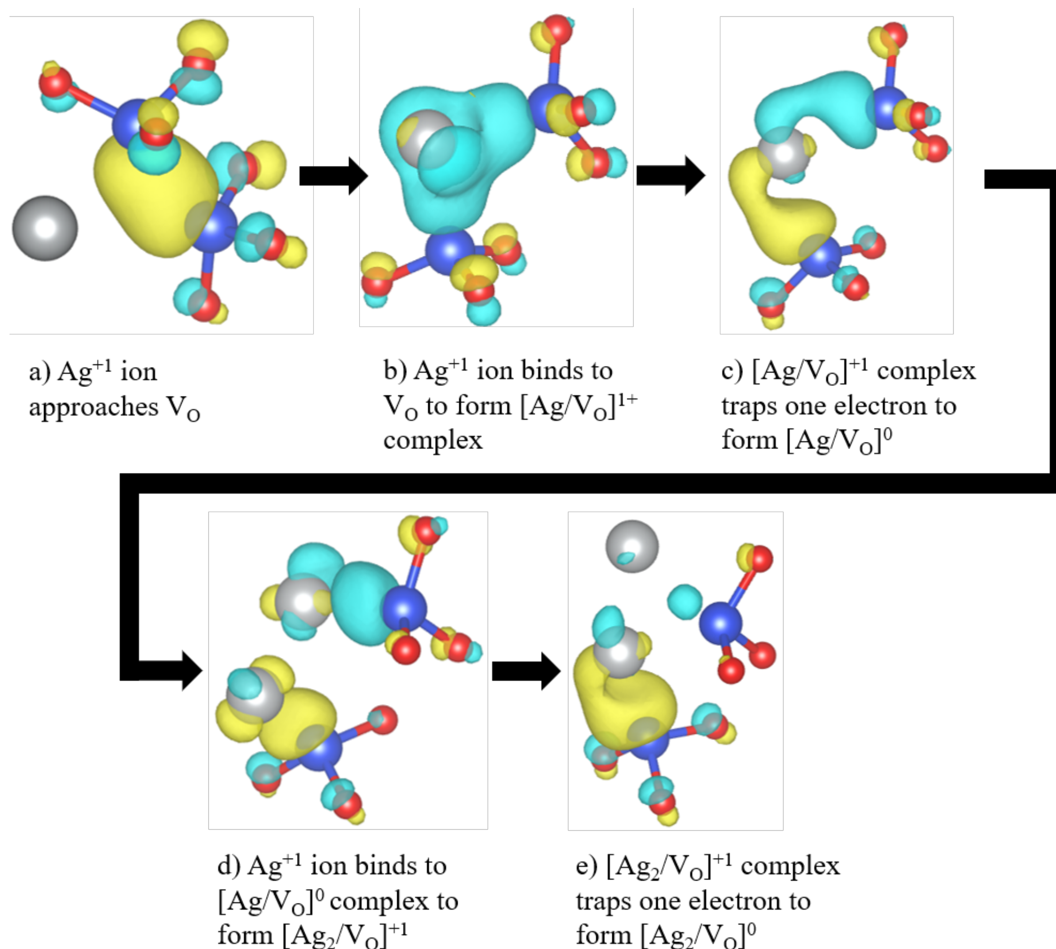

Figure 7.1: Schematic showing the mechanism of initial stages of Ag clustering in O vacancies. V_O acts as a Ag^{+1} reduction site and subsequent cluster nucleation site. The silver, blue and red spheres correspond to Ag, Si and O atoms, respectively. The positive and negative charge density are shown as blue and yellow iso-surfaces respectively at a value of ± 0.07.

second Ag^{+1} ion then approaches the $[Ag/V_O]^0$ complex giving $[Ag_2/V_O]^{+1}$ (Fig. 7.1d). $[Ag_2/V_O]^{+1}$ then traps an electron to form $[Ag_2/V_O]^0$ (Fig. 7.1e).

Subsequently, CI-NEB calculations were run to determine whether a second Ag^{+1} ion binds to a $[Ag/V_O]$ complex, with results shown in Table. 7.2. From this, the low forward barriers and high reverse barriers suggest that the second Ag^{+1} will also trap to the complex. In each case, the resulting $[Ag_2/V_O]^{+1}$ is favoured to trap an electron at the Ag and Pt Fermi energies.

To study the cluster nucleation process further, one V_O site was selected and the process of adding ions and trapping electrons was continued. From Table. 7.2

Table 7.1: The results of CI-NEB calculations for a Ag^{+1} ion to bind to five different $[Ag/V_O]^0$ complexes. Negative values correspond to images lower in energy (more energetically favoured). In each case, image 1 represents the Ag^{+1} ion 5 Å from the vacancy complex. The values in image 5 represent the binding energy of the Ag^{+1} ion to the vacancy complex.

	Energy of image in band (eV):				
	1	2	3	4	5
$[Ag/V_{O1}] + Ag^{+1} \rightarrow [Ag_2/V_{O1}]^{+1}$	0	0.29	-0.19	-0.43	-0.75
$[Ag/V_{O2}] + Ag^{+1} \rightarrow [Ag_2/V_{O2}]^{+1}$	0	0.01	0.22	-0.20	-0.46
$[Ag/V_{O3}] + Ag^{+1} \rightarrow [Ag_2/V_{O3}]^{+1}$	0	0.03	-0.29	-0.34	-0.32
$[Ag/V_{O4}] + Ag^{+1} \rightarrow [Ag_2/V_{O4}]^{+1}$	0	0.10	-0.50	-0.58	-0.77
$[Ag/V_{O5}] + Ag^{+1} \rightarrow [Ag_2/V_{O5}]^{+1}$	0	0.17	-0.82	-0.52	-1.05

Table 7.2: The results of CI-NEB calculations for Ag^{+1} ions to cluster at one $Ag_2/V_O]^0$ complex. Negative values correspond to images lower in energy (more energetically favoured). In each case, image 1 represents the Ag^{+1} ion 5 Å from the vacancy complex. The values in image 5 represent the binding energy of the Ag^{+1} ion to the vacancy complex .

	Energy of image in band (eV):				
	1	2	3	4	5
$[Ag_2/V_O]^{+1} + e^- \rightarrow [Ag_2/V_O]^0$	e^- trap at E_F = 3.60 eV				
$[Ag_2/V_O]^0 + Ag^{+1} \rightarrow [Ag_3/V_O]^{+1}$	0	0.34	-0.33	-0.36	-0.48
$[Ag_3/V_O]^{+1} + Ag^{+1} \rightarrow [Ag_4/V_O]^{+2}$	0	0.38	-0.03	-0.56	-1.09
$[Ag_4/V_O]^{+2} + 2e^- \rightarrow [Ag_4/V_O]^0$	e^- trap at E_F = 3.96 eV				
$[Ag_4/V_O]^0 + Ag^{+1} \rightarrow [Ag_5/V_O]^{+1}$	0	-0.03	-0.4	-0.88	-0.97

we see that the $[Ag_2/V_O]^{+1}$ complex for this site is favoured to trap an electron at 3.60 eV giving $[Ag_2/V_O]^0$ at both electrodes, with a structural relaxation energy of 1.08 eV. Adding a third Ag^{+1} to the system and running a CI-NEB gives a forward barrier of 0.34 eV and binding energy of 0.48 eV. In this case the $[Ag_3/V_O]^{+1}$ complex is favoured to trap an electron at a Fermi energy of 4.4 eV. As such, this complex would remain positive at the Pt electrode, but would trap an electron to form $[Ag_3/V_O]^0$ at the Ag electrode. A barrier of 0.38 eV and binding energy of 1.09 eV were then calculated for the formation of a $[Ag_4/V_O]^{+2}$ complex, which was favoured to trap two electrons at 3.96 eV, suggesting the neutral $[Ag_4/V_O]^0$ complex is favoured at both the Pt and Ag Fermi energies. The formation of the $[Ag_5/V_O]^{+1}$ complex was found to be a barrier-less process with a binding energy of 0.97 eV. From these calculations it is clear that the barriers for Ag^{+1} ions to bind

with the vacancy complexes are relatively low, with high binding energies. This provides a strong thermodynamic driver for the clustering process.

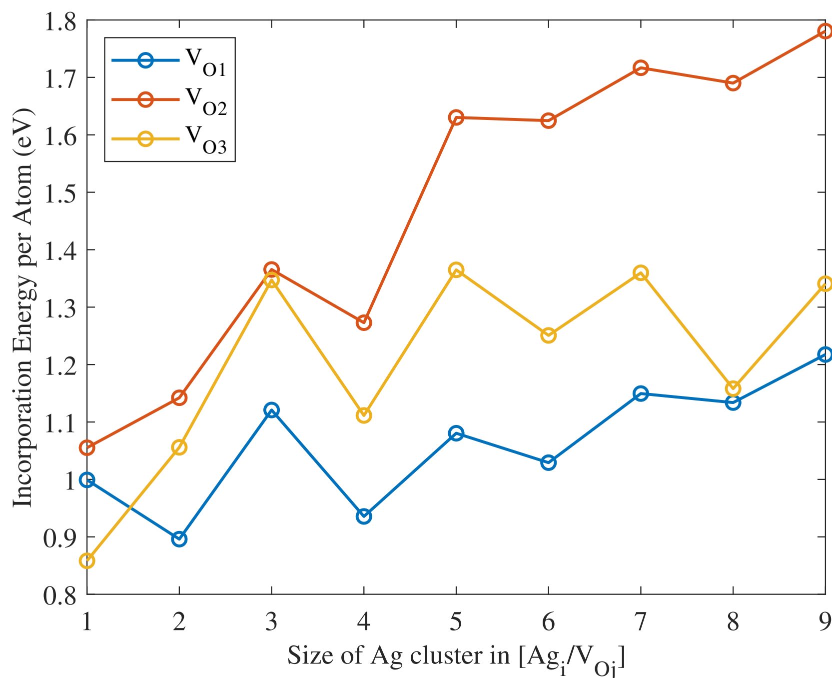

Figure 7.2: Graph showing the incorporation energy per atom of Ag clusters up to 9 atoms at 3 vacancy sites.

Using the same methodology of adding Ag^{+1} ions and trapping electrons, clusters at three V_O sites were produced to determine the incorporation energy per atom for [Ag_i/V_O] complexes for i = $1 \leq i \leq 9$ (Fig. 7.2). This was achieved by adding one Ag^{+1} ion at a time to [Ag_i/V_O] and optimising the geometry. Three methods were tested for Ag^{+1} ion insertion, where in the first, Ag^{+1} was inserted into void positions within 3 Å of the Ag cluster. In the second method, Ag^{+1} was added to the centre of the two Si atoms involved in the V_O and in the final method, Ag^{+1} was inserted to the centroid of the Ag cluster. For small clusters, adding Ag^{+1} to the centroid of the Ag cluster gave lower energy configurations, and for large clusters adding Ag^{+1} in voids close to the cluster gave lower energy configurations. The data presented in Fig. 7.2 are given for Ag^{+1} ions added in voids near the Ag cluster as this is most representative of the configurations to occur during cluster nucleation. Results show that the incorporation energy per Ag atom increases with

the size of the cluster. However, a large jump was not observed, suggesting that the clustering of Ag is energetically favourable up to 9 atoms. In this case a large jump or spike would relate to excessive strain in the lattice, potentially requiring the relaxation of the lattice parameters. It should be noted that some characteristic trends are seen such as a spike in incorporation energy for 3 atom clusters, corresponding to the low binding of Ag_3. A reduction is seen for Ag_4 clusters due to their higher stability.

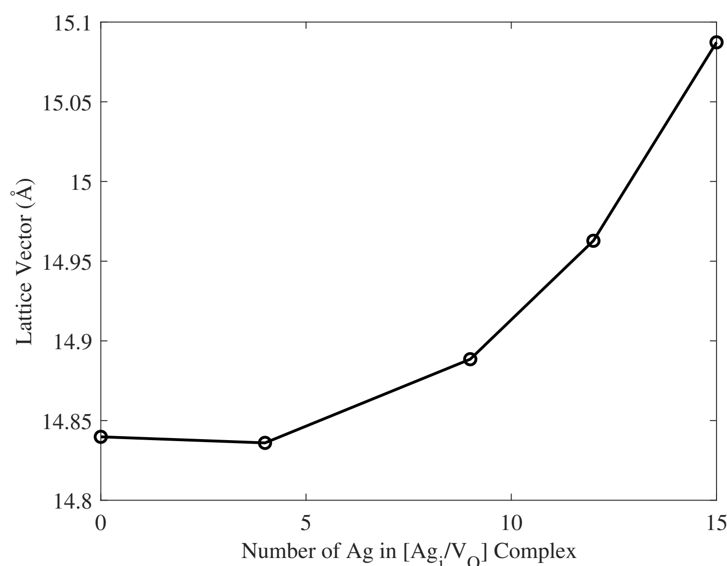

Figure 7.3: Graph showing the CP2K cell optimised relaxed lattice vector as a function of Ag cluster size.

As the Ag cluster grows larger, strain is expected to be induced into the lattice. This process can be very problematic in DFT due to the periodic nature of the calculations. As the strain increases from incorporating more Ag^{+1} ions, the cell is expected to impart strain onto its periodic neighbours, potentially skewing the results. To test these effects, the structures containing [Ag_i/V_O] complexes for i = 0, 3, 6, 9, 12 and 15 at one vacancy site were cell optimised, with the results shown on Fig. 7.3. A cell optimisation removes the constraint of volume thus allowing strain to be released as the lattice expands. The results show an exponential response, where up to 9 atoms, the lattice parameter is changed by only 3%. However, as the cluster grows to 15 atoms, the rate of expansion increases significantly. From

this we can expect that, for the specific V_O site and void, a 9 atom cluster can be incorporated without a large amount of strain induced.

To model the different morphologies of Ag clusters that can exist in a-SiO_2, a simulated anneal of a [Ag_9/V_O] complex was carried out. In this process *ab initio* molecular dynamics simulations were run for the [Ag_9/V_O] complex at 500 and 1000 K, as described in section 6.2.3 for 30 ps. For each temperature, the structure at every picosecond was extracted from the molecular dynamics simulation and cooled using a DFT geometry optimisation (Fig. 7.4a). Using these cooled geometries, static energy calculations were made for the isolated a-SiO_2 cells with the Ag_9 clusters removed (Fig. 7.4b) and the isolated Ag_9 clusters in vacuum (Fig. 7.4c) at every picosecond. The strain induced in the lattice can then be examined by comparing the energy difference between the isolated lattice at every picosecond to the t = 0 case. Similarly, the energy of the isolated Ag_9 clusters competed to the t = 0 Ag_9 energy shows whether the cluster finds new minima.

During the simulations, reorganisation of the Ag_9 cluster in the lattice occurred at 500 K though only negligible changes in the energy of the Ag_9 cluster were found (Fig. 7.4). At 1000 K, the changes in the morphology were more significant than in the 500 K simulation. Interestingly, the lowest energy Ag_9 cluster was only 0.13 eV lower in energy than the original cluster Ag_9 cluster (found at 1000 K). This suggests that the clusters developed by adding Ag^{+1} ions in voids are stable and energetically favourable. Furthermore, although the barrier for Ag_9 to change morphology in a-SiO_2 can be overcome at 1000 K within 1 ps simulation, there is little thermodynamic driver for this as the different structures have similar energies. Perhaps a more interesting observation is that energy of the isolated a-SiO_2 lattice at every picosecond shows significant variations at 1000 K (up to 5.5 eV). This suggests that a large amount of strain is induced in the lattice, but it is compensated by the interaction of the lattice with the Ag_9 cluster. Analysis comparing the 500 K and 1000 K simulations show that a Si-O tetrahedral rotation occurs at 1000 K signifying the largest difference between the simulations. By comparing the DFT cooled structures at every picosecond, the structures with the rotated Si-O bonds

were approximately 0.9 eV lower in energy. A CI-NEB calculation for this rotation shows a 0.7 eV barrier with the final energies 0.9 eV lower in energy. As such, it is suggested the thermal expansion of the Ag cluster coupled with the additional thermal energy were the cause of the additional dynamics at 1000 K.

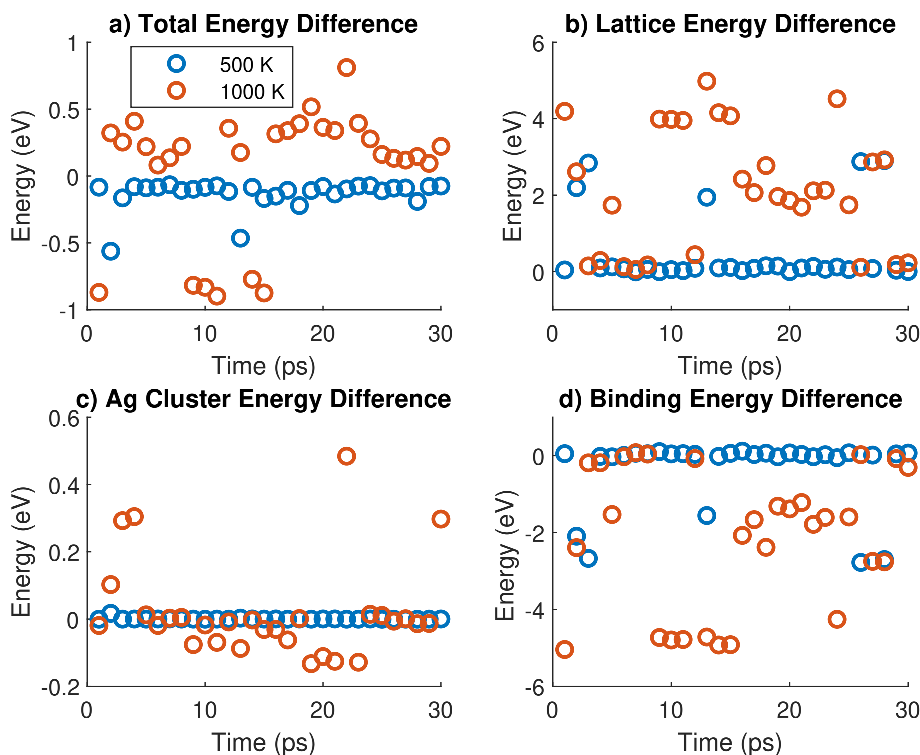

Figure 7.4: Graphs showing the energetics at each picosecond of 9 atom cluster during a MD simulated anneal at 500 K and 1000 K. a) The DFT re-optimised and cooled total energy of the system at each picosecond of the MD simulation including the lattice and the $[Ag_9/V_O]$ complex. b) The isolated energy of the 216 atom a-SiO_2 lattice at each picosecond of the MD simulation compared to the lattice at t = 0. c) The isolated energy of the 9 atom Ag cluster at each picosecond of the MD simulation compared to the cluster at t = 0. d) The binding energy of the 9 atom Ag cluster to the lattice at each picosecond of the MD simulation compared to t = 0.

As the strain induced increases exponentially as a function of the size of the Ag cluster, some method to determine the feasibility of applying DFT to study larger Ag clusters and the effects of strain on the SiO_2 lattice is required. In this regard, the clustering process was continued at one vacancy site to 15 atoms. A 2x2x2 supercell of the pristine 216-atom a-SiO_2 structure was then generated containing 1,728 atoms. The 15 atom Ag cluster was then embedded into a pristine 216-atom

cell and the pristine 1,728-atom supercell as shown in Fig. 7.5. In this case, the xyz positions of the 15 atom Ag cluster were added to the pristine 216-atom and 1,728-atom cells and the geometry was relaxed. Pristine refers to the structure of the 216-atom cell before defects such as the oxygen vacancy and Ag cluster were added. The objective for this calculation was to determine whether the relaxation of the amorphous network for each system is the same, giving an indication of the effects of periodic strain in a smaller cell. It turned out that the dissolution energy, lattice relaxation energy and the incorporation energy of the Ag cluster for both systems remained almost identical, as seen on Table 7.3. Furthermore, the 216-atom and 1,728-atom cells each relaxed to give the same bond angles and structure of the initial 15 atom cluster system generated using the clustering process method. This suggests that, whilst growing larger clusters does induce strain in the network, the strain is largely absorbed by the SiO_2 network without requiring the cell parameters to be relaxed.

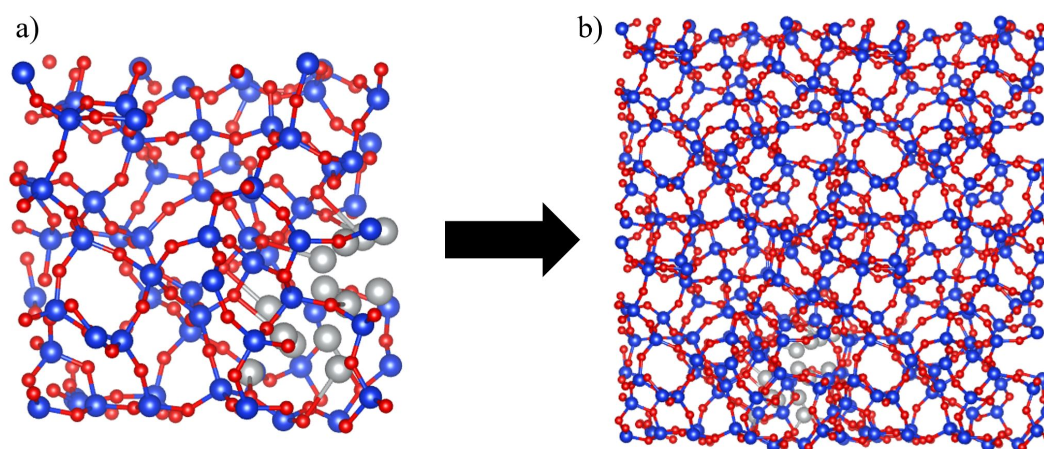

Figure 7.5: Shows the Ag cluster embedded into a pristine (a) 216-atom cell and a (b) 1,728-atom supercell. The silver, blue and red spheres correspond to Ag, Si and O atoms respectively.

7.3.2 Ag Cluster Induced Strain in a-SiO_2

To study the strain induced in the SiO_2 lattice, an $[Ag_i/V_O]^q$ complex for i = $0 \leq i \leq 15$ was calculated in the $-4 \leq q \leq 4$ charge states at one vacancy site using the same methodology described above. In this case, the complex was built by adding one Ag at a time at several void positions near the Ag cluster and the geometry optimised in

Table 7.3: Table comparing the Ag atom embedded in a pristine 216-atom cell to a pristine 2x2x2 supercell.

	216-atom cell	2x2x2 supercell
Dissolution Energy (eV)	23.66	23.65
Lattice Relaxation Energy (eV)	14.37	14.44
Incorporation Energy (eV)	12.46	12.40
Largest atomic displacement (Å)	0.93	0.92

each charge state. Fig. 7.6 shows the defect level positions along the a-SiO_2 band gap for $[Ag_i/V_O]^0$ for i = 0, 3, 6, 9, 12 and 15. As the Ag cluster grows to 15 atoms, a band begins to form at the SiO_2 VBM (Fig. 7.7), with additional states having strong Ag character. However, the nature of this band shifts once the cluster grows past 11 atoms, where initially there is only a small amount of mixing between the Ag band and the SiO_2 VBM. As the cluster grows past 11 atoms, the amount of mixing between Ag and O states at the VBM increases, resulting in O states being pulled into the Ag band. This effect is indicative of a stronger interaction between the Ag cluster and the lattice, and is observed though the formation of Ag-O bonds.

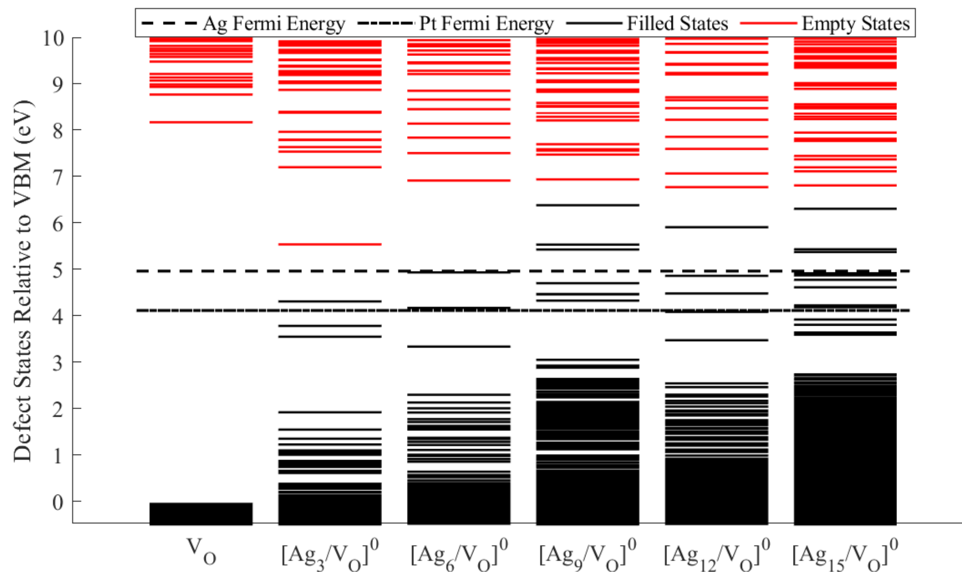

Figure 7.6: Graph showing the filled (black) and empty (red) state positions along the a-SiO_2 band gap for $[Ag_i/V_O]^0$ for i = 0, 3, 6, 9, 12 and 15

Further analysis of $[Ag_i/V_O]^q$ provides many significant insights into the way in which Ag clusters grow and they way in which strain is compensated in the lat-

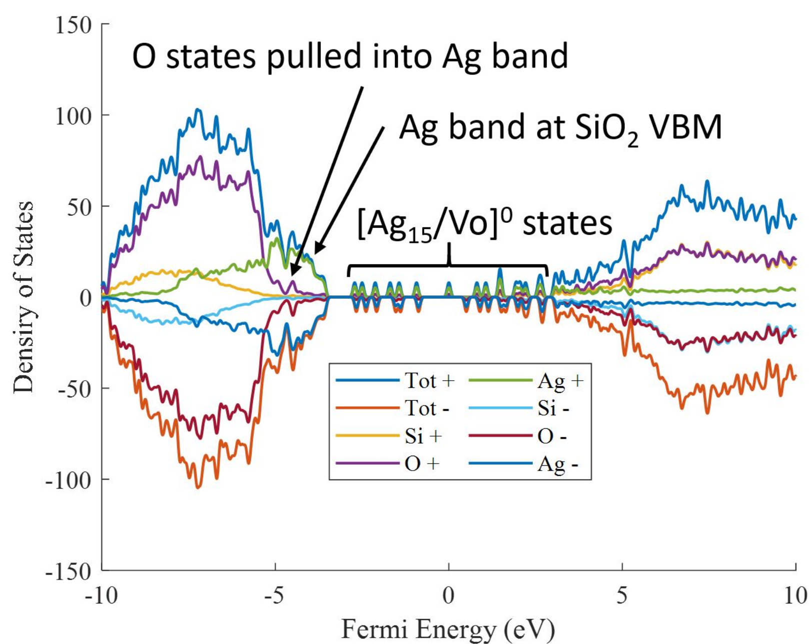

Figure 7.7: Graph showing the density of states for the $[Ag_{15}/V_O]^0$ complex.

tice. Perhaps the most important phenomenon observed is the spontaneous breaking of Si-O bonds as a result of adding a Ag^{+1} ion and relaxing the geometry. From Fig. 7.8 we see that as Ag clusters grow, more Si-O bonds break, with the effect more significant in the negative charge states. This is important as it shows that the clustering process is determined by electron injection and subsequently, by the Fermi energy. This is in agreement with calculations for Ag in α-quartz, where the electrode Fermi energy determined the charge state of Ag clusters. This is important as the binding energy of subsequent Ag^{+1} ions to $[Ag_i/V_O]^q$ is dependent on q.

Fig. 7.8 shows that two regimes for Ag clustering occurs, as seen by a much larger number of spontaneous bonds broken in negative charge states. To further test this theory, Si-O bonds were broken to determine if lower energy states could be found. More specifically, Si-O bonds that were part of wide angle O-Si-O bonds were selected and the O atoms were displaced such that the Si-O bond length was greater than 2.5 Å. Each structure was then geometry optimised to determine whether the Si-O bond would reform, or find another geometry. From this, a trend was found where Si-O bond breaking was energetically favourable for $[Ag_5/V_O]^{-3}$, $[Ag_6/V_O]^{-2}$, $[Ag_7/V_O]^{-2}$, $[Ag_8/V_O]^{-1}$, $[Ag_9/V_O]^{-1}$. The reason Si-O bonds did

Charge q	Size of Ag Cluster										
	5	6	7	8	9	10	11	12	13	14	15
+4	0	0	0	0	0	0	0	0	0	0	0
+3	0	0	0	0	0	0	0	0	0	0	1
+2	0	0	0	0	0	0	0	0	0	0	1
+1	0	0	0	0	0	0	0	0	1	1	2
0	0	0	0	0	0	0	0	1	0	1	1
-1	0	0	0	0	0	1	1	1	0	1	1
-2	0	0	0	0	1	2	2	1	2	2	1
-3	0	1	0	0	2	2	2	1	2	2	1
-4	1	2	2	1	2	2	2	2	3	2	2

Figure 7.8: Table showing the number of broken Si-O bonds as a function of charge state and Ag cluster size

not break spontaneously whilst growing the cluster can be understood by there being a barrier which needed to be overcome. In cases where bonds did break, electron injection and the metallic bonding between Ag^{+1} and $[Ag_i/V_O]^q$ each provided strain into the lattice, allowing the barrier to be overcome. Another phenomenon observed is a shift in the $[Ag_i/V_O]^q/SiO_2$ interaction depending on the charge state. Fig. 7.9 shows the ratio of Ag-Si bonds to Ag-O bonds. Thus we see that, as electrons are injected into the system, Si-O bonds become broken, with the Si atom forming a bond to the $[Ag_i/V_O]^q$ complex. The Ag-Si has been observed throughout calculations in the negative charge states, where Ag in previous cases interacted with Si in wide angle O-Si-O bonds. In the positive charge states, the Ag-O interaction is favoured. This is because the states in the band gap and at the VBM are $[Ag_i/V_O]^q$ states. Removing electrons from these states gives the Ag cluster a positive charge, which allows an electrostatic interaction with proximate lattice O. Again, this effect has been observed throughout calculations, beginning with the Ag^{+1} ion in α-quartz.

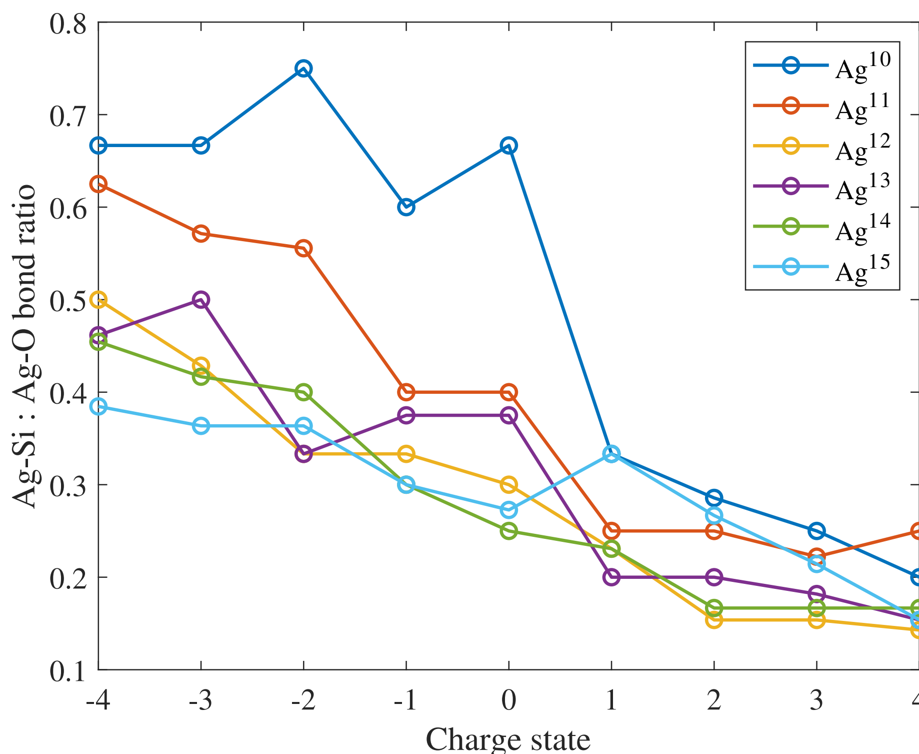

Figure 7.9: Graph comparing the ratio of Ag-Si bonds to Ag-O bonds to the charge state of the system.

7.3.3 Vacancy generation by electron injection

With electron injection shown to promote the breaking of Si-O bonds, a meaningful question is whether electron injection facilities the formation of O vacancies. In a previous study, it was shown that wide angle O-Si-O bonds are precursor sites for V_O generation [125]. In this process, electrons injected into a-SiO_2 trap onto the wide angle O-Si-O bonds. This results in the further widening of the O-Si-O bond angle and the weakening of a Si-O bond, thereby reducing the barrier for O to escape. As larger Ag clusters grow inside the network, more geometric distortion is observed. In some cases, this results in wide angle O-Si-O bonds forming. To test whether these sites combined with electron injection affect O vacancy formation around Ag clusters, the O vacancy formation energy of 17 O sites were calculated for the $[Ag_{15}/V_O]^q$ system.

In the first phase, a screening process was carried out using all structures generated whilst building the $[Ag_{15}/V_O]^q$ complex through the V_O mediated Ag cluster

nucleation mechanism. This includes the relaxed structures of $[Ag_1/V_O]^q$ through to $[Ag_{15}/V_O]^q$ in the $-4 \leq q \leq 4$ charge states. Using these structures, any O that was found to form a O-Si-O bond with angle greater that 130 ° was considered giving a total of 17 potential vacancy precursor sites. For each precursor site, the O atom was removed and the geometry optimised in the $-4 \leq q \leq 4$ charge states. The results are shown on Fig. 7.10, where the solid horizontal black lines represent the minimum and maximum V_O formation energy in the pristine cell sampled across all (144) O sites. The dashed line represents the mean V_O formation energy allowing a direct comparison. From this, we see that for every charge state, the V_O formation energy for some sites is lower than any found in the pristine state. Furthermore, we see that the V_O formation energy is lower in negative charge states, and is energetically favoured for one site. This confirms that the strain induced by the Ag cluster leads to reduced V_O formation energies, with the effect amplified by electron injection. This process would occur in situations where the electrode Fermi energy is closer to the SiO_2 CBM.

Fig. 7.11 shows the formation energy diagram for the $[Ag_{15}/V_O]^q$ complex. One can see that the +3-charge state is favoured at the Ag and Pt Fermi energies, with negative charge states favoured at Fermi energies above 6.95 eV. Fig. 7.12 shows the defect level positions of $[Ag_{15}/V_O]^q$ across the a-SiO_2 band gap. A number of states in the band gap, and most importantly, empty states in the proximity of the Ag and Pt Fermi energies for q = 2, 3 and 4 can be seen. From this, we can infer that the $[Ag_{15}/V_O]^q$ complex will be in the +3 charge state, where $[Ag_{15}/V_O]^{+3}$ complexes in proximity to each other could allow electron transport between Ag and Pt electrodes via trap assisted tunneling through the empty cluster states.

7.3.4 Molecular dynamics simulations

DFT molecular dynamics simulations were run for the $[Ag_{13}/V_O]^0$, $[Ag_{13}/V_O]^{-1}$ and $[Ag_{15}/V_O]^{+3}$ at 500 K and 1000 K, as described in section 6.2.3. Again, the simulations were run for 30 ps with a 1 fs time step using an NVT ensemble. For each temperature, the structure at every picosecond was extracted and geometry optimisation using DFT to give their local minima using the PBE functional. The

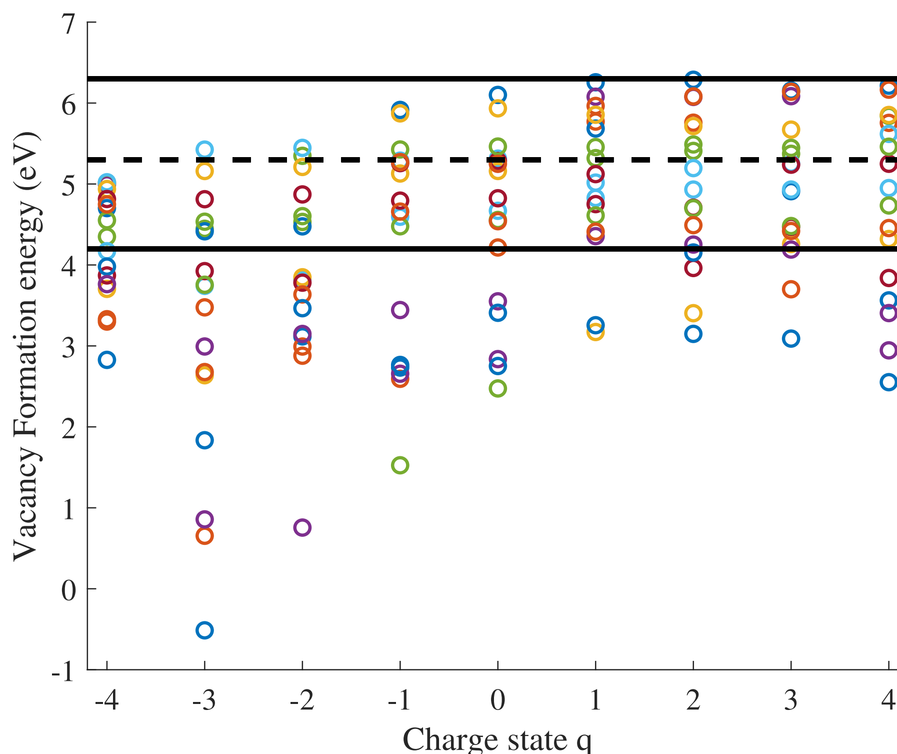

Figure 7.10: Graph showing the vacancy formation energy for 17 V_O sites around the $[Ag_{15}/V_O]^q$ complex in the -4 $\leq q \leq$ 4 charge states.

simulations of $[Ag_{13}/V_O]^0$ and $[Ag_{13}/V_O]^{-1}$ were run because spontaneous bond breaking was observed for $[Ag_{13}/V_O]^{+1}$ but not for the q = 0 and -1-charge states. As such, it was expected that some barrier needed to be overcome for a Si-O bond to break. In both cases, a Si-O bond did break at 500 K and 1000 K. The final structures optimised at 30 ps were between 3.0 and 3.5 eV lower in energy with the Si-O bond remaining broken throughout simulations. In both cases, and for each temperature the Si-O bond broke within 10 ps.

The MD simulation for $[Ag_{15}/V_O]^{+3}$ was run to study the interaction of $[Ag_{15}/V_O]$ with the lattice in the charge state favoured at the Ag and Pt Fermi energies. From this, an important effect was observed where the Si-O bond that had broken as a result of the cluster nucleation process opened to allow the Ag cluster to access a second nearby void. Before the Si-O bond was broken and in the pristine lattice the Si-O bond length was 1.6 Å. After growing the $[Ag_{15}/V_O]^{+3}$ through the clustering mechanism described above the Si-O bond broke, where the Si-O dis-

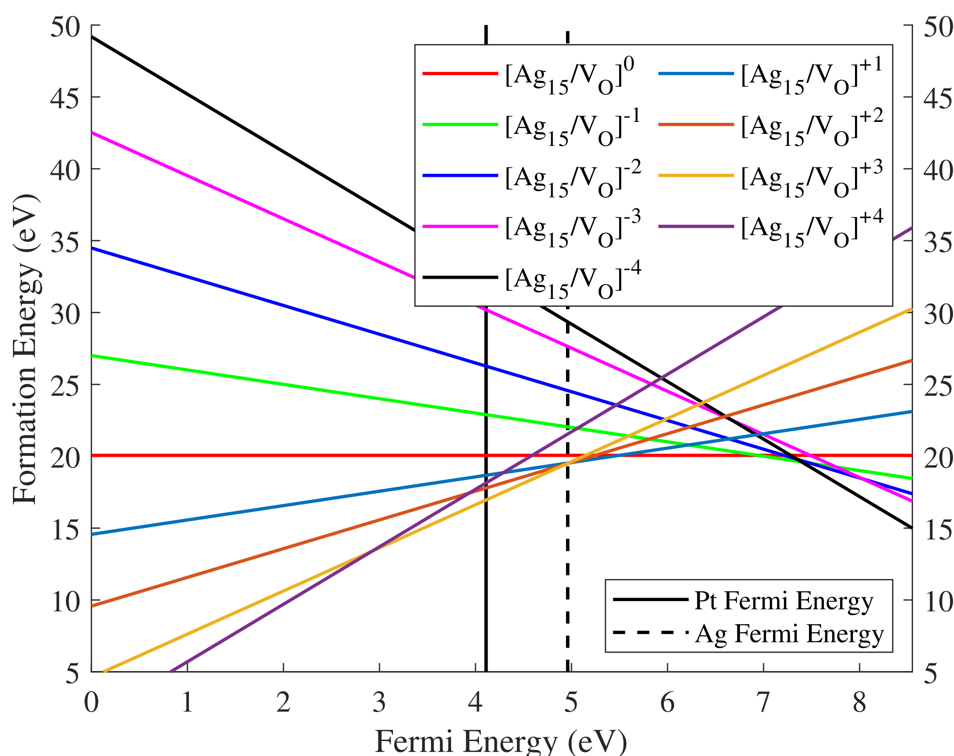

Figure 7.11: Formation energy diagram of the $[Ag_{15}/V_O]$ in a-SiO_2 relative to the VBM using the chemical potential calculated from Ag_2O

tance increased to 2.9 Å. This structure was then used as the starting point for the MD simulation, where the Si-O distance increased to between 3.5 and 4.5 Å through the MD simulation. Subsequently, the Ag cluster reorganised during the MD simulation such that Ag atoms started to explore the new void. By 15 picoseconds, three Ag atoms broke off from the $[Ag_{15}/V_O]^{+3}$ complex forming a Ag_3^{+1} trimer in the new void.

Fig. 7.13 shows the lowest energy structure found by geometry optimising the MD structures at every picosecond with the PBE0_TC_LRC functional. It can be seen that the broken Si-O bond opens access to a new void next to the $[Ag_{15}/V_O]^{+3}$ complex, where a 3 atom cluster is formed in the newly accessible void whilst a 12 atom cluster remains in the original void still interacting with the V_O site. The total energy of the two Ag cluster system was found to be 1.57 eV lower in energy than the $[Ag_{15}/V_O]^{+3}$ complex, suggesting Ag clusters can grow and expand into the a-SiO_2 lattice in this way. It should be noted that during the MD simulation the Ag_3^{+1}

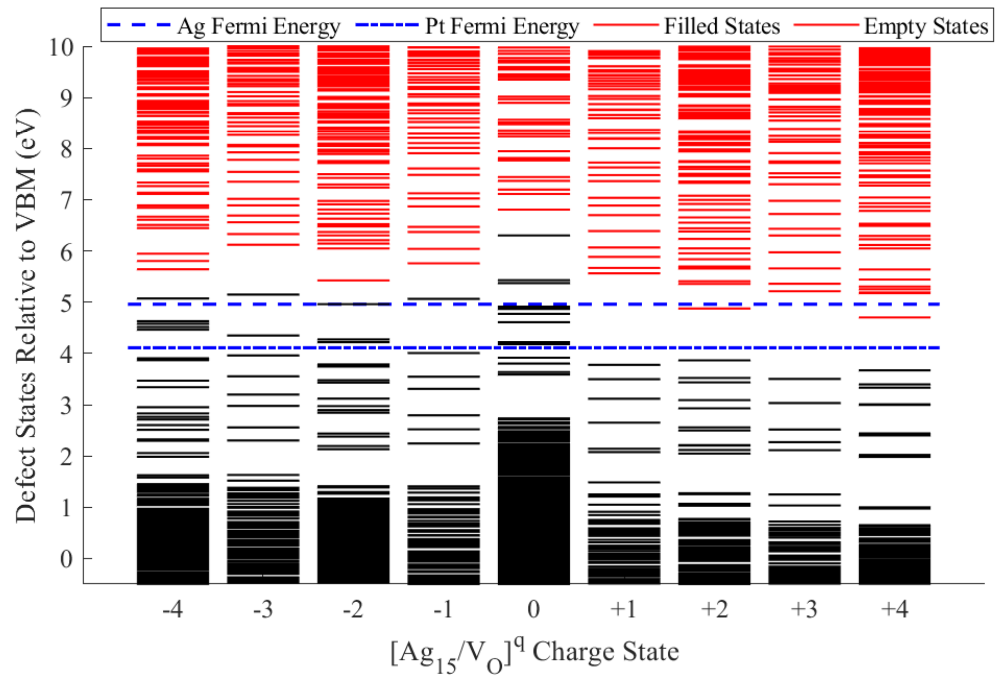

Figure 7.12: Graph showing the filled (black) and empty (red) state positions along the a-SiO_2 band gap for $[Ag_{15}/V_O]^q$ for the -4 $\leq q \leq$ 4 charge states

completely separated from the $[Ag_{15}/V_O]^{+3}$ complex. However, upon cooling via DFT geometry optimisation, the lowest energy state involved an interaction between Ag_3^{+1} and the new $[Ag_{12}/V_O]^{+2}$ complex with a Ag to Ag bond length of 2.77 Å

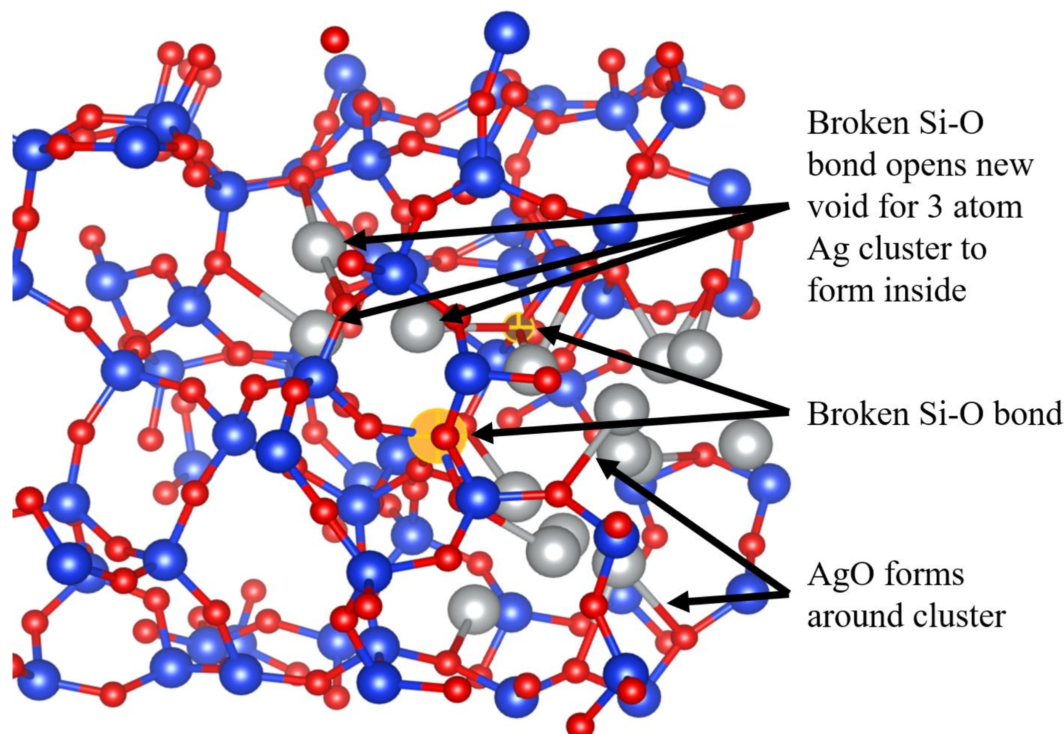

Figure 7.13: Schematic of the $[Ag_{15}/V_O]^{+3}$ complex after a MD simulation at 1000 K. After the widening of a Si-O bond to open access to a secondary void, a Ag_3^{+1} cluster breaks from $[Ag_{15}/V_O]^{+3}$ to form in the new void.

7.4 Summary of Main Results

7.4.1 Ag cluster nucleation

Ag cluster nucleation was studied by systematically by adding Ag^{+1} ions to the $[Ag/V_O]^0$ complex and relaxing the geometry in the $-4 \leq q \leq 4$ charge states. To model the initial stages of cluster nucleation, CI-NEB calculations were made for Ag^{+1} ions to approach and bind to $[AgV_O]^0$ up to $[Ag_5/V_O]^{+1}$. From this, it was found that the clustering process is thermodynamically favourable, with low barriers for Ag^{+1} to bind to each $[Ag_i/V_O]^j$ complex and high reverse barriers showing the stability of the cluster at the vacancy. In each case, at least on Ag atom remains bound to the original V_O site.

Using the same methodology of adding Ag^{+1} ions and trapping electrons, 9 Ag atom clusters at three V_O sites were created. The results show that, whilst the incorporation energy per Ag atom increases with the size of the cluster, the clustering of Ag is energetically favourable up to 9 atoms. An *ab initio* molecular dynamics

simulated anneal of one [Ag_9/V_O] complex at 1000 K showed considerable changes in the morphology of the Ag_9 cluster. By calculating the energy of the isolated Ag_9 clusters formed through the annealing, it was found that the energy of the cluster changed very little. This confirmed that the clusters developed by adding Ag^{+1} ions in voids are stable and energetically favourable. Instead, the energy of the isolated a-SiO_2 lattice (with the Ag_9 cluster removed) changed by up to 5 eV showing the rearrangement of the Ag_9 clusters affects the strain induced in the lattice. As a result, the clustering process is understood to be a trade between the energy gained by the metallic bonding between Ag in the cluster and the strain induced in the lattice. When Ag^{+1} ions bind to $[Ag_i/V_O]^j$, the energy gained through that bonding interaction compensates the strain introduced into the lattice. The compensation occurs specifically by reorganisation of the lattice around the Ag cluster through local distortions and Si-O bond breaking.

The strain induced in the lattice was studied at one vacancy site through a $[Ag_i/V_O]^q$ complex for i = $0 \leq i \leq 15$ in the $-4 \leq q \leq 4$ charge states. Results show the strain increases exponentially as a function of i, and is incorporated into the a-SiO_2 lattice through Si-O bond breaking. This was confirmed by embedding the resulting 15 atom Ag cluster into a 1,728-atom supercell (2x2x2 supercell of the pristine 216-atom a-SiO_2 structure). The bond lengths, bond angles, dissolution energy, lattice relaxation energy and the incorporation energy for the 15 atom cluster in a pristine 216-atom and the 1,728-atom supercell system were almost identical, suggesting that the strain induced by the Ag cluster is accurately represented in the 216-atom network.

As the Ag cluster grows to 15 atoms, a band was seen to form at the a-SiO_2 VBM with the additional states having strong Ag character. Below 11 atoms, there is only a small amount of mixing between the Ag band and the VBM. As the cluster grows past 11 atoms the amount of mixing between Ag and O states at the VBM increases, resulting in O states being pulled into the Ag band. This effect is indicative of a stronger interaction between the Ag cluster and the lattice, and is observed though the formation of Ag-O bonds. The $[Ag_{15}/V_O]^{+3}$ state is favoured at the

Ag and Pt Fermi energies, providing empty states in proximity to the Ag and Pt Fermi energies. From this, it can be inferred $[Ag_{15}/V_O]^{+3}$ complexes in proximity to each other will allow electron transport between Ag and Pt through trap assisted tunneling *via* the empty states.

During the development of the $[Ag_{15}/V_O]$ complex, Si-O bonds breaking was also seen to occur with increasing electron injection. This observation is important as it shows the clustering process is subsequently controlled by the Fermi energy of the proximate electrodes. As a result, not only will the number of empty states available for electron transport be altered, the binding energies for Ag^{+1} to $[Ag_i/V_O]^q$ will change, with binding energies expected to increase for more negative complexes. Furthermore, the $[Ag_i/V_O]^q/SiO_2$ interaction is dependant on the charge state, where as electrons are injected into the system more Si-O bonds are broken. The newly formed dangling Si atoms then interact strongly with the $[Ag_i/V_O]^q$ complex through the formation of Ag-Si bonds. In the positive charge states, the Ag-O interaction is favoured due to the states in the band gap at the Fermi energy belonging to the $[Ag_i/V_O]^q$ complex. Removing electrons from these states gives the Ag cluster a positive charge, which is compensated though an electrostatic interaction with proximate lattice O.

Calculations were also made for the V_O formation energy at 17 sites in proximity to the $[Ag_{15}/V_O]^q$ complex in the $-4 \leq q \leq 4$ charge states. From this, lower V_O formation energies were found in each charge state compared to the pristine lattice. The V_O formation energies were also found to be lower in negative charge states, and was found to be energetically favoured for one site in the -3-charge state. This suggests that the strain induced by the Ag cluster leads to reduced V_O formation energies, with the effect amplified by electron injection. This process would occur more frequently in situations where the electrode Fermi energy is closer to the SiO_2 CBM.

Ab initio molecular dynamics simulations were run for the $[Ag_{13}/V_O]^0$ and $[Ag_{13}/V_O]^{-1}$ systems show Si-O bond breaking at 500 K and 1000 K. The DFT cooled structures from the MD simulation containing broken Si-O bonds were found

to be between 3.0 and 3.5 eV lower in energy with the Si-O bond remaining broken. This shows the strain induced by Ag clustering reduces the barriers of Si-O bond breaking. Another MD simulation for $[Ag_{15}/V_O]^{+3}$ shows broken Si-O bonds can open to allow the Ag cluster to access a second nearby void. In this case an initial Si-O bond of length 1.6 Å (in the pristine lattice) increases to 2.9 Å as a result of the clustering mechanism of adding Ag^{+1} ions and relaxing the geometry. In the process of MD simulation, the Si-O distance increases to between 3.5 and 4.5 Å opening access to a new void next to the Ag cluster. Subsequently, the Ag cluster reorganises during the MD simulation such that Ag atoms explore the new void until three Ag atoms broke off from the $[Ag_{15}/V_O]^{+3}$ complex forming a Ag_3^{+1} trimer in the new void. The total energy of this two Ag cluster system was found to be 1.6 eV lower in energy than the original $[Ag_{15}/V_O]^{+3}$ complex. This marks the point at which the strain introduced into the lattice cannot be compensated only by the energy gained through metallic bonding. Instead, to reduce strain small Ag clusters can break from larger Ag clusters to grow into new voids made accessible by Si-O bond breaking. It is expected that Ag^{+1} ions will bind to the smaller clusters *via* the mechanism described in this chapter to form large clusters in proximity to each other. It is also important to note that Ag-Ag interaction remained between the newly formed Ag_3^{+1} trimer and the $[Ag_{12}/V_O]^{+2}$ complex. As such, it is expected that as the Ag_3^{+1} trimer grows, more bonding between the two clusters will occur until they coalesce, presenting an interesting area for future research.

7.5 Conclusion

A plausible initial mechanism of Ag cluster nucleation at V_O sites was studied in a-SiO_2 by adding Ag^{+1} ions to the $[Ag/V_O]^0$ complex and optimising the geometry. Clusters were found to form in voids next to V_O, where the resulting $[Ag_i/V_O]^j$ complexes are favoured to trap electrons depending on the Ag an Pt Fermi energies. *Ab initio* molecular dynamics simulated anneal of a $[Ag_9/V_O]$ complex at 1000 K shows that whilst the morphology of the Ag cluster change drastically, the energy of the cluster remains the same with the lowest energy cluster less than 0.2 eV lower in energy. Instead, the reorganisation of the Ag cluster in the amorphous network

effects the lattice strain which is compensated through local distortions and Si-O bond breaking. Through growing a [Ag_{15}/V_O] complex, it was then shown that the growth of the Ag cluster and electron injection are the two main contributors to strain and broken Si-O bonds, with more frequent bond breaking seen in negative charge states. Furthermore, electron injection was shown to reduce the V_O formation energy of V_O sites in proximity to the Ag cluster. Broken Si-O bonds were subsequently shown through *ab initio* molecular dynamics simulations of a $[Ag_{15}/V_O]^{+3}$ complex to open and allow access to secondary voids. In particular, a small Ag_3^{+1} trimer was shown to detach from the $Ag_{15}/V_O]^{+3}$ to form in the new void, releasing the strain induced in the network. It is expected that the Ag_3^{+1} trimer will grow according to the same mechanism of Ag^{+1} ion binding and electron injection. From this, it may coalesce with the original cluster whilst also opening new voids for subsequent clusters to form, presenting an important area for further research.

Chapter 8

Part I: Summary and Future Work

8.1 Summary

The first objective of the study was to develop a working model of Ag in crystalline silicon oxide with DFT. This was to ensure DFT can accurately and repeatably recreate the Ag-SiO_2 interaction, which is more clearly defined experimentally for crystalline systems. To achieve this, α-quartz was used as a test case and the Ag interactions with α-quartz were studied. This includes the modelling of the IR and RAMAN spectra of a pristine α-quartz cell, the EPR response of the Ag^0 interstitial in α-quartz and the absorption and photoluminescence spectra for the Ag^{+1} interstitial in α-quartz. The results in each case were all positive, confirming the viability of using DFT to study Ag-SiO_2-Pt RRAM. Subsequently, the properties of the Ag and α-quartz system relevant to Ag-SiO_2-Pt RRAM devices were modelled. This includes a study of the incorporation of Ag in α-quartz and the migration of Ag^0 and Ag^{+1} through α-quartz. From this, it was found that the Ag^{+1} ion is favoured at the Ag and Pt Fermi energies, and is also the more mobile species. Due to this result, some mechanism for Ag^{+1} reduction is required for Ag cluster nucleation to occur. In this regard, the interaction of Ag with O vacancies (V_O) was studied as a possible site for Ag^{+1} reduction and cluster nucleation. From this, it was shown that Ag^{+1} ions do indeed bind and reduce at O vacancies, subsequently allowing the nucleation of Ag clusters at the Ag and Pt Fermi energies.

The study was then expanded to the amorphous silicon dioxide (a-SiO_2) sys-

tem, where a similar methodology as described in the α-quartz study was used. This began with the development of a Ag-α-cristobalite interface to model the incorporation of Ag. From this, it was confirmed that Ag incorporates into a-SiO_2 as a Ag^{+1} ion. Ag was then studied in a-SiO_2 showing Ag remains in the +1-charge state at the Fermi energies of Ag and Pt. It was also found that Ag in any charge state preferentially resides in void like areas in the lattice. The diffusion of Ag^0 and Ag^{+1} was then studied using a 'ring' sampling method. From this, it was found that Ag^{+1} is very mobile through large rings and low density areas. By then modelling the diffusion of Ag^0 and Ag^{+1} in α-cristobalite, it was also found that both species are very mobile in grain boundaries and column boundaries. The interaction of the Ag^{+1} ion with O vacancies was then studied to determine how cluster nucleation may occur. By sampling every O in a 216-atom cell, 33 % and 11 % of O vacancies were found to act as Ag^{+1} reduction and cluster nucleation sites at the Ag and Pt Fermi energies respectively.

Subsequently, the Ag cluster nucleation process at O vacancy sites was modelled showing it is a thermodynamically favoured process. In this case, a Ag^{+1} ion can bind to an O vacancy to form a $[Ag/V_O]^{+1}$ complex. The $[Ag/V_O]^{+1}$ complex is then favoured to trap an electron to form $[Ag/V_O]^0$ at the Ag and Pt Fermi energies. Subsequently, additional Ag^{+1} ions can bind to the $[Ag_i/V_O]^j$ complex, where the complex continues to trap electrons from the Ag and Pt electrodes. This process was modeled at three vacancy sites up to 10 atoms. At one vacancy site, up to a 15 atom cluster was developed in this way showing the energy gained through the metallic Ag-Ag bonding compensates strain generated in the a-SiO_2 lattice. As a result, Si-O bonds break thereby reducing the barriers for O vacancy generation. Broken Si-O bonds were also shown to reduce the strain in the lattice, allowing Ag clusters to continue to grow. Molecular dynamics simulations carried out for the $[Ag_{15}/V_O]$ system found another interesting process. In this case, broken Si-O bonds opened access to proximate voids for the Ag cluster to explore. From this, a 3-atom Ag cluster was found to break from the large cluster to form into the new void. This process was found to minimise the overall strain generated in the lattice

and the total system energy. A filament of Ag clusters is suggested to grow in this way, describing the electroforming process in Ag-SiO_2-Pt RRAM devices.

8.2 Future Work

The original intention was to study Ag-SiO_2 devices *via* TEM in the second and third years of the PhD to complete the investigation. However, due to external factors this was not possible. In this regard there are several interesting areas for future work. The major discovery in this thesis is the ability of the oxygen vacancy to mediate Ag^{+1} reduction and Ag cluster nucleation. What remains is for this mechanism to be probed experimentally. Though difficult, it is possible through *in situ* TEM measurements on devices with artificially introduced O vacancies. In this case, several devices can be fabricated with different stoichiometries of SiO_x such as x = 1.9, 1.925, 1.95, 1.975 2.0. Alternatively, this could also be achieved by applying a negative bias to a SiO_2 device to generate vacancies as seen in the VCM mechanism. *In situ* stressing in each case would result in a shift from a low Ag^{+1} reduction rate regime to a high Ag^{+1} reduction rate regime as the concentration of O vacancies increases. Subsequently, a high reduction rate regime would result in a wider and more dense conductive filament as discussed in section 4.3.

Part II

Electrical Stress Induced Structural Dynamics in SiO_x RRAM Devices: An Electron Microscopy Study

9.1 Research Question

What are the fundamental mechanisms involved in the operation of SiO_x RRAM devices?

9.2 Outline

In this part of the thesis, electron microscopy techniques including TEM, STEM, EELS and EDX are used to characterise SiO_x based RRAM devices. Three device structures are studied in total, listed as; Au-Ti-SiO_x-Mo (Au-Ti), Ti-SiO_x-Mo (Ti) and Au-SiO_x-Mo (Au) RRAM devices. The top electrodes consist of Au-Ti, Ti and Au, respectively, grown onto a SiO_x dielectric layer (x $\approx$ 1.95) and a Mo bottom electrode. A stoichiometry of x $\approx$ 1.95 was selected to artificially introduce O vacancies into the dielectric layer to promote the VCM mechanism (see next section for more details). The Au-Ti devices are of particular interest due to their optimal RRAM properties including high endurance, high retention times and low switching voltages [15]. An important contributor to the high performance of the Au-Ti devices is the device microstructure, where the bottom electrode (Mo) is grown to have high levels of roughness (see section 3.2.3 for fabrication details). This is understood to result in the SiO_x layer possessing a columnar structure, which subsequently impacts the transport mechanisms involved in the operation of the devices [15]. However, the presence of a columnar structure has not been properly evaluated in the Au-Ti devices, whilst the role that the columnar structure plays in the transport mechanisms in the devices is not well understood. Furthermore, the Ti layer is only applied as a wetting layer to bind the Au and SiO_x layers. As a result the Ti is grown to a 5 nm thickness, and subsequently, the exact role the Ti layer plays in device operation is unclear.

The aim of this work is to characterise the Au-Ti device in order to elucidate the role played by the film and interface microstructure in device operation. I will use TEM and STEM for direct imaging, and EELS and EDX for chemical characterisation. To achieve that, the Au-Ti devices are prepared into TEM lamellas (see

section 3.3.3), which give an approximately 50 - 100 nm thick slice of the device to be imaged. As a result, the rough interfaces in the device are very difficult to characterise due to the variation of the sample along the electron beam path. To solve this problem, Ti-SiO_x-Mo (Ti) and Au-SiO_x-Mo (Au) devices were grown with minimal interface roughness. It is intended that the characterisation of these Ti and Au devices will provide a benchmark to analyse the dynamics expected in the Au-Ti device. The differentiation is important as the Ti and Au devices are understood to operate under competing mechanisms. The Ti devices are suggested to operate through an ECM mechanism (see section 4.3 for a detailed description), which involves the incorporation of electrode metal into the SiO_x layer to form a conductive filament. The Au devices are conversely thought to operate under the VCM mechanism (see section 9.3 for a detailed description), where O vacancies are generated in SiO_x by electron injection. Electron transport then occurs *via* trap assisted tunneling through the vacancy sites. As such, it is intended that studying the Ti and Au devices separately will allow the role of each mechanism in the Au-Ti device to be better understood.

The results in this part are split into three chapters with the Ti, Au and Au-Ti devices discussed individually. This involves a characterisation of the devices in their pristine and electroformed states through a combination of TEM, STEM, EELS and EDX. The purpose of this is to first provide a time-zero of the devices before any electroforming steps are applied. This is followed by an analysis of the devices after +15 V and -15 V electroforming with a current compliance of 1 mA. From this, the electrical stress induced structural dynamics of each device is studied. The Ti and Au devices are discussed first with the view that each device can provide insight into the structure of the Au-Ti device. In particular, consideration is given to the electrode/SiO_x interfaces and the SiO_x microstructure.

9.3 Part II: Background & Literature

Over the past decade a wealth of different RRAM devices and structures have been studied to replace FLASH memory, which is at its limit of optimisation [126]. In this regard, silicon oxide based RRAM devices present a number of important qualities that make them an attractive candidate for future memory technologies. To begin with, silicon oxide devices are CMOS compatible, allowing easier integration into current microelectronic systems. Furthermore, silicon oxide is an incredibly abundant material reducing the possibility of issues with scarcity or spiraling costs. Perhaps the most interesting feature of silicon oxide RRAM devices is their ability to operate under a number of resistive switching mechanisms. In the first part of this thesis, a case study of Ag-SiO_2-Pt RRAM devices was carried out where the ECM mechanism is prevalent. As such, an in depth discussion of the ECM mechanism can be found in section 4.3. The other important resistive switching mechanism is the VCM mechanism, which will be discussed in this section with regard to the Au-Ti, Ti and Au devices characterised in this part of the thesis. A review of other resistive switching mechanisms can be found in the literature [9].

9.3.1 VCM mechanism in SiO_x RRAM devices

VCM memory cells can have the same (active/top electrode) metal-insulator-metal (ohmic/bottom electrode) structure as used in ECM memories. However, there are different requirements on the properties of the metals used, where instead they are selected for their oxygen affinity and workfunction. More specifically, the active electrode is selected to have a low O affinity, whilst the ohmic electrode can be of the same metal (symmetric RRAM device) or have a high O affinity (asymmetric RRAM device). The dielectric layer is then chosen for the potential of ion and electron mobility. This brings with it an important distinction between VCM memories and ECM memories, where in VCM memories the active electrode metal does not incorporate into the SiO_x layer. For this work Au was selected as the active electrode metal, though it should be noted that other candidates such as Pt have been studied extensively [59].

With the pristine RRAM device initially in an insulating state, an electroform-

ing process is first applied to form a conductive filament or path within device oxide layer [127]. In VCM devices, this is typically achieved through the application of a negative bias at the active electrode, resulting in the generation of O^{-2} ions. The O^{-2} ions are understood to migrate and accumulate at the ohmic electrode which has the same or higher O affinity. This is due to the electric field gradient and field assisted diffusion. Electron transport then occurs through the oxide layer *via* trap assisted tunnelling though the defect states in the oxide layer, such as O vacancies or other intrinsic defect traps. It should be noted that the occurrence of the VCM mechanism is interesting as the O vacancy determined conductive filament/path is intrinsic to the properties of SiO_x. In extreme cases it has been observed that a filament of Si nano-crystals is formed instead during the this process [128].

Resistance switching has been studied in amorphous silicon sub-oxide (SiO_x) very extensively, with the ECM and VCM mechanisms each shown to occur [13, 60, 129, 128]. The use of SiO_x (with x $\approx$ 1.95) in this study is to artificially create an oxygen vacancy rich environment in the dielectric layer. This results in defect states in the SiO_x band gap, which have been shown to occur at Fermi level positions approximately 1.6 eV below the SiO_2 CBM [130]. The vacancies subsequently behave as electron trap centres through which electrons can tunnel across the oxide layer *via* trap-assisted tunnelling mechanism [129]. In this case, the Fermi level of the metal relative to the SiO_x band gap, and the subsequent bias applied, will determine the probability of electron transport in this way. A current compliance is typically used during electroforming to prevent a hard dielectric breakdown of the oxide layer.

9.3.2 O Vacancy Generation and Electron Transport in SiO_x RRAM devices

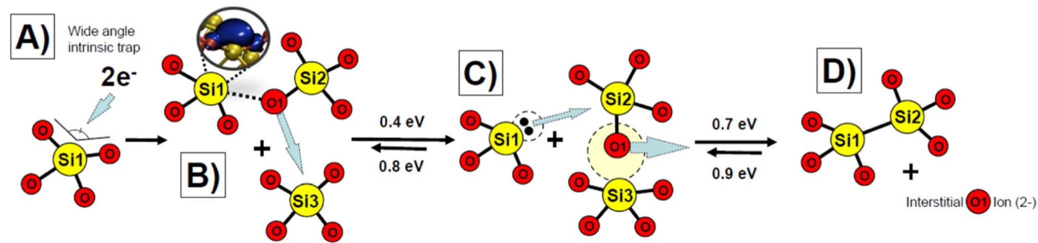

Figure 9.1: Schematic showing the O vacancy generation process. A) two electrons trap at an intrinsic wide angle (> 132° O-Si-O bond. B) The trapped electrons lead to the lengthening and weakening of an Si-O bond. C) The Si-O bond breaks leaving two electrons trapped in a three coordinated Si atom. D) An O vacancy is formed after the O^{-2} interstitial diffuses away

It was mentioned above that O^{-2} ions and O vacancies are produced during the electroforming phase. This process has been studied where a mechanism involving intrinsic electron traps in SiO_2 is suggested (see Fig. 9.1). In this case, DFT calculations show that electrons may trap at intrinsic wide angle O-Si-O bonds (>132 °) at Fermi energies of approximately 3.2 eV below the SiO_2 CBM [125]. From this, Si-O bonds are weakened leading to reduced barriers for O vacancy generation [131]. In this case, a 0.4 eV barrier is required to break the initial Si-O bond and a 0.7 eV barrier to form the O vacancy and O^{-2} interstitial. The concentration of the wide angle traps was estimated to be $\approx 10^{19}cm^{-3}$, whilst their presence was experimentally confirmed though optical absorption measurements [125]. For this mechanism to occur in the devices in this study, the Fermi energy of the active electrode metal (Au-Ti, Au and Ti) becomes a controlling factor in the O vacancy generation process. The workfunctions of Au and Ti are 5.10 eV and 4.33 eV respectively, whilst the SiO_2 CBM is found at 0.75 eV below vacuum level [132]. This crudely puts the Au and Ti Fermi levels at 4.35 and 3.58 eV below the SiO_2 CBM assuming there are no major shifts due to band bending and contact potential. The application of a negative potential to a metal raises its Fermi level due to additional electrons filling previously empty states. As a result, it is consistent to suggest that applying a negative bias to Au and Ti will raise their respective Fermi levels to the 3.2 eV below

the SiO_2 CBM required to generate O vacancies through the suggested mechanism.

DFT calculations also show that O vacancies trap electrons at Fermi energies of approximately 1.6 eV below the SiO_2 CBM. It is expected that, as a more negative bias is applied to either Au or Ti, the Fermi level of each metal will shift towards 1.6 eV below the SiO_2 CBM. This subsequently increases the probability of electron injection into the vacancy sites, and therefore transport across the SiO_2 layer. In the case of SiO_x, it is expected that the increased number of O vacancies will facilitate electron transport through this mechanism.

9.4 Methods

The objective of this part of the thesis is to characterise the Ti, Au and Au-Ti devices with a view of understanding their operation as a computer memory. The growth process of each device is described in detail in section 3.2.3. The devices were then electroformed, where the voltage was increased across the device from 0 V to +15 V (positive electroformed) or -15 V (negative electroformed) and back to 0 V in increments of 0.05 V. In each case, the bias was applied at the top electrode with the bottom electrode (Mo) kept grounded. The current compliance for each electroforming sweep was set to 1 mA. The current compliance is used to ensure that hard dielectric breakdown of the devices does not occur. Three TEM lamellas were prepared from each of the Ti, Au and Au-Ti devices with one taken from a pristine device, one taken from a positive electroformed device and one from a negative electroformed device. TEM lamellas were prepared using an FEI Helios Nanolab 600 focused ion beam after the deposition of a protective Pt layer as described in section 3.3.3.

The TEM lamellas were then characterised using a combination of TEM, STEM, EELS and EDX. In each case, measurements were carried out using a FEI Titan S/TEM microscope. An in depth discussion of the FEI Titan microscope and its use can be found in Chapter 3. Before measurements, the TEM lamellas were cleaned in an O:Ar plasma for up to 5 minutes. An acceleration voltage of 200 kV was used to maximise the resolution of the images, whilst minimising the damage caused by the high energy electrons. A camera length of 195 mm was used for all STEM images and 60 mm for all EELS measurements. The reduced camera length for EELS spectra was used to maximise the electron counts (discussed in section 3.3.2). EEL spectra were acquired using a Gatan imaging filter (GIF) Tridiem detector with a 2.5 mm aperture, a collection semi-angle of 26 mrad and a beam convergence semi-angle of 14 mrad unless otherwise stated. The acquisition time for EELS measurements was set to values between 50 and 250 ms per pixel. Before each measurement, different acquisition times were tested in a separate region to maximise the EELS signal to noise ratio whilst ensuring minimal damage to the

device. Damage was tested by taking STEM images of the test regions before and after the test EELS measurements. This appears in STEM as changes in contrast, resolution and structural features. All data processing was carried out using the Digital Micrograph software. A first degree log polynomial background was used to best fit the EELS spectra as discussed in section 3.3.2.2. EDX measurements were taken using an EDAX (Model: TOPS 30 OST) EDX detector as discussed in section 3.3.2.3. For each EDX measurement, the electron beam current was raised until the EDX counts were approximately 800 to 1000 counts per second for the Si K peak. Subsequently, a low dwell time of 1 ms was used to acquire the EDX spectrum using a continuous raster scanning pattern.

9.4.1 EELS Fine Structure

Chemical analysis through electron microscopy can be a very powerful tool to characterise materials at the microscopic scale. EELS in particular not only allows the presence of different elements to be detected through the generation of an edge in an EEL spectrum, the edge itself contains characteristic information about the binding and local structure of each element detected. As discussed in section 3.3.1.4, an EELS edge occurs at the energies required to excite electrons into unoccupied states. These energies are characteristic to the local bonding environment of the element being detected. In this work, EELS is used to measure the Si $L_{2,3}$, Ti $L_{2,3}$ and O K edges, where the 'fine structure' characteristics of each edge allows a qualitative assessment of local chemistry.

Fig. 9.2 shows EELS spectra measured for a TiO_2/SiO_2 thin film stack [133]. The top curve corresponds to the EEL spectra summed across the TiO_2/SiO_2 stack, whilst middle and bottom curves show EEL spectra taken at the TiO_2 and SiO_2 layers, respectively. The top and middle curves (containing TiO_2) show the presence of an O K edge prepeak which is formed when O binds with transition metal d-states. More specifically, the prepeak is due to the excitation of electrons into unoccupied O 2p - Ti 3d hybridised states [134]. It is important to note that this prepeak is not observed in the bottom curve corresponding to SiO_2. The O K edge prepeak has also been shown to occur when O binds to Mo through excitation into unoccupied O

2p - Mo 4d hybridised states [135]. As such, the presence of the O K edge prepeak allows O in an SiO_x environment to be distinguished from O in TiO_x and MoO_x environments. This differentiation is used extensively in this work as an invaluable method to detect transition metal oxide inside the SiO_x layers in the devices.

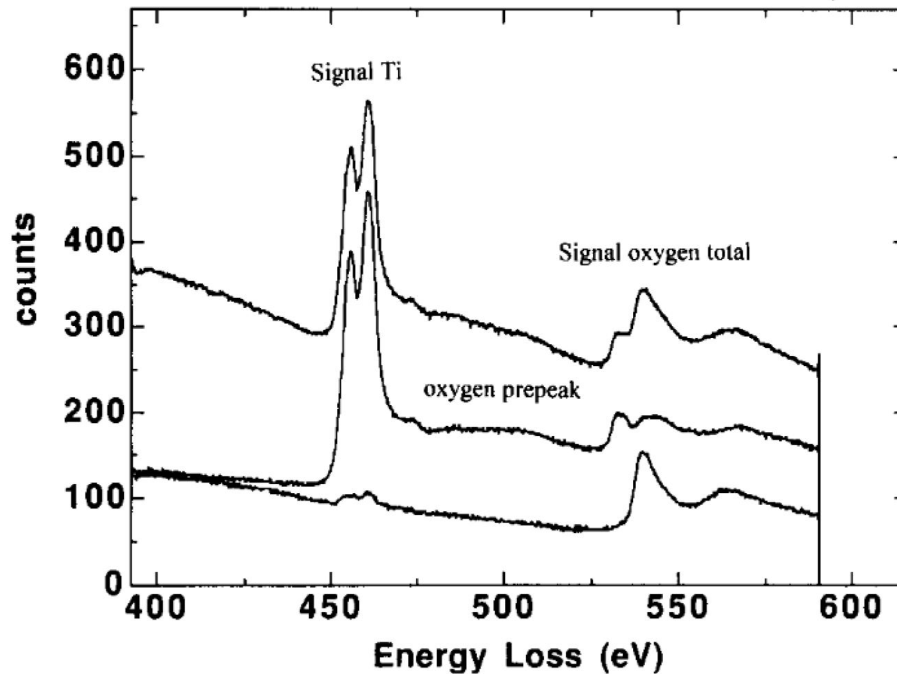

Figure 9.2: EELS spectra of the Ti $L_{2,3}$ and O K edges taken on a TiO_2/SiO_2 stack. The top curve corresponds to the total EELS spectrum summed across the TiO_2/SiO_2 stack, the middle curve is the sum of EELS spectra taken at the centre of the TiO_2 layer and the bottom curve is the sum of spectra taken at the centre of the SiO_2 layer. [133]

Fig. 9.3 shows the Si $L_{2,3}$ edge measured across an interface between Si and SiO_2, where the Si $L_{2,3}$ edge onset is seen to shift from 99.8 eV for pure Si to 106 and 108 eV for SiO_2 [136]. The cause of this shift is due to changes in the local bonding of Si, where Si in pure Si is in the Si^{0+} oxidation state compared to the Si^{4+} oxidation state in SiO_2. This allows the presence of reduced SiO_x to be detected through the analysis of the Si $L_{2,3}$ edge fine structure and the presence of any shoulders at the edge onset.

A similar analysis can be obtained for the Ti $L_{2,3}$ and O K edges as shown on Fig. 9.4, where it can be seen that the positions and ratios of each edge changes with the stoichiometry of TiO_x [137]. The cause of again is that the oxidation states of

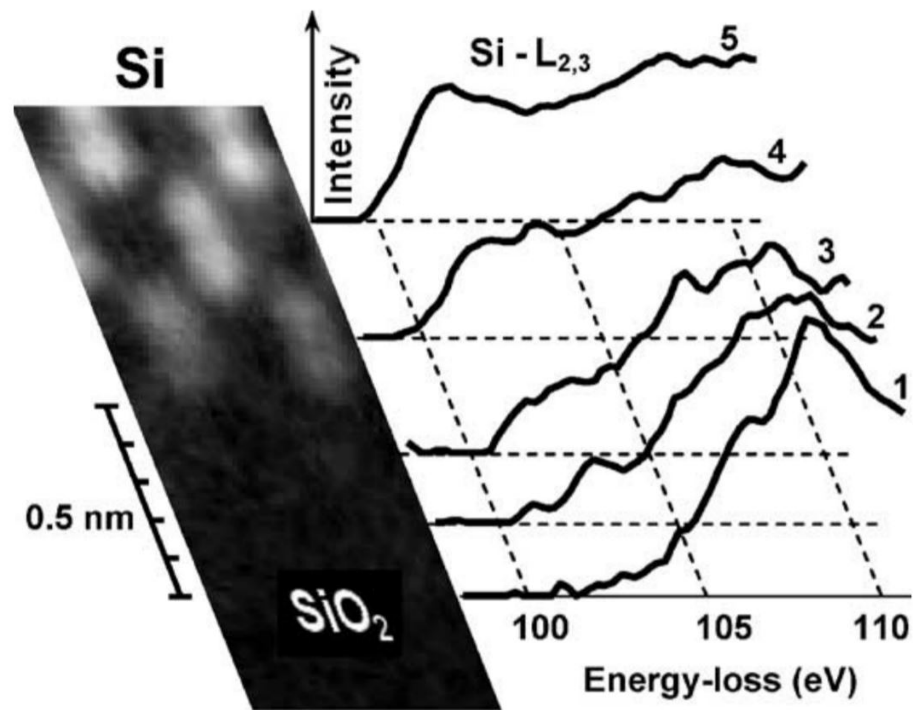

Figure 9.3: EELS spectra of the Si $L_{2,3}$ edge taken across a SiO_2/Si interface. The bottom curve (1) corresponds to the EELS spectrum measured in SiO_2, whilst the top curve (5) is measured in a Si region. The intermediate spectra (2-4) represent SiO_x regions of decreasing O content, respectively. [136]

Ti and O are changing in each case. An important observation is the trend that the Ti $L_{2,3}$ edge onset energy increases to higher energies from TiO to TiO_2, providing a qualitative measure of the Ti oxidation state.

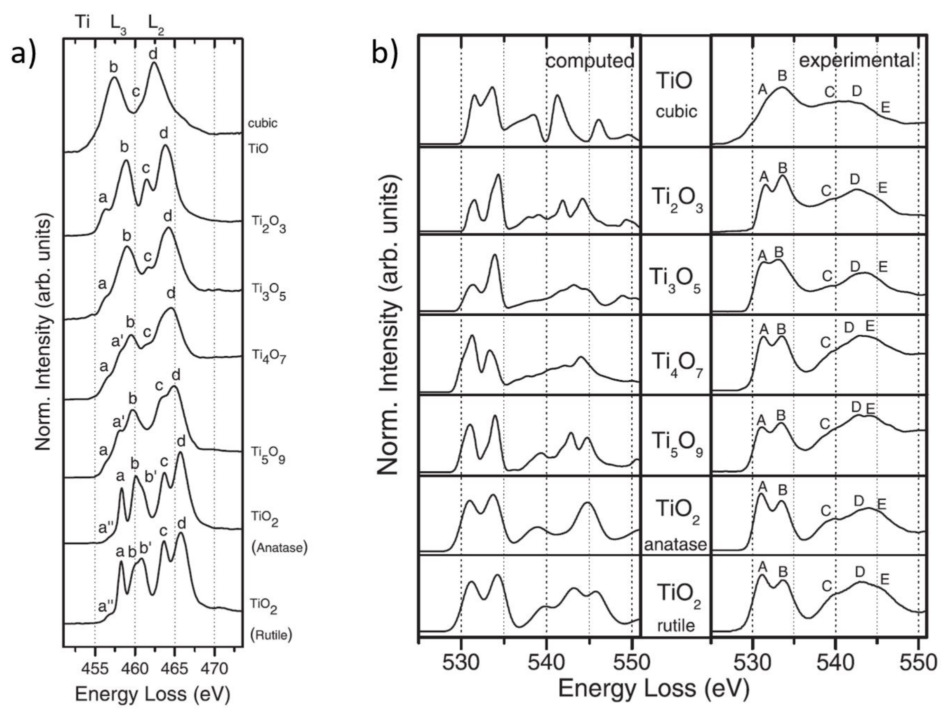

Figure 9.4: EEL spectra of the a) Ti $L_{2,3}$ edge and b) O K edge measured for TiO_x where x = $1 \leq x \leq 2$. [137]

9.4.2 Average Scan

A major consideration when collecting EELS data is the damage to the sample caused by the electron beam. This changes the local chemistry of the sample and results in an alteration of the corresponding EELS signal. To combat this problem an 'average scan' was introduced to accurately and effectively characterise the devices. The average scan involves sweeping the electron beam horizontally during a single scan to spread the damage caused by a long EELS acquisition time. This drastically improves signal to noise ratio of the EELS measurements, allowing the fine structure of the EELS edges to be more clear and comparable.

Fig. 9.5. shows a HAADF image of the Ti-SiO_x-Mo device, where a horizontal white 80 nm long line can be seen at the Ti/SiO_x interface. For each average scan measurement, an EELS acquisition time of 10 s was selected and the beam was swept horizontally over an 80 nm line to give the average EELS signal (shown by the white line on Fig. 9.5). This allows measurements to be taken in regions such as the metal/SiO_x interfaces, as well as horizontal regions of a fixed distance from each interface.

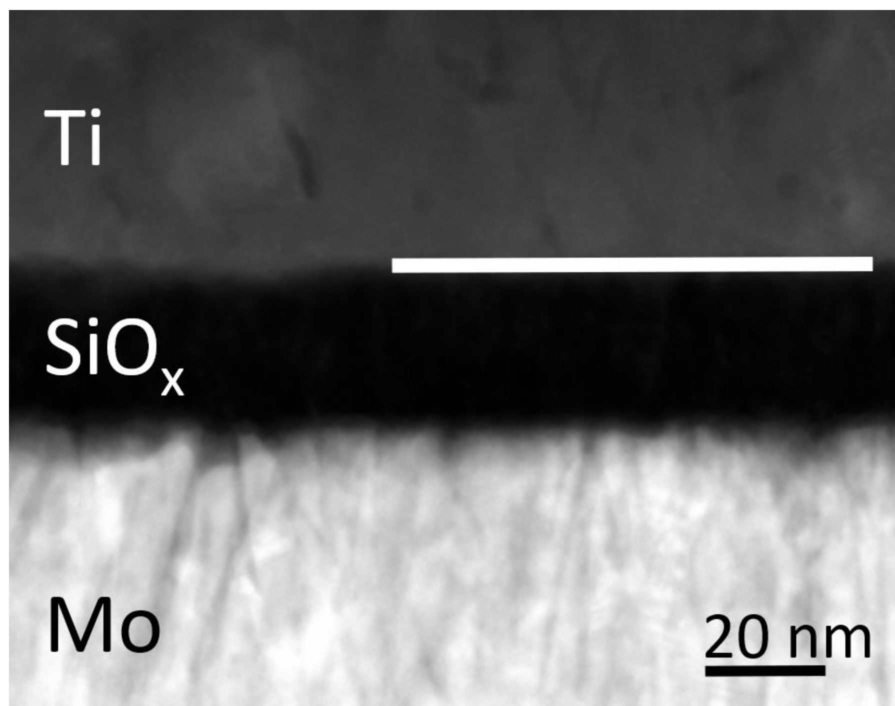

Figure 9.5: HAADF image of a Ti-SiO_x-Mo RRAM device. The horizontal white line marks the region at the Ti/SiO_x from which an EELS average scan is taken

Chapter 10

Ti-SiO$_x$-Mo (Ti) RRAM device

10.1 Introduction

The Ti-SiO$_x$-Mo (Ti) device does not exhibit repeatable resistive switching, and as a result, will perform poorly as a computer memory. Instead, the electroforming process in the Ti device is studied to provide a more complete understanding of the Au-Ti-SiO$_x$-Mo device (Au-Ti). As such, it is key to understand the similarities and differences between the Ti and Au-Ti devices to determine which properties of the Ti device are important to study. A fabrication summary of both devices can be found in section 3.2.3. The SiO$_x$ layer for both devices was grown using the same reactive sputtering technique, however, the nature of the Mo and Ti layers differ greatly. In the Au-Ti device, the Mo layer is grown to have increased surface roughness through magnetron sputtering. This is thought to lead to columnar structure in the SiO$_x$ layer, impacting the transport mechanisms across the device [15]. Furthermore, the Ti layer is applied as a wetting layer to improve adhesion between the Au and SiO$_x$ layers. As a result, the Ti layer is very thin (5 nm) making a characterisation of the Ti/SiO$_x$ interface very difficult due to the high levels of roughness.

The Mo layer in the Ti device is grown *via* thermal evaporation to have minimal roughness, allowing a more accurate study of the SiO$_x$/Mo interface. The reduced roughness of the SiO$_x$/Mo interface is expected to translate to a smoother Ti/SiO$_x$ interface, subsequently allowing a more accurate characterisation. As a result, the Ti

device allows both the metal-oxide interfaces in the Au-Ti to be characterised more accurately, potentially providing insight into device operation. Of particular interest is the oxidation of the Ti and Mo layers at the interface as well as the determination of, if any, metal incorporation into the SiO$_x$ layer. This is the key area of interest in this chapter, where metal incorporation suggests that the Ti device operates under the ECM mechanism (discussed in detail in Part I of the thesis). In ECM devices, metal incorporates into the dielectric layer to form a conductive filament. Electron transport is then facilitated by the conductive filament to provide a low resistance state. Additionally, the microstructure of the SiO$_x$ layer is another important area to investigate. Specifically, the presence and nature of columnar structure is of particular interest. The added benefit of studying the Ti device, with comparatively smoother interfaces that the Au-Ti device, is that the effect of Mo roughness on the SiO$_x$ microstructure can be probed.

In this chapter, the methods described in section 9.4 are used to characterise the Ti device in its pristine and electroformed states. This involves a combination of STEM and EELS to understand the microstructure of the pristine device post fabrication. The same combination of STEM and EELS is then used to characterise the devices after positive (+15 V, 1 mA current compliance) and negative (-15 V, 1 mA current compliance) electroforming to provide a direct comparison. From this, it is intended that the chemical changes observed post stressing will give insight into the structural dynamics due to electrical stress that occurs in the Au-Ti device and SiO$_x$ devices in general.

10.2 Pristine Ti-SiO$_x$-Mo (Ti) RRAM device

10.2.1 HAADF Analysis

Fig. 10.1 shows a HAADF STEM image of the pristine Ti device, where the thickness of the Mo, SiO$_x$ and Ti layers are measured to be approximately 70 nm, 25 nm and 80 nm, respectively. Comparing these thicknesses to the values expected from fabrication (65 nm, 25 nm and 85 nm, respectively) shows that, whilst the reactive sputtering technique gives an accurate deposition rate and thickness, the thermal

evaporation method is inaccurate with the Mo and Ti layers having an error of +5 nm and -5 nm, respectively. It should be noted that the Mo and Ti layers each have a high degree of roughness adding uncertainty into the measurement. Fig. 10.1 also shows that the roughness at the SiO_x/Mo interface is seen to shape the SiO_x layer, which has a very constant thickness across the device. This leads to the roughness at the SiO_x/Mo interface projected at the Ti/SiO_x interface. The patterning effect is discussed in more detail for the Au-Ti device, where the increased roughness exaggerates the effect (see section 12.2.1).

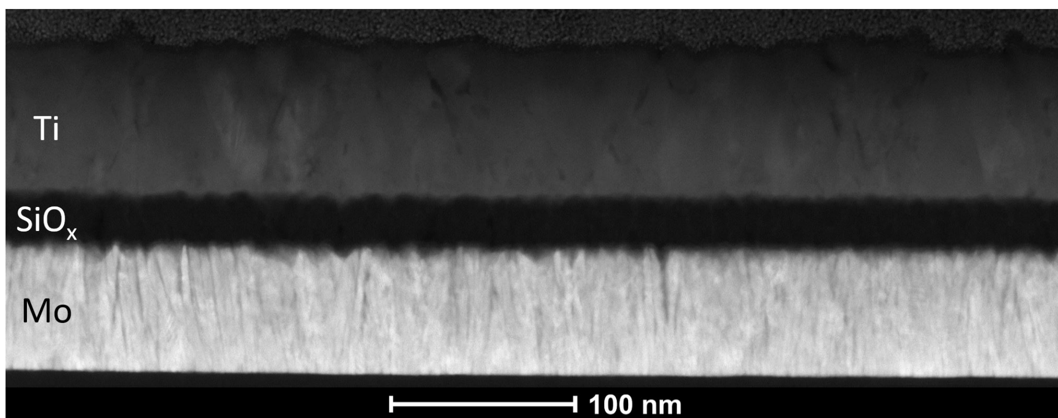

Figure 10.1: HAADF image of the pristine Ti device

Fig. 10.2 shows that the Mo layer contains very long and thin columns. The columnar structure can be seen to form during the initial phases of Mo growth, where some columns begin to dominate over others as growth continues. The roughness of the Mo layer is found to be a result of the columnar structure, where the peaks of the Mo layer occur at the column bulk positions and the troughs occur where the columns coalesce. The low HAADF intensity regions in between the columns suggests that the column boundaries contain considerably less material than the column bulk. The two horizontal red lines on Fig. 10.2 represent the min/max of the Mo layer roughness, which was found to give the min/max roughness to be 11 nm.

The columnar structure and roughness of the Mo layer leads to columnar structure and patterning of the SiO_x layer. From Fig. 10.3, this effect is shown to occur very distinctly at the troughs of the SiO_x/Mo interface. At the trough locations

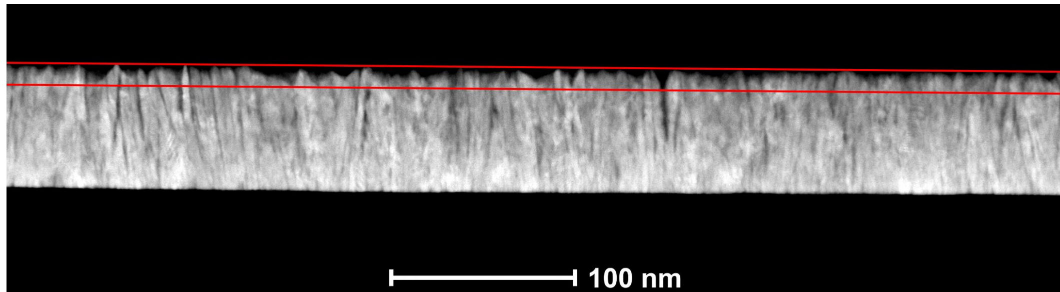

Figure 10.2: HAADF image of the Mo layer in the Ti device. The horizontal red lines mark the minimum and maximum heights of the interface, from which the min/max roughness is measured to be 11 nm

shown on Fig. 10.3a (marked by blue arrows), very dark or very bright boundaries are formed in the SiO_x layer shown more clearly on Fig. 10.3b. The width of these boundaries is seen to vary greatly in the device with little correlation found between the trough width and boundary width. The height of the boundaries is also variable with some propagating a few nm into SiO_x and others spanning the entire SiO_x layer. The normalised intensity profile taken along the SiO_x layer, marked by the vertical red lines on Fig. 10.3b, is shown on Fig. 10.3c. The four largest spikes in the intensity (marked with blue arrows) each occur at trough regions at the SiO_x/Mo interface. Three of these spikes correspond to the intensity of the SiO_x layer being significantly reduced, where the intensity drops to as low as 10 %. In HAADF images, a major contributor to the intensity (or brightness) is Z-contrast as discussed in section 3.3.2.1. A 90 % drop in intensity therefore suggests the SiO_x layer contains low-density regions or even voids at the SiO_x/Mo interface troughs. Conversely, one spike shows that the intensity of a boundary spanning the SiO_x layer is considerably increased. In this case, it is suggested that the boundary contains metal that has incorporated into the void boundary, locally increasing the density.

Fig. 10.4 shows a similar HAADF image where a large dark region is formed in the SiO_x layer at a trough in the SiO_x/Mo interface. Fig. 10.4c shows the normalised intensity of the SiO_x layer within the vertical red lines marked on Fig. 10.4b. It can be seen that the HAADF intensity drops significantly to 2.3 % compared to the brightest point in the SiO_x profile and 4.4 % compared to the mean intensity of the SiO_x profile. Again, such a drastic drop suggests that this region is a void due to the

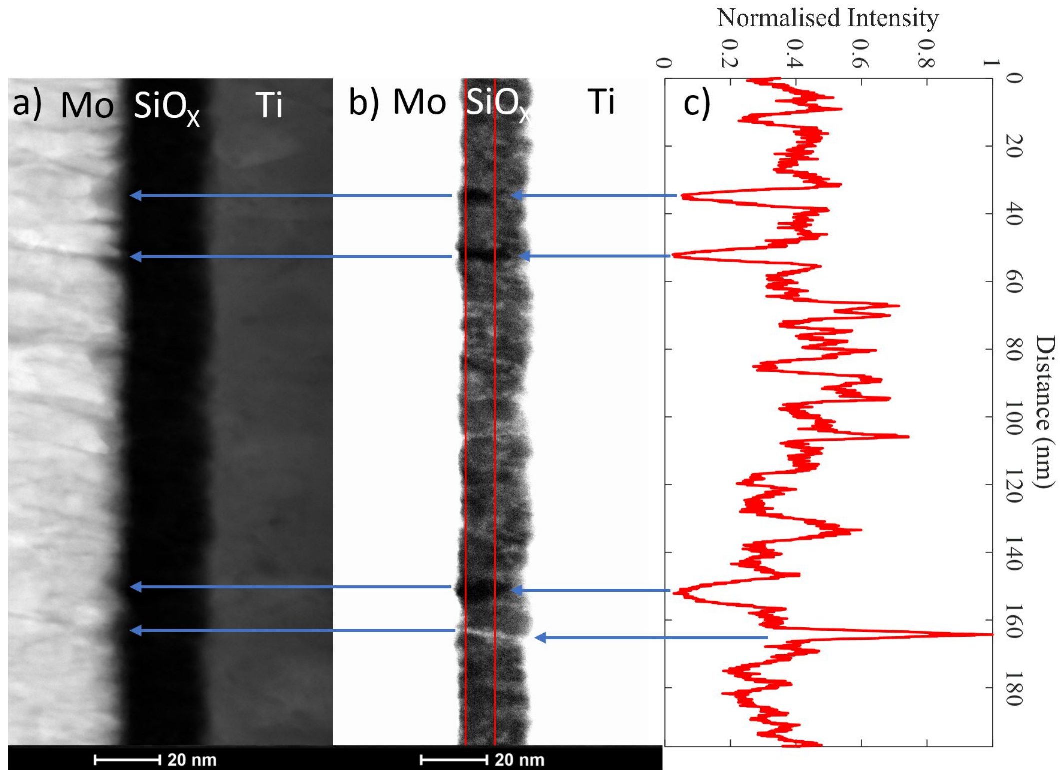

Figure 10.3: HAADF image of the Ti device showing the effect of the SiO_x/Mo interface roughness on SiO_x microstructure. a) HAADF image of the Ti device, b) HAADF image of the Ti device with the intensity limits adjusted to elucidate the SiO_x layer. The vertical red lines mark the region the normalised HAADF intensity profile c) is taken. The blue arrows show the position of peaks in the normalised HAADF intensity occur at trough positions in the SiO_x/Mo interface

small likelihood of such a low density SiO_x occurring. Also from Fig. 10.4b, bright conical regions can be seen in the SiO_x layer at the Ti/SiO_x interface. The bright regions protrude from troughs in the Ti layer, which in turn are located at troughs in the Mo/SiO_x interface. The cause of the bright regions is expected to be due to Ti incorporating into SiO_x to partially fill void areas.

Fig. 10.5 shows a HAADF STEM image of the Ti electrode. From this the Ti layer is seen to be polycrystalline. The min/max roughness of Ti at the Ti/SiO_x interface was measured to be 7 nm.

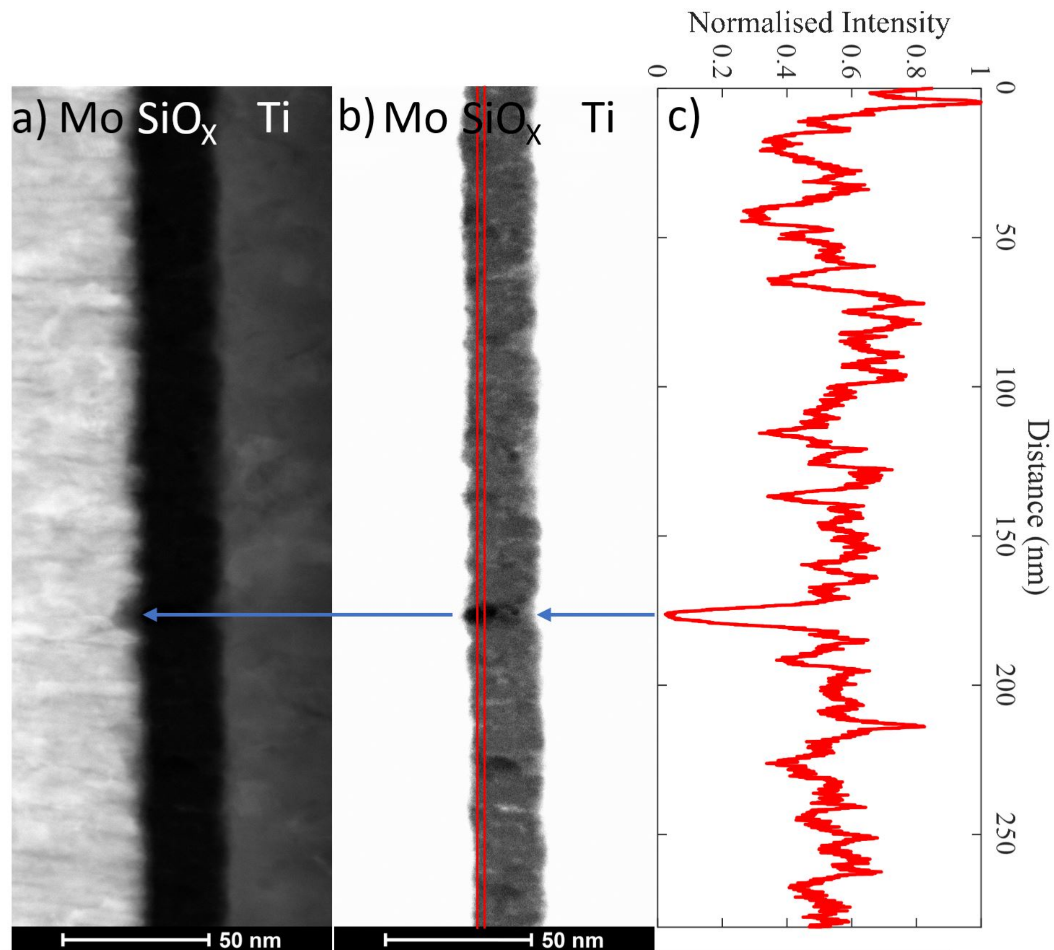

Figure 10.4: HAADF analysis of the Ti device showing the presence of a void region located at a large trough at the SiO$_x$/Mo interface. a) HAADF image of the Ti device, b) HAADF image of the Ti device with the intensity limits adjusted to elucidate the SiO$_x$ layer. The vertical red lines mark the region the normalised HAADF intensity profile c) is taken. The blue arrows show the normalised HAADF is significantly reduced at the trough position in the SiO$_x$/Mo interface

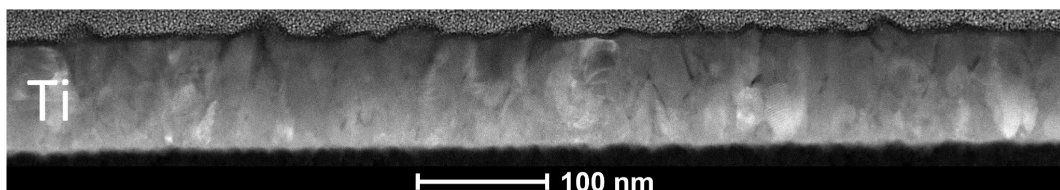

Figure 10.5: HAADF image of the Ti layer, showing the layer is polycrystalline

10.2.2 EELS Analysis

Characterisation of the pristine Ti device was continued through EELS measurements. Results are shown on Fig. 10.6, where b) to d) give image maps of the extracted EELS Ti $L_{2,3}$, O K and Si $L_{2,3}$ edges respectively. The vertical blue lines on Fig. 10.6 mark the region from which the line profile shown on Fig. 10.7 is taken. The same methods and markings are used for all EELS measurements discussed in this chapter.

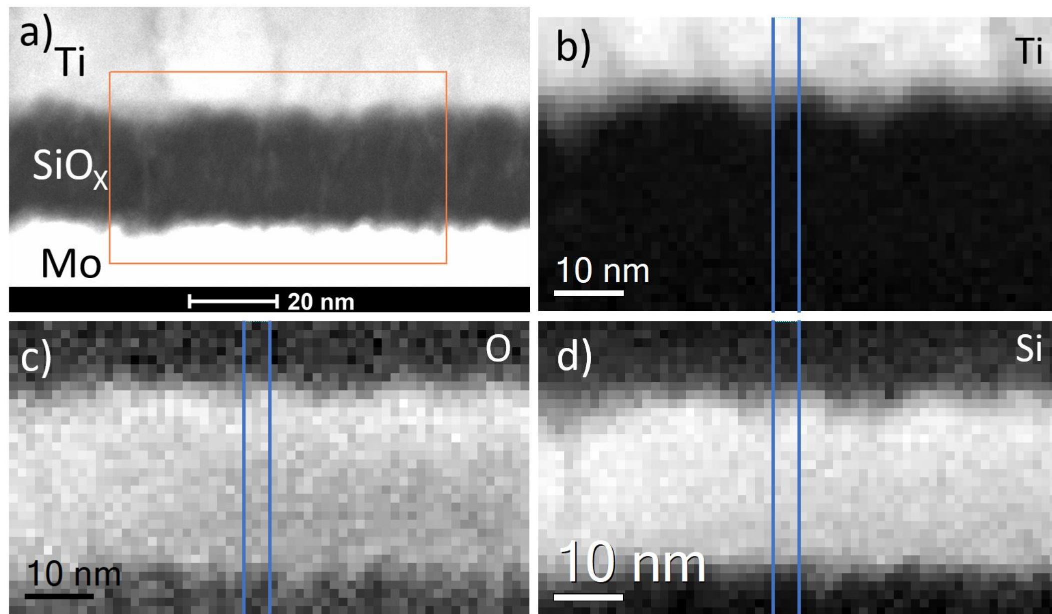

Figure 10.6: EELS data for the pristine Ti device. a) shows a HAADF image of the device where an EELS measurement is taken within the orange box. The extracted Ti $L_{2,3}$, O K and Si $L_{2,3}$ edge maps are shown in b) - d) respectively

The Ti image map on Fig. 10.6b shows that the Ti layer has approximately 9 nm of roughness. The patterning of the Ti layer can be seen in the Si image map, where the respective troughs align. Interestingly, to the left of the EELS measurement, the HAADF image shows a column of bright intensity in the SiO$_x$ layer spanning from Mo to Ti. This region can be seen to occur at a trough of the Ti/SiO$_x$ interface. In the same region, the O and Si image maps c) and d) respectively show reduced intensity at the column region. This suggests that the bright column is likely due to metal incorporation.

Fig. 10.7 shows that the O K edge is detected in the Ti layer before the Si $L_{2,3}$

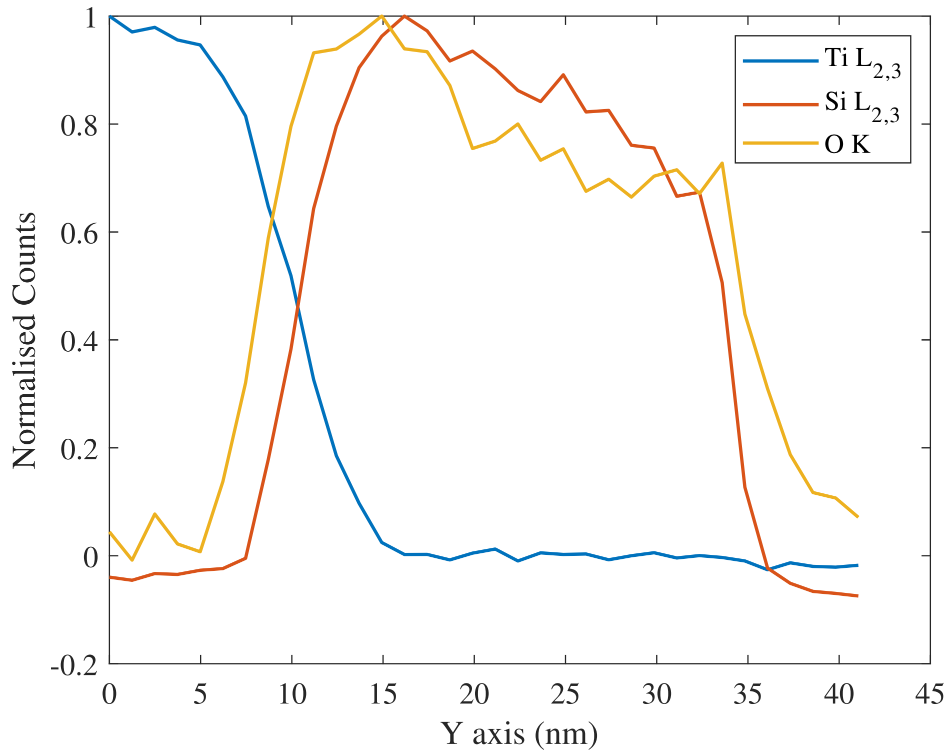

Figure 10.7: Line profile of the Ti $L_{2,3}$, O K and Si $L_{2,3}$ edges for Ti device taken within the blue vertical lines marked in Fig. 10.6

edge. From this, it is determined that approximately 2.4 nm of Ti is oxidised along the Ti/SiO_x interface. It should also be noted that the counts for O and Si in SiO_x are highest near the Ti layer and reduce towards Mo. This is suggested to be a result of a number of factors beginning with the patterning of SiO_x onto Mo. The HAADF images of the pristine Ti device show void (or low density) regions form at troughs in the SiO_x/Mo interface. This in turn would lead to a reduction in EELS counts near Mo. Additionally, as Ti scavenges O from SiO_x to form TiO_x, O is expected to accumulate near Ti increasing the counts near the Ti/SiO_x interface.

A separate EELS measurement was taken to analyse the O K edge prepeak, which is formed when the O p-states interact with metal d-states (as discussed in section 9.4.1). This allows the O K edge counts from SiO_x to be separated from transition metal oxide states. Fig. 10.8 shows an EELS measurement where the Ti $L_{2,3}$, O K (total), O K prepeak (O_{Pre}) and O K SiO_x (O_{Si}) edges are extracted. From this, it can be seen that both Ti and Mo are oxidised at the interfaces (Fig. 10.8d).

The corresponding line profiles (Fig. 10.9), show the Ti electrode is considerably more oxidised than Mo.

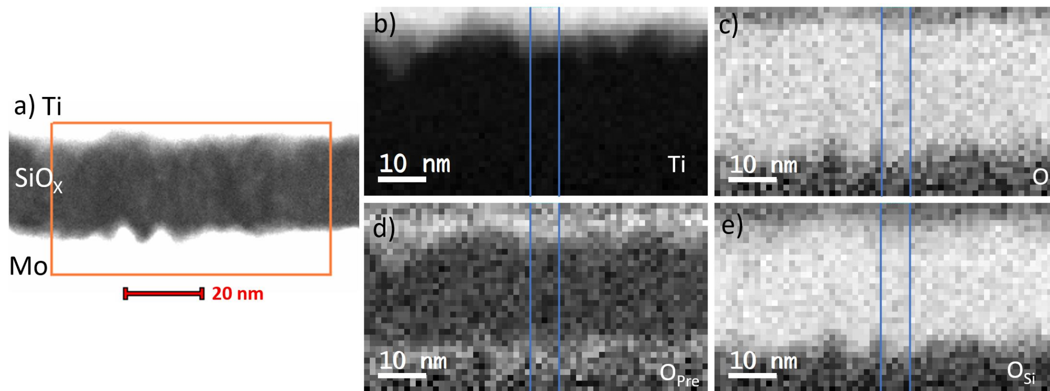

Figure 10.8: EELS data for the pristine Ti device. a) shows a HAADF image of the device where an EELS measurement is taken within the orange box. The extracted Ti $L_{2,3}$, O K (total), O K prepeak (O_{Pre}) and O K SiO$_x$ (O_{Si}) edge maps are shown in b) - e) respectively

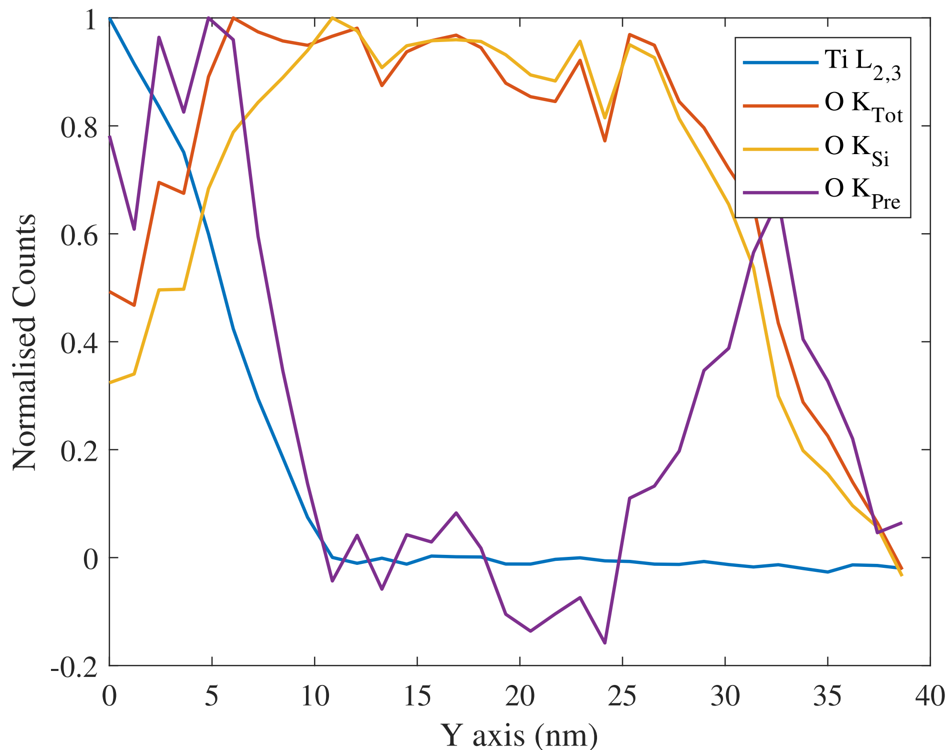

Figure 10.9: Line profile of the Ti $L_{2,3}$, O K (total), O K prepeak (O_{Pre}) and O K SiO$_x$ (O_{Si}) edges for Ti device taken within the blue vertical lines marked in Fig. 10.8

Fig. 10.10 shows the results of average scans (see section 9.4.2) of the Ti $L_{2,3}$

and O K edges along the Ti/SiO$_x$ interface, and inside the SiO$_x$ layer in increments of 2 nm from Ti. The results confirm the Ti electrode is highly oxidised given the presence of the O K edge prepeak at the Ti/SiO$_x$ interface. Ti is detected in the SiO$_x$ layer, where the intensity of the Ti L$_{2,3}$ edge gradually decreases until only traces are detected 10 nm from the Ti/SiO$_x$ interface. No Ti L$_{2,3}$ signal was detected 12 nm into SiO$_x$ from the Ti layer. Analysis of the Ti L$_{2,3}$ edge fine structure shows that two trends occur as scans are taken in SiO$_x$ away from the Ti/SiO$_x$ interface. Firstly, the Ti L$_{2,3}$ edge onset gradually shifts up in energy from 452 eV (Ti/SiO$_x$ interface) to 459 eV (10 nm in SiO$_x$ below Ti). Secondly, the ratio of the Ti L$_2$ edge and the Ti L$_3$ edge counts changes further into SiO$_x$. The L$_2$ edge is initially higher in magnitude than the L$_3$ edge at the Ti/SiO$_x$ interface. The L$_3$ and L$_2$ edges then tend towards equal magnitude as the average scans are taken incrementally away from Ti. As a result, the L$_2$ and L$_3$ edge have an equal number of counts 8 nm into SiO$_x$. The changes in edge onset energy and peak height ratio show that Ti is more oxidised the further it is detected into SiO$_x$ (see section 9.4.1).

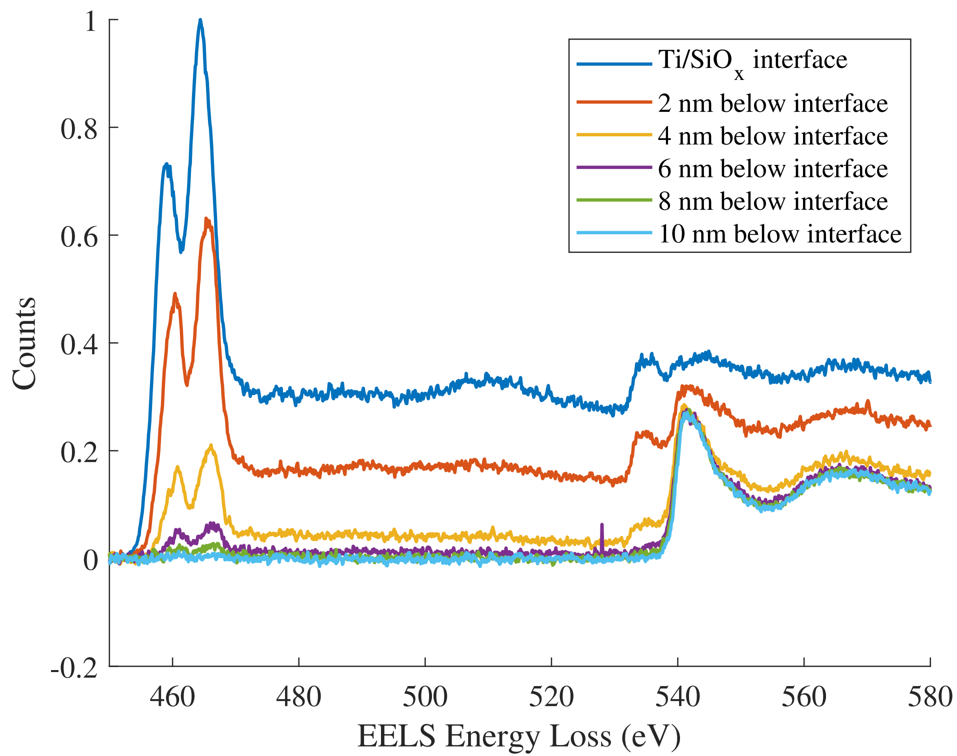

Figure 10.10: EELS spectra taken across the Ti/SiO$_x$ interface and up to 10 nm into the SiO$_x$ layer. Measurements in the SiO$_x$ layer were taken in increments of 2 nm away from the Ti/SiO$_x$ interface measurement. For each spectra, the average scan method as described in section 9.4.2 was used to collect the data.

10.3 Electroformed Ti-SiO$_x$-Mo (Ti) RRAM device

10.3.1 IV curve

To determine the IV characteristics of the Ti device, four Ti devices were each swept under a positive bias (+15 V) and another four under a negative bias (-15 V). For each sweep, the voltage was increased from 0 V to +15 V or -15 V, respectively, and back to 0 V in increments of 0.05 V. The current compliance for each sweep was set to 1 mA to prevent a hard dielectric breakdown of the devices. The IV characteristics for both positive and negative electroforming were very repeatable showing consistency across devices. TEM lamellas were prepared for one positive electroformed device and one negative electroformed device, with the respective IV curves shown on Fig. 10.11.

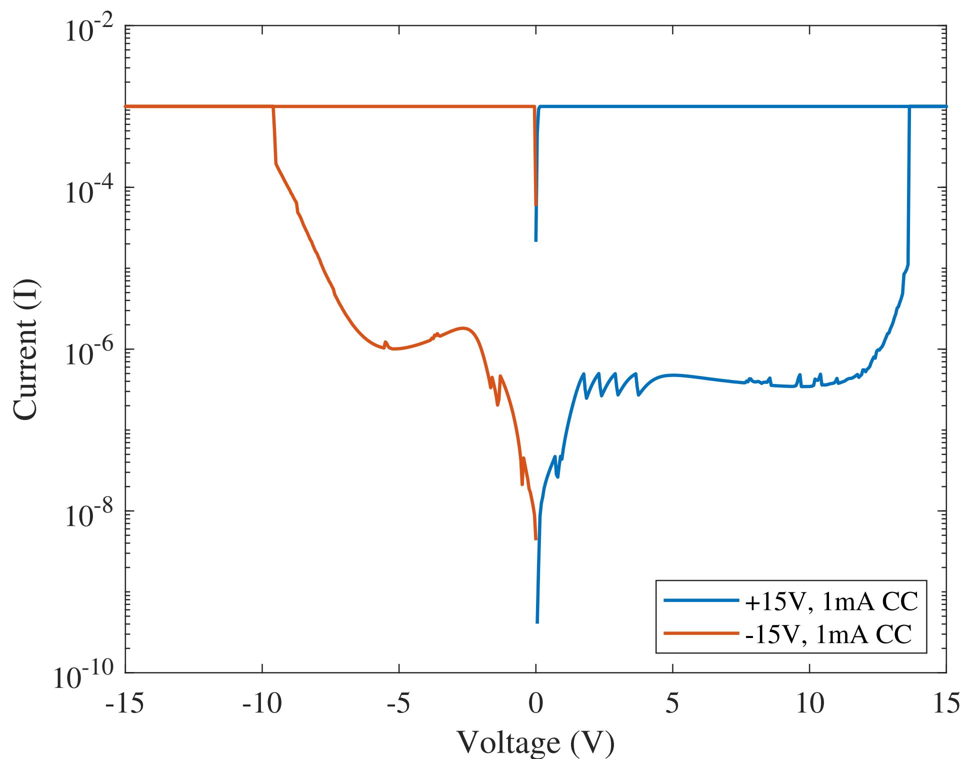

Figure 10.11: IV curves of the Ti device after positive (blue) and negative (orange) electroforming.

Under a positive bias, a non-linear rise in the current is seen as the voltage is increased from 0 to 2 V. The current then remains relatively constant at 10^{-7}A as the voltage is increased to 11 V. The current then increases drastically as the voltage

is increased from 11 V until it reaches the 1 mA current compliance at 13.7 V. As the voltage is swept back to 0 V the current measured remains at 1 mA marking a clear change in the resistance of the device. Under a negative bias, a sharp rise in the current is detected until -2.6 V. Interestingly, the current then decreases as the voltage is increased further dropping from 1.8x10^{-6}A at -2.6 V to 1.1x10^{-6}A at -6 V. Subsequently, the current rises sharply to the 1 mA current compliance reaching saturation at -9.6 V. Again, the current remains at 1 mA as the voltage is swept back to 0 V marking a clear resistance change.

Comparing the Ti device under positive and negative electroforming, the 1 mA current compliance was reached at 13.7 V and -9.6 V, respectively. This difference suggests that the mechanisms involved in the soft dielectric breakdown of the device under each bias is markedly different. The cause of this difference is expected to be due to a combination of factors beginning with the electron transport into defects within the device under bias. In this case, a positive or negative bias has an opposite effect on the Fermi level of the Ti electrode relative to the SiO$_x$ band gap. Under a positive bias, the Fermi level shifts downwards with respect to the band gap compared to an upward shift for a negative bias. This in turn affects the probability of electron and hole injection from the Ti electrode into defects in the SiO$_x$ layer. However, the exact mechanisms are unclear without a characterisation of the devices. The metal-oxide interfaces and the subsequent charging of the interfaces under bias are expected to play a significant role. In a similar fashion, the polarity of the bias is also expected to determine if electrode metal incorporates into the SiO$_x$ layer. This is because Ti usually adopts positive charge states, and is only expected to incorporate under a positive bias [138].

10.3.2 Positive electroformed Ti Device

Fig. 10.12 shows a HAADF image of the positive electroformed Ti device. From this, it can be seen that there still exist dark regions at the trough locations at the SiO$_x$/Mo interface. However, a much higher concentration of bright regions can be seen protruding from the Ti/SiO$_x$ interface compared to the pristine device. This is indicative of additional Ti diffusing into SiO$_x$ as a result of positive electroforming.

In some cases these bright regions span the SiO$_x$ layer, though it is important to note that this may also be due to Mo incorporation from the SiO$_x$/Mo interface.

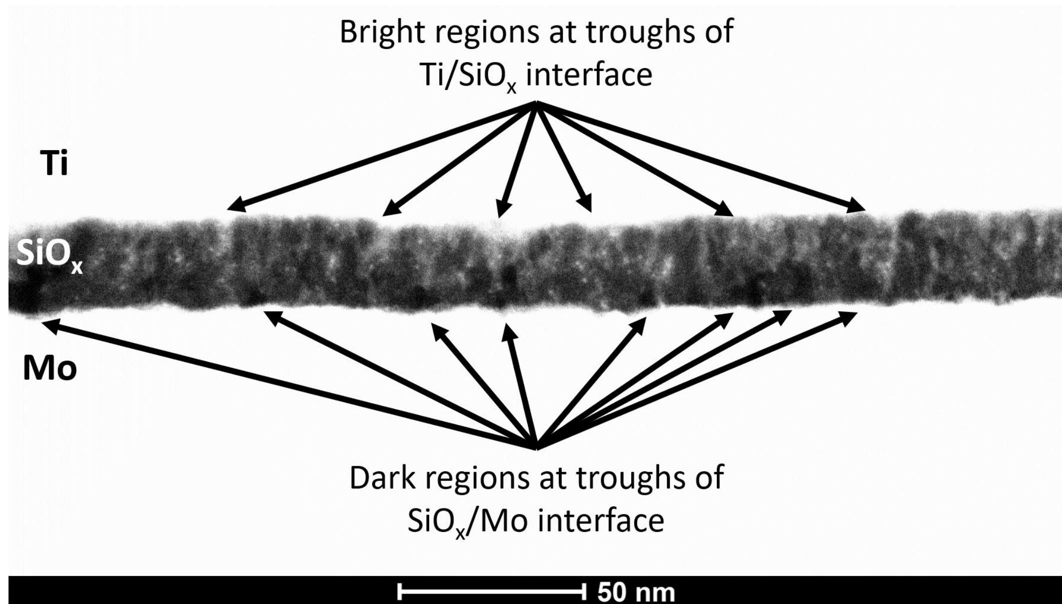

Figure 10.12: HAADF image of the positive electroformed Ti device. Dark regions in the SiO$_x$ layer are marked at the troughs of the SiO$_x$/Mo interface whilst bright regions in the SiO$_x$ can be seen at the Ti/SiO$_x$ interface.

Fig. 10.13 shows the results of an EELS measurement on the positive electroformed Ti device, where the extracted Ti $L_{2,3}$, Si $L_{2,3}$ and O K edges are shown on b) through d). Fig. 10.13a shows a HAADF image of the device, where the EELS measurement is taken within the orange box. From Fig. 10.13a it can be seen that the measurement is taken in a region where there is a large trough in the SiO$_x$/Mo interface. The vertical blue lines on Fig. 10.13 mark two regions (R1 and R2) where line profiles of the Ti $L_{2,3}$, Si $L_{2,3}$ and O K edges are taken and shown on Fig. 10.14. In this case, R1 marks a relatively smooth region of the SiO$_x$/Mo interface, whilst the large trough occurs in R2. Comparing R1 and R2, the line profiles on Fig. 10.14 show the trough region is filled with Si and O, with the Si $L_{2,3}$ and O K edge counts dropping to between 20 and 40 % of the SiO$_x$ bulk. Interestingly, the Ti incorporation at each region is very similar, where Ti can be measured up to 15 nm into SiO$_x$. From R2 in the extracted Ti $L_{2,3}$ image map (Fig. 10.13b), Ti can be seen to protrude into SiO$_x$ in the form of a thin rod from a trough of the Ti/SiO$_x$ interface. This is suggested to be Ti filling a columnar boundary in SiO$_x$,

which is formed from the trough of the SiO_x/Mo interface. Multiple less intense rods can also be seen protruding from the Ti/SiO_x interface again appearing to form filaments in SiO_x.

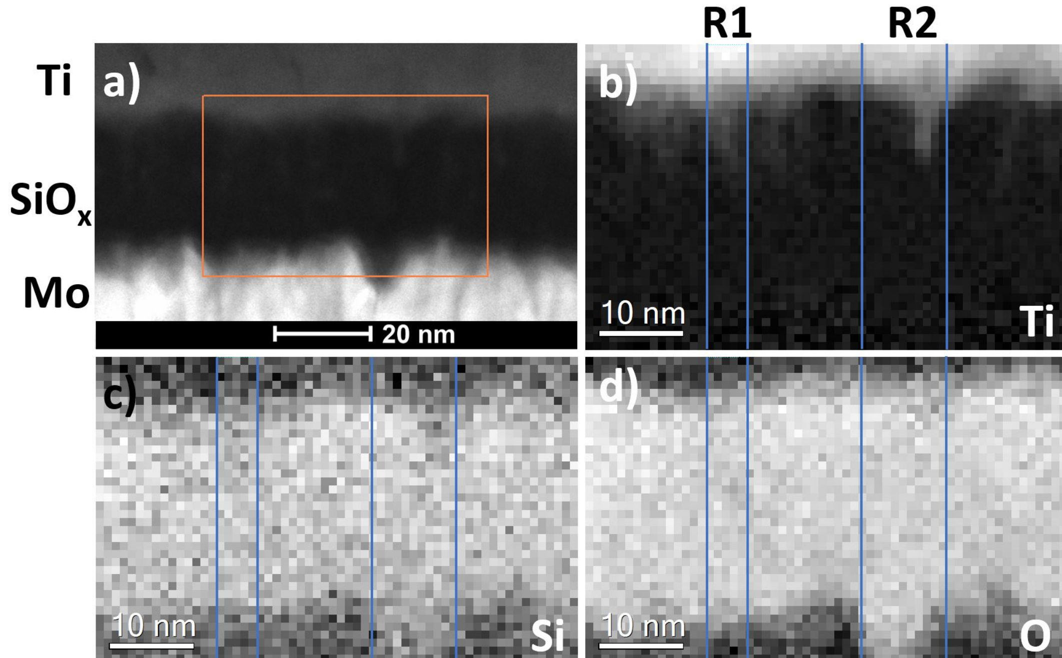

Figure 10.13: EELS data for the positive electroformed Ti device. a) shows a HAADF image of the device where an EELS measurement is taken within the orange box. The extracted Ti $L_{2,3}$, Si $L_{2,3}$ and O K edge maps are shown on b) - d) respectively. The blue lines mark two regions (R1 and R2) from which the lineprofiles shown on Fig. 10.14 are taken.

Figs. 10.15 and 10.16 show an EELS measurement of Ti $L_{2,3}$ and O K edges taken for the positive electroformed Ti device. In this case, the O K edge contribution to the EELS spectrum is separable into the O K edge prepeak component and the O K edge from SiO_x component. Fig. 10.15a shows a HAADF image of the Ti device, where the EELS measurement is taken within the orange box. The extracted Ti $L_{2,3}$, O K edge (total), O K edge prepeak and O K edge for SiO_x image maps are shown on b) through e) respectively. The blue lines on b) through e) mark the regions from which the line profiles on Fig. 10.16 are shown.

The results show the Ti electrode is oxidised at the Ti/SiO_x interface, with the O K edge prepeak image map suggesting between 5 to 10 nm of the Ti electrode is oxidised (compared to 2.4 nm for the pristine device). The Ti line profile shown

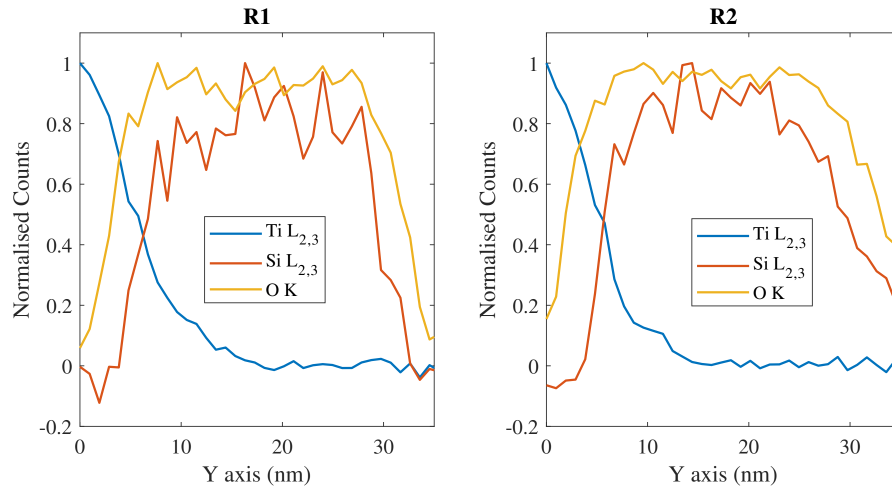

Figure 10.14: Line profiles of the Ti $L_{2,3}$, Si $L_{2,3}$ and O K edges for positive electroformed Ti device taken within two regions (R1 and R2) marked by the blue vertical lines on Fig. 10.13

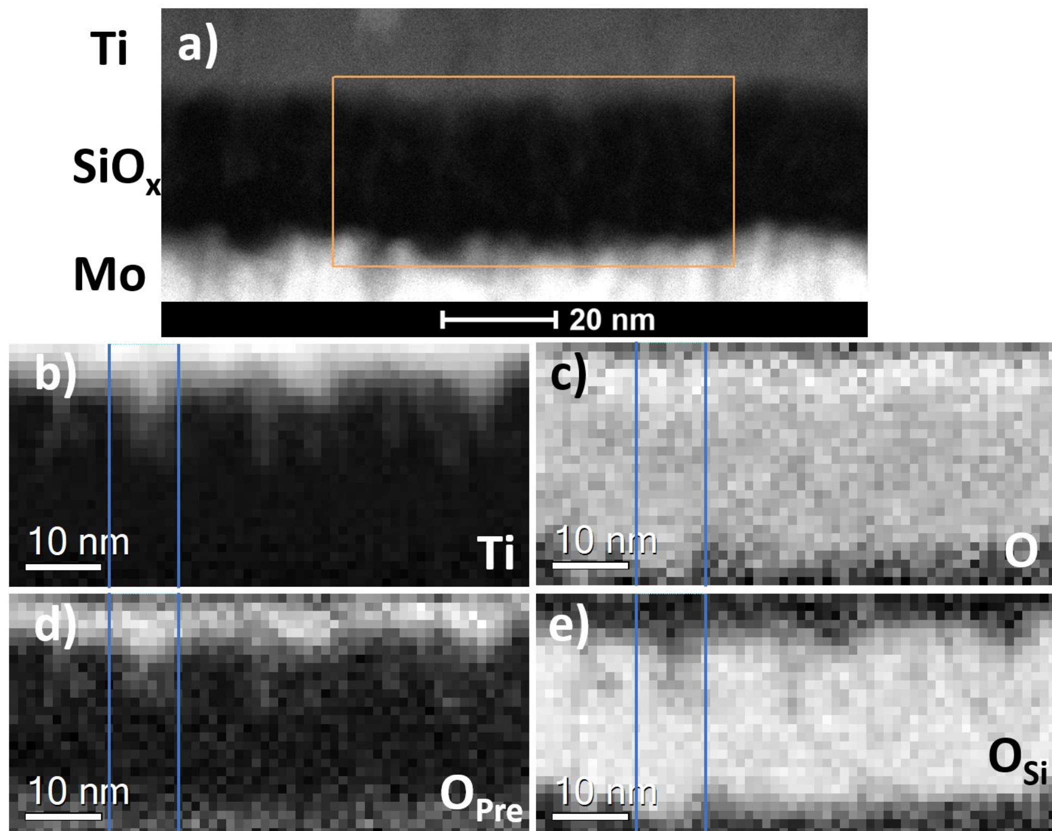

Figure 10.15: EELS data for the positive electroformed Ti device. a) shows a HAADF image of the device where an EELS measurement is taken within the orange box. The extracted Ti $L_{2,3}$, O K (total), O K prepeak (O_{Pre}) and O K SiO_x (O_{Si}) edge maps are shown on b) - e) respectively. The blue lines mark the region from which the lineprofiles shown on Fig. 10.16 are taken.

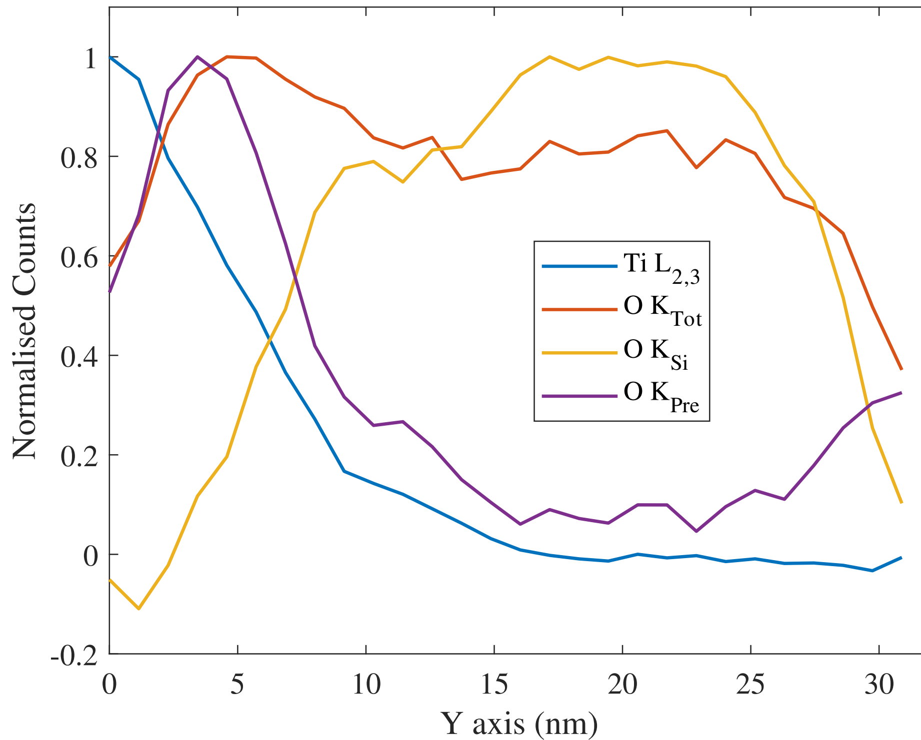

Figure 10.16: Line profiles of the Ti $L_{2,3}$, O K (total), O K prepeak (O_{Pre}) and O K SiO$_x$ (O_{Si}) edges for the positive electroformed Ti device taken within the blue vertical lines marked on Fig. 10.15

on Fig. 10.16 is taken at a region where Ti has incorporated into SiO$_x$, showing Ti has incorporated at least 15 nm into SiO$_x$. The features of the Ti $L_{2,3}$ and O K edge prepeak image maps are very similar, suggesting that the Ti that has incorporated into SiO$_x$ is oxidised. Furthermore, the O K edge prepeak is seen throughout the SiO$_x$ layer, where the counts at 15 nm into SiO$_x$ (region where Ti $L_{2,3}$ edge drops to 0%) is 6 % compared to those at the Ti/SiO$_x$ interface. This signal remains near 6 % until 20 nm from the Ti/SiO$_x$ interface where it increases toward the SiO$_x$/Mo interface. The total O K edge prepeak counts at the SiO$_x$/Mo interface are 30 % of that measured at the Ti/SiO$_x$ interface. This suggests that Mo incorporates into the SiO$_x$ layer and is subsequently oxidised, whilst Mo electrode is also oxidised. With the O K edge prepeak being detected across the whole SiO$_x$ layer, it can be suggested that the low resistance state is a result of TiO$_x$ and MoO$_x$ formation in SiO$_x$. It is also important to note that the total O K edge signal across the SiO$_x$ bulk

is 20 % lower than at the Ti/SiO_x interface, showing the accumulation of O in the Ti/SiO_x interface region.

Fig. 10.17 shows the results of average EELS scans (see section 9.4.2) taken for the positive electroformed Ti device along the Ti/SiO_x interface and in the SiO_x layer. Scans were taken for the Ti $L_{2,3}$ and O K edges up to 18 nm into SiO_x at increments of 2 nm away from the Ti/SiO_x interface. Fig. 10.17 shows the EELS spectra detected up to 12 nm into SiO_x from the Ti/SiO_x interface, where the Ti $L_{2,3}$ edge is clearly discernible. The Ti $L_{2,3}$ edge was subsequently detected up to 16 nm, where only trace signal was detected and could not be discerned at 18 nm. Compared to the pristine device, where no Ti $L_{2,3}$ signal was measured at 12 nm, the results show additional Ti incorporates into SiO_x during positive electroforming.

Furthermore, the Ti $L_{2,3}$ counts at each depth compared to the Ti/SiO_x interface are considerably higher in the positive electroformed device compared to the pristine (see Fig. 10.23 for a direct comparison). Interestingly, the edge onset of the Ti $L_{2,3}$ signal has constant energy from 2 nm into SiO_x through to 12 nm into SiO_x. This suggests the oxidation state of Ti is itself relatively constant. This is different to the pristine device, where the Ti $L_{2,3}$ edge onset shifts upwards in energy deeper into SiO_x. This suggests that not only is additional Ti incorporated into SiO_x during electroforming, more O is scavenged from SiO_x to reduce Ti. This includes the Ti that is incorporated post fabrication and the Ti that is incorporated due to positive electroforming.

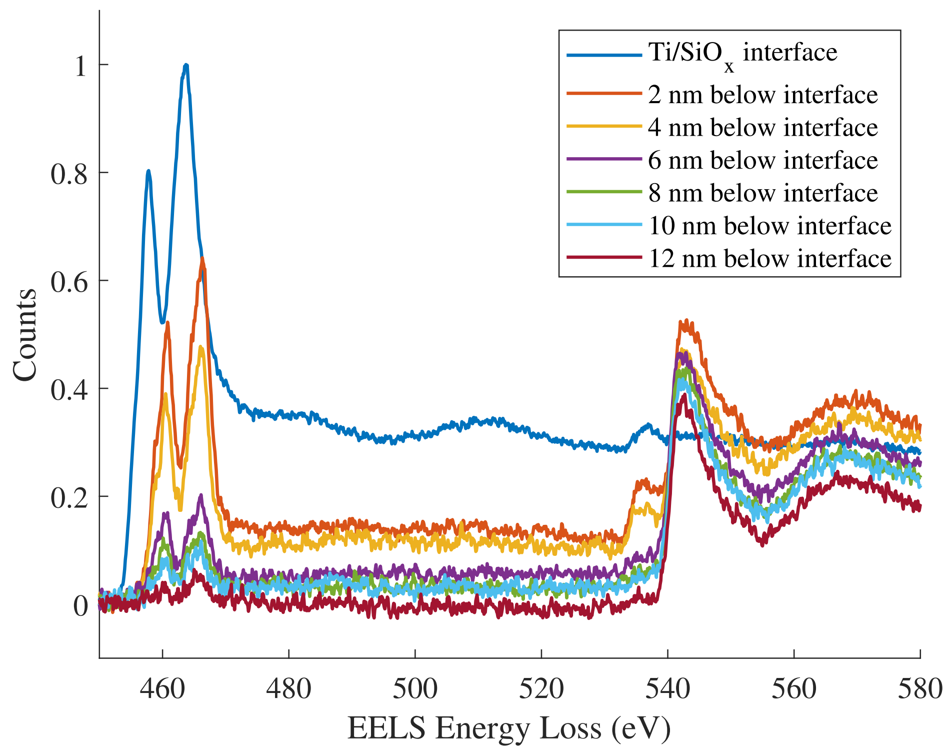

Figure 10.17: EELS spectra taken across the Ti/SiO$_x$ interface and up to 12 nm into the SiO$_x$ layer for the positive electroformed Ti device. Measurements in the SiO$_x$ layer were taken in increments of 2 nm below the Ti/SiO$_x$ interface measurement. For each spectra, the average scan method as described in section 9.4.2 was used to collect the data.

10.3.3 Negative Electroformed Ti Device

Fig. 10.18 shows the results of an EELS measurement taken for the negative electroformed Ti device, where extracted Ti $L_{2,3}$, Si $L_{2,3}$ and O K edges are given on b) through d). Fig. 10.18a shows a HAADF image of the device, where the EELS measurement is taken within the orange box. The blue lines mark the regions the line profiles shown on Fig. 10.19 are taken.

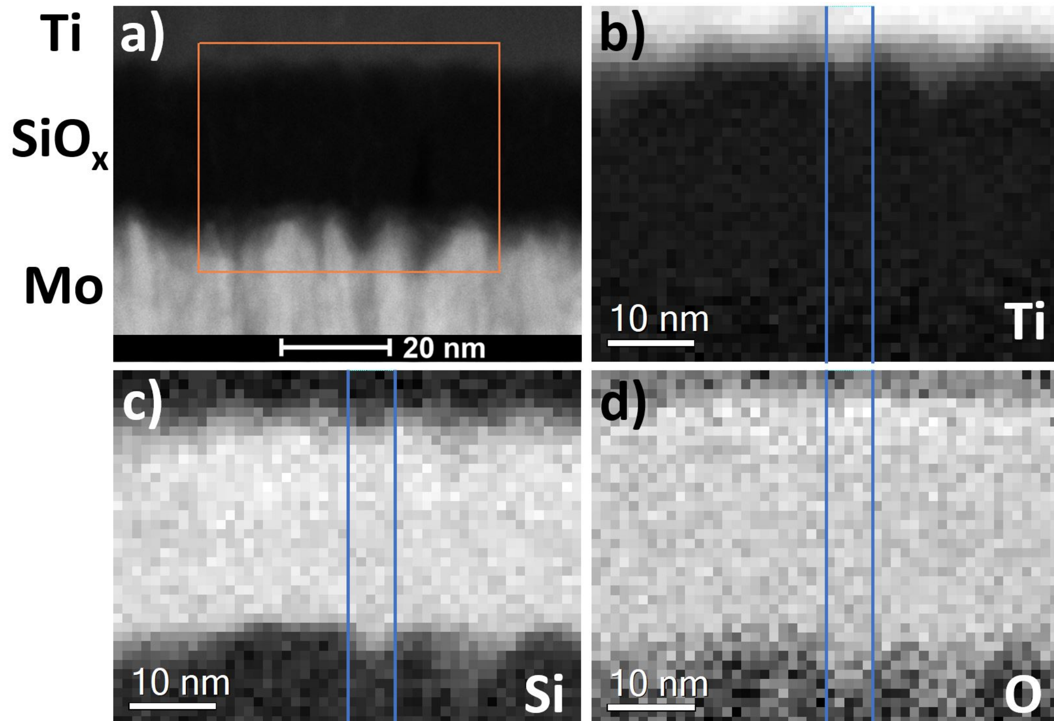

Figure 10.18: EELS data for the negative electroformed Ti device. a) shows a HAADF image of the device where an EELS measurement is taken within the orange box. The extracted Ti $L_{2,3}$, Si $L_{2,3}$ and O K edge maps are shown on b) - d) respectively. The blue lines mark the from which the lineprofiles shown on Fig. 10.19 are taken.

The HAADF image shows the EELS measurement is taken in a region of high SiO$_x$/Mo interface roughness, where two large troughs can be seen. The extracted Ti $L_{2,3}$ edge map on Fig. 10.18b shows the Ti electrode patterns to the troughs at the SiO$_x$/Mo interface. However, no Ti signal is detected in the SiO$_x$ layer at these regions. This suggests that any Ti incorporated into SiO$_x$ is below the detection limit of the measurement marking a clear difference to the positive electroformed device. Fig. 10.19 shows the O K edge is detected between 4 and 5 nm either side

of the Si $L_{2,3}$ edge. This suggests that approximately 4 to 5 nm of the Ti/SiO_x and SiO_x/Mo interfaces are oxidised. The O K edge is also seen to be at a maximum at the Ti/SiO_x interface, reducing across SiO_x with an almost constant gradient to 75 % at the SiO_x/Mo interface. This is similar to the positive electroformed device, showing O scavenging by the Ti at the Ti/SiO_x interface.

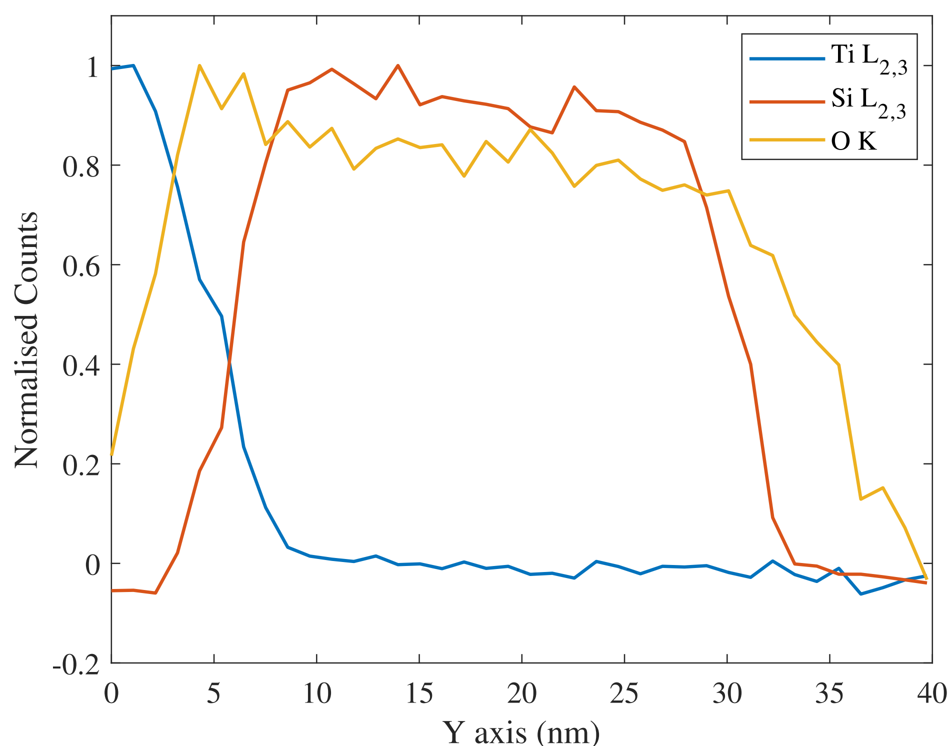

Figure 10.19: Line profiles of the Ti $L_{2,3}$, Si $L_{2,3}$ and O K edges for negative electroformed Ti device taken within the region marked by the blue vertical lines on Fig. 10.18

Figs. 10.20 and 10.21 show an EELS measurement of Ti $L_{2,3}$ and O K edges taken for the negative electroformed Ti device. Fig. 10.20a shows a HAADF image where the EELS spectrum is taken within the orange box. The extracted Ti $L_{2,3}$, O K edge (total), O K edge prepeak and O K edge for SiO_x image maps are shown on b) through e) respectively. The blue lines on b) through e) mark the regions from which the line profiles on Fig.10.21 are shown. From Fig. 10.21, it can be seen that the Ti $L_{2,3}$ signal counts reduce to 0% 6 nm into SiO_x (compared to 15 nm for the positive electroformed device). Similarly, whilst the O K edge prepeak image map

and line profile shows the Ti and Mo electrodes are both oxidised, the O K edge prepeak counts reduce to near 0% in the SiO$_x$ bulk suggesting metal oxide does not form in the SiO$_x$ bulk. Instead, it is suggested that the low resistance state is due to electron injection into O vacancies in the SiO$_x$ layer.

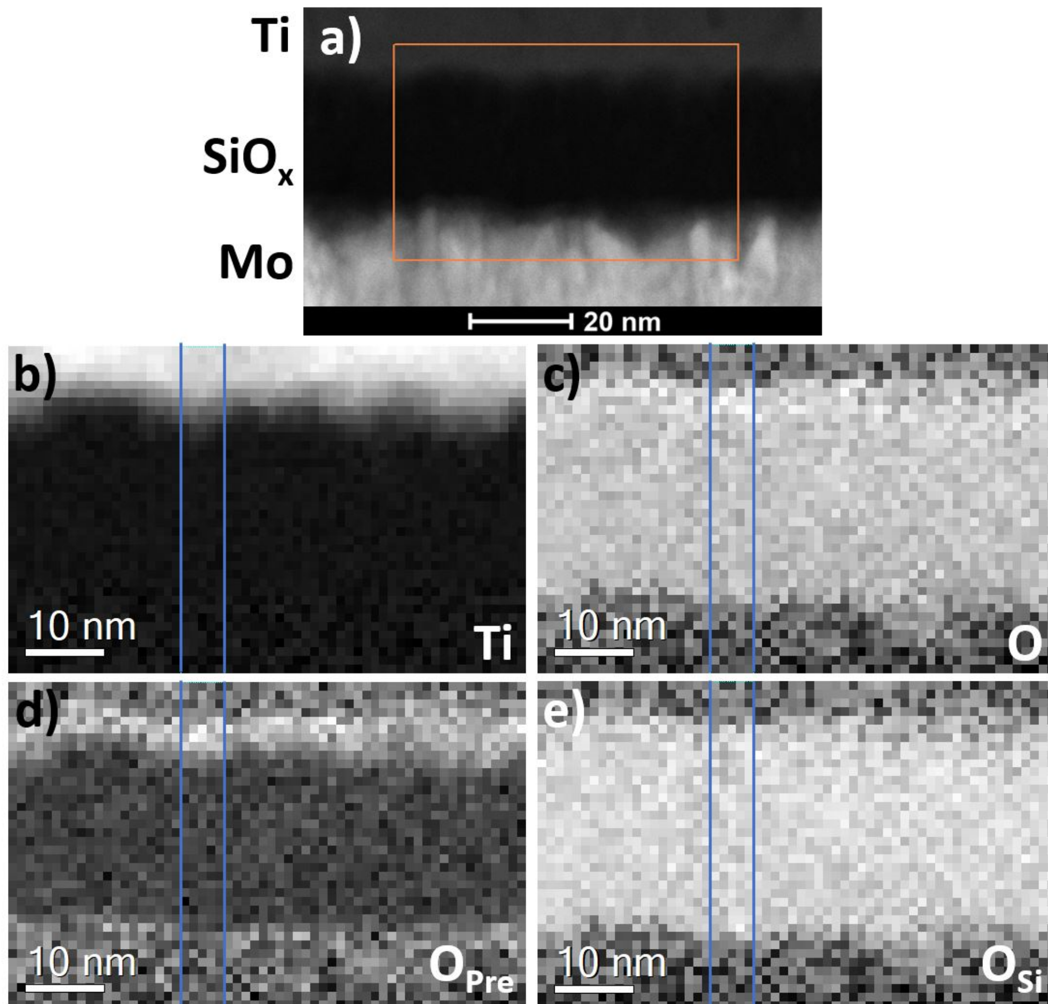

Figure 10.20: EELS data for the negative electroformed Ti device. a) shows a HAADF image of the device where an EELS measurement is taken within the orange box. The extracted Ti $L_{2,3}$, O K (total), O K prepeak (O_{Pre}) and O K SiO$_x$ (O_{Si}) edge maps are shown on b) - e) respectively. The blue lines mark the region from which the lineprofiles shown on Fig. 10.21 are taken.

Fig. 10.22 shows the results of averaged EELS scans taken for the negative electroformed Ti device along the Ti/SiO$_x$ interface and in the SiO$_x$ layer. Scans were taken for the Ti $L_{2,3}$ and O K edges up to 12 nm into SiO$_x$ at increments of 2 nm away from the Ti/SiO$_x$ interface. From Fig. 10.22, the Ti $L_{2,3}$ edge can be detected

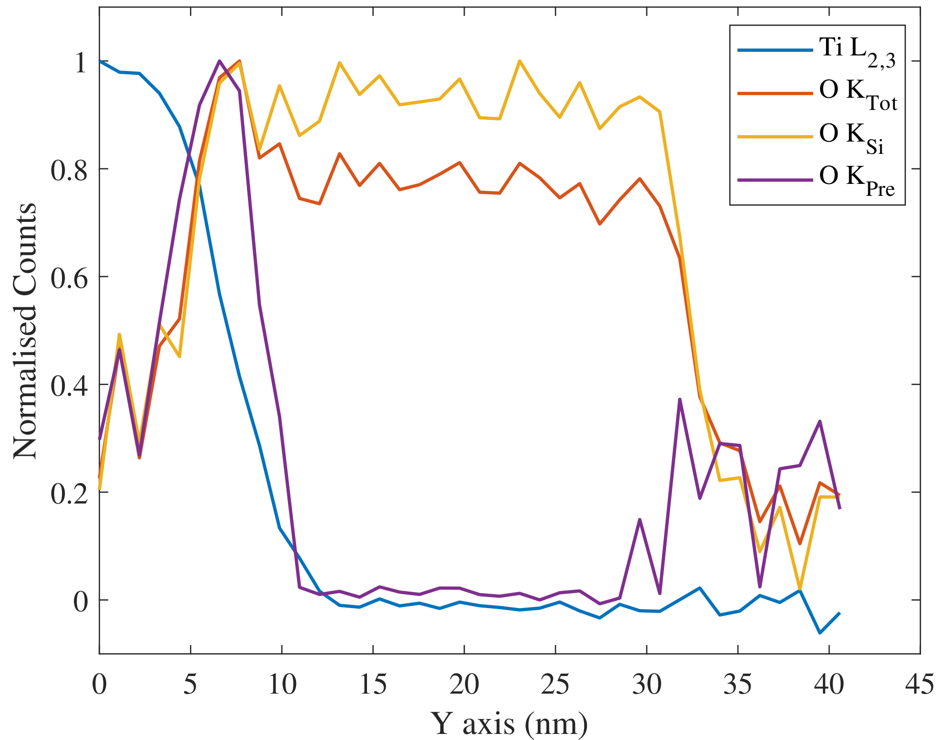

Figure 10.21: Line profiles of the Ti $L_{2,3}$, O K (total), O K prepeak (O_{Pre}) and O K SiO_x (O_{Si}) edges for negative electroformed Ti device taken within the blue vertical lines marked on Fig. 10.20

up to 10 nm into SiO_x from the Ti/SiO_x interface, similar to the pristine device. The Ti $L_{2,3}$ edge intensities in SiO_x compared to the Ti/SiO_x interface are consistent with the pristine device (see Fig. 10.23 for a direct comparison). Additionally, the Ti $L_{2,3}$ edge onset is seen to increase in energy deeper into SiO_x suggesting Ti is more oxidised as a function of distance from the Ti/SiO_x interface. The results are similar to the pristine device suggesting no additional Ti incorporates into SiO_x from negative electroforming whilst the existing Ti has not scavenged additional O.

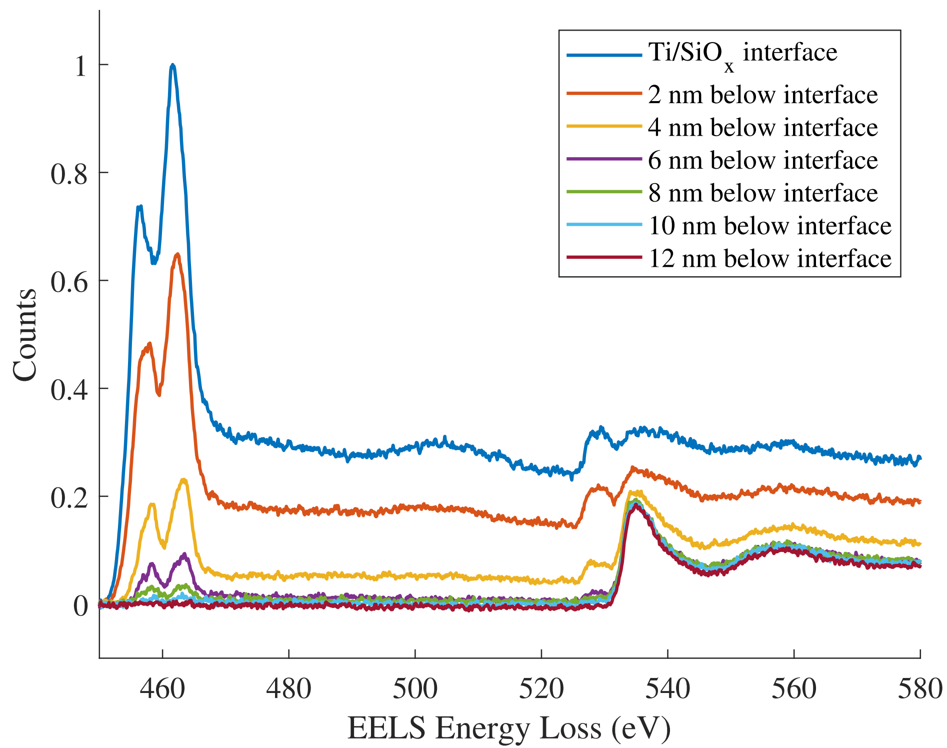

Figure 10.22: EELS spectra taken across the Ti/SiO_x interface and up to 12 nm into the SiO_x layer for the negative electroformed Ti device. Measurements in the SiO_x layer were taken in increments of 2 nm below the Ti/SiO_x interface measurement. For each spectra, the average scan method as described in section 9.4.2 was used to collect the data.

10.3.4 Ti Device comparison

The effects of electroforming in the Ti device can be understood by the migration of Ti and O in the device. Fig. 10.23 shows the normalised Ti $L_{2,3}$ edge counts measured through averaged EELS scans taken for the pristine, positive and negative electroformed devices. From this, it can be seen Ti incorporates up to 10 nm into SiO_x post fabrication. After positive electroforming, additional Ti is incorporated into SiO_x. As a result, Ti is not only detected further into SiO_x, but an increased amount of Ti is detected at a given distance from the Ti/SiO_x interface. Specifically, the Ti $L_{2,3}$ edge counts are 2.2 times higher 4 nm into SiO_x and 10 times higher at 8 nm into SiO_x. This confirms the bright regions protruding from the Ti/SiO_x interface in HAADF images are due to Ti incorporation. Under negative electroforming, no additional Ti is incorporated.

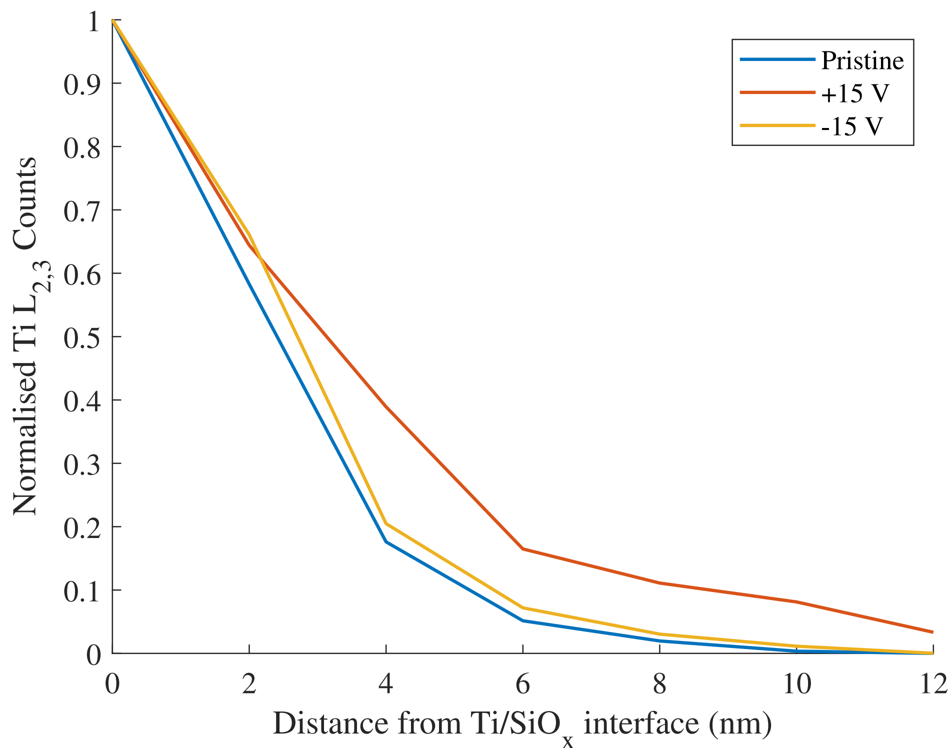

Figure 10.23: Graph showing the normalised Ti $L_{2,3}$ counts as a function of distance from the Ti/SiO_x interface. For all data points, the counts were determined through analysis of the 'averaged scan' results on Figs. 10.10, 10.17 and 10.22 respectively.

Fig. 10.24 shows a comparison of the O K edge (total) counts measured across

the Ti device in the pristine, positive and negative electroformed states. To obtain the data, the total O K edge was extracted across the entire EELS image maps shown on Figs. 10.8, 10.15 and 10.20. In the pristine device, the total O counts remain relatively constant across the SiO$_x$ layer. This differs in the electroformed devices, where O accumulation at the Ti electrode is observed. In each case, the total O counts reduce from a maximum at the Ti/SiO$_x$ interface to 78% for the positive electroformed device and 80% in the negative electroformed device at the SiO$_x$/Mo interface.

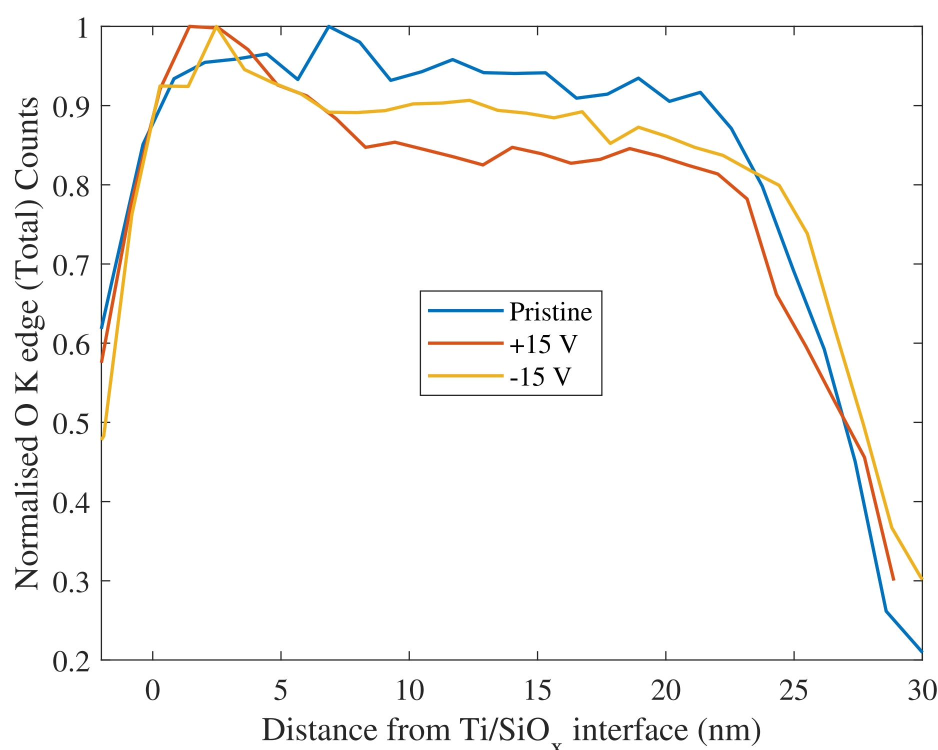

Figure 10.24: Graph showing the normalised O K edge (total) counts as a function of distance from the Ti/SiO$_x$ interface. For all data points, the counts were determined through analysis of the complete EELS O K edge maps shown on Figs. 10.8, 10.15 and 10.20 respectively.

Fig. 10.25 shows the ratio of Ti $L_{2,3}$ counts to the O K edge prepeak counts taken from the averaged scan measurements for each device. In this case, a higher ratio represents a less oxidised TiO$_x$. The results confirm previous observations that the incorporated Ti in the pristine and negative electroformed devices becomes more oxidised as a function of depth from the Ti/SiO$_x$ interface. Furthermore, the results

show that Ti is in a lower oxidation state in the positive electroformed device. This again supports the low resistance state in the positive electroformed device being due to electron transport through TiO$_x$ in the SiO$_x$ layer.

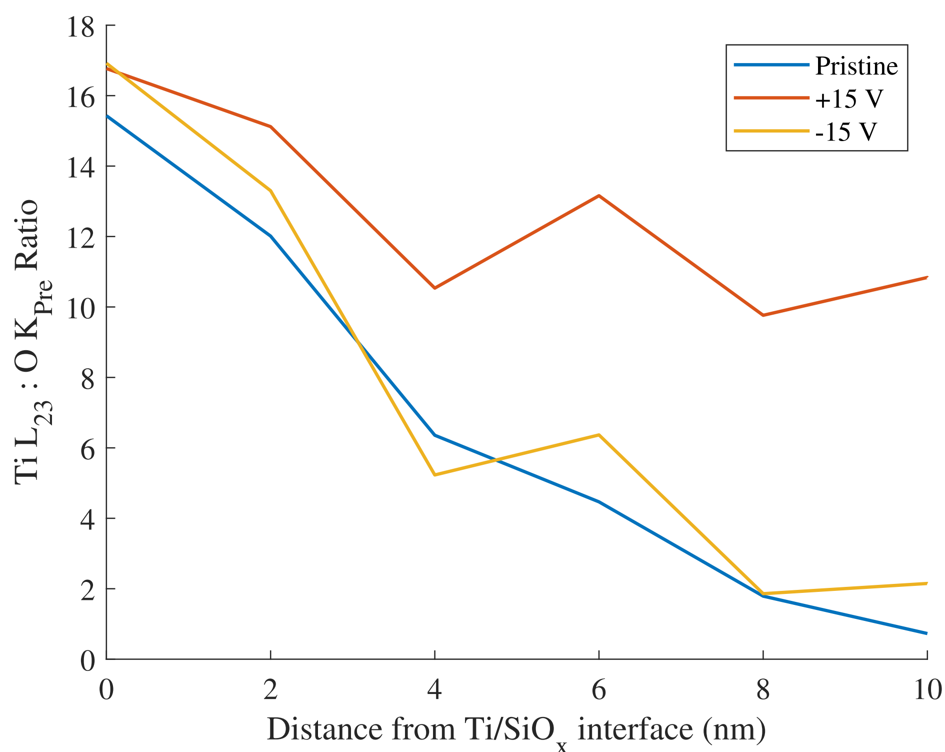

Figure 10.25: Graph showing the normalised Ti $L_{2,3}$ to O K edge prepeak counts as a function of distance from the Ti/SiO$_x$ interface. For all data points, the counts were determined through analysis of the 'averaged scan' results on Figs. 10.10, 10.17 and 10.22 respectively.

10.4 Summary of Main Results

10.4.1 Device Microstructure (Pristine)

The thickness of the Mo, SiO_x and Ti layers were measured to be approximately 70 nm, 25 nm and 80 nm, respectively. However, it should be noted that variability in the thickness measurement is introduced due to the high levels of interface roughness. The Mo layer was found to consist of very long and thin columns, which were seen to form during the initial phases of Mo growth at the Mo/substrate interface. The peaks of the columns were found to form the peaks of the Mo layer roughness, whilst the troughs were seen to occur where columns coalesced. The min/max roughness of the Mo layer was measured to be 11 nm though HAADF images.

The roughness of the Mo layer was found to pattern the SiO_x layer and subsequently the Ti layer above. HAADF imaging showed very dark contrast regions form in SiO_x at the trough regions of the SiO_x/Mo interface. In some cases, the HAADF intensity in these dark contrast regions dropped to below 5% compared with the mean SiO_x intensity, suggesting that these regions are void like, containing very little or no material. The width and height of these regions were seen to be very variable with the only constant being they occurred at trough regions at the SiO_x/Mo interface. Specifically, the width of the regions were of similar or smaller width to the respective trough. The height of the boundaries varied from a few nm to 25 nm, in which case they spanned the entire SiO_x layer. As a result, it was seen in EELS measurements that the Si $L_{2,3}$ and O K edge counts were at a maximum near the Ti/SiO_x interface and a minimum near the SiO_x/Mo interface. It should be noted that in a very small number of cases, bright regions were found at the trough positions at the SiO_x/Mo interface, where these bright regions would form a filament spanning the oxide.

The thickness of the SiO_x layer was seen to be very uniform at 25 nm, leading to the SiO_x/Mo interface features being patterned to the Ti/SiO_x interface. Additionally, bright regions in HAADF images were seen to protrude from the Ti electrode into SiO_x, suggesting the incorporation of Ti into the oxide layer. This was confirmed through EELS measurements of the pristine Ti device, where the Ti $L_{2,3}$

edge could be detected up to 10 nm into SiO_x from the Ti/SiO_x interface. Analysis of the Ti $L_{2,3}$ edge shows Ti is increasingly oxidised as a function of depth from the Ti/SiO_x interface. Another important observation was that both the Ti and Mo electrodes were oxidised. EELS measurements suggest approximately 2.4 nm of the Ti electrode is oxidised, whilst 1 to 2 nm of Mo is oxidised. Through measurement of the O K edge prepeak, it was found that the Ti electrode is very uniformly oxidised along the interface with an almost constant thickness (except at regions where Ti was seen to incorporate into SiO_x).

10.4.2 Structural Dynamics Due to Electrical Stress

The processes involved in positive and negative electroforming were seen to show some key similarities and key differences. In both cases the accumulation of O at the Ti/SiO_x interface was observed. For this to occur, the source of the accumulated O must be either the SiO_x layer itself or from the environment. In this case, the Ti electrode is assumed to seal the Ti device from the environment leaving the source to be the SiO_x layer. As a result, the accumulation of O at the Ti/SiO_x interface suggests the formation of new O vacancies in the SiO_x layer. The oxide formation enthalpy for TiO_2, SiO_2, MoO_3 from Ti, Si and Mo is 944 kJ/mol, 910.7 kJ/mol and 745.1 kJ/mol, respectively, [139]. In this case, the oxide formation enthalpy can be understood as the chemical affinity of each element to oxygen, where a higher energy value represents a higher affinity. As a result, the scavenging of O by Ti is to be expected thermodynamically. The impact of the O vacancies generated in the SiO_x layer subsequently depends on the polarity of the bias.

DFT calculations show O vacancies trap electrons at Fermi energies of approximately 1.6 eV below the SiO_2 conduction band as discussed in section 9.3. In the Ti device where SiO_x is grown to be x = $\approx$ 1.95, it is expected electrons will trap at similar Fermi energies. Comparatively, the Ti Fermi energy is 3.58 eV below the SiO_2 conduction band [132]. As such, the application of a negative bias would shift the Ti Fermi energy upwards, towards the SiO_2 conduction band, increasing the probability of electron injection into the vacancy sites [123]. Therefore, it is suggested that the low resistance state in the negative electroformed device is due

to electron transport through the O vacancy sites *via* trap assisted tunneling.

Under a positive bias, however, the Fermi energy of Ti is expected to shift downwards in energy relative to the SiO_x band gap [123]. This in turn reduces the probability of O vacancy generation or electron transport through vacancy sites. Instead, EELS measurements show positive electroforming leads to Ti and Mo incorporation into SiO_x. Through detection of the O K edge prepeak, metal-oxide was found to form throughout the SiO_x layer. Furthermore, the average scan results suggest that Ti is in a lower oxidation state in the positive electroformed device. In this case, it is suggested that the low resistance state similar to the ECM mechanism where TiO_x and MoO_x filaments facilitate electron transport, where both TiO_x and MoO_x have been shown to be conducting at low oxidation states [140, 141, 142].

10.5 Conclusion

The results in this chapter show the growth methods of the Ti device leads to some interesting features in the device microstructure. The roughness of the Mo layer was found to lead to void like regions forming at the trough positions at the SiO_x/Mo interface. Subsequently, because the SiO_x layer thickness was very uniform, the Mo roughness was found to pattern the Ti/SiO_x interface. Ti was found to incorporate from the Ti/SiO_x trough positions post fabrication up to 10 nm into SiO_x. Additionally, both the Ti and Mo electrodes were found to be oxidised with greater oxidation occurring at the Ti/SiO_x interface. Post electroforming, O was found to accumulate at the Ti/SiO_x interface under both positive and negative bias. However, only under positive bias was additional metal incorporated into SiO_x. As a result, the low resistance state in the positive electroformed device is suggested to be due to electron transport through TiO_x and MoO_x filaments in SiO_x. In the negative electroformed device, the low resistance state is suggested to be due to electron transport through defect sites in SiO_x such as O vacancies.

Chapter 11

Au-SiO$_x$-Mo (Au) RRAM device

11.1 Introduction

The Au-SiO$_x$-Mo (Au) RRAM device discussed in this chapter was grown simultaneously with the Ti-SiO$_x$-Mo (Ti) device to provide a basis for the interactions expected to be observed in the Au-Ti-SiO$_x$-Mo (Au-Ti) device. In this case, the Mo and SiO$_x$ layers were grown on the same base wafer before being cleaved and patterned with the Au and Ti top electrodes respectively (see section 3.2.3 for further details). Subsequently, the Au and Ti devices were stored in the same container under the same conditions until TEM lamella preparation (as described in section 3.3.3). This was intended to allow a direct comparison between the microstructure of the devices.

As discussed previously, the Au-Ti device performs with optimal RRAM properties including fast switching times, high retention, high endurance and low switching voltages [15]. However the Au device, much like the Ti device, does not perform well as a memory with repeatable resistive switching not observed. Instead, the Au device was grown to provide insight into the VCM aspects of operation expected to occur in the Au-Ti device. This is because the Ti layer in the Au-Ti device is grown to be 5 nm thick for use as a wetting layer to help bind the Au and SiO$_x$ layers. This limits the amount of Ti available in the Au-Ti device available for ECM operation. In the Ti device, Ti and Mo incorporation was found to play a significant role in the electroforming process (see previous chapter). In the Au device, however, Au

is not expected to incorporate into the SiO_x layer. As a result, the VCM mechanism is expected to play a more significant role in device operation (see section 9.3). This is where electron injection under electroforming creates O vacancies in the SiO_x layer. The O vacancies subsequently provide a path for electron transport through the SiO_x layer *via* trap assisted tunneling. As such, the movement of O is of primary interest in this chapter. Though difficult to observe directly, a focus will be applied to the gross O movement in the electroformed devices compared to the pristine device. This includes a study of the oxidation of the electrodes before and after electroforming. The Mo layer in the Au and Ti devices is grown to have less surface roughness than the Au-Ti device. This reduces the variability of the interfaces along the path of the electron beam, allowing the interface chemistry to be sampled more accurately. It should also be noted that the incorporation of Mo into SiO_x is still expected, and remains an important area of study.

The methods described in section 9.4 are used in this chapter to characterise the Au device in its pristine and electroformed states. This follows the same methodology as applied in the previous chapter when characterising the Ti device. In this case, a combination of STEM, EELS and EDX are used to understand the microstructure of the pristine device post fabrication. The same combination of STEM, EELS and EDX is then used to characterise the devices after positive (+15 V, 1 mA current compliance) and negative (-15 V, 1 mA current compliance) electroforming to provide a direct comparison. From this, it is intended that the chemical changes observed post stressing will give insight into the structural dynamics due to electrical stress that occurs in the Au-Ti device and SiO_x devices in general.

11.2 Pristine Au-SiO_x-Mo (Au) RRAM device

11.2.1 HAADF Analysis

Fig. 11.1 shows a HAADF STEM image of the pristine Au device, where the thickness of the Mo, SiO_x and Au layers are measured to be approximately 70 nm, 25 nm and 85 nm respectively. It should be noted that as with the Ti device, the Mo

and Au layers each have a high degree of roughness, making an exact determination impossible.

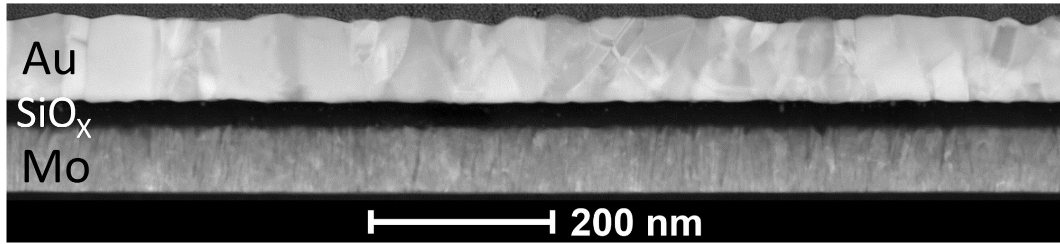

Figure 11.1: HAADF image of the pristine Au device

Imaging of the Mo layer in the Ti and Au devices finds that they each have the same thickness and structure (see section 10.2.1 for further analysis). This did not translate to the SiO_x layer however, where the results show the properties the oxide layers in the Au and Ti devices are markedly different. Fig. 11.2 gives a HAADF of the pristine Au device with the contrast set to elucidate the SiO_x layer. This shows the presence of a high concentration of large clusters in SiO_x in proximity to the Au electrode. This is significantly different to the Ti device where no such clusters were observed in SiO_x. Another major difference compared to the Ti device is the lack of void like regions in SiO_x near the SiO_x/Mo interface. Instead, many bright regions are observed at the SiO_x/Mo interface suggesting the incorporation of Mo into SiO_x. Fig. 11.3 shows the normalised HAADF intensity profile of the Au and Ti devices highlighting this difference. The profiles were taken across the entire HAADF images shown in Figs. 11.1 and 10.1 respectively. In the Au device, the intensity of the SiO_x layer is highest at the SiO_x/Mo interface corresponding to more or more dense material. The intensity then decreases linearly until the Au/SiO_x interface. This suggests that Mo diffuses into SiO_x during or post fabrication, with the concentration of Mo decreasing linearly until the Au interface. In contrast, the intensity of the SiO_x layer in the Ti device is at a minimum near the SiO_x/Mo interface. The intensity then increases until it plateaus to a constant intensity halfway (12.5 nm) into the SiO_x layer, then rises sharply as it approaches the Ti electrode. The reduced intensity near the SiO_x/Mo interface in the Ti device is due to the presence of void like regions found at trough regions at the SiO_x/Mo interface (see section

10.2.1). The subsequent increase in HAADF intensity near the Ti electrode can then be explained by the incorporation of Ti.

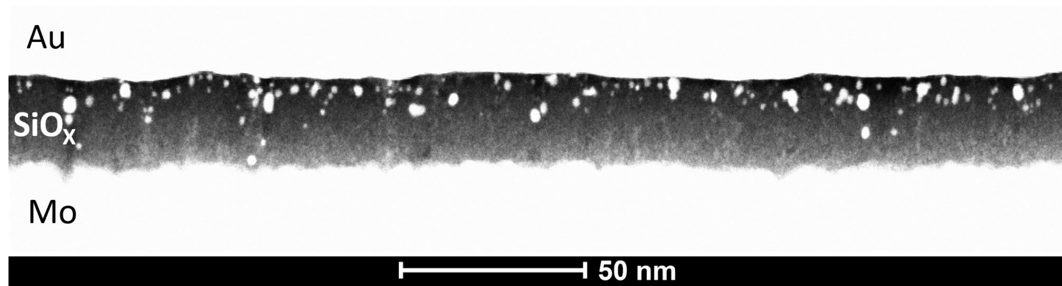

Figure 11.2: HAADF image of the pristine Au device with the contrast adjusted to highlight the SiO$_x$ layer

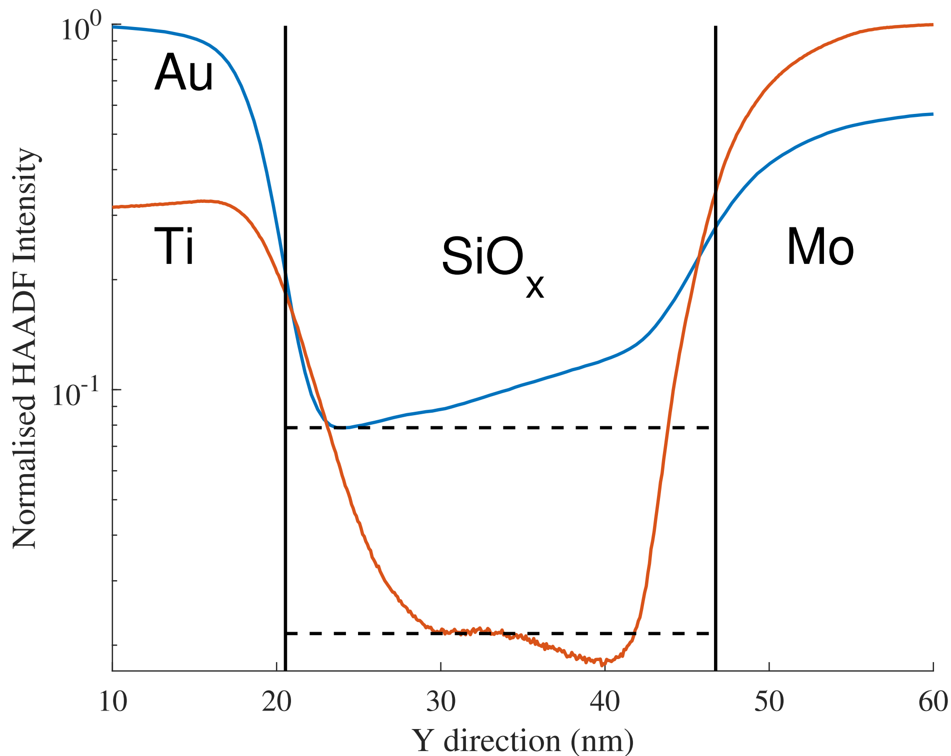

Figure 11.3: Graph showing the normalised HAADF intensity taken for the Au (blue line) and Ti (orange line) devices respectively.

A HAADF image of the Au electrode can be seen on Fig. 11.4, showing the Au layer is polycrystalline. The Au/SiO$_x$ interface is very smooth compared to SiO$_x$/Mo, with a min/max roughness of 6 nm. In general the grain boundaries in the Au layer appear to propagate from peak positions at the Au/SiO$_x$ interface, though

this is inconsistent along the device.

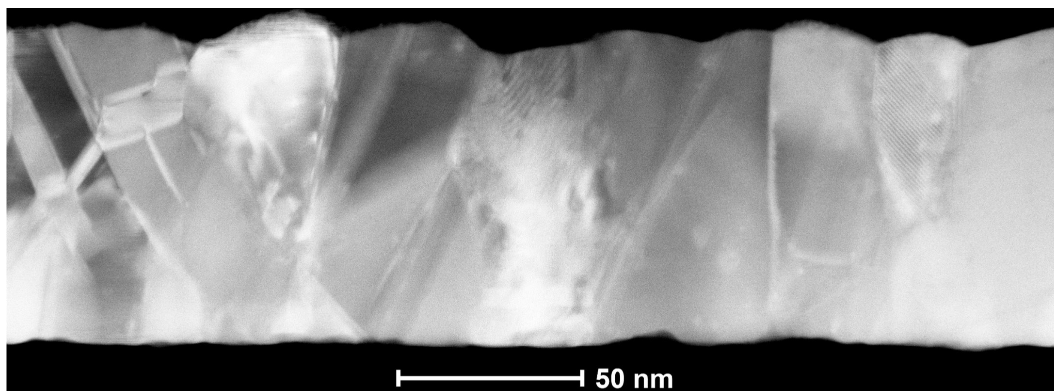

Figure 11.4: HAADF image of the Au electrode of the Au device

11.2.2 EDX Analysis

EDX measurements were taken for the pristine Au device, with the results shown on Fig. 11.5. From this, it can be seen there is little interaction between the Au and SiO_x layers, with no O detected in the Au layer and no Au detected in the SiO_x layer. Instead the bright clusters in the SiO_x layer are suggested to consist of Mo, which is detected in the SiO_x layer. The results also show both Mo and Si are detected at the SiO_x/Mo interface suggesting the possible formation of mixed MoO_x and SiO_x. Interestingly, the Mo layer is found to give a high O peak showing it has oxidised to form MoO_x. It should be noted that this was not observed in the Ti device where instead Ti was the primary scavenger of O.

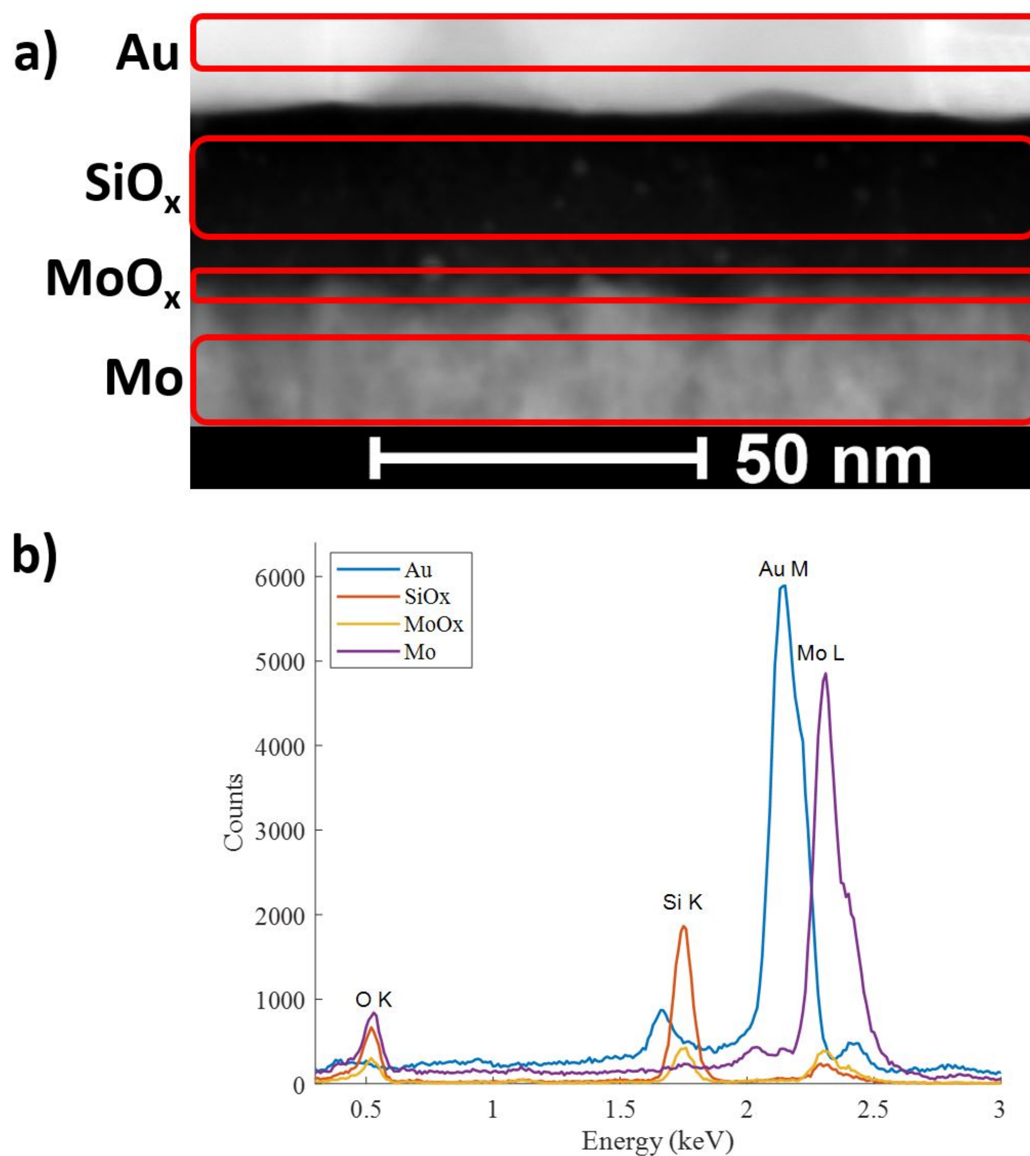

Figure 11.5: EDX results taken across the pristine Au device. a) shows an HAADF image of the pristine Au device, where the EDX spectra for the Au, SiO_x, MoO_x and Mo regions (marked by red boxes) are given on b) respectively.

11.2.3 EELS Analysis

EELS measurements were also taken for the pristine Au device (Fig. 11.6), confirming the oxidation of the Mo layer at the SiO$_x$/Mo interface. A HAADF image of the device can be seen on Fig. 11.6a where the EEL spectrum is taken within the orange box. Fig. 11.6b shows the same region with the contrast adjusted to highlight the presence of metal clusters (bright regions) in the SiO$_x$ layer. The extracted Mo M$_3$, Si L$_{2,3}$ and O K EELS edge image maps can be seen on c) to e). The vertical blue lines mark the regions from which line profiles graphed on Fig. 11.7 are taken. The same markings are used for all EELS data presented in the remainder of this chapter.

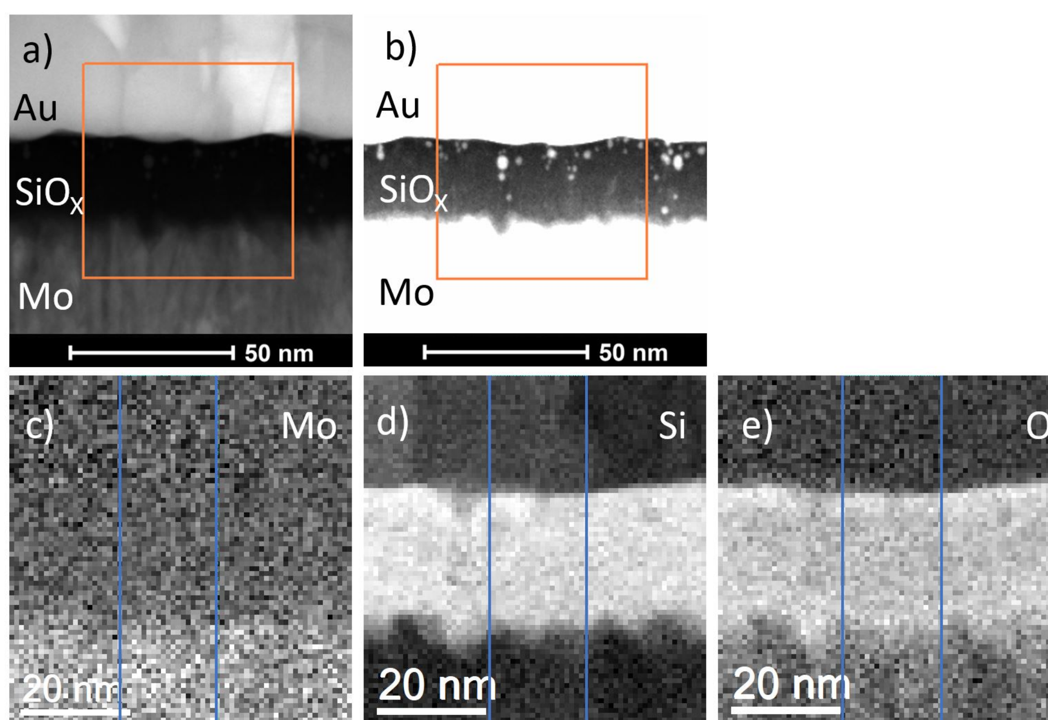

Figure 11.6: EELS data for the pristine Au device. a) shows a HAADF image of the device where the EELS measurement is taken within the orange box. b) shows the same HAADF image with the contrast limits set to show the SiO$_x$ layer. The extracted Mo M$_3$, Si L$_{2,3}$ and O K edge maps are shown on c) - e) respectively

The extracted Si and O maps on Fig. 11.6 show sharp interfaces between SiO$_x$ and Au suggesting minimal mixing at the Au/SiO$_x$ interface. However, the accumulation of O near the Au/SiO$_x$ interface was observed, and can be seen more clearly from the line profile of the O K edge (Fig. 11.7). This phenomenon has been ob-

served previously in literature, where it is suggested to be the result of Au-Si bonds forming at Ag/SiO_2 interfaces [143]. Once the Au-Si bonds form, it is suggested SiO_2 in proximity to the interface reduces to intermediate oxidation states. In this case, the SiO_2 is very strained due to the interfacial transition from SiO_2 to Au through the Si bonding. This subsequently results in the liberation of O which accumulates in a region near the Ag/SiO_2 interface. The same process is suggested to occur in the Au device, where the liberated O binds to SiO_x near the reduced Au/SiO_x region.

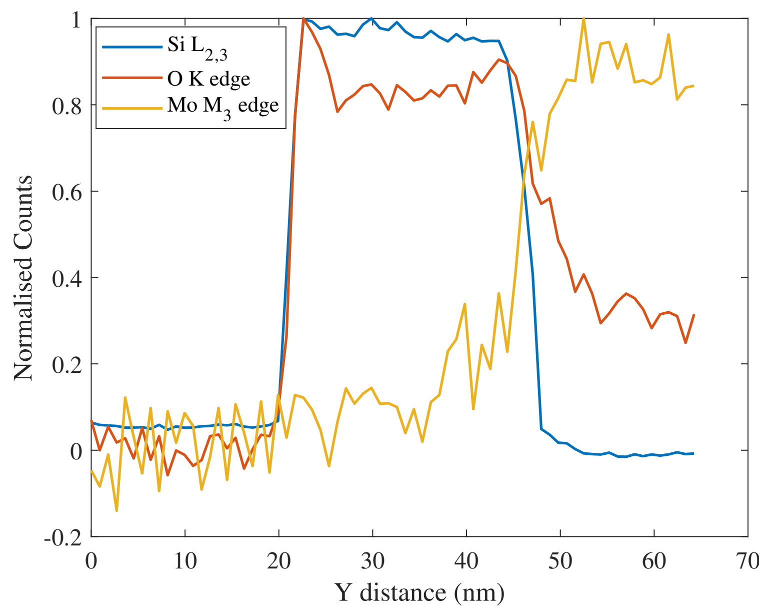

Figure 11.7: Line profile of the Si $L_{2,3}$, O K and Mo M_3 edges for Au device taken within the blue vertical lines marked on Fig. 11.6

The EELS data also confirms two major processes occur at the SiO_x/Mo interface. The line profile on Fig. 11.7 shows a strong O K edge signal measured in Mo whilst, the Mo M_3 edge is similarly detected in SiO_x. The Mo M_3 edge counts gradually decrease from the Mo electrode to near zero 15 nm into SiO_x. It can therefore be seen that not only is the Mo layer oxidised, Mo incorporates into SiO_x. This confirms the observations from HAADF imaging and EDX analysis, proving that the bright intensity of the SiO_x near the SiO_x/Mo interface is due to Mo incorporation.

Fig. 11.8 shows the results of another EELS measurement of the pristine Au device, where the extracted O K edge (SiO_x) and O K edge prepeak components

are shown on c) and d) respectively. The vertical blue lines on c) and d) mark the regions from which the line profiles displayed on Fig. 11.9 are taken. The results confirm the accumulation of O near the Au/SiO$_x$ interface observed in the previous measurement where a large spike is seen for the O K edge (SiO$_x$) profile. This shows an O rich SiO$_x$ region supporting of the mechanism discussed above. The O K edge prepeak is also detected in the SiO$_x$, following a similar trajectory to the Mo M$_3$ profile shown on Fig. 11.7. As such, it is suggested that the Mo that incorporates into SiO$_x$ is oxidised. It can also be seen that the Mo electrode itself is oxidised, with the O K edge prepeak measured 10 nm into Mo from the SiO$_x$/Mo interface.

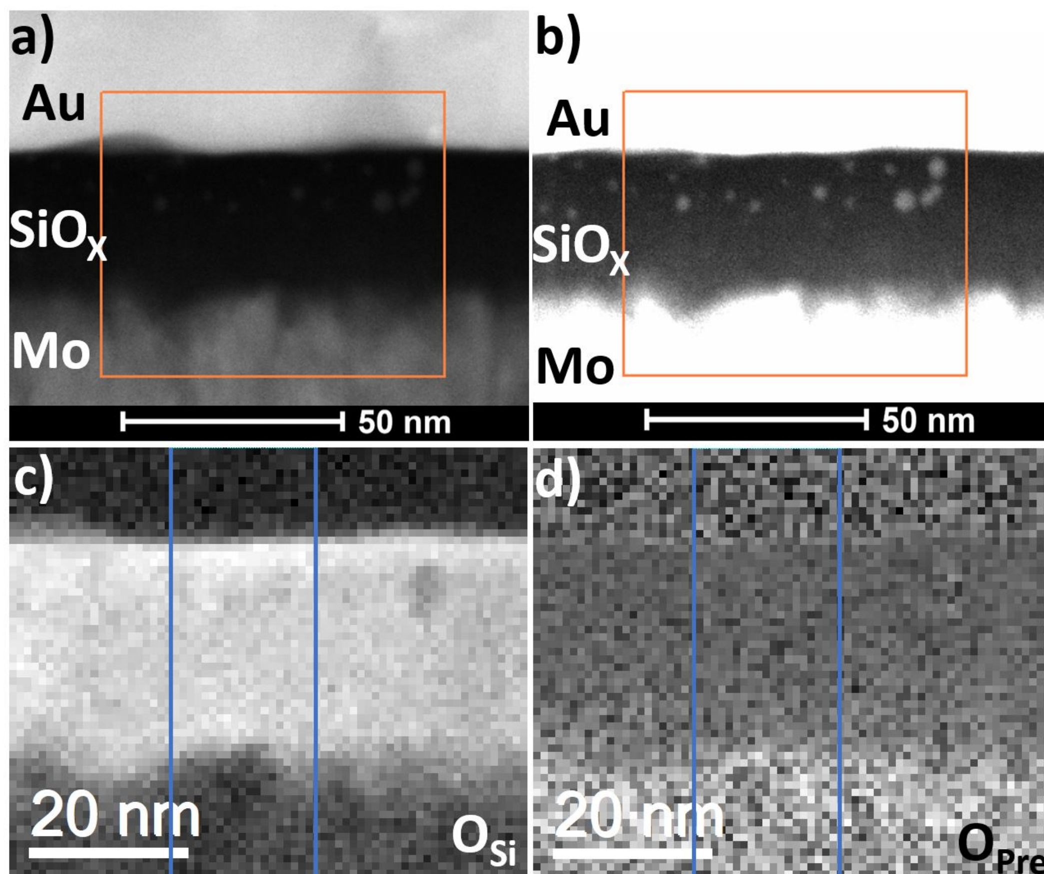

Figure 11.8: EELS data for the pristine Au device. a) shows a HAADF image of the device where the EELS measurement is taken within the orange box. b) shows the same HAADF image with the contrast limits set to show the SiO$_x$ layer. The extracted O K edge and O K edge prepeak maps are shown on c) and d) respectively

Average scans (see section 9.4.2) of the O K edge were also taken across the

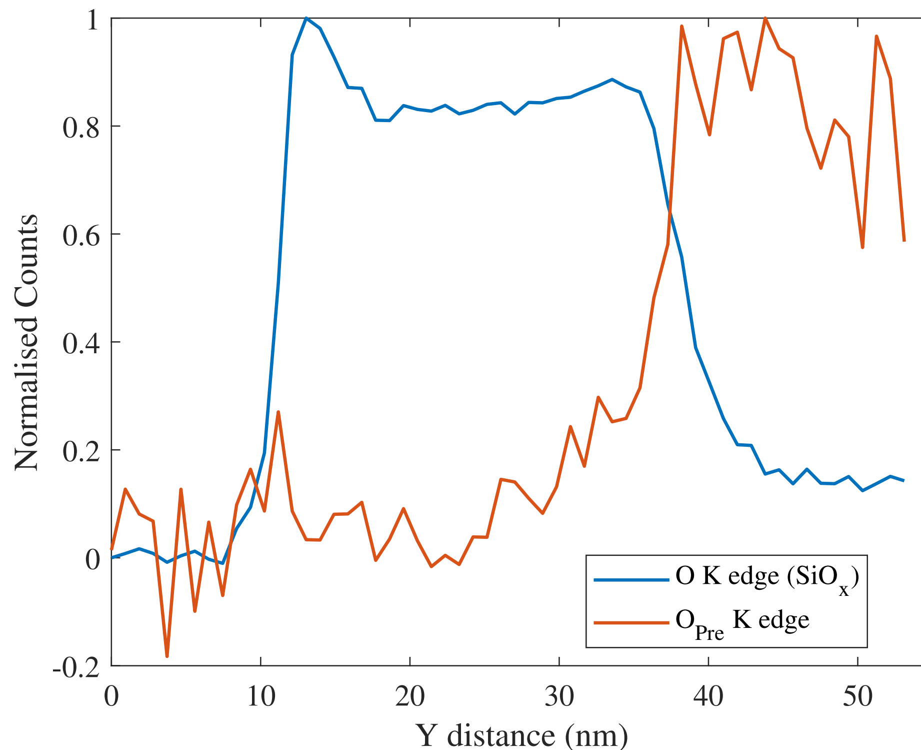

Figure 11.9: Line profile of the O K edge and O K edge prepeak for Au device taken within the blue vertical lines marked on Fig. 11.8

pristine Au device. This includes measurements along the Au/SiO$_x$ interface and in the SiO$_x$ layer at increments of 5 nm away below the Au/SiO$_x$ interface (Fig. 11.10). The results show the O K edge prepeak is not detected at the Au/SiO$_x$ interface confirming Au oxide does not form, again supporting the formation of Au-Si bonds at the interface. The average scans taken in the SiO$_x$ layer at increments of 5 nm from the Au/SiO$_x$ interface show the O K edge (SiO$_x$) counts remain constant. However, in the same regions the O K edge prepeak (onset at 525 eV for MoO$_x$) counts increase in magnitude as scans are taken towards the SiO$_x$/Mo interface. This confirms the formation of MoO$_x$ in the SiO$_x$ layer, with the concentration of Mo reducing gradually with distance away from the SiO$_x$/Mo interface. The O K edge prepeak then reaches a maximum 5 nm into the Mo layer, showing Mo has scavenged O from SiO$_x$. A higher signal is detected 5 nm into Mo due to the variability of the interface roughness, with more Mo and MoO$_x$ being detected 5 nm down.

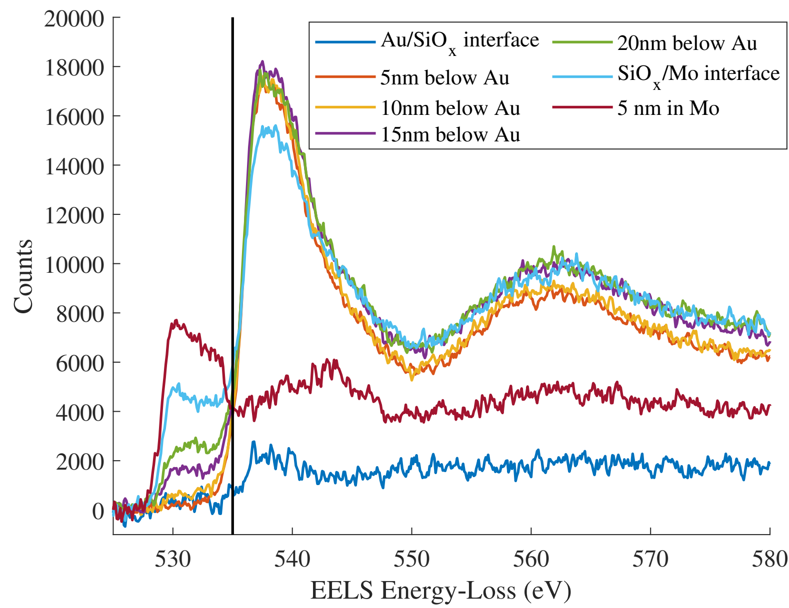

Figure 11.10: Plots of the extracted O K edge taken across the pristine Au device

Fig. 11.11 shows the results of averaged scans taken at the SiO$_x$/Mo interface and in the Mo layer at increments of 10 nm below the SiO$_x$/Mo interface. From this, it can be seen that the maximum oxidation of Mo occurs at the SiO$_x$/Mo interface. The O K edge prepeak counts then gradually reduce as a function of distance from the SiO$_x$/Mo interface. However, it is important to note that O is still detected 60 nm below the SiO$_x$/Mo interface showing that O is very mobile in Mo.

Fig. 11.12 shows the Mo M_3 taken for the Au device located at 390 eV. Unfortunately, due to the low signal to noise ratio, the Mo M_2 edge could not be resolved. As a result the oxidation state of Mo cannot be determined in this work [135].

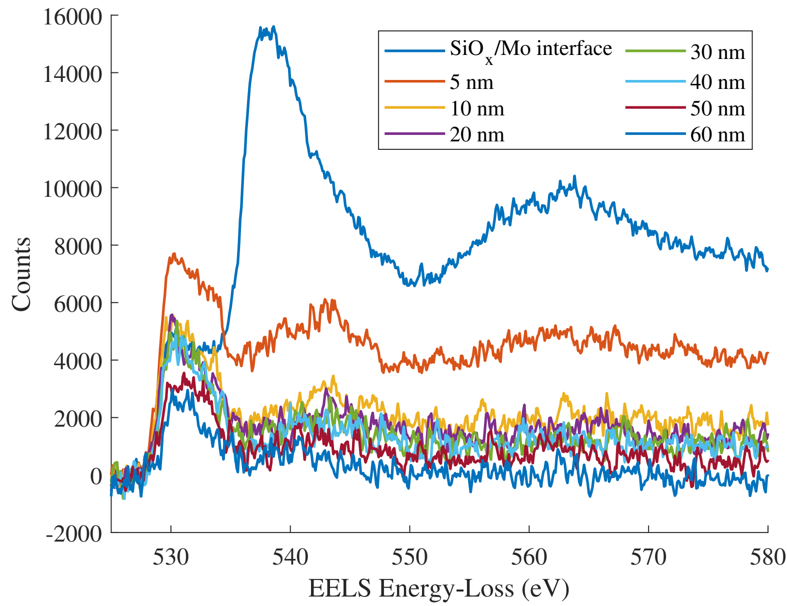

Figure 11.11: Graphs of the extracted O K edge taken in the Mo layer of the pristine Au device

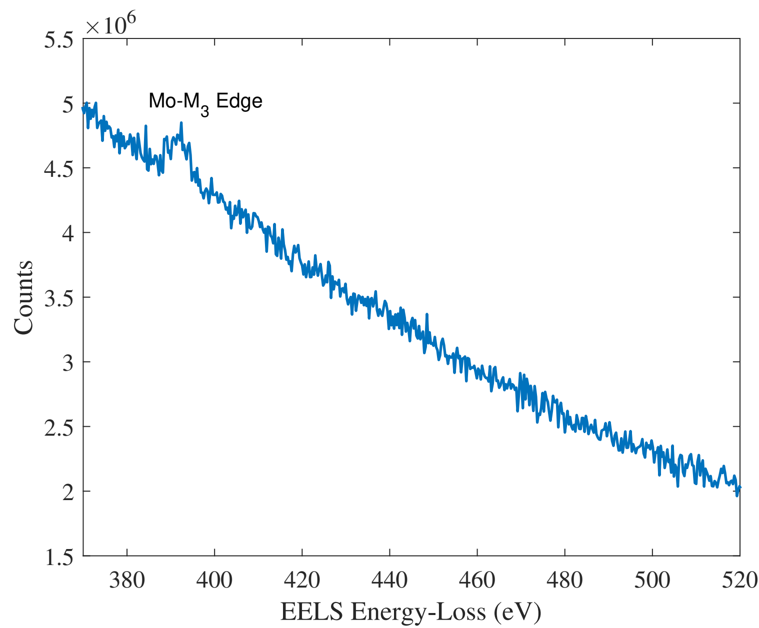

Figure 11.12: Raw EELS signal in the 370 - 520 eV range taken for the Au device, showing the Mo M_3 edge

11.3 Electroformed Au-SiO$_x$-Mo (Au) RRAM device

11.3.1 IV curve

Four IV curves were collected for the Au device under positive electroforming and another four under negative electroforming. In each sweep, the voltage was increased from 0 V to +15 V or -15 V respectively and reduced back to 0 V in increments of 0.05 V. The current compliance for each sweep was set to 1 mA to prevent the hard dielectric breakdown of the devices. Similar to the Ti device, the IV characteristics for both positive and negative electroforming in each device were very repeatable showing consistency across devices. TEM lamellas were subsequently prepared for one positive electroformed device and one negative electroformed device, with the respective IV curves shown on Fig. 11.13.

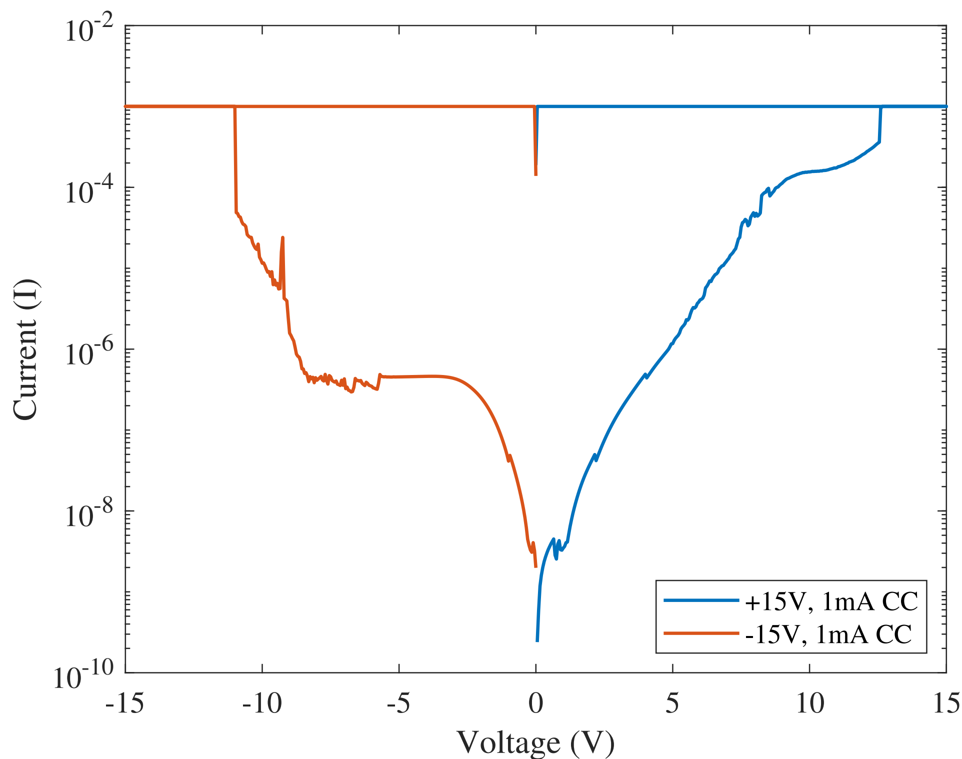

Figure 11.13: IV curves of the Au device after positive (orange) and negative (blue) electroforming.

From Fig. 11.13, it can be seen that the IV response of the Au device under positive and negative electroforming is very different. Under positive electroforming, the current increases exponentially with the applied voltage until 9 V. At 9 V

the rate of increase of the current slows until 12.5 V where the current rises from 0.3 mA to 1 mA at 12.65 V very sharply. The causes of the IV response are unclear, requiring the chemistry of the devices to be analysed first. It is suggested that in a similar fashion to the Ti device, additional Mo incorporates into the SiO$_x$ layer to provide a path for electron transport.

Under a negative bias, the IV response more closely resembles the negative electroforming response of the Ti device. In this case, the current increases to 3.9x10^{-7}A at -2.65V where it plateaus until -8.4 V. From 8.4 V the current increases sharply until it reaches the current compliance limit of 1 mA at -11 V. Interestingly, under negative bias both the Au and Ti device show the initial rise in current from 0 to 2.65 V at which point the current in each device reaches a plateau (Ti = 1.8x10^{-6}A). The current compliance is then reached at -11 V for the Au device compared to -9.6 V for the Ti device. This difference can be understood to be the result of the metal work functions, which are 5.1 and 4.3 eV for Au and Ti respectively [132] whilst the SiO_2 conduction band minimum (CBM) is found at 0.75 eV below vacuum level [144]. This crudely puts the Au and Ti Fermi energies at 4.4 and 3.6 eV below the SiO_2 CBM. O vacancies have been shown to trap electrons at a Fermi energy of 1.6 eV below the CBM. Subsequently, a more negative voltage is required to bring the Au Fermi energy to the level where electrons can be injected into the vacancy sites compared to Ti.

11.3.2 Positive electroformed Au Device

11.3.2.1 HAADF Analysis

Fig. 11.14 shows a HAADF image of the Au device after positive electroforming. From this, a MoO$_x$ layer can be seen to develop at the SiO$_x$/Mo interface which gives a brighter contrast than SiO$_x$ and less bright contrast compared to Mo. From Fig. 11.14, the thickness of the layer can be seen to gradually increase from the 6 nm (left of Fig. 11.14) to 19 nm (right of Fig. 11.14). Across the Au device, the MoO$_x$ layer formed multiple flat hill like features measuring 2 to 4 μ*m* wide and up to 20 nm in thickness.

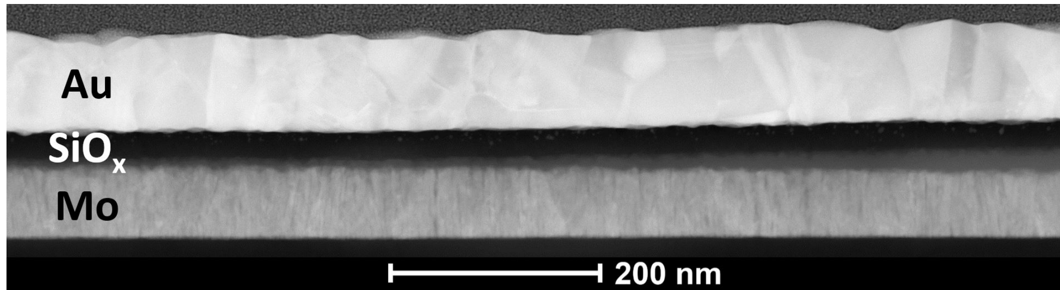

Figure 11.14: HAADF image of the positive electroformed Au device. A layer can be seen to form between the SiO_x and Mo layers from the left to the right of the image.

11.3.2.2 EDX Analysis

EDX measurements for the positive electroformed Au device can be seen on Fig. 11.15, where a) shows a HAADF image of the device. The red boxes mark the regions from which the EDX spectra on b) are taken. The EDX spectrum taken from the Au layer shows it contains both Au and Si, indicating Si has incorporated into Au. Previous literature shows meta-stable states of mixed Au-Si can form at the interface between Au and Si [143]. As such, it is suggested that Ag-Si bond formation in the pristine device may provide an intermediate step to the mixed Au-Si formation during positive electroforming. It should be noted that the exact mechanism for this is unclear and presents an interesting area for future research. However, in the Au-Ti device the Au layer is separated by Ti preventing the Ag-Si interaction and formation of mixed Au-Si.

The EDX spectrum was measured at two regions (R1 and R2) in the SiO_x layer. R1 marks the region in SiO_x in proximity to the Au/SiO_x interface and R2 marks the bulk SiO_x. From this, it can be seen that R1 contains Mo but does not contain Au. The ratio of the Mo to Si peaks suggests there is approximately 5 times more Mo on average in R2 than in R1. From this, it can be concluded that Mo diffuses deep into SiO_x to proximity to the Au/SiO_x interface. The EDX measurements also confirm that the layer formed between the SiO_x and Mo layers in the HAADF images is MoO_x. In this case, both Mo and O are detected whilst no Si or Au is detected. Importantly, the Mo layer is also seen to contain O, showing the Mo electrode is oxidised.

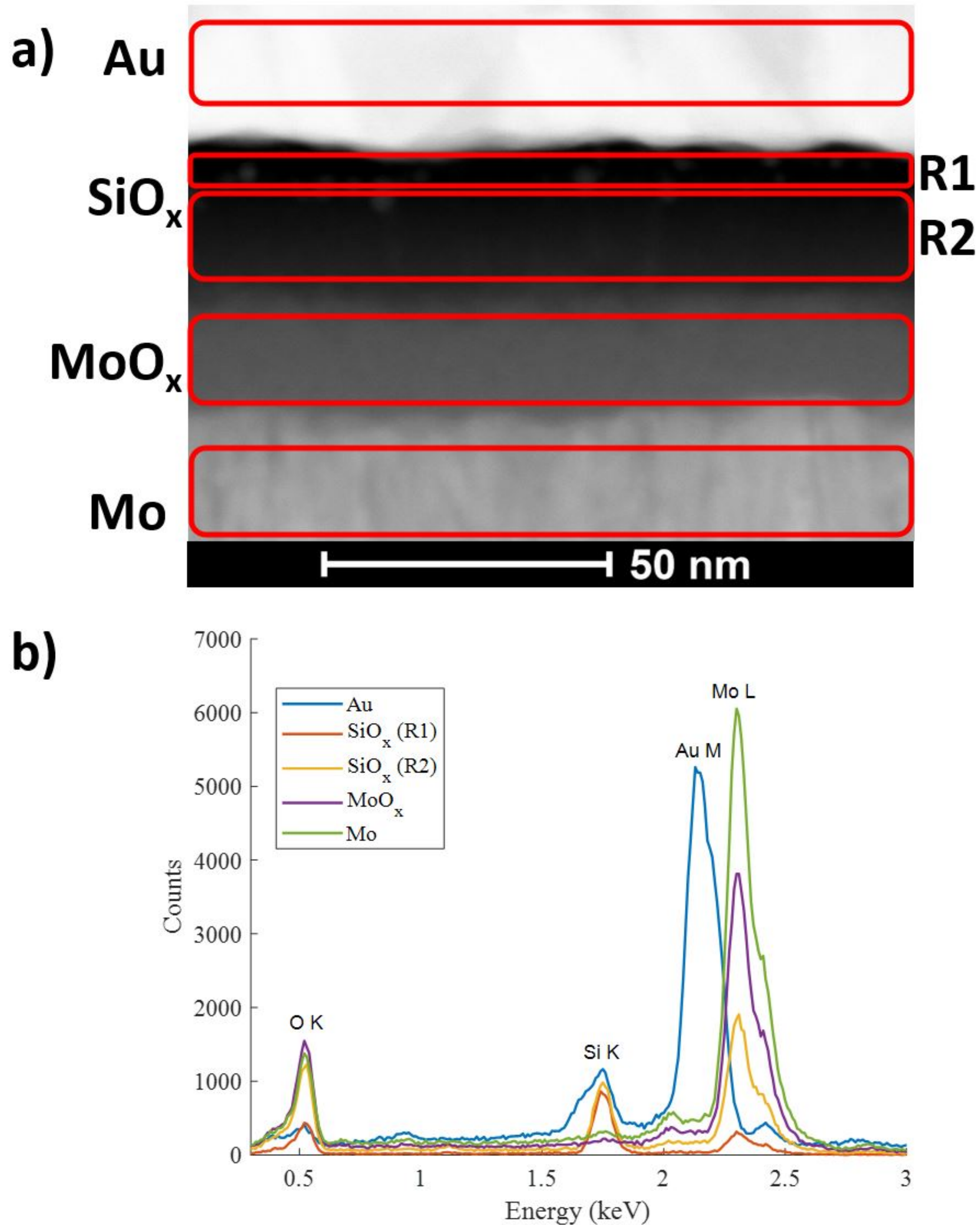

Figure 11.15: EDX results taken across the positive electroformed Au device. a) HAADF image of the positive electroformed Au device, where the EDX spectra for the Au, SiO$_x$ (R1 and R2), MoO$_x$ and Mo regions (marked by red boxes) are given in b) respectively.

11.3.2.3 EELS Analysis

Fig. 11.16 shows the results of an EELS measurement of the Si $L_{2,3}$ and O K edges taken for the positive electroformed device. Fig. 11.16a shows a HAADF image of the device, where the EELS measurement is taken within the orange box. From this

two important observations can be made. Firstly, the extracted Si $L_{2,3}$ edge image map shows three distinct regions of contrast. The brightest region corresponds to the SiO_x layer, whilst the Au layer shows brighter contrast than the Mo or MoO_x regions. This supports the formation of a meta-stable mixed Ag-Si state observed previously in the literature [143]. Interestingly, the contrast of the extracted Si $L_{2,3}$ edge in the Au electrode region is very uniform suggesting that the mixed Ag-Si is also uniform. The second important feature is in the O K edge image map, where the O K edge is detected beneath the SiO_x region confirming the existence of the MoO_x layer discussed in the previous section.

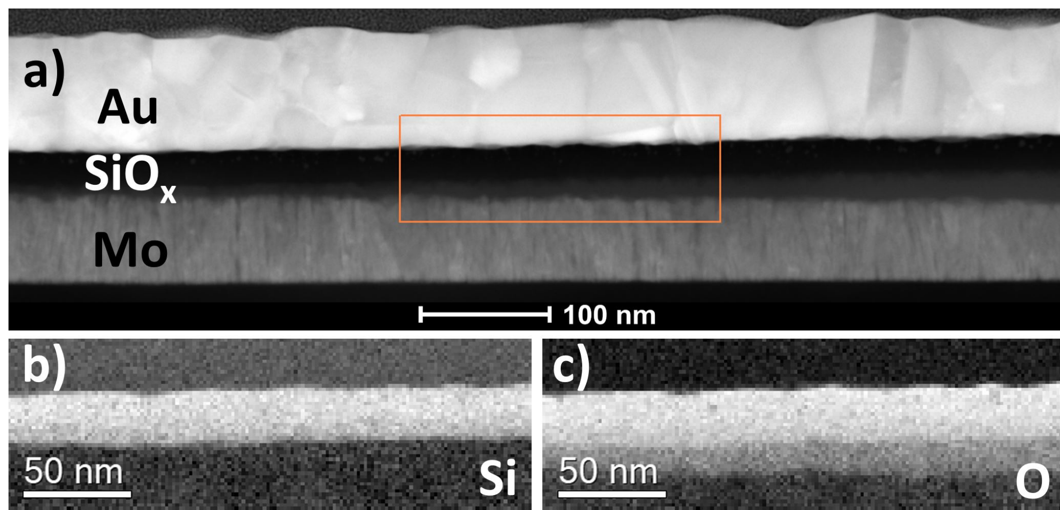

Figure 11.16: EELS data for the positive electroformed Au device. a) HAADF image of the device where an EELS measurement is taken within the orange box. The extracted Si $L_{2,3}$ and O K edge maps are shown on b) and C) respectively.

Figs. 11.17 and 11.18 show the results of another EELS measurement on the positive electroformed Au device. In this case the total O K edge, O K edge (SiO_x) and O K edge prepeak components are extracted and displayed in b) through d). The vertical blue lines on Fig. 11.17 mark the regions where the line profiles on Fig. 11.18 are taken. From the total O K edge image map, the SiO_x and MoO_x layers can be seen to have different contrast. In this case, the O signal in the MoO_x layer is approximately 40% lower than that detected in the SiO_x layer. The line profile of the O K edge (SiO_x) in Fig. 11.18 shows SiO_x stops abruptly at the SiO_x/MoO_x interface showing minimal mixing. Conversely, the O K edge prepeak counts tail

off into the SiO_x layer confirming the Mo incorporation throughout the SiO_x layer. Interestingly, a spike in the O K edge prepeak can be seen at the Au/SiO_x interface, suggesting that some O is accumulated at the Au/SiO_x interface and interacts with Au.

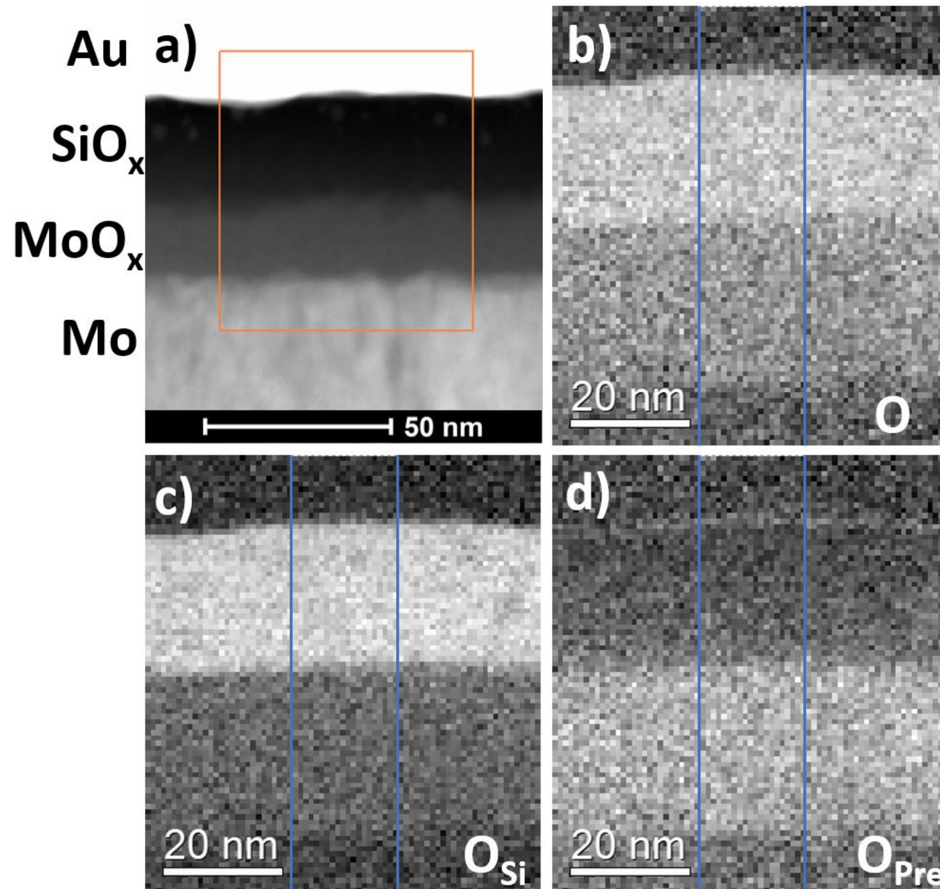

Figure 11.17: EELS data for the positive electroformed Au device. a) HAADF image of the device where an EELS measurement is taken within the orange box. The extracted O K (total), O K prepeak (O_{Pre}) and O K SiO_x (O_{Si}) edge maps are shown on b) - d) respectively. The blue lines mark the region from which the lineprofiles shown in Fig. 11.18 are taken.

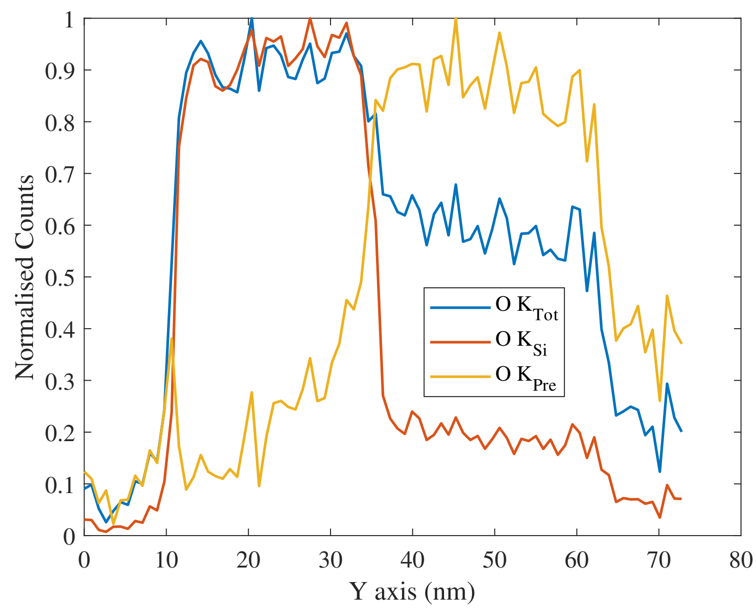

Figure 11.18: Line profiles of the O K (total), O K prepeak (O_{Pre}) and O K SiO_x (O_{Si}) edges for positive electroformed Au device taken within the blue vertical lines marked in Fig. 11.17

11.3.3 Negative Electroformed Au Device

11.3.3.1 HAADF Analysis

Fig. 11.19 shows a HAADF image of the negative electroformed Au device. From this, a MoO_x layer can be seen to have formed between the SiO_x and Mo layers across the entire device. The thickness of the MoO_x layer was measured to vary between 5 and 23 nm across the lamella. This differs from the positive electroformed device where MoO_x only forms in some regions, exhibiting hill like features across the lamella. Additionally, MoO_x can be seen to form at the Mo/substrate interface. This again was not observed in the positive electroformed device.

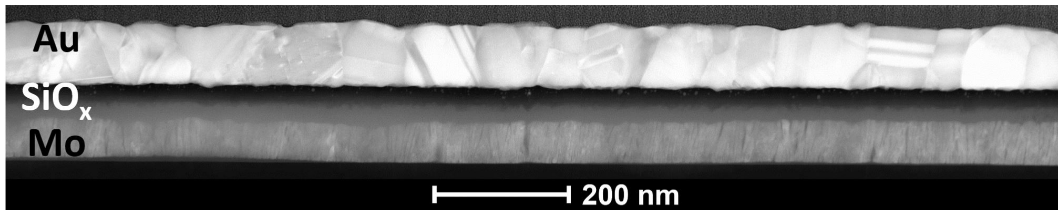

Figure 11.19: HAADF image of the negative electroformed Au device.

11.3.3.2 EDX Analysis

EDX measurements for the negative electroformed Au device can be seen in Fig. 11.20, where a) shows a HAADF image of the device. The red boxes mark the regions from which the EDX spectra in b) are taken. The results show formation of four distinct layers , where the Au electrode comprises of Au only, the SiO_x layer comprises of Si and O with small amounts of Mo, the MoO_x layer contains Mo and O only and the Mo layer contains Mo and O only. The difference between the Mo and MoO_x layers is the reduced ratio of O counts to Mo counts in the Mo layer compared to MoO_x.

The first observation to be made is that the negative electroforming was not found to produce a mixed Au-Si in the Au layer, which was observed in the positive electroformed device. The exact causes of this are unclear and beyond the scope of this work. Furthermore, and consistent across the Au device measurements in the pristine and electroformed states, Au was not found in SiO_x. Mo, however, is detected in both the SiO_x and MoO_x layers, again consistent with the other mea-

surements.

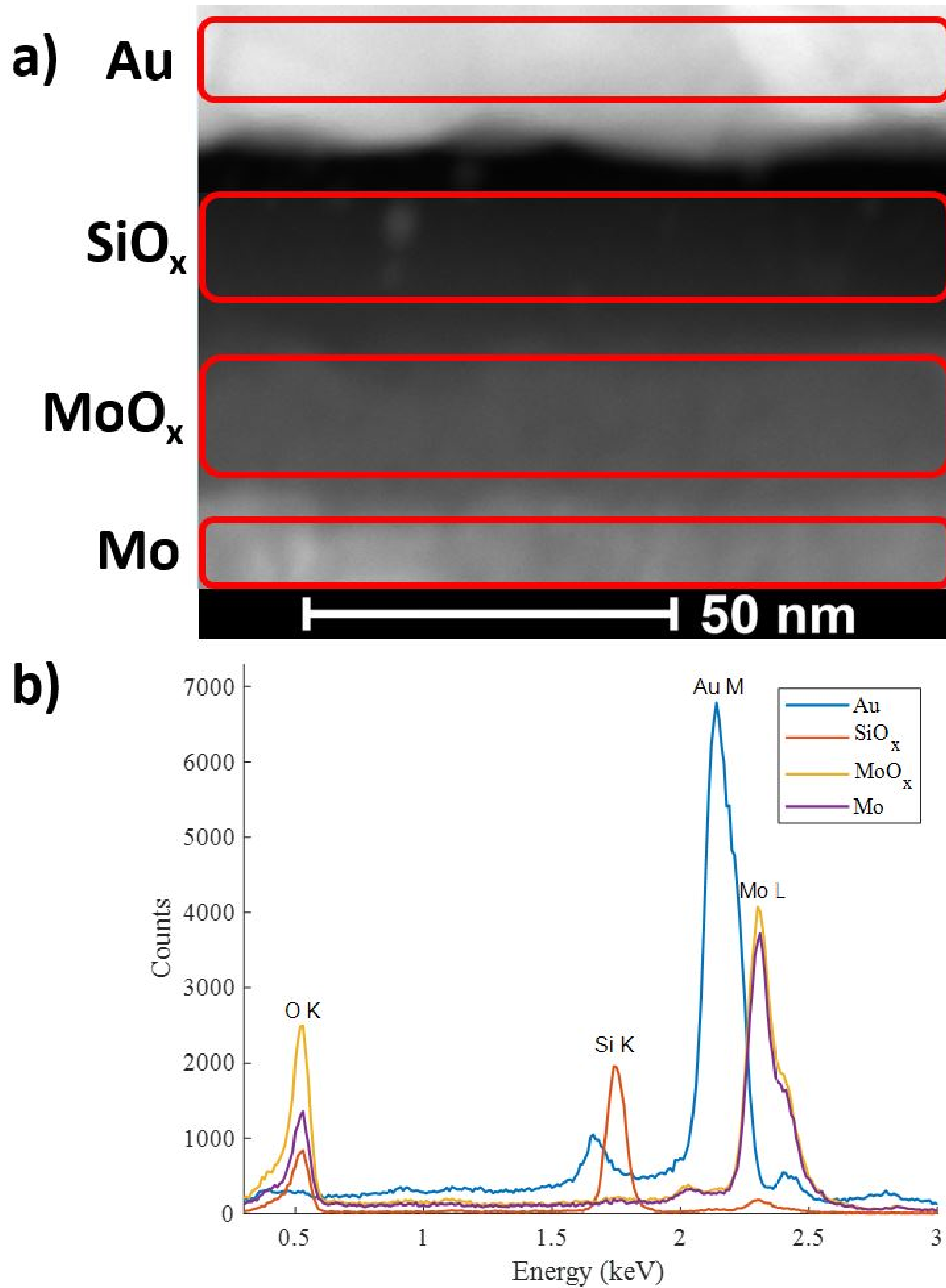

Figure 11.20: EDX results taken across the negative electroformed Au device. a) HAADF image of the positive electroformed Au device, where the EDX spectra for the Au, SiO_x, MoO_x and Mo regions (marked by red boxes) are given in b) respectively.

11.3.3.3 EELS Analysis

Fig. 11.21 shows the results of an EELS measurement of the negative electroformed device where the extracted Si $L_{2,3}$ and O K edges are given in b) and c), respectively. In Fig. 11.21a), a HAADF image of the device is shown where the EELS measurement is taken within the orange box. The extracted Si $L_{2,3}$ edge image map shows Si is only detected in the SiO_x region. This differs from the positive electroformed device where Si was detected in the Au layer. Furthermore, the O K edge is detected in the Mo layer, marking the formation of MoO_x at the SiO_x/Mo interface. The formation of MoO_x at the SiO_x/Mo interface is observed for both the negative and positive electroformed devices. However, the nature of the MoO_x layer is different in that a constant layer is formed in the negative electroformed device suggesting that more MoO_x is formed.

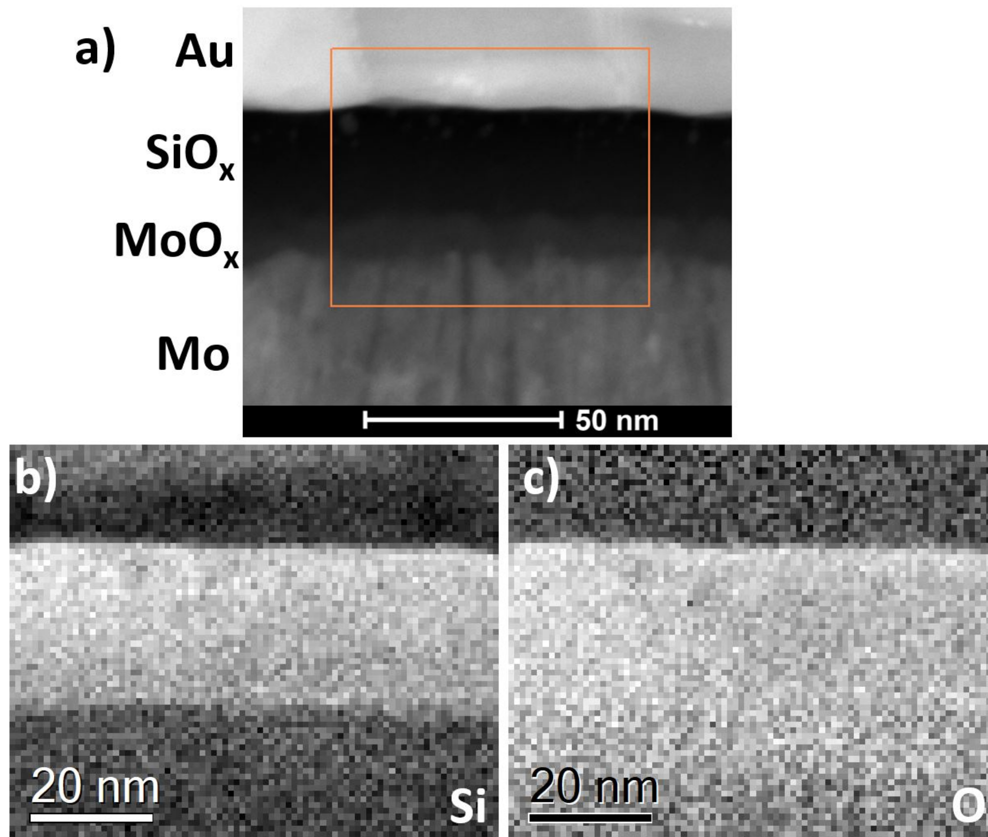

Figure 11.21: EELS data for the negative electroformed Au device. a) HAADF image of the device where an EELS measurement is taken within the orange box. The extracted Si $L_{2,3}$ and O K edge maps are shown in b) and c), respectively.

A further EELS measurement of the negative electroformed device shows that the oxidation of the Mo layer is significantly higher than compared to the positive electroformed device. Fig. 11.22 shows the results of the EELS measurement, where the O K edge was measured in a region where a large trough occurs at the MoO_x/Mo interface. The trough region can be seen in the HAADF image shown in a) whilst the extracted O K edge (total), O K edge (SiO_x) and O K edge prepeak image maps are shown in b) through d), respectively. From this, it can be seen that a strong O K edge signal is detected in the Mo layer at the Mo column boundary region. This suggests that under negative electroforming, not only is O expelled from SiO_x to allow the formation of MoO_x, but additional O diffuses into the Mo layer. Analysis of the EELS edge shows that the component is due to the O K edge prepeak, which shows the diffusion of O into the column boundaries in Mo. This in turn leads to increased oxidation of the column boundary region. This is a similar effect to the metal incorporation into the SiO_x column boundaries observed in the previous chapter. This presents an important result by confirming the ability of Mo boundaries to facilitate O transport, whilst also showing a preference for Mo column boundaries to be oxidised over the Mo column bulk as a result.

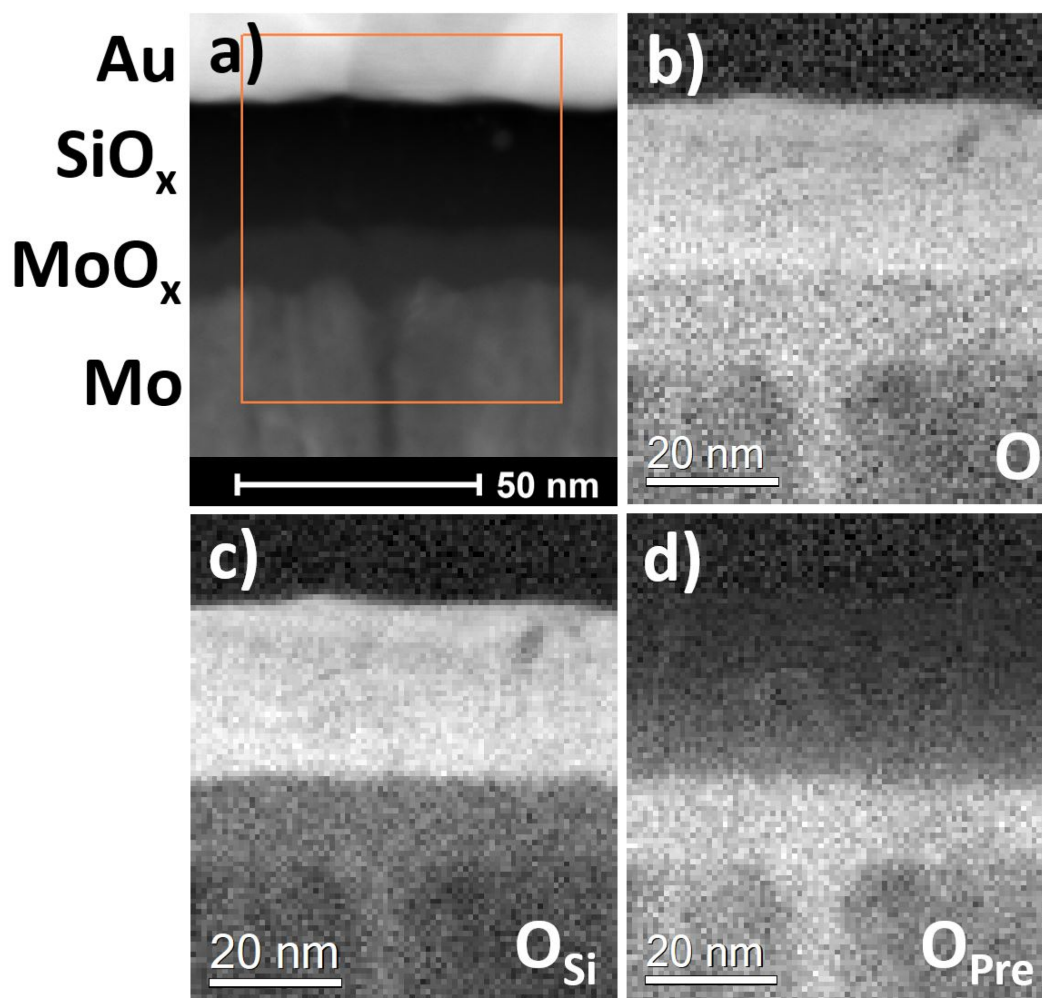

Figure 11.22: EELS data for the positive electroformed Au device. a) HAADF image of the device where an EELS measurement is taken within the orange box. The extracted O K (total), O K SiO_x (O_{Si}) and O K prepeak (O_{Pre}) edge maps are shown in b) - d) respectively.

11.3.4 Au Device Comparison

The polarity of the electroforming applied to the Au device shows some interesting results, which can be summarised on Figs. 11.23 and 11.24. Each of these graphs were obtained by taking average scans (see section 9.4.2 for further details) of the pristine, positive and negative electroformed Au devices. Measurements were taken at the Au/SiO_x interface for each device, then in the SiO_x, MoO_x and Mo layers at increments of 5 nm from the Au/SiO_x interface. From this, Fig. 11.23 shows the total O K edge counts as a function of depth from the Au/SiO_x interface. From this, it can be seen that more O is released from SiO_x after negative electroforming. This results in a thicker MoO_x layer compared to the positive electroformed device and more O incorporated into the Mo layer. In this case, O K edge counts can be detected 70 nm away from the Au/SiO_x interface, which marks the half way point in the Mo layer. At this point the O K edge counts detected are more than 3 times higher compared to the pristine or positive electroformed devices. This shows that, whilst electroforming of either polarity results in the formation of MoO_x, only in negative electroformed device does O diffuse into Mo. This is to be expected if the O produced is in the form of O^{-2} ions, as suggested in section 9.3.

Another key difference can be observed in Fig. 11.24, which shows the O K edge prepeak taken from averaged scans across each device. In this case, it can be seen that negative electroforming results in a higher intensity of O K edge prepeak signal in the SiO_x layer compared to the pristine device, whilst a lower O K edge prepeak was found in the positive electroformed device. This data can be interpreted in two ways. It could show that Mo incorporates into SiO_x to form MoO_x under a negative bias whilst Mo diffuses out of SiO_x under a positive bias. Conversely, the amount of Mo in SiO_x can be relatively constant in each device, where instead the oxidation state of Mo is changed. Due to the low signal to noise ratio of the Mo EELS edges an exact determination was not possible. However, an estimation is possible through analysis of the EDX Si:Mo peak ratios in SiO_x for each device, which was found to be 7.9, 0.52 and 10.76 for the pristine, positive and negative electroformed devices, respectively. This shows that the Si counts were higher than

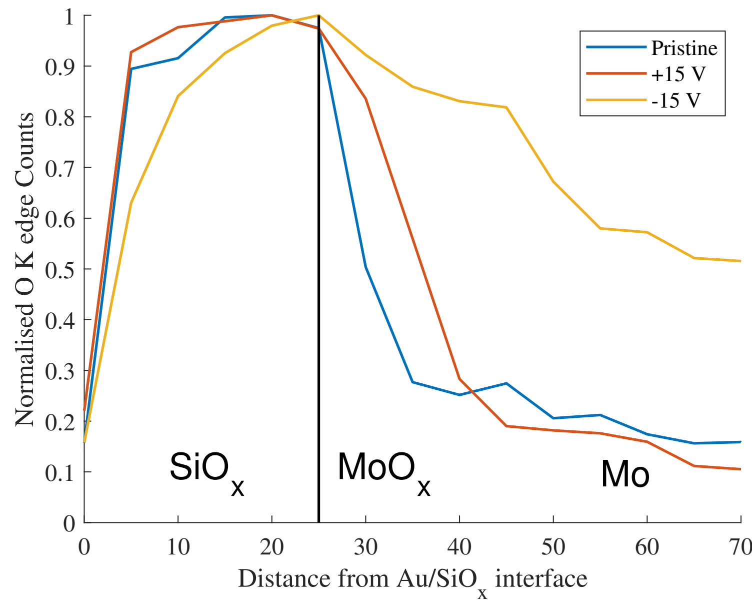

Figure 11.23: Graph showing the normalised O K edge counts as a function of distance from the Au/SiO_x interface. For all data points, the counts were determined through analysis of 'averaged scans' taken at the Au/SiO_x interface and in the SiO_x and Mo layers. In this case, average scans were taken as described in section 9.4.2, in increments of 5 nm from the Au/SiO_x interface.

Mo in the pristine and negative electroformed devices, whilst the Mo counts were higher than Si in the positive electroformed device. This provides a qualitative assessment of the devices showing that Mo does incorporate into SiO_x during positive electroforming and diffuses out of SiO_x during negative electroforming. The EELS O K edge prepeak results can then be interpreted as showing that the Mo in the positive electroformed device is in a lower oxidation state. This is consistent with the notion that the low resistance state in the positive electroformed device is due to electron transport through MoO_x. This can be determined more precisely using techniques such as ion-beam XPS, presenting an interesting area for future research.

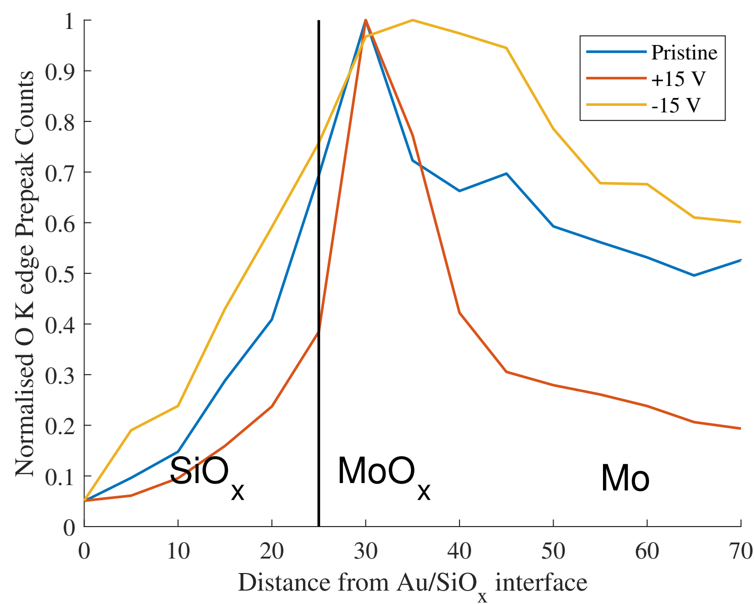

Figure 11.24: Graph showing the normalised O K edge prepeak counts as a function of distance from the Au/SiO_x interface. For all data points, the counts were determined through analysis of 'averaged scans' taken at the Au/SiO_x interface and in the SiO_x and Mo layers. In this case, average scans were taken as described in section 9.4.2, in increments of 5 nm from the Au/SiO_x interface.

11.4 Summary of Main Results

11.4.1 Device Microstructure (Pristine)

The thickness of the Mo, SiO_x and Au layers was measured to be approximately 70 nm, 25 nm and 85 nm, respectively, through HAADF imaging. The structure of the Mo layer was found to be the same as the Ti device, containing long thin columns that are seen to form during the initial phases of Mo growth at the Mo/substrate interface. This in turn results in the min/max roughness of the Mo layer to be 11 nm, where the column peaks were found at maxima points and minima points were found where the columns coalesced. The structure of the SiO_x/Mo interface, however, was markedly different in the Au device compared to the Ti device. Oxidation of Mo was observed at the interface, with Mo found to incorporate into SiO_x. Both of these effects were observed in the Ti device, though to a much lesser extent. The incorporation of Mo was seen in HAADF images of the Au device, where bright regions protrude from the Mo layer into SiO_x. HAADF imaging also showed a high concentration of bright clusters in the SiO_x layer in proximity to the Au/SiO_x interface. In each case, the bright contrast is suggested to be due to Mo incorporation, which is detected through EDX and EELS measurements. It should be noted that no Au was detected to incorporate into the SiO_x layer through EDX suggesting the clusters contain Mo only. Compared to the Ti device, there were no dark regions in HAADF images at the troughs of the SiO_x/Mo interface. Instead, the results show that the oxidation along the entire SiO_x/Mo interface forms a thin MoO_x layer.

11.4.2 Structural Dynamics Due to Electrical Stress

The EDX results show no Au incorporation into SiO_x, neither in the pristine nor in the electroformed states. As a result, the low resistance state in the Au device is fundamentally different to that seen in the Ti device, where Ti, O and Mo transport play a key role. In particular, TiO_x was detected up to 15 nm from the Ti/SiO_x interface providing a potential path for electron transport. Instead, the low resistance states in the Au device relies solely on the movement of O and Mo. In each case a MoO_x layer is formed, though the nature of this layer was found to be different. In the

positive electroformed device, flat hill regions of MoO_x were found in between the SiO_x and Mo layers ranging 2 to 4 μm wide. Conversely, a consistent layer of MoO_x was found to form across the entire lamella in the negative electroformed device. From this, it is suggested that the negative bias promotes O vacancy generation in the SiO_x layer. This is consistent with the literature, where DFT calculations for SiO_2 show that electrons may trap at intrinsic wide angle O-Si-O bonds at Fermi energies of approximately 3.2 eV below the SiO_2 conduction band [125]. As a result, Si-O bonds are weakened leading to reduced barriers for O vacancy generation [131]. The Au work function is 5.1 eV [132], whilst the SiO_2 conduction band minimum (CBM) is found at 0.75 eV below vacuum level [144]. Au is known to form minimal interaction with SiO_2 interfaces, such that the bonding is dominated by van der Waals interactions. Therefore, it is reasonable to assume the work function shift is not significant. As such, the Au Fermi energy is estimated to be approximately 4.4 eV below the SiO_2 CBM. By applying a negative bias, the Fermi energy of Au will shift upwards toward the 3.2 eV bellow the SiO_2 CBM required to generate O vacancies. Subsequently, DFT calculations show that O vacancies trap electrons at Fermi energies of approximately 1.6 eV below the conduction band in SiO_2. Therefore, under a negative bias there is an increased probability of electron injection into the vacancy sites. It can then be suggested that the low resistance state in the negative electroformed Au device is due to electron transport through O vacancy sites *via* trap assisted tunneling.

Under positive electroforming, the Au device displayed many interesting properties. Firstly, a mixed Au-Si state was found in the Au electrode showing the incorporation of Si into Au. Furthermore, the total O K edge counts measured in the SiO_x layer gave a similar profile to the pristine device. The only major difference was the hill like MoO_x features and the increased oxidation of the Mo electrode. EDX measurements showed an increase in the Mo:Si counts ratio in the SiO_x layer suggesting the incorporation of Mo during positive electroforming. Additionally, EELS measurements for the positive electroformed device shows less O K edge prepeak counts in SiO_x compared to the pristine device. From this, it can be deter-

mined that the Mo in the SiO_x layer is at a lower oxidation state compared to the any Mo that has incorporated in the pristine and negative electroformed devices. As such, it is suggested that electron transport occurs through the MoO_x, where phases of $x < 3$ have been shown to be conducting. It has also been shown that amorphous MoO_x has a high work function energy of approximately 6.6 eV [145]. This crudely puts the MoO_x Fermi energy at 5.85 eV below the SiO_x CBM. With the Au Fermi energy at 4.4 eV below the SiO_2 CBM, a positive voltage is required to allow transport through MoO_x. The results for the positive electroformed device are therefore consistent with previous literature. However, it should be noted that the work function values given in this section are determined for SiO_2 whilst the SiO_x layer in the Au device has $x = 1.95$. Whilst there may be some deviation in the values, it is expected that the mechanisms discussed will be representative of the Au device.

11.5 Conclusion

The results in this chapter show that using Au as the top electrode material leads to some interesting features with key differences to the Ti device. In the Ti device, the roughness of the Mo layer was found to lead to void regions at the trough positions at the SiO_x/Mo interface. In the Au device, however, void like regions were not observed. Instead increased amount of Mo was seen to incorporate into SiO_x from fabrication. EELS and EDX measurements show that the incorporated Mo is oxidised, where the O K edge prepeak was measured throughout the SiO_x layer and in proximity to the Au/SiO_x interface. Post electroforming, MoO_x layers were found to form at the SiO_x/Mo interface with the effect more pronounced in the negative electroformed device. The formation of MoO_x in turn suggests the formation of O vacancies in the SiO_x layer. As a result, in the negative electroformed device, the low resistance state is suggested to be due to electron transport through defect sites in SiO_x such as O vacancies. Conversely, the low resistance state in the positive electroformed device is suggested to be due to electron transport through MoO_x. In this case, Mo was found to incorporate into SiO_x during electroforming, with the results suggesting the incorporated Mo is in a lowerer oxidation state compared to the pristine and negative electroformed devices.

Chapter 12

Au-Ti-SiO_x-Mo (Au-Ti) RRAM device

12.1 Introduction

Characterisation of the Ti (chapter 10) and Au (chapter 11) devices has shown the occurrence of a number of interesting processes in SiO_x RRAM devices. Following this, it is likely that the Au-Ti device will share properties from both the Au and Ti devices, beginning with the incorporation of electrode metal into the SiO_x layer in the pristine and electroformed states. In the Ti device, this was primarily Ti (with some Mo incorporating) whilst in the Au device, Mo was found to incorporate. In the Au-Ti device, the Ti layer is applied as a wetting layer such that it is only 5 nm thick (see section 3.2.3 for fabrication summary). In this case, it remains to be seen whether and to what extent Ti and Mo incorporate. A major difference between the Au and Ti devices was the nature of the SiO_x/Mo interface. Void regions were found in the Ti device at the troughs of the SiO_x/Mo interface, whilst no such regions were found in the Au device. This was a very interesting outcome as the SiO_x and Mo layers for the Au and Ti devices were deposited simultaneously on the same Si base wafer. The cause of this difference was suggested to be due to the relative O affinities of Ti, Mo and Au. In this case, Ti is favoured to oxidise whilst Au is not. Subsequently, in the Au device, more O was available to oxidise Mo to form MoO_x at the SiO_x/Mo interface. With Ti limited to a 5 nm layer in the Au-Ti device, it is unclear how the SiO_x will pattern to the Mo layer. Furthermore, the Au-Ti device is thought to operate under both the ECM and VCM mechanisms. In the

Au and Ti devices, the results show that positive electroforming utilised the ECM mechanism whilst negative electroforming utilised the VCM mechanism. As such, it is important to test whether this holds true to the Au-Ti device and to what extent.

In this chapter, the methods described in section 9.4 are used to characterise the Au-Ti device in its pristine and electroformed states. This involves a combination of TEM, STEM and EELS to understand the microstructure of the pristine device post fabrication. The combination of TEM, STEM and EELS is then used to characterise the devices after positive (+15 V, 1 mA current compliance) and negative (-15 V, 1 mA current compliance) electroforming to provide a direct comparison. From this, it is intended that the chemical changes observed post stressing will give insight into the electroforming mechanisms that occur in the Au-Ti device and SiO_x devices in general.

12.2 Pristine Au-Ti-SiO_x-Mo (Au-Ti) Device

12.2.1 HAADF Analysis

Fig. 12.1 shows BF and HAADF STEM images of the pristine Au-Ti device. This gives the thickness of the sputtered Mo and SiO_x layers to be 210 nm and 35 nm, respectively, matching the expected values from growth. The Ti and Au layers were expected to be 5 nm and 100 nm, respectively, giving a total of 105 nm. However, due to the high levels of interface roughness an exact determination of the Ti thickness was impossible. Instead, the thickness of the Au-Ti layer was found to be 110 nm giving a 5 nm error.

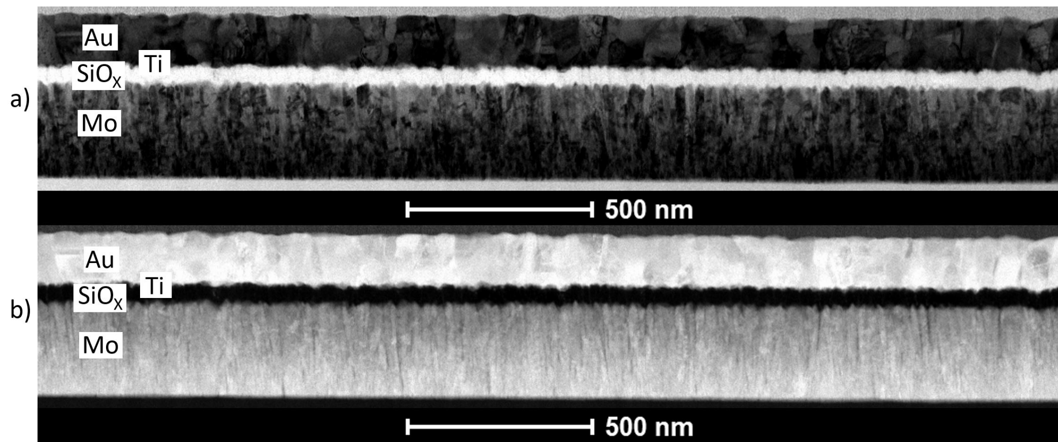

Figure 12.1: a) STEM BF and b) STEM HAADF image of a pristine Au-Ti-SiO_x-Mo device.

Fig. 12.2 shows that the Mo layer consists of long thin columns similar to the Ti and Au devices. This is an important observation as the Mo layer in the Au-Ti device was grown *via* magnetron sputtering compared to thermal evaporation used in the Ti and Au devices. In a similar fashion to the Ti and Au devices, columns are seen to form at the initial stages of Mo deposition, with some columns dominating as growth continues. Also from Fig. 12.2, it can be seen that the Au layer is polycrystalline, as seen in the Au device.

The Mo min/max roughness was measured across several HAADF images of the pristine Au-Ti device where horizontal lines were drawn at the minimum and maximum positions at the SiO_x/Mo interface (marked as red lines on Fig. 12.2). By then measuring the distance between the two lines, the min/max roughness of the

Au-Ti device was found to be 18 nm (compared to 11 nm in the Au and Ti devices). In each case, the roughness was found to be due to the columnar structure of the Mo layer, with maximum positions at Mo column peaks and minimum positions at Mo column boundaries or where the Mo columns coalesce. The local roughness was found to be very variable compared to the Ti and Au devices, where the concentration of rough areas with respect to to smooth areas is significantly higher.

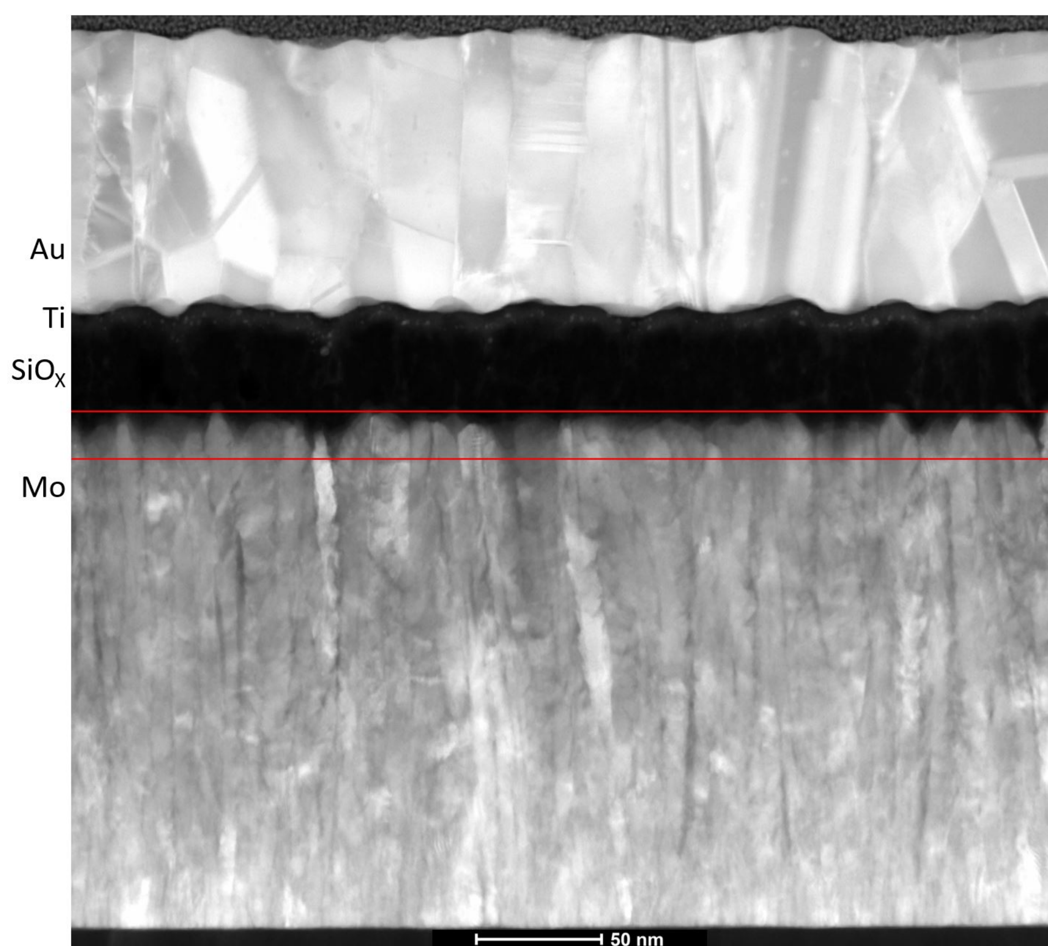

Figure 12.2: STEM HAADF image of a pristine Au-Ti-SiO_x-Mo device. The two horizontal red lines are separated by 18nm to mark the min/max of the Mo electrode roughness.

Fig. 12.3 shows a HAADF image of the Au-Ti device with the intensity limits adjusted to elucidate the Ti layer. During imaging, a diffraction pattern through this area was not observed suggesting that the layer is amorphous. However, in Fig. 12.3 small bright clusters can be seen ranging from 1 to 5 nm in size. The nature

of these clusters could not be directly probed, though previous studies show the existence of Ti clusters forming in amorphous TiO_2 layers. In this case, the clusters were confirmed to be Ti through observable TEM diffraction patterns [146]. The EELS measurements taken for the Ti device show that Ti at the Ti/SiO_x interface is heavily oxidised. As a result, it is suggested that these clusters are Ti crystals that have not scavenged O from the SiO_x layer. It should also be noted that these clusters may also contain Au.

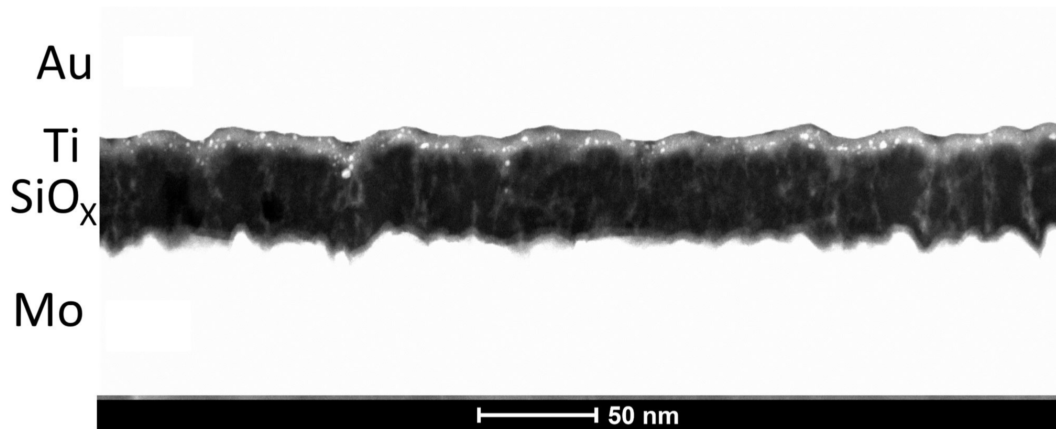

Figure 12.3: STEM HAADF of a pristine Au-Ti-SiO_x-Mo device showing bright clusters in the Ti layer

Similar to the Au and Ti devices, the morphology of the Au-Ti/SiO_x interface was found to pattern to the Mo electrode beneath. From Fig. 12.4 it can be seen that peak and trough regions at the Mo electrode shapes and patterns the SiO_x layer, followed by the Ti and Au layers. In the initial phases of SiO_x sputter deposition, SiO_x islands are suggested to form at the peaks of the Mo layer [63]. As deposition continues, the islands grow and coalesce to form a columnar structure. As a result, column bulk regions occur at the Mo peak positions and column boundary regions occur at the Mo trough positions. This is consistent with the HAADF images (Fig. 12.5), which show that the column boundaries propagate from troughs at the SiO_x/Mo interface. Interestingly, these column boundaries appear bright in the HAADF images, indicating that they contain more or more dense material. This is in contrast to the Ti device, where the majority of these boundaries have a darker contrast. It is expected that the bright contrast is a result of Mo, Ti and Au incorpo-

ration into the column boundaries during and post fabrication.

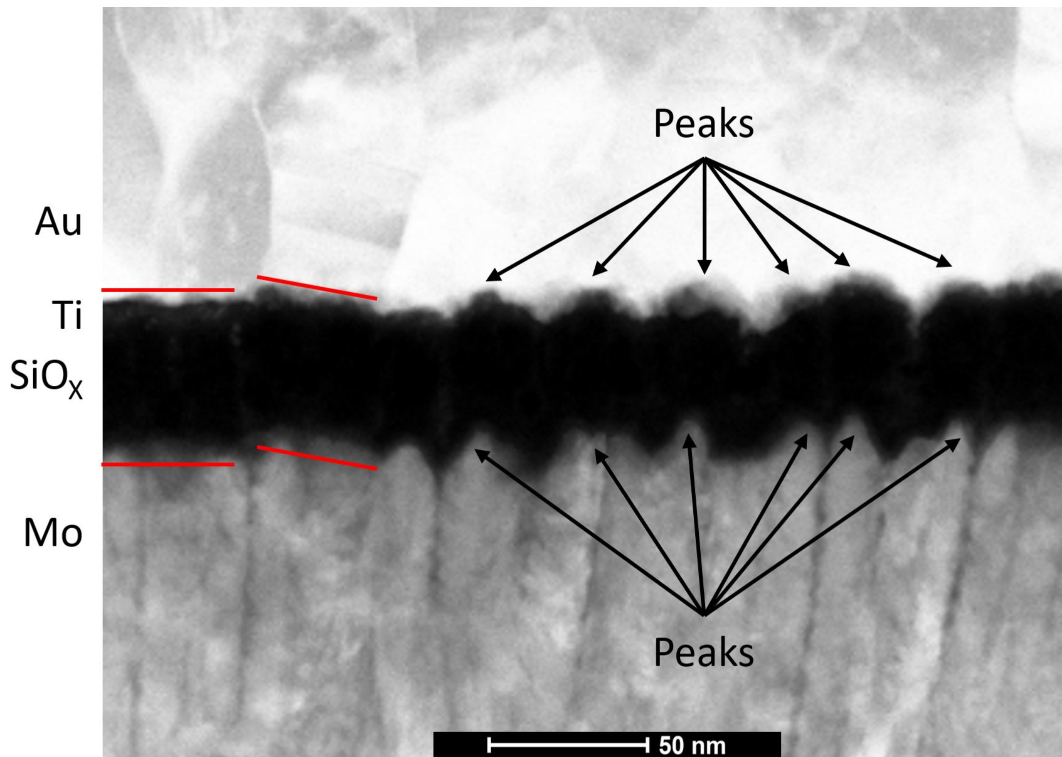

Figure 12.4: STEM HAADF image of a pristine Au-Ti-SiO$_x$-Mo device showing the patterning of the top (Au-Ti) electrode to the Mo electrode roughness. The peaks marked for the Mo electrode match the peak locations of the Au-Ti electrode. The red lines show the more smooth regions in the Mo electrode also pattern to the Au-Ti electrode.

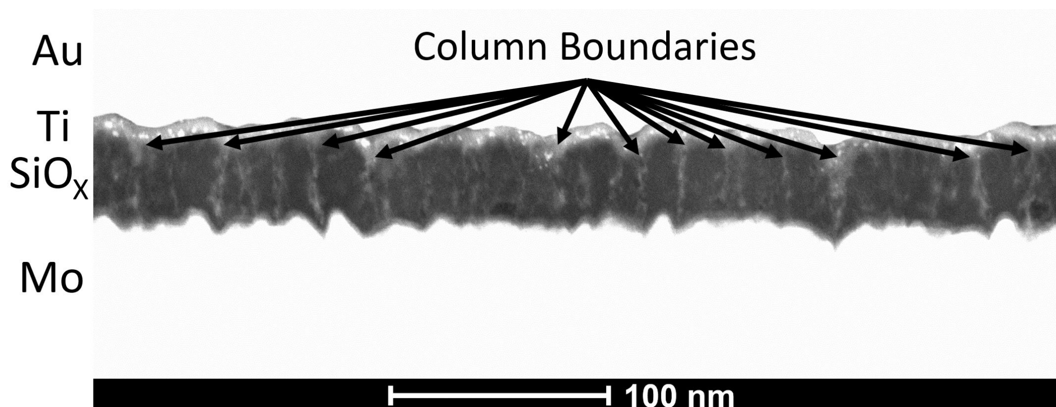

Figure 12.5: HAADF STEM image of a pristine Au-Ti-SiO$_x$-Mo device highlighting bright vertical column boundaries protruding from troughs at the SiO$_x$/Mo interface

In addition to the column boundaries, imaging shows that metallic clusters form in the SiO$_x$ layer. Fig. 12.6 shows TEM, HAADF and BF images of the same

region of a pristine Au-Ti device. From the TEM image (Fig. 12.6a), several small metallic clusters can be seen approximately 5 nm in diameter in the SiO$_x$ layer, with each cluster also visible in the HAADF (Fig. 12.6b) and BF (Fig. 12.6c) images. These clusters were found to form throughout the Au-Ti device, with imaging confirming they form in the column boundary regions. The composition of these clusters is characterised in the next section.

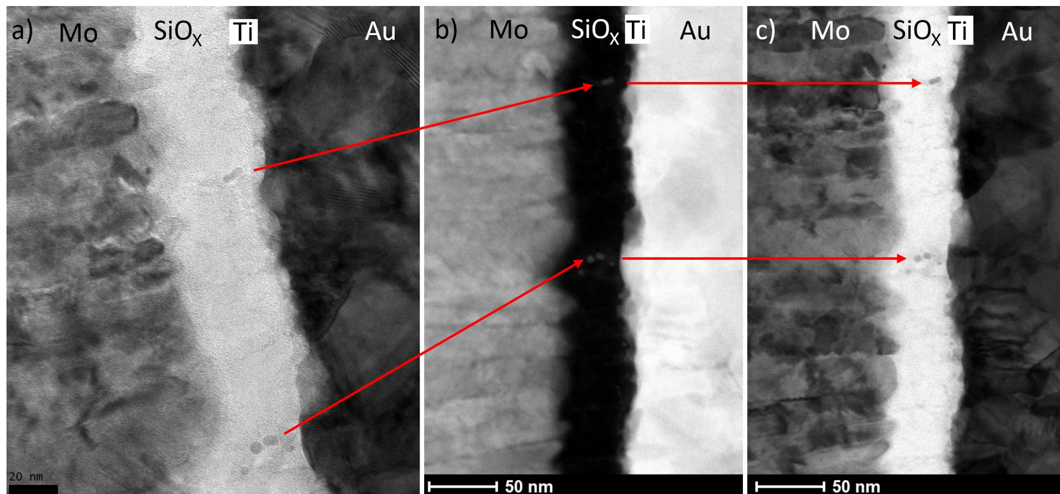

Figure 12.6: a) TEM image, b) HAADF STEM image and c) BF STEM image of a pristine Au-Ti-SiO$_x$-Mo device with metallic clusters formed in the SiO$_x$ layer.

A TEM image of one cluster in the SiO$_x$ layer is shown on Fig. 12.7. From this, a line profile (blue line) is taken orthogonal to the lattice lines as shown on Fig. 12.8. The lattice spacing of the cluster was found to be 0.237 ± 0.005 nm, matching well to the Ti hexagonal closed packed [002] lattice plane of spacing 0.234 nm [147].

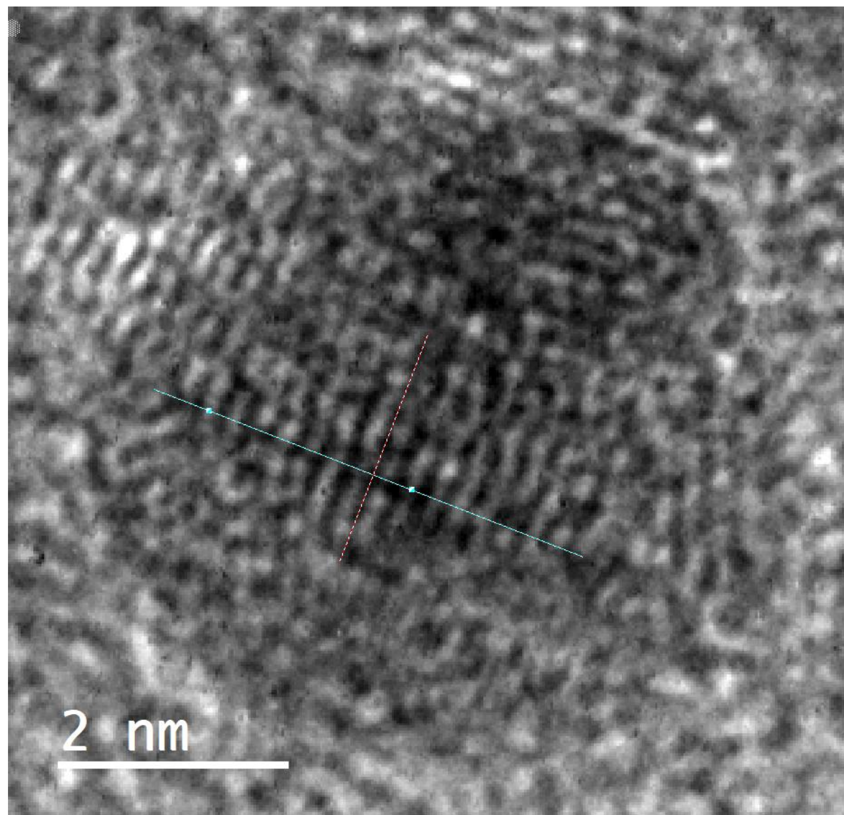

Figure 12.7: TEM image of metal cluster in SiO_x showing metallic nature. The blue line represents the region from which a line profile is taken.

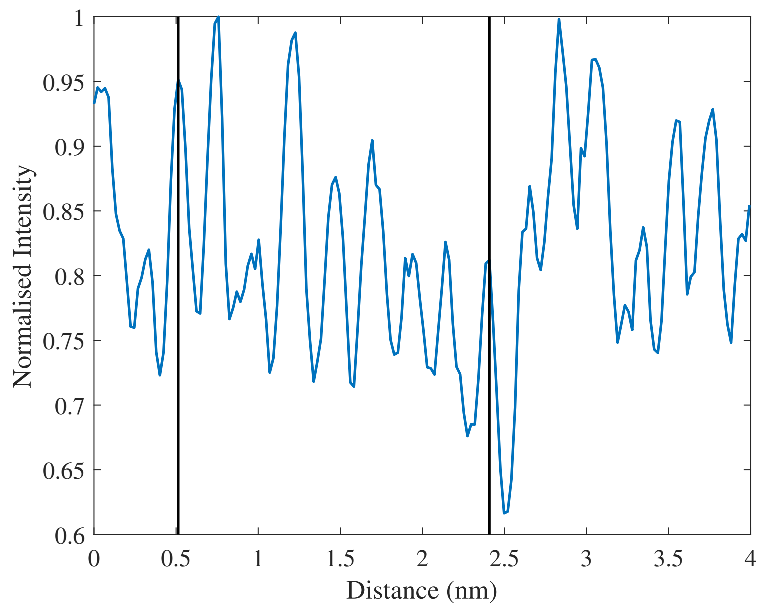

Figure 12.8: Profile taken from blue line on Fig. 12.7 showing the periodic and metallic nature of a cluster found in SiO_x. The vertical black lines represent the peak positions from which the lattice spacing for the metallic cluster is calculated.

12.2.2 EDX Analysis

To analyse the nature of the clusters observed in the SiO$_x$ layer more thoroughly, EDX measurements were made showing the clusters are of different composition depending on their location. From Fig. 12.9 it can be seen that the bright cluster regions contain mixtures of Mo, Ti and Au. Importantly, the cluster regions close to the Au-Ti electrodes contain Au, Ti and Mo, whilst the regions near Mo contain primarily Mo with traces of Ti. This shows both Mo and Ti are very mobile in the column boundaries. The EDX counts detected for Ti were found to reduce away from the Ti electrode, giving higher concentrations of Ti near the Ti layer. Conversely, the counts for Mo were found to be less dependent on the distance from the Mo electrode, where a high number of Mo counts was seen at bright cluster regions irrespective of the position in SiO$_x$. The results also show Au is only detected in the SiO$_x$ layer in proximity to the Au-Ti electrode, and is not detected near Mo. It should be noted that the total metal incorporation is still very limited as the devices are in a pristine, insulating state.

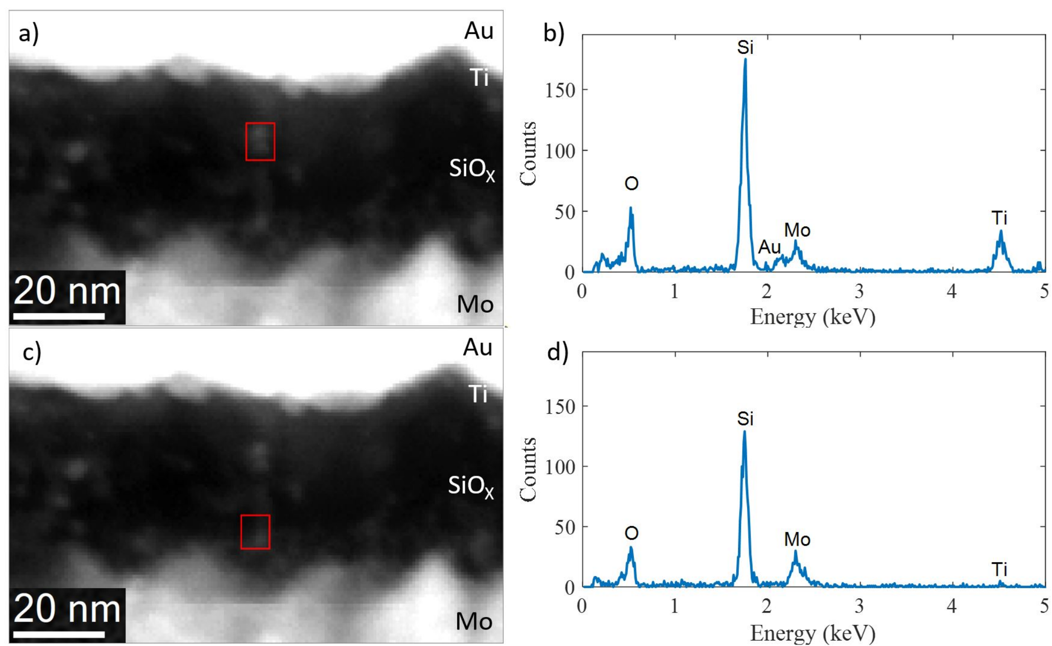

Figure 12.9: EDX measurements taken in the pristine Au-Ti device. The red box in a) and c) mark the regions the EDX spectra shown in b) and d) are collected respectively

12.2.3 EELS Analysis

Fig. 12.10a shows a HAADF image of the pristine Au-Ti device, where an EELS measurement was taken within the orange box. From this, the extracted O K, Ti $L_{2,3}$ and Si $L_{2,3}$ edge image maps are found in b) through d), respectively. The EELS measurement allows the Ti layer to be observed directly, showing that it is very uniform and is patterned by the SiO_x layer. A direct measurement of the thickness is not possible due to the roughness of the device. However, the full-width half-maximum of the Ti EELS counts was measured to be approximately 10 nm. The intensity of the EELS Ti $L_{2,3}$ edge (Fig. 12.10c) was found to be higher at peak regions of the Ti/SiO_x interface and lower at trough regions. The reduced brightness of Ti intensity at the trough regions is suggested to be a result of Ti incorporating into the SiO_x layer at the column boundaries (which are located at those trough regions). From the extracted EELS signals for O and Si (Fig. 12.10b and d respectively), the ratio of O and Si was calculated as seen in Fig. 12.11. From this, a higher O to Si ratio is observed at the Ti and Mo layers showing both are oxidised, with Ti having the highest O:Si ratio. However, no changes have been seen in the SiO_x layer, suggesting the stoichiometry of the SiO_x bulk is very uniform.

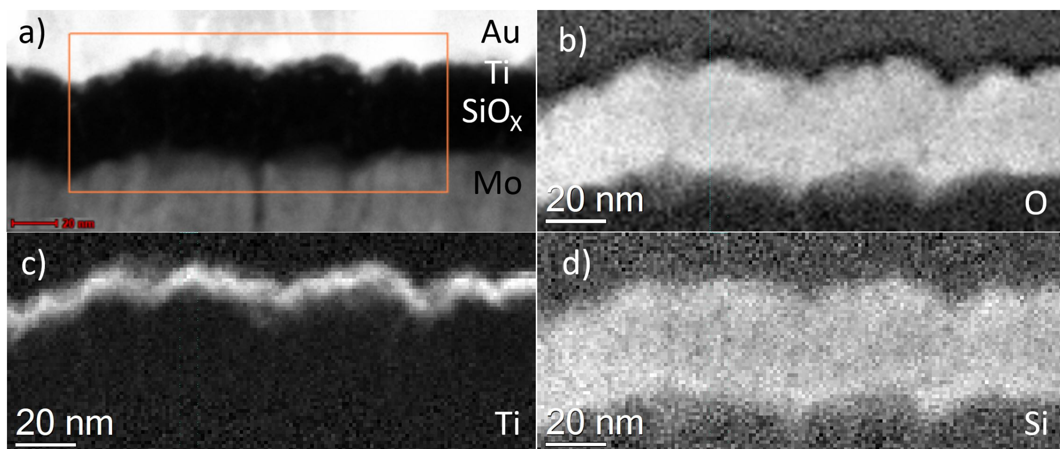

Figure 12.10: EELS data for the pristine Au-Ti device. a) HAADF image of the device where the EELS measurement is taken within the orange box. The extracted O K, Ti $L_{2,3}$ and Si $L_{2,3}$ edge maps are shown on b) - d) respectively

Fig. 12.12 shows a further EELS measurement, where the extracted Ti $L_{2,3}$, O

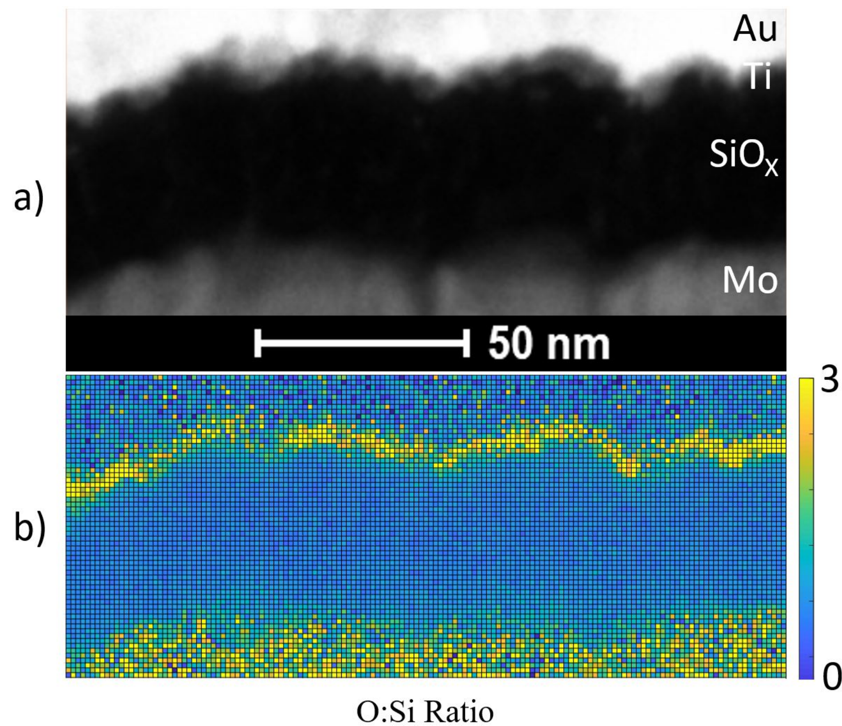

O:Si Ratio

Figure 12.11: Shows the O:Si ratio taken of the pristine Au-Ti device. a) HAADF image of the region within which the O K and Si $L_{2,3}$ edges are measured. b) shows the ratio of the O K edge to Si $L_{2,3}$ edge, calculated by dividing the extracted image maps of each EELS signal

K (total), O K prepeak (O_{Pre}) and O K SiO_x (O_{Si}) edge image maps can be seen on b) through e) respectively. The vertical blue lines on Fig. 12.12 represent the area from which the line profiles shown on Fig. 12.13 are taken. The O K edge prepeak, as discussed in section 9.4.1 is due to the excitation of electrons into unoccupied O 2p - metal d hybridized states which form in TiO_x and MoO_x. The Ti $L_{2,3}$ (Fig. 12.12b), and O K edge prepeak (Fig. 12.12d) maps are almost superimposable, indicating the Ti layer is oxidised. The O K edge prepeak map shows the Mo region has a very slightly higher contrast than the SiO_x layer, suggesting Mo is partially oxidised. The oxidation of Ti and Mo can also be seen from the line profiles on Fig. 12.13. The Ti $L_{2,3}$ and O K edge prepeak profiles are almost identical, suggesting all of the Ti layer is oxidised. Fig. 12.13 also shows that the O signal in SiO_x is highest near the Au-Ti/SiO_x interface and reduced near the SiO_x/Mo interface. This can be understood to be a similar phenomenon to that observed in the Ti device. In the Ti device, regions giving dark contrast in HAADF images at the SiO_x/Mo

interface were found suggesting voids form at interface trough positions. In the Au-Ti device, it is suggested that low density regions form at the trough positions, as can be seen on the O K (total) and O K SiO_x edge image maps.

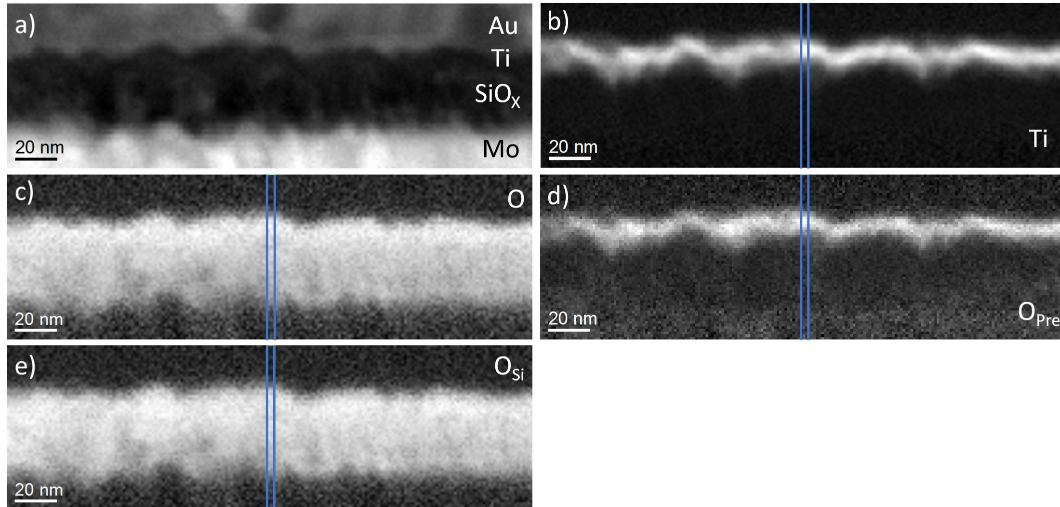

Figure 12.12: EELS data for the pristine Au-Ti device. a) HAADF image of the device where the EELS measurement is taken. The extracted Ti $L_{2,3}$, O K edge (total), O K edge (prepeak) and O K edge (SiO_x) maps are shown on b) - e) respectively

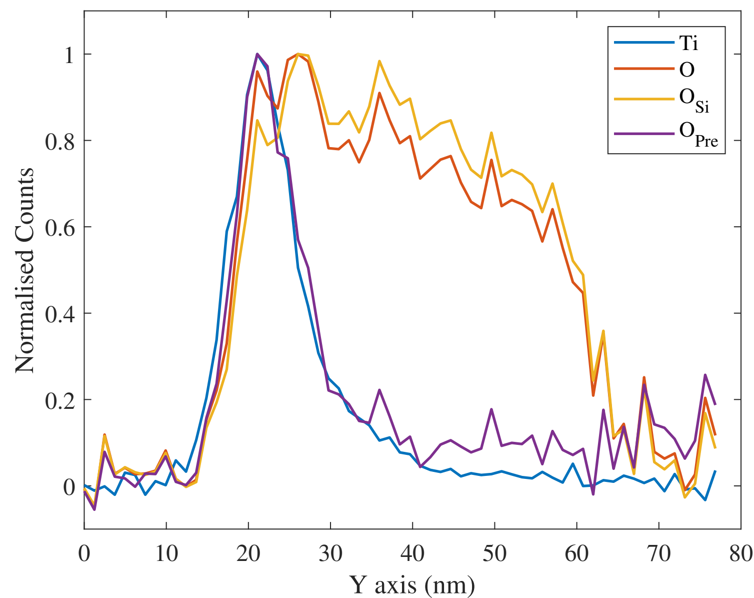

Figure 12.13: Line profile of the Ti $L_{2,3}$, O K edge (total), O K edge (prepeak) and O K edge (SiO_x) taken within the blue lines marked on Fig. 12.12

12.3 Columnar Boundaries

Fig. 12.14 shows the results of an EELS measurement of the Si $L_{2,3}$ edge taken over a column boundary region. From this, it is clear that the columns are vertical and protrude from the troughs at the SiO_x/Mo interface. Fig. 12.14b shows the extracted Si $L_{2,3}$ where the column bulk and column boundary regions are marked by blue and orange boxes, respectively. The Si $L_{2,3}$ edge for the two regions can be seen in c), where the edge onset for both regions can be seen to occur at the same energy. Furthermore, the shape of the Si $L_{2,3}$ edge in each region is identical. The only difference observed is the amplitude of the edge, where the column boundary region gives 27 % fewer counts. In this case, the counts were measured across an 8 eV width starting from the edge onset at 105 eV. This suggests that the oxidation state of SiO_x is the same at the column bulk and column boundary regions. It then follows that the column boundaries are void like because there would be changes expected in the Si $L_{2,3}$ edge if SiO_x had a 27 % lower density.

Fig. 12.15 shows a line profile taken of the Si $L_{2,3}$ edge for the same EELS measurement. It demonstrates that the Si $L_{2,3}$ counts are reduced by 32 % and 25 % respectively over two column boundary regions across the whole device. In each case, the regions of reduced intensity are approximately 5 nm wide, which matches boundary widths observed through HAADF imaging. This suggests the boundaries are in the range of 5 nm if they consist of low density SiO_x. Conversely, a reduction of 32 % of Si material over 5 nm would correlate to a void of approximately 1.7 nm wide (if a void is considered to contain no material). To confirm whether the boundaries are void like or low density regions, techniques such as TEM/STEM tomography are necessary and provide an important area for future work.

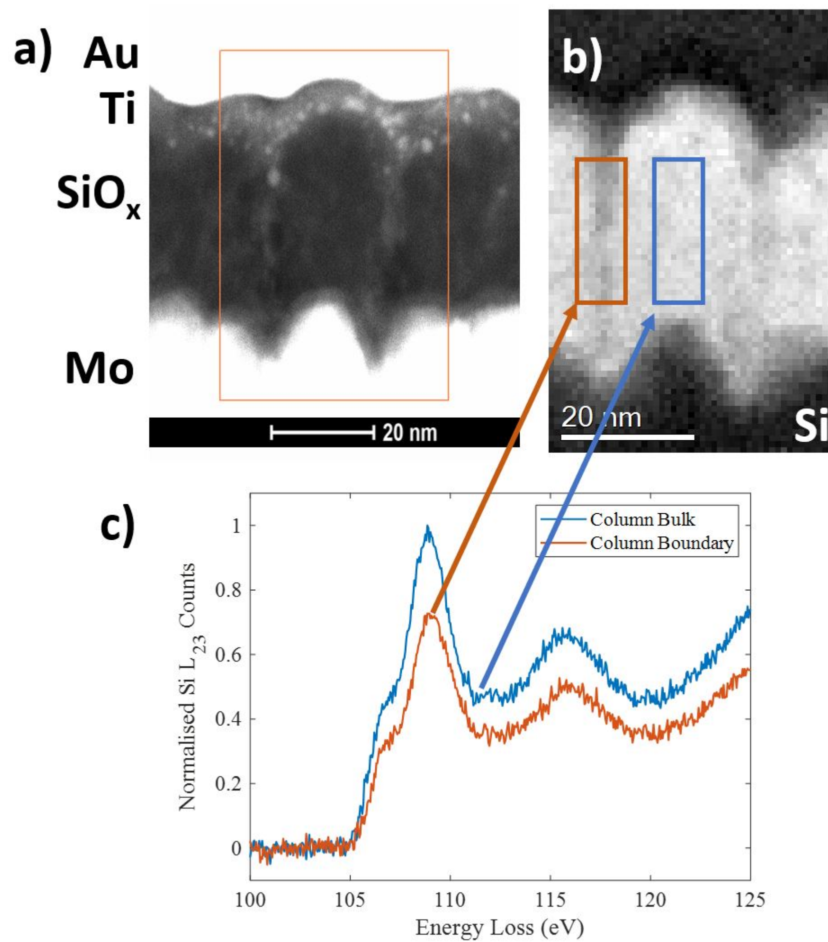

Figure 12.14: EELS measurement of columnar boundaries in the pristine Au-Ti device. a) HAADF image where the EELS measurement of the Si $L_{2,3}$ edge shown on b) is taken. The orange and blue boxes on b) mark column boundary and column bulk regions from which the Si $L_{2,3}$ spectra shown on c) are taken

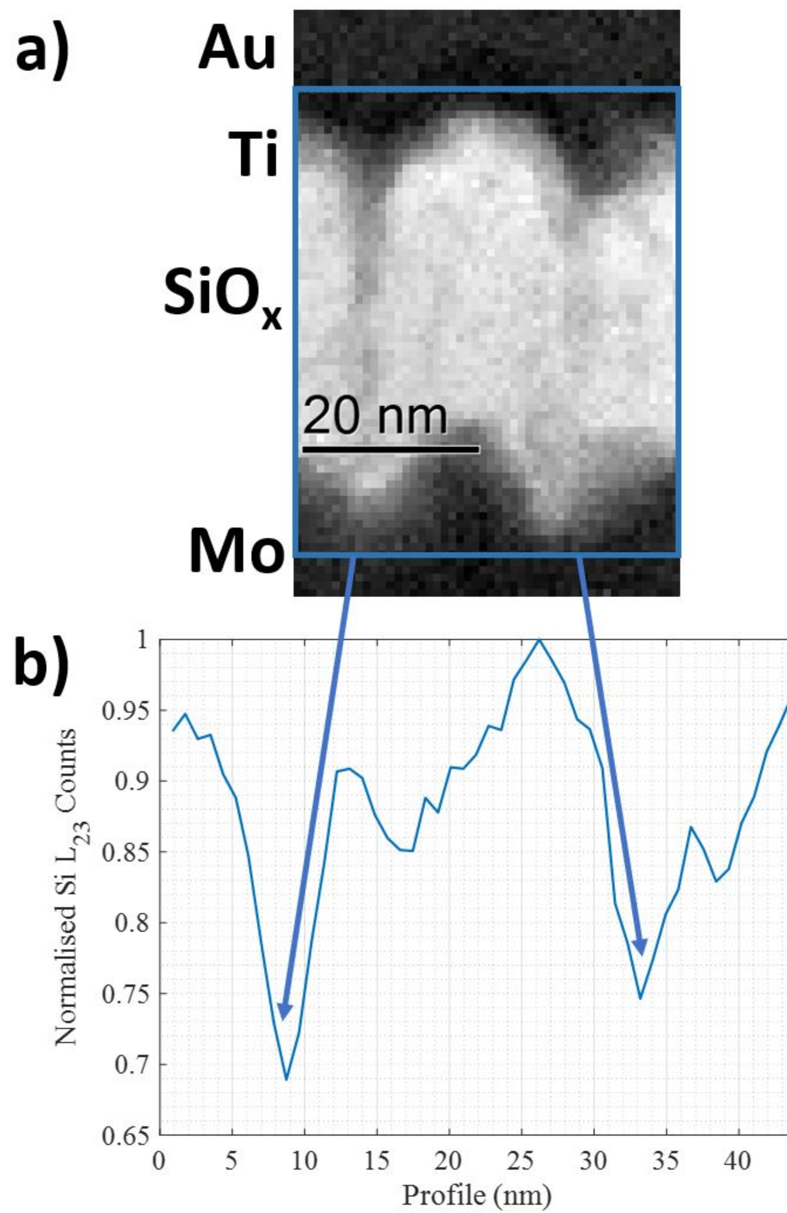

Figure 12.15: a) An Si $L_{2,3}$ edge image map of columnar boundaries in the pristine Au-Ti device. b) Line profile taken across the image map a) showing the reduction in Si $L_{2,3}$ in the columnar boundary regions.

12.4 Electroformed Au-Ti-SiO_x-Mo (Au-Ti) RRAM device

12.4.1 IV curve

The IV curves of the positive and negative electroformed Au-Ti device characterised in this chapter are shown on Fig. 12.16. In each case, the voltage was swept from 0 to +15 V or -15 V respectively, and back to 0 V in increments of 0.05 V. A current compliance of 1 mA was used to prevent the hard dielectric breakdown of the devices. The results show that a permanent resistance change was only achieved under positive electroforming. In this case, the current was seen to increase from 0 V to reach a plateau at 5 V. Subsequently, a sharp rise in current was seen from 7.4 V until the compliance of 1mA was reached at 8 V. The two step rise in current, from 0 to 5 V and then from 7.4 to 8 V suggests two different transport mechanisms are occurring. Though the exact causes are unclear, it is suggested that the slower rise in current between 0 to 5 V is due to metal incorporation into the SiO_x layer whilst the sharp rise between 7.4 V to 8 V is due to electron transport through metal oxide in the SiO_x layer.

The negative electroforming IV curve shows that there is a resistance change as the voltage is decreased to -15 V. This is a two step process, where there is a sharp rise in current observed from 0 to -2.68 V where a small plateau is reached before another rise between -3.22 V to 9.66 V where the 1 mA current compliance is reached. As the voltage is swept back to 0 V the current reduces from the 1 mA current compliance at -8.81 V showing there is some resistance change. However, at 0 V the device returns to a high resistance state.

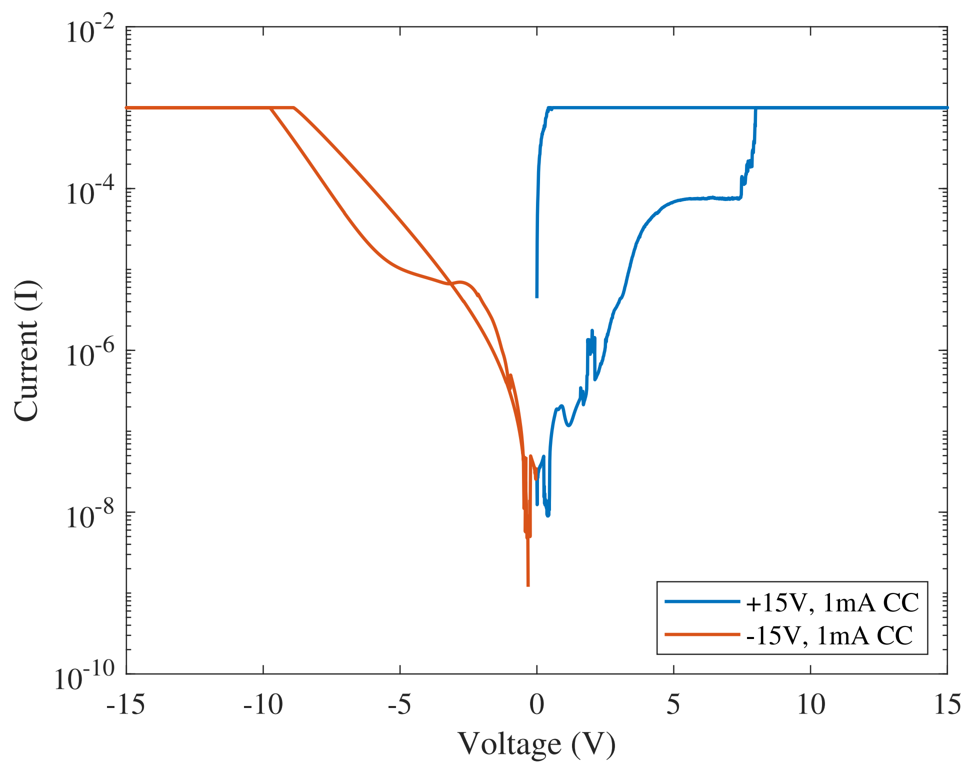

Figure 12.16: IV curves of the Au-Ti device after positive (blue) and negative (orange) electroforming.

12.4.2 Positive electroformed Au-Ti Device

12.4.2.1 EELS Analysis

Fig. 12.17 shows the results of an EELS measurement on the positive electroformed Au-Ti device. a) shows a HAADF image of the device, where the EELS measurement is taken within the orange box. The extracted Si $L_{2,3}$, Ti $L_{2,3}$, O K edge (total), O K edge (SiO_x) and O K edge prepeak components are shown in b) through f), respectively. The blue lines of Fig. 12.21 show two regions (R1 and R2) from which the line profiles on Fig. 12.18 are taken. R1 marks a region where there is a large trough at the SiO_x/Mo interface whilst R2 marks a small trough region.

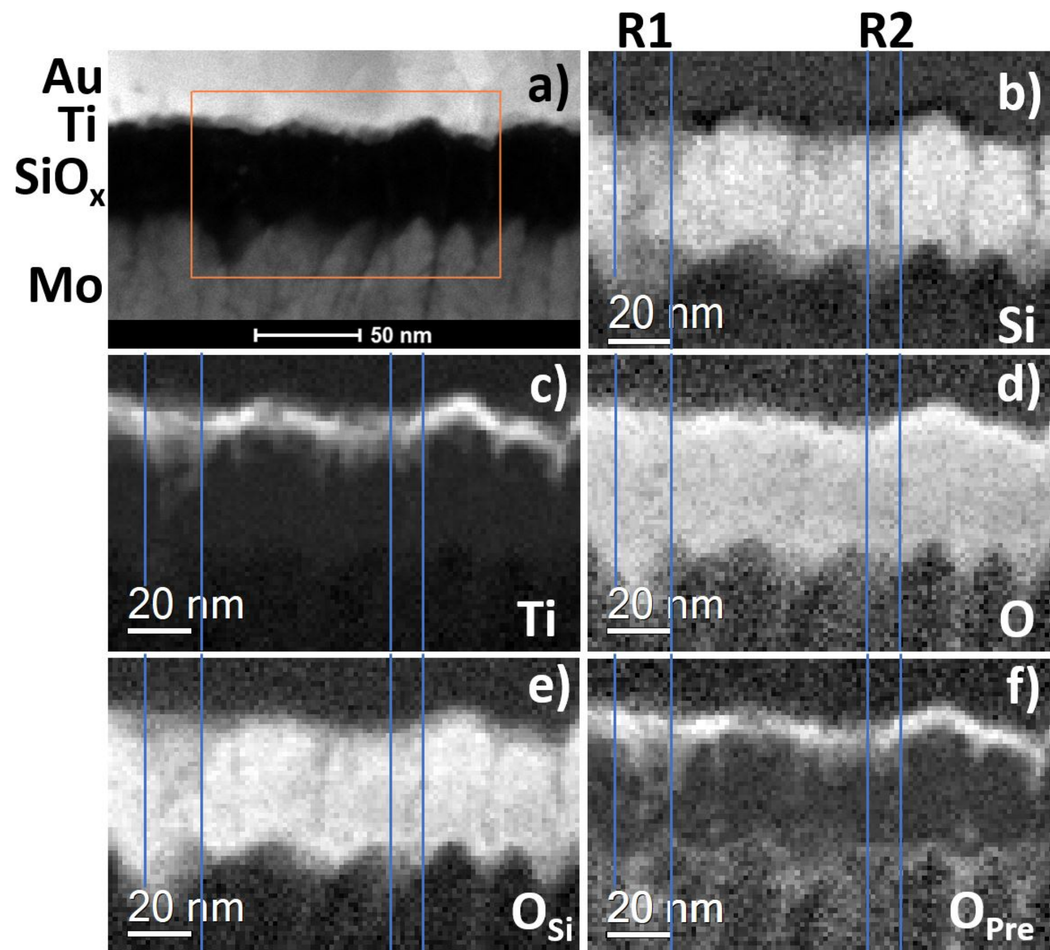

Figure 12.17: EELS data for the positive electroformed Au-Ti device. a) HAADF image of the device where an EELS measurement is taken within the orange box. The extracted Si $L_{2,3}$, Ti $L_{2,3}$, O K (total), O K SiO_x (O_{Si}) and O K prepeak (O_{Pre}) edge maps are shown on b) - f) respectively. The blue lines mark the region from which the lineprofiles shown in Fig. 12.18 are taken.

The Si $L_{2,3}$ image map shows that Si deficient column boundaries are formed that span the entire SiO_x layer, bridging the Mo electrode to the Au-Ti electrode. It can also be seen that these boundaries form at the troughs of the SiO_x/Mo interface. The column boundary patterns are not observed in the O K edge (total) map, however, where instead it can be seen that O fills the boundary regions in the form of metal oxide. By comparing the O K edge components, the O K edge (SiO_x) map matches the Si $L_{2,3}$ map, whilst the O K edge prepeak follows the column boundary regions. The Ti map in turn shows rods protrude from the troughs of the Ti/SiO_x interface into the SiO_x column boundaries. The O K edge prepeak can be detected not only in the regions where Ti is detected, but also in regions near the SiO_x/Mo interface. This demonstrates the incorporation of Mo and the formation of MoO_x.

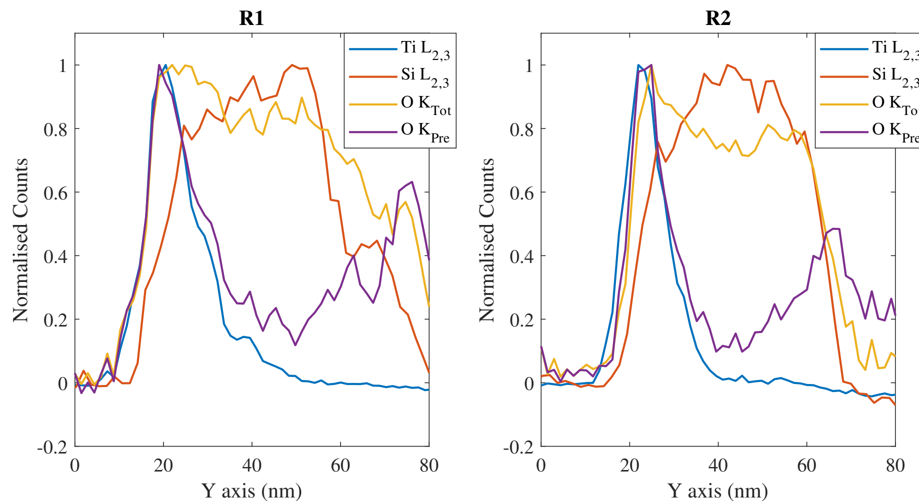

Figure 12.18: Line profiles of the Ti $L_{2,3}$, Si $L_{2,3}$, O K (total) and O K prepeak (O_{Pre}) edges for positive electroformed Au-Ti device taken within regions marked by the blue vertical lines in Fig. 12.17

The Ti line profile in R1 shows that Ti is detected up to 10 nm from the SiO_x/Mo interface. In this case, the O K edge prepeak follows the same trajectory as Ti, where the O K edge prepeak signal reaches a minimum at the point the Ti signal reduces to zero. In this case, the O K edge prepeak counts are 12 % of the counts detected at the Ti layer. The O K edge prepeak signal then rises to reach 63 % at the Mo layer. This indicates that there is a consistent filament of metal oxide in the SiO_x layer, containing both TiO_x and MoO_x. As such, it is suggested that the

low resistance state is due to electron transport through TiO_x and MoO_x that has formed in the SiO_x column boundaries.

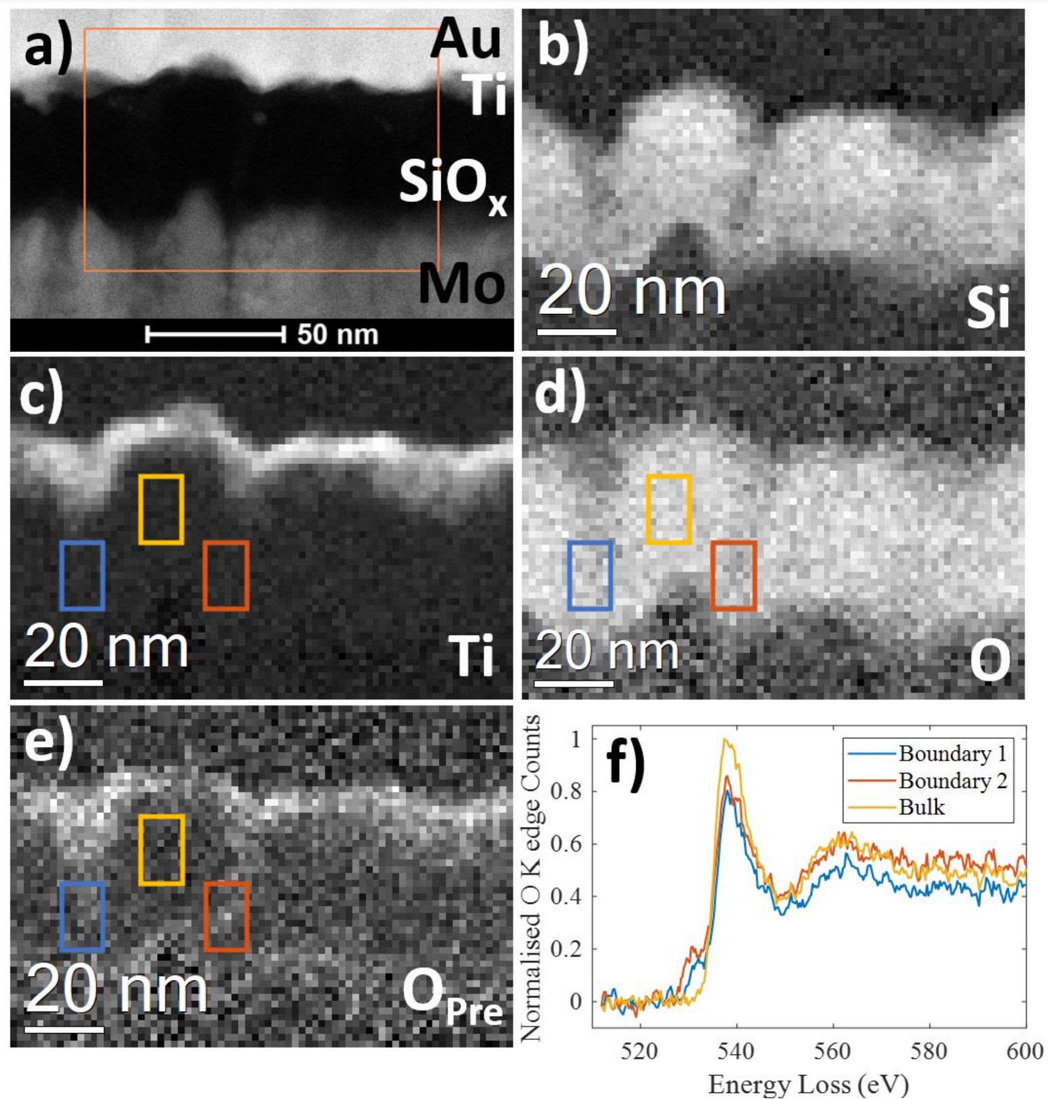

Figure 12.19: EELS data for the positive electroformed Au-Ti device. a) HAADF image of the device where an EELS measurement is taken within the orange box. The extracted Si $L_{2,3}$, Ti $L_{2,3}$, O K (total) and O K prepeak (O_{Pre}) edge maps are shown on b) - e) respectively. f) shows the O K edge spectra for the column boundary (blue and orange boxes) and column bulk (yellow box) regions.

Fig. 12.19 shows the results of another EELS measurement taken in a region where there are distinct column boundaries in the SiO_x layer. The left of the HAADF image in a) shows there is a sharp peak at the SiO_x/Mo interface, which has a trough on either side. The extracted Si $L_{2,3}$ edge (Fig. 12.19b) shows two distinct column boundaries protruding from the troughs at the SiO_x/Mo interface,

where the intensity in the image map is reduced by 34 % and 18 % respectively compared to the bulk Si intensity. The extracted Ti $L_{2,3}$ edge, O K edge and O K edge prepeak image maps are shown in c) through e), respectively. Each image map contains three boxes, which mark the column boundary 1 (blue), column boundary 2 (orange) and column bulk (yellow) regions. The boxes were placed in the column boundary and bulk regions where no Ti $L_{2,3}$ signal was detected. The summed EELS O K edge signal from these marked regions (Fig. 12.19f) shows the presence of the O K edge prepeak at the column boundaries and not in the column bulk. This confirms that the column boundary regions contain MoO_x, whilst no metal oxide is formed in column bulk. The results therefore show that both TiO_x and MoO_x form in the column boundaries after positive electroforming. In this case, TiO_x protrudes from the Ti/SiO_x interface and MoO_x protrudes from the SiO_x/Mo interface to form a continuous metal oxide filament in the SiO_x column boundaries.

12.4.3 Negative electroformed Au-Ti Device

12.4.3.1 SEM Analysis

Negative electroforming of the Au-Ti device showed a very different response to the positive electroformed device. During the electroforming process, bubbles were seen to form on the devices. Fig. 12.20 shows a series of SEM images of one bubble taken during lamella fabrication, measuring 24 μm wide. Images show the bubble forms due to the delamination of the Au-Ti device from the SiO_2 substrate layer on the base wafer. c) and d) show the Mo layer either side of the bubble is separated from the substrate at both ends. During the negative electroforming of the Au device, O was found to diffuse through the column boundaries in the Mo layer. As such, it is expected the delamination occurs due to the accumulation of O at the Mo/SiO_2 substrate interface.

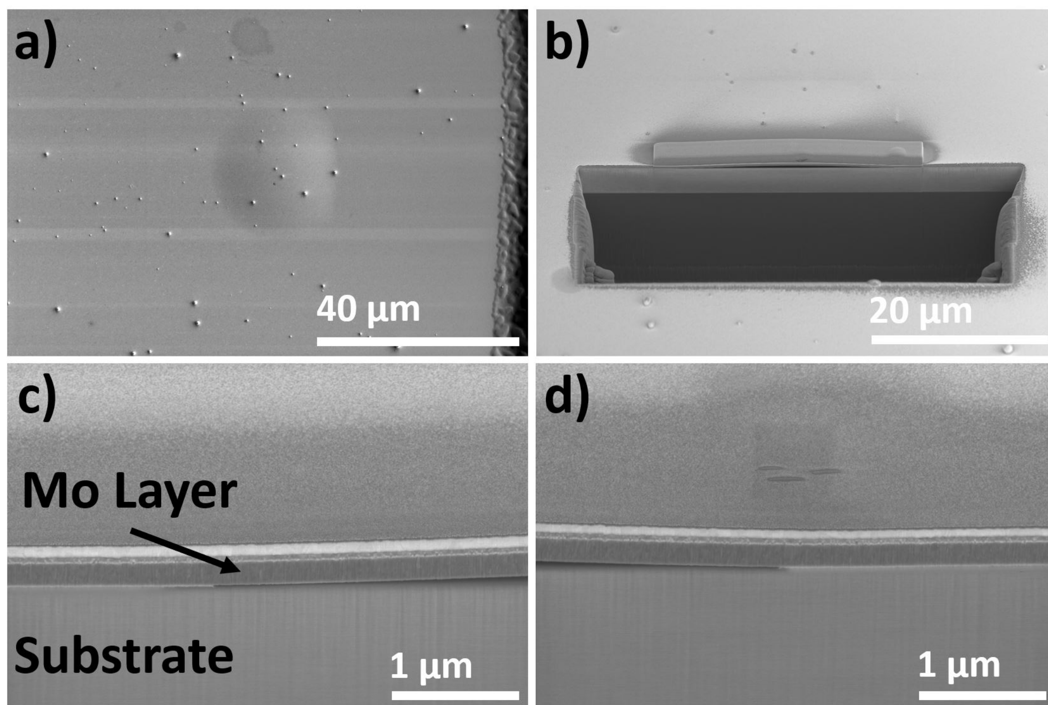

Figure 12.20: SEM images of the negative electroformed Au-Ti device. a) An example bubble that appears during electroforming, whilst b) shows the a trench formed by ion beam milling during lamella preparation. c) and d) show SEM images of the Mo layer delaminated from the substrate

12.4.3.2 EELS Analysis

Fig. 12.21 show the results of an EELS measurement on the negative electroformed Au-Ti device, where the Ti $L_{2,3}$, O K edge (total), O K edge (SiO_x) and O K edge prepeak components are extracted on b) through e) respectively. The blue lines on Fig. 12.21 mark the regions where the line profiles on Fig. 12.22 are taken.

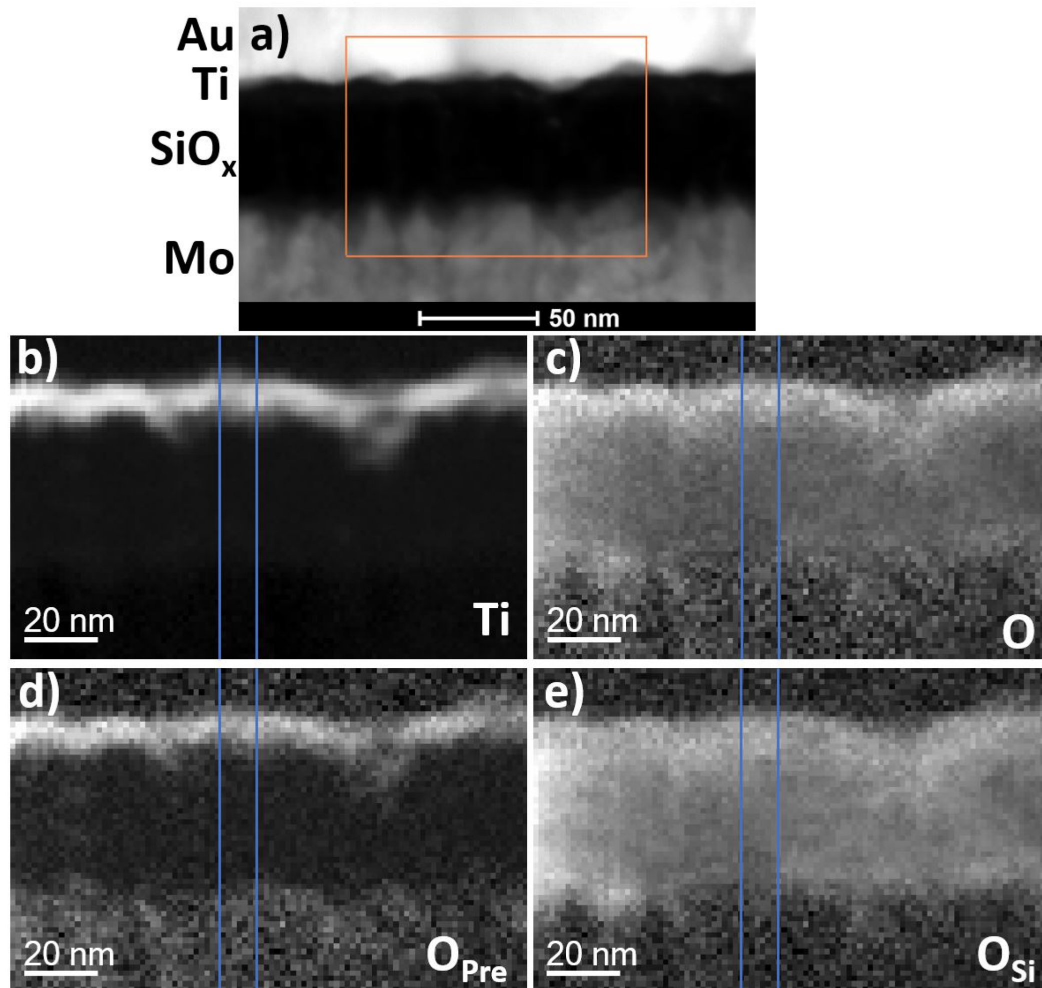

Figure 12.21: EELS data for the negative electroformed Au-Ti device. a) HAADF image of the device where an EELS measurement is taken within the orange box. The extracted Ti $L_{2,3}$, O K (total), O K prepeak (O_{Pre}) and O K SiO_x (O_{Si}) edge maps are shown on b) - e) respectively. The blue lines mark the region from which the lineprofiles shown on Fig. 12.22 are taken.

The extracted Ti $L_{2,3}$ image map shows that no Ti is incorporated into SiO_x. Instead, the O K edge image maps show reduced O counts suggesting O has been expelled from SiO_x. The line profile on Fig. 12.22 shows O is retained by the Ti

layer, whilst the concentration of O then reduces gradually across the SiO$_x$ layer to 30 % at the SiO$_x$/Mo interface. O is also detected in the Mo layer, where the concentration continues to reduce gradually confirming the ejection of O from the SiO$_x$ layer. It is therefore expected that the delamination of the Au-Ti device from the substrate is due to the build up of O at the SiO$_x$/Mo interface. The low resistance state is therefore suggested to be due to electron transport *via* O vacancies formed in the SiO$_x$ layer. It should also be noted that no patterning was observed in the O K edge map. This is important as it suggests that the columnar structure does not play a significant role in the O vacancy generation across the SiO$_x$ layer in this device.

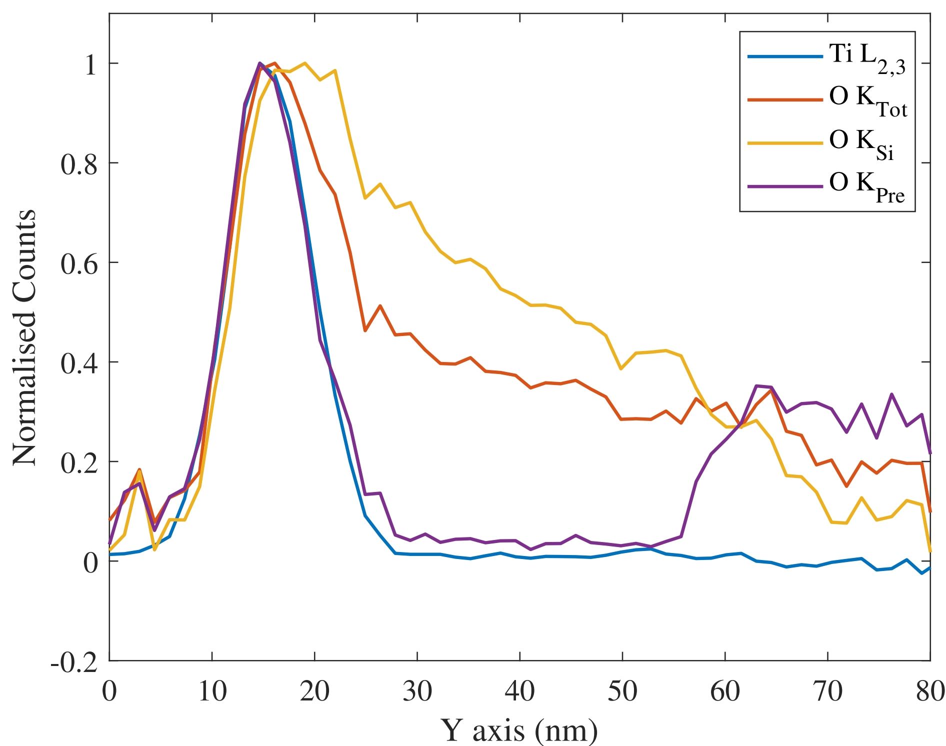

Figure 12.22: Line profiles of the Ti L$_{2,3}$, O K (total), O K prepeak (O$_{Pre}$) and O K SiO$_x$ (O$_{Si}$) edges for negative electroformed Au-Ti device taken within the blue vertical lines marked in Fig. 12.21

12.4.3.3 HAADF Analysis

It should be noted that whilst no metal incorporation was detected in the EELS measurements, either through the Ti L$_{2,3}$ edge or the O K edge prepeak, HAADF imaging shows that the column boundaries still appear bright in the negative electro-

formed device (Fig. 12.23). This is consistent with the pristine device, suggesting that there is still metal/metal oxide in the boundaries. However, the quantity of this is below the detection limit of the EELS measurement.

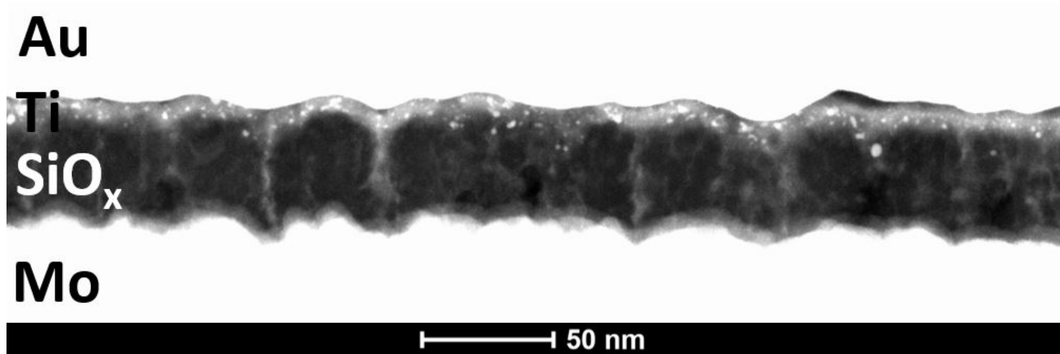

Figure 12.23: HAADF image of the negative electroformed Au-Ti device

12.5 Summary of Main Results

12.5.1 Device Microstructure (Pristine)

The Au-Ti device shows a mixture of properties from the Au and Ti devices. Similar to the Ti device, significant patterning of the SiO_x layer to Mo was observed through the formation of columnar boundaries. In this case, the column boundaries were found to form at the troughs of the SiO_x/Mo interface and protrude through the SiO_x layer to the Au-Ti/SiO_x interface. The increased roughness of the Mo layer in the Au-Ti device was found to lead to a greater concentration of these boundaries compared to the Ti device. The nature of the boundaries was also very different compared to the Ti device, where the majority of boundaries in the Au-Ti device span across the SiO_x layer with bright contrast in HAADF images. EELS and EDX maps of the boundaries show they contain both Ti and Mo (plus Au in proximity to the Au-Ti electrode). This is an important observation as it shows the column boundaries facilitate electrode metal transport in the pristine state. Finding both Mo and Ti is interesting as this differs from the Ti and Au devices where primarily one metal (Ti or Mo, respectively) was seen to incorporate into SiO_x. The incorporation of both Ti and Mo is suggested to be a result of two factors. Firstly, the increased concentration of column boundaries provides more paths to metal to incorporate, therefore allowing additional metal incorporation. Secondly, the limited amount of Ti in the device creates less competition for O. The oxide formation enthalpy for TiO_2, SiO_2, MoO_3 from Ti, Si and Mo is 944 kJ/mol, 910.7 kJ/mol and 745.1 kJ/mol, respectively [139]. With the limited O scavenging by Ti, more O is available to form mixed Mo-Si oxide in SiO_x [148]. It is also important to note that the Mo layer in the Au-Ti device was grown using sputter deposition with the intention of developing a more rough SiO_x/Mo interface. It is also possible that the increased roughness or the sputtering technique itself facilitates Mo incorporation.

12.5.2 Structural Dynamics Due to Electrical Stress

The effects of positive and negative electroforming in the Au-Ti device are consistent with those observed in the Au and Ti devices. Under a positive bias, Ti and Mo

are incorporated into the SiO_x layer through the column boundaries. Once incorporated, both Ti and Mo are oxidised through the scavenging of O from SiO_x. In this case, both TiO_x and MoO_x were detected through EELS measurements of the O K edge prepeak. This results in a low resistance state consisting of continuous metal-oxide filaments in the SiO_x column boundaries. Additionally, the accumulation of O at the Ti layer was observed as well as the oxidation of the Mo electrode at the SiO_x/Mo interface.

Under a negative bias, O was found to be expelled from the SiO_x layer. EELS measurements of the O K edge show that O is retained by the Ti layer in the form of TiO_x. The O K edge counts in the SiO_x layer at the Ti/SiO_x interface were detected to be 80 % of the counts in the TiO_x layer. Furthermore, the O K edge counts reduce with an almost constant gradient through the SiO_x layer to 30 % at the SiO_x/Mo interface. In contrast to the positive electroformed device, the columnar microstructure in the SiO_x layer did not appear to play any significant role in O vacancy generation. This was observed through EELS image maps of the O K edge where O was uniformly lost from the column boundaries and column bulk. The O K edge was detected at the SiO_x/Mo interface and in Mo showing that the Mo layer had become oxidised. SEM images during the lamella preparation of the negative electroformed device showed the Au-Ti device delamination between the Mo layer and the substrate. As such, it is suggested that the low resistance state is due to the formation of O vacancies in the SiO_x layer. The O generated from this is suggested to diffuse through the Mo layer *via* field assisted diffusion to accumulate at the Mo/substrate causing the delamination of the device. The mechanisms for O vacancy generation and the subsequent electron transport across the vacancies are discussed in section 9.3.

The resistive switching behaviour in the Au-Ti devices occurs after negative electroforming. As stated, it is suggested that the low resistance state is due to electron transport *via* O vacancies. To reset the devices to a high resistance state, a positive bias is then applied. With HAADF images showing that metal is still incorporated into the SiO_x layer, it is suggested that a positive bias results in the

reduction of the metal oxide in the SiO_x layer. In the Au and Ti devices, not only did metal incorporate into SiO_x after positive electroforming to form metal oxide, the metal oxide in the SiO_x layer was found to be in a lower oxidation state compared to the pristine and negative electroformed devices. In the Au-Ti device, a similar process is suggested to occur on the reset (positive) bias where the metal oxide in the SiO_x layer is reduced to lower oxidation states. In this case O is released from the metal oxide to recombine to O vacancies creating a high resistance state. In this way, it is reasonable to suggest the resistive switching phenomenon is due to O transport from SiO_x to TiO_x and MoO_x and in the reverse direction. In this case, negative bias leads to O vacancies in SiO_x and metal oxide formation whilst a positive bias leads to the reduction of metal oxide and SiO_x O/O vacancy recombination. In this case, the columnar structure plays a vital role as this is where metal has incorporated into the SiO_x layer. It is also likely that additional metal may incorporate into SiO_x during the reset (positive bias) phase. This would increase the amount of metal oxide in the device able to facilitate resistive switching.

12.6 Conclusion

The Au-Ti device shows significant patterning of the SiO_x layer to roughness of the Mo layer. Column boundaries were found to form at the troughs of the SiO_x/Mo interface and protrude through the SiO_x layer to the Au-Ti/SiO_x interface. EELS and EDX maps of the boundaries show that they contain both Ti and Mo plus Au in proximity to the Au-Ti electrode showing the column boundaries facilitate electrode metal transport, even in the pristine state. The effects of positive and negative electroforming in the Au-Ti device is consistent with that observed in the Au and Ti devices. Under a positive bias, Ti and Mo is incorporated into the SiO_x layer through the column boundaries. The low resistance state is suggested to be due to electron transport through continuous metal-oxide (containing TiO_x and MoO_x) filaments in the SiO_x column boundaries. Conversely under a negative bias, O was found to be expelled from the SiO_x layer and through the Mo electrode leading to the delamination of the device at the Mo/substrate interface. The low resistance state in this case is suggested to be due to electron transport through the O vacancies in the SiO_x layer via trap assisted tunneling. The resistive switching phenomenon is suggested to be due to O transport from SiO_x to TiO_x and MoO_x (set) and in the reverse direction for the reset operation.

Chapter 13

Part II: Summary and Future Work

13.1 Summary

In this part of the thesis, electron microscopy was used to study Au-Ti-SiO_x-Mo (Au-Ti), Ti-SiO_x-Mo (Ti) and Au-SiO_x-Mo (Au) RRAM devices, where x $\approx$ 1.95. The reduced oxide in this case was used to artificially create O vacancies in the oxide layer, promoting the VCM mechanism. Of particular interest are the Au-Ti devices which perform well as computer memory, showing optimal properties such as low switching voltages, high endurance and high retention times. In this case, the Ti layer is applied as a wetting layer between Au and SiO_x and is only 5 nm thick. Comparatively, the Ti and Au devices do not show repeatable resistive switching, and are studied to gain a better understating of the Au-Ti device. The SiO_x and Mo layers in the Au and Ti devices were grown simultaneously on the same base wafer before being cleaved and patterned with the Au and Ti electrodes respectively. The Au-Ti, Au and Ti devices were each characterised in their pristine and electroformed states. To electroform the devices, bias was applied from 0 to +15 V or -15 V for positive or negative electroforming respectively, and back to 0 V in increments of 0.05 V. A current compliance of 1 mA was kept during electroforming to prevent the hard dielectric breakdown of each device.

The characterisation of each device in the pristine state shows the patterning of the SiO_x layer to the rough features of the Mo electrode. In this case, the patterning was determined to be affected by the O affinity of the top electrode. In the Ti

device, Ti was seen to scavenge O from the SiO_x layer whilst the Mo layer showed minimal oxidation. Instead, void regions in the SiO_x layer were found at the trough positions of the SiO_x/Mo interface. Furthermore, both Ti and Mo were found to incorporate into the SiO_x layer. Comparatively in the Au device, no oxidation of Au occurred and no voids were found at the SiO_x/Mo interface. Instead, considerable oxidation of the Mo electrode was seen and a large amount of Mo was detected to have incorporated into the SiO_x layer (compared to the Ti device). This is an important observation as the SiO_x and Mo layers were grown together in the Au and Ti devices, showing the choice of top electrode has far reaching implications towards the structure of the device. The Au-Ti device shows a combination of behaviours between the Au and Ti devices, where columnar boundaries were found to form at the SiO_x/Mo interface trough positions. In this case, the columns were found to span the oxide and facilitate the incorporation of Ti and Mo. This resulted in the column boundary regions appearing with bright contrast in STEM imaging due to the Ti and Mo incorporation. It should be noted that Au was also detected in the column boundaries in proximity to the Au-Ti electrode.

Under positive electroforming, each device was found to show an ECM type response. In each case, additional metal was found to incorporate into the SiO_x layer. In the Ti device this consisted of Ti and Mo incorporation, whilst only Mo incorporation was seen in the Au device. In both cases, it was also determined that the oxidation state of the metal incorporated during positive electroforming was lower than in the pristine state. Similarly, both Ti and Mo were found to incorporate in the Au-Ti device, where the process was facilitated by the columnar boundaries in SiO_x. It is therefore suggested that the low resistance state in all three devices is due to electron transport through reduced TiO_x and/or MoO_x in the SiO_x layer. In the case of the Au-Ti device, these reduced metal-oxide filaments are located in column boundaries which span the SiO_x layer.

Conversely, negative electroforming in each device was shown to lead to O vacancies forming in the SiO_x layer. This was exaggerated in the Au device where a thick MoO_x layer was found to form and the SiO_x/Mo interface. In this case,

the expulsion of O through the Mo electrode column boundaries was also detected, resulting in the delamination of the Au-Ti device at the Mo/substrate interface. In the Au-Ti device, a similar reduction of the SiO_x layer was observed suggesting the low resistance state is due to electron transport through O vacancies. The subsequent resistive switching phenomenon in the Au-Ti device is suggested to be due to O exchange between the O vacancies and metal oxide (TiO_x and MoO_x) in the SiO_x layer. In the set state during a negative bias, the reduction of SiO_x is suggested to occur where the O binds to further oxidise TiO_x and MoO_x in the SiO_x column boundaries. In the reset state, the positive bias it is suggested to reduce TiO_x and MoO_x, where the released O recombines with O vacancies in SiO_x.

13.2 Future Work

The future work for part II of the thesis revolves around developing theoretical models of the Au-Ti device. In particular, a model of the metal filaments in the SiO_x columnar boundaries through DFT is expected to provide considerable insight into the operation of the device. Of particular importance is to develop a model of the O exchange between the metal-oxide filaments in the column boundaries and the SiO_x column bulk. Subsequently, the role of electrode Fermi energy and bias can be explored to determine if the resistive switching mechanism suggested in the previous section is feasible.

Chapter 14

Final Conclusions

The main objective of this thesis has been to develop a greater understanding of the dynamics involved in silicon oxide RRAM devices under electrical stress at the atomic and microscopic scales. However, it was not possible to study the same RRAM devices through both DFT and TEM. Instead, studies were carried out for DFT and TEM for different devices with the results given in Parts I and II of the thesis, respectively. In Part I of the thesis, the ECM mechanism in Ag/SiO_2 devices was investigated through DFT, with the models developed for the incorporation, diffusion, reduction and clustering of Ag metal in SiO_2. In Part II of the thesis, TEM was used to observe the structural dynamical processes involved in Me-SiO_x-Mo (Me = Au-Ti, Au and Ti) RRAM devices. This was achieved through characterisation of each device in their pristine and electroformed states. The results in each case show considerable overlap and provide a basis for the breakdown mechanisms in silicon oxide.

The controlling factor of the filament morphology was presence of columnar boundaries in the oxide layer. DFT calculations in this thesis show that Ag metal preferentially incorporates into silicon oxide through grain boundaries (though can also incorporate into large void like regions in the oxide surface). Subsequently, the metal is very mobile in the grain boundaries due to a requirement for low density regions to migrate. This is confirmed in through TEM measurements, where electrode metal oxide filaments were detected in the column boundary regions. These subsequently are shown to give the RRAM devices ECM resistive switching characteristics. Additionally, the devices concurrently show VCM properties, where electron injection was shown to lead to O vacancy creation through both DFT and TEM

methods. In this case, O and O vacancy dynamics were found to be pivotal in the operation of the devices. In this case, O exchange between the incorporated metal and O vacancies is suggested to give rise to the resistive switching phenomenon. As a result, properties such as the stoichiometry of the oxide layer and the electrode metal O affinity are shown to strongly affect device operation.

Bibliography

[1] Soumitra Dutta and Bruno Lanvin. *The Global Information Technology Report 2014 Rewards and Risks of Big Data*. 2014.

[2] Cong Xu, Xiangyu Dong, P. Jouppi Norman, and Yuan Xie. Design implications of memristor-based RRAM cross-point structures. *2011 Design, Automation & Test in Europe*, pages 1–6, 2011.

[3] Adnan Mehonic and Anthony J. Kenyon. Emulating the electrical activity of the neuron using a silicon oxide RRAM cell. *Frontiers in Neuroscience*, 10(FEB), 2016.

[4] T. W. Hickmott. Low-frequency negative resistance in thin anodic oxide films. *Journal of Applied Physics*, 33(9):2669–2682, 1962.

[5] K. L. Chopra. Avalanche-induced negative resistance in thin oxide films. *Journal of Applied Physics*, 36(1):184–187, 1965.

[6] W. R. Hiatt and T. W. Hickmott. Bistable switching in niobium oxide diodes. *Applied Physics Letters*, 6(6):106–108, 1965.

[7] G. Dearnaley, A. M Stoneham, and D. V. Morgan. Electrical Phenomena in Amorphous Oxide Films. *Rep. Prog. Phys.*, 33:1129–1191, 1970.

[8] Daniele Ielmini. Resistive switching memories based on metal oxides: mechanisms, reliability and scaling. *Semiconductor Science and Technology*, (6), 2016.

[9] Rainer Waser, Regina Dittmann, Ceorgi Staikov, and Kristof Szot. Redox-based resistive switching memories nanoionic mechanisms, prospects, and challenges. *Advanced Materials*, 21(25-26):2632–2663, 2009.

[10] Yuchao Yang, Peng Gao, Linze Li, Xiaoqing Pan, Stefan Tappertzhofen, ShinHyun Choi, Rainer Waser, Ilia Valov, and Wei D Lu. Electrochemical dynamics of nanoscale metallic inclusions in dielectrics. *Nature communications*, 5(May):4232, 2014.

[11] Yuchao Yang, Peng Gao, Siddharth Gaba, Ting Chang, Xiaoqing Pan, and Wei Lu. Observation of conducting filament growth in nanoscale resistive memories. *Nature Communications*, 3:732, 2012.

[12] Haitao Sun, Qi Liu, Congfei Li, Shibing Long, Hangbing Lv, Chong Bi, Zongliang Huo, Ling Li, and Ming Liu. Direct Observation of Conversion Between Threshold Switching and Memory Switching Induced by Conductive Filament Morphology. *Advanced Functional Materials*, 24(36):5679–5686, 2014.

[13] D Liu, H Cheng, R Peng, and Y Yin. Two resistive switching behaviors in Ag/SiO_2/Pt memristors. In *2016 IEEE 16th International Conference on Nanotechnology (IEEE-NANO)*, 2016.

[14] D Yu, L F Liu, B Chen, F F Zhang, B Gao, Y H Fu, X Y Liu, J F Kang, and X Zhang. Multilevel resistive switching characteristics in Ag/SiO_2/Pt RRAM devices. In *2011 IEEE International Conference of Electron Devices and Solid-State Circuits*, 2011.

[15] M. S. Munde, A. Mehonic, W. H. Ng, M. Buckwell, L. Montesi, M. Bosman, A. L. Shluger, and A. J. Kenyon. Intrinsic Resistance Switching in Amorphous Silicon Suboxides: The Role of Columnar Microstructure. *Scientific Reports*, 7(1):9274, 2017.

[16] Andrew R Leach. *Molecular modelling : principles and applications*. Prentice Hall, second edition, 2001.

[17] Joost Vandevondele, Matthias Krack, Fawzi Mohamed, Michele Parrinello, Thomas Chassaing, and Jürg Hutter. Quickstep: Fast and accurate density functional calculations using a mixed Gaussian and plane waves approach. *Computer Physics Communications*, 167(2):103–128, 2005.

[18] Thomas D Kühne, Marcella Iannuzzi, Mauro Del Ben, Vladimir V Rybkin, Patrick Seewald, Frederick Stein, Teodoro Laino, Rustam Z Khaliullin, Ole Schütt, Florian Schiffmann, Dorothea Golze, Jan Wilhelm, Sergey Chulkov, Mohammad Hossein Bani-Hashemian, Valéry Weber, Urban Borštnik, Mathieu Taillefumier, Alice Shoshana Jakobovits, Alfio Lazzaro, Hans Pabst, Tiziano Müller, Robert Schade, Manuel Guidon, Samuel Andermatt, Nico Holmberg, Gregory K Schenter, Anna Hehn, Augustin Bussy, Fabian Belleflamme, Gloria Tabacchi, Andreas Glöß, Michael Lass, Iain Bethune, Christopher J Mundy, Christian Plessl, Matt Watkins, Joost VandeVondele, Matthias Krack, and Jürg Hutter. CP2K: An electronic structure and molecular dynamics software package - Quickstep: Efficient and accurate electronic structure calculations. *The Journal of Chemical Physics*, 152(19):194103, 2020.

[19] G Kresse and J Furthmüller. Efficiency of ab-initio total energy calculations for metals and semiconductors using a plane-wave basis set. *Computational Materials Science*, 6(1):15–50, 1996.

[20] G Kresse and D Joubert. From ultrasoft pseudopotentials to the projector augmented-wave method. *Phys. Rev. B*, (3), 1999.

[21] M D Segall, Philip J D Lindan, M J Probert, C J Pickard, P J Hasnip, S J Clark, and M C Payne. First-principles simulation: ideas, illustrations and the CASTEP code. *Journal of Physics: Condensed Matter*, (11), 2002.

[22] Frank Jensen. Atomic orbital basis sets. *WIREs Computational Molecular Science*, 3(3):273–295, 2013.

[23] G Kresse and J Furthmüller. Efficient iterative schemes for ab initio total-energy calculations using a plane-wave basis set. *Phys. Rev. B*, (16), 1996.

[24] Geralf Lippert, Jurg Hutter, and Michele Parrinello. A hybrid Gaussian and plane wave density functional scheme. *Molecular Physics*, 92(3):477–488, 1997.

[25] S Goedecker, M Teter, and J Hutter. Separable dual-space Gaussian pseudopotentials. *Phys. Rev. B*, (3), 1996.

[26] Jonathon Cottom, Anton Bochkarev, Emilia Olsson, Kamal Patel, Manveer Munde, Jürgen Spitaler, Maxim N Popov, Michel Bosman, and Alexander L Shluger. Modeling of Diffusion and Incorporation of Interstitial Oxygen Ions at the TiN/SiO_2 Interface. *ACS Applied Materials & Interfaces*, (39), 2019.

[27] K Patel, J Cottom, M Bosman, A J Kenyon, and A L Shluger. An oxygen vacancy mediated Ag reduction and nucleation mechanism in SiO_2 RRAM devices. *Microelectronics Reliability*, 98:144–152, 2019.

[28] M. Krack. Pseudopotentials for H to Kr optimized for gradient-corrected exchange-correlation functionals. *Theoretical Chemistry Accounts*, 114(1-3):145–152, 2005.

[29] C Hartwigsen, S Goedecker, and J Hutter. Relativistic separable dual-space Gaussian pseudopotentials from H to Rn. *Phys. Rev. B*, (7), 1998.

[30] D M Ceperley and B J Alder. Ground State of the Electron Gas by a Stochastic Method. *Physical Review Letters*, (7), 1980.

[31] J P Perdew, K Burke, and M Ernzerhof. Generalized Gradient Approximation Made Simple. *Physical review letters*, 77(18):3865–3868, 1996.

[32] P Hohenberg and W Kohn. Inhomogeneous Electron Gas. *Phys. Rev.*, (3B), 1964.

[33] A. K. Rajagopal and J. Callaway. Inhomogeneous electron gas. *Physical Review B*, 7(5):1912–1919, 1973.

[34] A. D. Becke. Density-functional exchange-energy approximation with correct asymptotic behavior. *Physical Review A*, 38(6):3098–3100, 1988.

[35] Kieron Burke, John P Perdew, and Yue Wang. Derivation of a Generalized Gradient Approximation: The PW91 Density Functional. In John F Dobson, Giovanni Vignale, and Mukunda P Das, editors, *Electronic Density Functional Theory: Recent Progress and New Directions*, pages 81–111. Springer US, Boston, MA, 1998.

[36] Stefan Grimme. Density functional theory with London dispersion corrections. *WIREs Computational Molecular Science*, 1(2):211–228, 2011.

[37] Victor Polo, Elfi Kraka, and Dieter Cremer. Electron correlation and the self-interaction error of density functional theory. *Molecular Physics*, 100(11):1771–1790, 2002.

[38] Paula Mori-Sánchez, Aron J Cohen, and Weitao Yang. Many-electron self-interaction error in approximate density functionals. *The Journal of Chemical Physics*, 125(20):201102, 2006.

[39] Yan Zhao and Donald G Truhlar. Density Functional for Spectroscopy: No Long-Range Self-Interaction Error, Good Performance for Rydberg and Charge-Transfer States, and Better Performance on Average than B3LYP for Ground States. *The Journal of Physical Chemistry A*, (49), 2006.

[40] Manuel Guidon, Jürg Hutter, and Joost VandeVondele. Robust periodic Hartree-Fock exchange for large-scale simulations using Gaussian basis sets. *Journal of Chemical Theory and Computation*, 5(11):3010–3021, 2009.

[41] Manuel Guidon, Jürg Hutter, and Joost VandeVondele. Auxiliary Density Matrix Methods for HartreeFock Exchange Calculations. *Journal of Chemical Theory and Computation*, 6(8):2348–2364, 2010.

[42] S B Zhang and John E Northrup. Chemical potential dependence of defect formation energies in GaAs: Application to Ga self-diffusion. *Physical Review Letters*, (17), 1991.

[43] Stephan Lany and Alex Zunger. Assessment of correction methods for the band-gap problem and for finite-size effects in supercell defect calculations: Case studies for ZnO and GaAs. *Physical Review B*, 78(23):235104, 2008.

[44] Gianfranco Pacchioni, Anna Maria Ferrari, Antonio M Márquez, and Francesc Illas. Importance of Madelung potential in quantum chemical modeling of ionic surfaces. *Journal of Computational Chemistry*, (5), 1997.

[45] M Leslie and N J Gillan. The energy and elastic dipole tensor of defects in ionic crystals calculated by the supercell method. *Journal of Physics C: Solid State Physics*, (5), 1985.

[46] Daniel Sheppard, Rye Terrell, and Graeme Henkelman. Optimization methods for finding minimum energy paths. *The Journal of Chemical Physics*, 128(13):134106, 2008.

[47] Graeme Henkelman, Blas P Uberuaga, and Hannes Jónsson. A climbing image nudged elastic band method for finding saddle points and minimum energy paths. *The Journal of Chemical Physics*, 113(22):9901–9904, 2000.

[48] Hannes Jónsson, Greg Mills, and Karsten W Jacobson. Nudged elastic band method for finding minimum energy paths of transitions. In *Classical and Quantum Dynamics in Condensed Phase Simulations*, pages 385–404. World Scientific, 1998.

[49] R Elber and M Karplus. A method for determining reaction paths in large molecules: Application to myoglobin. *Chemical Physics Letters*, 139(5):375–380, 1987.

[50] D. C. Rapaport, Robin L. Blumberg, Susan R. McKay, and Wolfgang Christian. The Art of Molecular Dynamics Simulation. *Computers in Physics*, 1996.

[51] G Kresse and J Hafner. Ab initio molecular dynamics for liquid metals. *Phys. Rev. B*, (1), 1993.

[52] Christian Lubich. *From Quantum to Classical Molecular Dynamics: Reduced Models and Numerical Analysis*. American Chemical Society, 2009.

[53] J. Dana. Honeycutt and Hans C Andersen. Molecular dynamics study of melting and freezing of small Lennard-Jones clusters. *The Journal of Physical Chemistry*, (19), 1987.

[54] Loup Verlet. Computer "Experiments" on Classical Fluids. I. Thermodynamical Properties of Lennard-Jones Molecules. *Phys. Rev.*, (1), 1967.

[55] Tahir Çagin and John R Ray. Fundamental treatment of molecular-dynamics ensembles. *Phys. Rev. A*, (1), 1988.

[56] Hans C Andersen. Molecular dynamics simulations at constant pressure and/or temperature. *The Journal of Chemical Physics*, 72(4):2384–2393, 1980.

[57] Shūichi Nosé. A molecular dynamics method for simulations in the canonical ensemble. *Molecular Physics*, 52(2):255–268, 1984.

[58] D J Evans and B L Holian. The Nose–Hoover thermostat. *The Journal of Chemical Physics*, 83(8):4069–4074, 1985.

[59] Adnan Mehonic, Sébastien Cueff, Maciej Wojdak, Stephen Hudziak, Christophe Labbé, Richard Rizk, and Anthony J Kenyon. Electrically tailored resistance switching in silicon oxide. *Nanotechnology*, 23(45):455201, 2012.

[60] Adnan Mehonic, Mark Buckwell, Luca Montesi, Manveer Singh Munde, David Gao, Stephen Hudziak, Richard J. Chater, Sarah Fearn, David Mcphail, Michel Bosman, Alexander L. Shluger, and Anthony J. Kenyon. Nanoscale Transformations in Metastable, Amorphous, Silicon-Rich Silica. *Advanced Materials*, pages 7486–7493, 2016.

[61] S. Jun, T. E. McKnight, A. V. Melechko, M. L. Simpson, and P. D. Rack. Characterisation of reactively sputtered silicon oxide for thin-film transistor fabrication. *Electronics Letters*, (14), 2005.

[62] John A Thornton. Influence of apparatus geometry and deposition conditions on the structure and topography of thick sputtered coatings. *Journal of Vacuum Science and Technology*, 11(4):666–670, 1974.

[63] G S Bales and A Zangwill. Macroscopic model for columnar growth of amorphous films by sputter deposition. *Journal of Vacuum Science & Technology A*, 9(1):145–149, 1991.

[64] André Anders. A structure zone diagram including plasma-based deposition and ion etching. *Thin Solid Films*, 518(15):4087–4090, 2010.

[65] Peter M. Martin. *Handbook of Deposition Technologies for Films and Coatings*. William Andrew Publishing, third edition, 2010.

[66] M Knoll and E Ruska. Beitrag zur geometrischen Elektronenoptik. I. *Annalen der Physik*, 404(5):607–640, 1932.

[67] Gerd Binnig and Heinrich Rohrer. Scanning tunneling microscopy—from birth to adolescence. *Rev. Mod. Phys.*, (3), 1987.

[68] R. F. Egerton. Electron energy-loss spectroscopy in the TEM. *Reports on Progress in Physics*, 72(2):016502, 2009.

[69] John C. Russ. Energy Dispersive Spectrometers. In *Fundamentals of Energy Dispersive X-ray Analysis*. Butterworth-Heinemann, 1984.

[70] David B. Williams and C. Barry Carter. *Transmission electron microscopy: A textbook for materials science*. Springer, second edition, 2009.

[71] Max Haider, Harald Rose, Stephan Uhlemann, Eugen Schwan, Bernd Kabius, and Knut Urban. A spherical-aberration-corrected 200kV transmission electron microscope. *Ultramicroscopy*, 75(1):53–60, 1998.

[72] Akira Ishimaru. *Electromagnetic Wave Propagation, Radiation, and Scattering*. Wiley Online Books, 2017.

[73] Jun Yamasaki, Yuya Ubata, and Hidehiro Yasuda. Empirical determination of transmission attenuation curves in mass–thickness contrast TEM imaging. *Ultramicroscopy*, 200:20–27, 2019.

[74] M Wilkens, M L Jenkins, and K.-H. Katerbau. TEM diffraction contrast of lattice defects causing strain contrast and structure factor contrast simultaneously. *physica status solidi (a)*, 39(1):103–107, 1977.

[75] Max T Otten. High-Angle annular dark-field imaging on a tem/stem system. *Journal of Electron Microscopy Technique*, 17(2):221–230, 1991.

[76] C Jeanguillaume and C Colliex. Spectrum-image: The next step in EELS digital acquisition and processing. *Ultramicroscopy*, 28:252–257, 1989.

[77] Ondrej L. Krivanek, Alexander J. Gubbens, and Niklas Dellby. Developments in EELS instrumentation for spectroscopy and imaging. *Microsc. Microanal. Microstruct.*, 2(2):315–332, 1991.

[78] Kin Leong Pey, Nagarajan Raghavan, Xing Wu, Wenhu Liu, Xiang Li, Michel Bosman, Kalya Shubhakar, Zin Zar Lwin, Yining Chen, Hailang Qin, and Thomas Kauerauf. Physical analysis of breakdown in high-κ/metal gate stacks using TEM/EELS and STM for reliability enhancement (invited). *Microelectronic Engineering*, 88(7):1365–1372, 2011.

[79] M Bosman, Y Zhang, C K Cheng, X Li, X Wu, K L Pey, C T Lin, Y W Chen, S H Hsu, and C H Hsu. The distribution of chemical elements in Al- or La-capped high-κ metal gate stacks. *Applied Physics Letters*, 97(10):103504, 2010.

[80] Xing Wu, Kun Li, Nagarajan Raghavan, Michel Bosman, Qing-Xiao Wang, Dongkyu Cha, Xi-Xiang Zhang, and Kin-Leong Pey. Uncorrelated multiple conductive filament nucleation and rupture in ultra-thin high-κ dielectric based resistive random access memory. *Applied Physics Letters*, 99(9):93502, 2011.

[81] Phuc D. Ngo. Energy Dispersive Spectroscopy. In Lawrence C. Wagner, editor, *Failure Analysis of Integrated Circuits*. 1999.

[82] Joachim Mayer, Lucille A Giannuzzi, Takeo Kamino, and Joseph Michael. TEM Sample Preparation and FIB-Induced Damage. *MRS Bulletin*, 32(5):400–407, 2007.

[83] J Joshua Yang, Dmitri B Strukov, and Duncan R Stewart. Memristive devices for computing. *Nature Nanotechnology*, 8(1):13–24, 2013.

[84] R. M. Ferullo, G. R. Garda, P. G. Belelli, M. M. Branda, and N. J. Castellani. Deposition of small Cu, Ag and Au particles on reduced SiO_2. *Journal of Molecular Structure: THEOCHEM*, 769(1-3):217–223, 2006.

[85] Ming He and Toh Ming Lu. Metal-Dielectric Interfaces in Gigascale Electronics: Thermal and Electrical Stability. *Springer Series in Materials Science*, 157(1), 2012.

[86] Nikita I. Vakula, Gulnara M. Kuramshina, Leonid G. Gorb, Frances Hill, and Jerzy Leszczynski. Adsorption and diffusion of a silver atom and its cation on α-SiO_2 (0 0 1): Comparison of a pure surface with a surface containing an Al defect. *Chemical Physics Letters*, 567:27–33, 2013.

[87] J. D. McBrayer, R. M. Swanson, and T. W. Sigmon. Diffusion of Metals in Silicon Dioxide. *Journal of The Electrochemical Society*, 133(6):1242, 1986.

[88] A Suzuki and Y Mishin. Atomic mechanisms of grain boundary diffusion: Low versus high temperatures. *Journal of Materials Science*, 40(12):3155–3161, 2005.

[89] Anne Simo, Jorg Polte, Norbert Pfander, Ulla Vainio, Franziska Emmerling, and Klaus Rademann. Formation mechanism of silver nanoparticles stabilized in glassy matrices. *Journal of the American Chemical Society*, 134(45):18824–18833, 2012.

[90] Stefan Wackerow, Gerhard Seifert, and Amin Abdolvand. Homogenous silver-doped nanocomposite glass. *Opt. Mater. Express*, (7), 2011.

[91] Qingsheng Ran, Richard W. Schmude, Karl A. Gingerich, Dale W. Wilhite, and Joseph E. Kingcade. Dissociation energy and enthalpy of formation of gaseous silver dimer. *The Journal of Physical Chemistry*, 97(32):8535–8540, 1993.

[92] D. M. Guzman, N. Onofrio, and A. Strachan. First principles investigation of copper and silver intercalated molybdenum disulfide. *Journal of Applied Physics*, 121(5):055703, 2017.

[93] P H Davis and J A Weil. Silver atom center in α-quartz. *Journal of Physics and Chemistry of Solids*, 39(7):775–780, 1978.

[94] P H Davis, C Y Huang, and J A Weil. Paramagnetic aluminum-silver centers in α-quartz. *Journal of Physics and Chemistry of Solids*, 39(8):897–899, 1978.

[95] John H Mackey. EPR Study of Impurity-Related Color Centers in Germanium-Doped Quartz. *The Journal of Chemical Physics*, 39(1):74–83, 1963.

[96] Anatoly Trukhin and Kaspars Truhins. Luminescence of alpha-quartz. *arXiv: Materials Science*, (1209.4200), 2012.

[97] Joost VandeVondele and Jürg Hutter. Gaussian basis sets for accurate calculations on molecular systems in gas and condensed phases. *The Journal of Chemical Physics*, 127(11):114105, 2007.

[98] John P. Perdew, Kieron Burke, and Matthias Ernzerhof. Generalized Gradient Approximation Made Simple. *Physical Review Letters*, 77(18):3865–3868, 1996.

[99] A D Becke. Density-functional exchange-energy approximation with correct asymptotic behavior. *Phys. Rev. A*, (6), 1988.

[100] Chengteh Lee, Weitao Yang, and Robert G Parr. Development of the Colle-Salvetti correlation-energy formula into a functional of the electron density. *Phys. Rev. B*, (2), 1988.

[101] P J Stephens, F J Devlin, C F Chabalowski, and M J Frisch. Ab Initio Calculation of Vibrational Absorption and Circular Dichroism Spectra Using Density Functional Force Fields. *The Journal of Physical Chemistry*, (45), 1994.

[102] Jack Strand, Sergey K Chulkov, Matthew B Watkins, and Alexander L Shluger. First principles calculations of optical properties for oxygen vacancies in binary metal oxides. *The Journal of Chemical Physics*, 150(4):44702, 2019.

[103] John A. Weil and James R. Bolton. *Electron Paramagnetic Resonance: Elementary Theory and Practical Applications, Second Edition*. John Wiley & Sons, 2006.

[104] Frank Jensen. The Basis Set Convergence of Spin Spin Coupling Constants Calculated by Density Functional Methods. *Journal of Chemical Theory and Computation*, (5), 2006.

[105] G Gruber, J Cottom, R Meszaros, M Koch, G Pobegen, T Aichinger, D Peters, and P Hadley. Electrically detected magnetic resonance of carbon dangling bonds at the Si-face 4H-SiC/SiO_2 interface. *Journal of Applied Physics*, 123(16):161514, 2018.

[106] Robert K Sato and Paul F McMillan. An infrared and Raman study of the isotopic species of α-quartz. *The Journal of Physical Chemistry*, (13), 1987.

[107] E.R. Lippincott, A. Vanvalkenburg, C.E. Weir, and E.N. Bunting. Infrared studies on polymorphs of silicon dioxide and germanium dioxide. *Journal of Research of the National Bureau of Standards*, 1958.

[108] Jeppe Gavnholt, Thomas Olsen, Mads Engelund, and Jakob Schiøtz. Δ self-consistent field method to obtain potential energy surfaces of excited molecules on surfaces. *Phys. Rev. B*, (7), 2008.

[109] T C Nason, G R Yang, K H Park, T M Lu, T C Nason, G Yang, K Park, and T Lu. Study of silver diffusion into Si (111) and SiO_2 at moderate temperatures. *Journal of Applied Physics*, 70(3):1392–1396, 1991.

[110] Yuchao Yang, Peng Gao, Siddharth Gaba, Ting Chang, Xiaoqing Pan, and Wei Lu. Observation of conducting filament growth in nanoscale resistive memories. *Nature Communications*, 3:732, 2012.

[111] Sanghamitra Mukhopadhyay, Peter V Sushko, A Marshall Stoneham, and Alexander L Shluger. Modeling of the structure and properties of oxygen vacancies in amorphous silica. *Phys. Rev. B*, (19), 2004.

[112] Mingyang Chen, Jason E Dyer, Keijing Li, and David A Dixon. Prediction of Structures and Atomization Energies of Small Silver Clusters. *The Journal of Physical Chemistry A*, (34), 2013.

[113] Albert Rimola, Dominique Costa, Mariona Sodupe, Jean-François Lambert, and Piero Ugliengo. Silica Surface Features and Their Role in the Adsorp-

tion of Biomolecules: Computational Modeling and Experiments. *Chemical Reviews*, (6), 2013.

[114] L T Zhuravlev. The surface chemistry of amorphous silica. Zhuravlev model. *Colloids and Surfaces A: Physicochemical and Engineering Aspects*, 173(1):1–38, 2000.

[115] Aleix Comas-Vives. Amorphous SiO_2 surface models: energetics of the dehydroxylation process, strain, ab initio atomistic thermodynamics and IR spectroscopic signatures. *Phys. Chem. Chem. Phys.*, 18(10):7475–7482, 2016.

[116] Fernando Rascón, Raphael Wischert, and Christophe Copéret. Molecular nature of support effects in single-site heterogeneous catalysts: silica vs alumina. *Chem. Sci.*, 2(8):1449–1456, 2011.

[117] E Masetti, J Bulir, S Gagliardi, V Janicki, A Krasilnikova, G Di Santo, and C Coluzza. Ellipsometric and XPS analysis of the interface between silver and SiO_2, TiO_2 and SiNx thin films. *Thin Solid Films*, 456:468–472, 2004.

[118] Al Moatasem El-Sayed, Matthew B. Watkins, Alexander L. Shluger, and Valeri V. Afanas'ev. Identification of intrinsic electron trapping sites in bulk amorphous silica from ab initio calculations. *Microelectronic Engineering*, 109:68–71, 2013.

[119] W. Martienssen and Hans Warlimont. *Springer Handbook of Condensed Matter and Materials Data*. Springer-Verlag Berlin Heidelberg, first edition, 2005.

[120] Katharina Vollmayr, Walter Kob, and Kurt Binder. Cooling-rate effects in amorphous silica: A computer-simulation study. *Phys. Rev. B*, (22), 1996.

[121] Lester Guttman. Ring structure of the crystalline and amorphous forms of silicon dioxide. *Journal of Non-Crystalline Solids*, 116(2):145–147, 1990.

[122] Yunliang Yue, Yu Song, and Xu Zuo. First principles study of oxygen vacancy defects in amorphous SiO_2. *AIP Advances*, 7(1):15309, 2017.

[123] Kwan Chi Kao. *Dielectric Phenomena in Solids*. Academic Press, 2004.

[124] J Joshua Yang, Dmitri B Strukov, and Duncan R Stewart. Memristive devices for computing. *Nature nanotechnology*, 8(1):13–24, 2013.

[125] Al Moatasem El-Sayed, Matthew B. Watkins, Alexander L. Shluger, and Valeri V. Afanas'ev. Identification of intrinsic electron trapping sites in bulk amorphous silica from ab initio calculations. *Microelectronic Engineering*, 109:68–71, 2013.

[126] Ting-Chang Chang, Kuan-Chang Chang, Tsung-Ming Tsai, Tian-Jian Chu, and Simon M Sze. Resistance random access memory. *Materials Today*, 19(5):254–264, 2016.

[127] A Mehonic, A Vrajitoarea, S Cueff, S Hudziak, H Howe, C Labbé, R Rizk, M Pepper, and A J Kenyon. Quantum Conductance in Silicon Oxide Resistive Memory Devices. *Scientific Reports*, 3:2708, 2013.

[128] Gunuk Wang, Yang Yang, Jae-Hwang Lee, Vera Abramova, Huilong Fei, Gedeng Ruan, Edwin L Thomas, and James M Tour. Nanoporous Silicon Oxide Memory. *Nano Letters*, (8), 2014.

[129] Adnan Mehonic, Sébastien Cueff, Maciej Wojdak, Stephen Hudziak, Olivier Jambois, Christophe Labbé, Blas Garrido, Richard Rizk, and Anthony J Kenyon. Resistive switching in silicon suboxide films. *Journal of Applied Physics*, 111(7):74507, 2012.

[130] Manveer S. Munde, David Z. Gao, and Alexander L. Shluger. Diffusion and aggregation of oxygen vacancies in amorphous silica. *Journal of Physics: Condensed Matter*, 29(24):245701, 2017.

[131] David Z Gao, Al-Moatasem El-Sayed, and Alexander L Shluger. A mechanism for Frenkel defect creation in amorphous SiO_2 facilitated by electron injection. *Nanotechnology*, 27(50):505207, 2016.

[132] D E Eastman. Photoelectric Work Functions of Transition, Rare-Earth, and Noble Metals. *Physical Review B*, (1), 1970.

[133] K Yu-Zhang, G Boisjolly, J Rivory, L Kilian, and C Colliex. Characterization of TiO_2/SiO_2 multilayers by high resolution transmission electron microscopy and electron energy loss spectroscopy. *Thin Solid Films*, 253(1):299–302, 1994.

[134] H Kurata, E Lefèvre, C Colliex, and R Brydson. Electron-energy-loss near-edge structures in the oxygen K-edge spectra of transition-metal oxides. *Phys. Rev. B*, (20), 1993.

[135] L Lajaunie, F Boucher, R Dessapt, and P Moreau. Quantitative use of electron energy-loss spectroscopy Mo-$M_{2,3}$ edges for the study of molybdenum oxides. *Ultramicroscopy*, 149:1–8, 2015.

[136] Wolfgang Windl, Tao Liang, Sergei Lopatin, and Gerd Duscher. Modeling and characterization of atomically sharp "perfect" Ge/SiO_2 interfaces. *Materials Science and Engineering: B*, 114-115:156–161, 2004.

[137] E Stoyanov, F Langenhorst, and G Steinle-Neumann. The effect of valence state and site geometry on Ti $L_{3,2}$ and O K electron energy-loss spectra of Ti_xO_y phases. *American Mineralogist*, (4), 2007.

[138] Chun Hu, Yuchao Tang, Zheng Jiang, Zhengping Hao, Hongxiao Tang, and Po Keung Wong. Characterization and photocatalytic activity of noble-metal-supported surface TiO_2/SiO_2. *Applied Catalysis A: General*, 253(2):389–396, 2003.

[139] Michiko Yoshitake, Shinjiro Yagyu, and Toyohiro Chikyow. A Numerical Formula for General Prediction of Interface Bonding between Alu-

mina and Aluminum-Containing Alloys. *International Journal of Metals*, 2014:120840, 2014.

[140] K Inzani, M Nematollahi, F Vullum-Bruer, T Grande, T W Reenaas, and S M Selbach. Electronic properties of reduced molybdenum oxides. *Phys. Chem. Chem. Phys.*, 19(13):9232–9245, 2017.

[141] André L Fernandes Cauduro, Zacarias E Fabrim, Mehrad Ahmadpour, Paulo F P Fichtner, Søren Hassing, Horst-Günter Rubahn, and Morten Madsen. Tuning the optoelectronic properties of amorphous MoO_x films by reactive sputtering. *Applied Physics Letters*, 106(20):202101, 2015.

[142] O Banakh, P E Schmid, R Sanjinés, and F Lévy. Electrical and optical properties of TiO_x thin films deposited by reactive magnetron sputtering. *Surface and Coatings Technology*, 151-152:272–275, 2002.

[143] B Satpati, P V Satyam, T Som, and B N Dev. Nanoscale ion-beam mixing in Au–Si and Ag–Si eutectic systems. *Applied Physics A*, 79(3):447–451, 2004.

[144] Nobuyuki Fujimura, Akio Ohta, Hideki Murakami, Katsunori Makihara, A Ohta, H Murakami, S Higashi, Kai Han, Xiaolei Wang, Li Yuan, Nguyen Xuan Truyen, N Tatemizo, S Imada, Y Miura, Nobuyuki Fujimura, and Seiichi Miyazaki. Evaluation of valence band top and electron affinity of SiO_2 and Si-based semiconductors using X-ray photoelectron spectroscopy. *Jpn. J. Appl. Phys*, 55:8–6, 2016.

[145] Corsin Battaglia, Xingtian Yin, Maxwell Zheng, Ian D Sharp, Teresa Chen, Stephen McDonnell, Angelica Azcatl, Carlo Carraro, Biwu Ma, Roya Maboudian, Robert. M Wallace, and Ali Javey. Hole Selective MoO_x Contact for Silicon Solar Cells. *Nano Letters*, (2), 2014.

[146] M Lottiaux, C Boulesteix, G Nihoul, F Varnier, F Flory, R Galindo, and E Pelletier. Morphology and structure of TiO_2 thin layers vs. thickness and substrate temperature. *Thin Solid Films*, 170(1):107–126, 1989.

[147] Egle Conforto and Daniel Caillard. A fast method for determining favourable orientation relationships and interface planes: Application to titanium–titanium hydrides transformations. *Acta Materialia*, 55(3):785–798, 2007.

[148] P Jonnard, C Bonnelle, A Bosseboeuf, K Danaie, and E Beauprez. Investigation of an Mo/SiO_2 interface by electron-induced x-ray emission spectroscopy. *Surface and Interface Analysis*, (4), 2000.